Czech Technical University in Prague
Faculty of Electrical Engineering
Department of Electric Drives and Traction

BIFURCATION ANALYSIS AND CONTROL METHODS FOR INDUCTIVELY COUPLED POWER TRANSFER

Doctoral Thesis

Ing. Michal Košík

Prague, July 2021

Ph.D. Program: Electrical Engineering and Information Technology, P2612
Branch of Study: Electrical Machines, Apparatus and Drives, 2642V004

Supervisor: Prof. Ing. Jiří Lettl, CSc.

Declaration

I hereby declare that I have written my doctoral thesis on my own and I have used only the literature listed at the end of the doctoral thesis in the references.

…….

Michal Košík

Acknowledgement

This thesis is the result of my Ph.D. studies at the Department of Electric Drives and Traction, Faculty of Electrical Engineering, Czech Technical University in Prague. They provided me with support, equipment and help. The submitted work was also partly supported by the internal student grants of the CTU in Prague.

I would like to give my thanks to my colleagues, who helped me during my study at the university. Namely they are Ing. Jan Bauer, Ph.D., Ing. Pavel Skarolek, Ing. Pavel Karlovský, Ph.D., prof. Ing. Václav Papež, CSc., Ing. František Mazánek, and Ing. Pavel Hrzina, Ph.D.

Further, I would like to thank my supervisor, prof. Ing. Jiří Lettl, CSc, for his support, guidance, and the advices he gave me during my Ph.D. studies.

Also, I would like to give thanks to Aaron D. Scher for great collaboration on the research of inductive power transfer and for a valuable feedback.

Finally, I would like to express my gratitude to my parents, my family, and my close friends for their care and support.

Abstract

The field of inductive power transfer (IPT) experienced fast development in last thirty years. Thanks to the improved safety, durability, and ease of use in comparison with the conductive connection, IPT founds its use in many applications, such as industrial systems (material handling systems, cranes, etc.), portable consumer electronics (cellular phones, smart watches, electric toothbrushes, etc.), electric vehicles (charging of battery electric vehicles and powering of railway electric vehicles), medical applications (e.g., biomedical implants), special applications (clean or corrosive environments) and others.

During the operation of the IPT systems bifurcation occurs under certain circumstances, which negatively affects the operation. The term "bifurcation" refers to splitting of a single frequency in which the phase of the input impedance equals zero into three. This work is aimed to analyze bifurcation and examine the control methods to prevent its occurrence or mitigate the connected negative effects. However, there is another phenomenon closely related to bifurcation, which is called frequency splitting. The term "frequency splitting" refers to the splitting of the single output power maximum into two at different frequencies. While these two important phenomena are related, they are commonly analyzed separately without examining an underlying principle or mechanism that links them together. To rectify this, frequency splitting is also incorporated in the analysis presented in this work.

First part of the thesis prepares a framework for bifurcation and frequency splitting analysis and evaluation. In the literature, there exists a convenient description of bifurcation based on generalized system parameters, but there is no such counterpart for frequency splitting. Novel general parameter model presented in this work establishes a normalized description of both the bifurcation and frequency splitting phenomena based only three parameters. Experimental measurements and simulations are used to verify the presented model and results. The description of bifurcation and frequency splitting is summarized in the Q_L state diagram, which is a novel versatile tool for the visual evaluation.

Under this framework, the bifurcation and frequency splitting phenomena are analyzed in the second part of the thesis. The mechanism of phenomena emergence is examined together with the influence of equivalent circuit parameters (e.g., coil inductances, resonance frequency, etc.).

The third part evaluates the impacts of bifurcation and frequency splitting phenomena on the selection of the operating area and the IPT system regulation.

The fourth part of the work examines the control methods to prevent or mitigate negative effects on IPT system operation resulting from the bifurcation and frequency splitting phenomena. These methods are divided between passive (design based) and active (measures adjusting the system during operation). Selected methods are evaluated by measurements and simulations.

The thesis contributions can be summarized as follows. Current description of the bifurcation and frequency splitting phenomena is rather fractured and confusing. The thesis clearly defines the concepts, unifies their mathematical descriptions, and analyses the underlying connections between the phenomena. A novel approach for bifurcation and frequency splitting phenomena evaluation in IPT systems is presented (general parameter model), which uses novel visualization tools (Q_L state diagram and its sections). The work provides an evaluation and theoretical background for bifurcation and frequency splitting control methods.

Keywords

Inductive power transfer, wireless power transfer, resonance, bifurcation, frequency splitting.

Abstrakt

Technologie bezkontaktního přenosu zažila v posledních třiceti letech prudký rozvoj. Díky lepší bezpečnosti, odolnosti a ergonomii v porovnání s vodivým propojením nalézá bezkontaktní přenos své uplatnění v řadě aplikací, jako jsou průmyslové systémy (montážní linky, jeřáby apod.), přenosná spotřební elektronika (mobilní telefony, chytré hodinky, elektrické zubní kartáčky atd.), elektrická vozidla (dobíjení bateriových elektrických vozidel a napájení závislých trakčních vozidel), medicínské přístroje (např. implantáty), speciální aplikace (čistá nebo naopak korozivní prostředí) a další.

Za určitých okolností nastává během činnosti bezkontaktních systémů bifurkace, která negativně ovlivňuje činnost zařízení. Termín „bifurkace“ označuje štěpení jediné frekvence, na které je fáze vstupní impedance rovna nule, na tři. Tato práce cílí provést analýzu bifurkace a prozkoumat řídicí metody určené k potlačení jejího výskytu nebo případně zmírnění negativních jevů spojených s bifurkací. Nicméně další podobný bifurkaci se projevuje během činnosti zařízení. Tímto jevem je „štěpení frekvence“ (frequency splitting), což označuje štěpení jediného maxima výstupního výkonu na dvě, která nastávají na jiných frekvencích. Ačkoliv jsou tyto jevy příbuzné, jsou typicky analyzovány každý zvlášť, aniž by byl prozkoumán možný základní mechanismus, který by je spojoval dohromady. Aby se toto napravilo, štěpení frekvence je zahrnuto do analýzy prezentované v této práci.

První část disertační práce představuje matematický rámec pro analýzu a vyhodnocení bifurkace a štěpení frekvence. V literatuře lze nalézt výhodný matematický popis bifurkace založený na obecných parametrech, avšak zatím neexistuje podobný popis štěpení frekvence. Nový model obecných parametrů (general paramter model) prezentovaný v této práci zavádí normalizovaný popis obou jevů založený jen na třech parametrech. Prezentovaný model a výsledky jsou ověřeny pomocí experimentálních měření a simulací. Popis bifurkace a štěpení frekvence je shrnut v Q_L stavovém diagramu (Q_L state diagram), což je nový všestranný nástroj k vizuální analýze.

Bifurkace a štěpení frekvence jsou popsány v rámci prezentovaného modelu popsány v druhé časti práce. Mechanismus vzniku daných jevů je prozkoumán spolu s analýzou vlivu parametrů náhradního obvodového schématu, jako jsou například indukčnosti cívek, rezonanční frekvence atd.

Třetí část práce se zabývá vyhodnocením dopadů bifurkace a štěpení frekvence na výběr pracovní oblasti a na regulaci.

Čtvrtá část práce vyhodnocuje metody řízení bifurkace a štěpení frekvence, které buď zabrání jejich výskytu, nebo zmírní jejich negativní dopady na činnost systému bezkontaktního přenosu. Tyto metody se dělí na pasivní (použité v návrhové fázi) a na aktivní (opatření upravující činnost systému za provozu). Vybrané metody jsou otestovány měřením a simulací.

Přínosy této práce mohou být shrnuty následovně: Současný popis bifurkace a štěpení frekvence je poněkud roztříštěný a matoucí. Tato práce jasně vymezuje jednotlivé pojmy, sjednocuje matematický popis a analyzuje základní mechanismus spojující tyto jevy. Nový přístup pro vyhodnocení jevů bifurkace a štěpení frekvence v systémech pro bezkontaktní přenos energie je prezentován (model obecných parametrů), který využívá nový nástroj pro vizuální analýzu (Q_L stavový diagram). Tato práce také prezentuje vyhodnocení a teoretické pozadí pro metody řízení bifurkace a štěpení frekvence.

Klíčová slova

Bezkontaktní přenos energie, indukční přenos energie, rezonance, bifurkace, štěpení frekvence.

List of Content

List of Figures

List of Tables

List of Used Acronyms

EXISTING ACRONYMS

AC	Alternating current.
AET	Acoustic energy transfer.
AIM	Adaptive impedance matching.
BPP	Bipolar pad.
CP	Circular pad.
CPT	In this thesis refers to the capacitive power transfer. However, some cited sources use acronym CPT for contactless power transfer while addressing IPT. This is noted in the thesis text along the source reference.
CSV	Comma separated values.
DC	Direct current.
DDP	Double D pad.
DDQP	Double D – quadrature pad.
DLCC	Double-sided LCC (compensation topology).
EMC	Electromagnetic compatibility.
EMI	Electromagnetic interference.
ESR	Equivalent series resistance.
EV	Electric vehicle.
FEM	Finite element method.
FPP	Flux-pipe pad.
GaN	Gallium nitride.
HF	High frequency.
ICPT	Inductively coupled power transfer. ICPT is same as IPT.
IPT	Inductive power transfer.
ISM	Industrial, scientific and medical radio band.
OLEV	On-line electric vehicle. Dynamically charged EV.
PLL	Phase-locked loop.
MPT	Microwave power transfer.
PCB	Printed circuit board.
PFC	Power factor correction.
PP	Parallel-parallel (compensation topology).
PS	Parallel-series (compensation topology).
RF	Radio frequency.
SiC	Silicon carbide.
SP	Series-parallel (compensation topology).
SS	Series-series (compensation topology).
TPBP	Three-phase bipolar pad.
TPP	Tripolar pad.
WoS	Web of Science.
WoW	Workshop on Emerging Technologies: Wireless Power.
WPT	Wireless power transfer. In this work used as the overall term encompassing AET, CPT, IPT, MPT, etc.
WPTC	Wireless Power Transfer Conference.
WPW	Wireless Power Week.
ZCS	Zero-current switching.
ZPA	Zero-phase angle. At ZPA frequencies the phase angle φ_{in} between the input current $\hat{I}_{in}$ and voltage $\hat{V}_{in}$ is equal to zero.
ZVS	Zero voltage switching.

NEWLY INTRODUCED ACRONYMS

IAB	Input amplitude bifurcation, defined as splitting of the input impedance amplitude Z minimum. Describes also splitting of the input current amplitude I_{in}.

OAB Output amplitude bifurcation (frequency splitting), defined as splitting of the output power P_{out} maximum. Describes also splitting of the output current and voltage amplitudes I_{out}, V_{out} and input active power P_{in} maximum.

PB Phase bifurcation, defined as splitting of the initial ZPA frequency corresponding to the resonance frequency f_0.

BB1 First bifurcation boundary, at which Z minimum (IAB) or P_{out} maximum (OAB) begins to move away from the resonance frequency f_0. $\mathrm{BB1_i}$ is connected with IAB and $\mathrm{BB1_o}$ with OAB.

BB2 Second bifurcation boundary, at IAB or OAB occurs (Z minimum or P_{out} maximum splits). $\mathrm{BB2_i}$ refers to IAB and $\mathrm{BB2_o}$ to OAB.

BB3 Third bifurcation boundary, at which PB occurs.

RG1 1st region of the course of bifurcation, in which no bifurcation phenomena occur. The operating point is above BB1 in the Q_L state diagram. $\mathrm{RG1_i}$ refers to IAB and $\mathrm{RG1_o}$ to OAB.

RG2 2nd region of the course of bifurcation, in which the minimum of Z (IAB) or maximum of P_{out} (OAB) moves away from the resonance frequency f_0. The operating point is between BB1 and BB2 in the Q_L state diagram. $\mathrm{RG2_i}$ refers to IAB and $\mathrm{RG2_o}$ to OAB.

RG3 3rd region of the course of bifurcation, in which the amplitude bifurcation (IAB or OAB) occurs but PB does not. The operating point is between BB2 and BB3 in Q_L state diagram. $\mathrm{RG3_i}$ refers to IAB and $\mathrm{RG3_o}$ to OAB.

RG4 4th region of the course of bifurcation, in which both amplitude bifurcation (IAB or OAB) and PB occur. The operating point is below BB3 in Q_L state diagram. The same for both IAB and OAB.

List of Used Symbols

$\hat{X}$ refers to a phasor represented by complex number, X to its amplitude

C_p	Primary compensation capacity.
C_s	Secondary compensation capacity.
f	Operating frequency.
f_0	Resonance frequency.
f_{0p}	Primary resonance frequency.
f_{0s}	Secondary resonance frequency.
$\hat{I}_{in}$	Input current. Used as reference. I_{in} marks its amplitude.
$\hat{I}_{out}$	Output current. I_{out} marks its amplitude.
k	Coupling coefficient.
L_{CS}	Current shunt inductance.
L_p	Primary coil inductance.
L_s	Secondary coil inductance.
M	Mutual inductance.
P_{in}	Input active power.
P_{out}	Output active power.
P_{rc}	Received active power.
P_{tr}	Transferred active power.
Q_{Lp}	Primary side loaded quality factor.
Q_{Ls}	Secondary side loaded quality factor.
Q_p	Primary coil quality factor.
Q_s	Secondary coil quality factor.
R_{CS}	Current shunt resistance.
R_L	Equivalent load resistance.
R_p	Primary ESR.
R_r	Reflected resistance. Real part of the reflected impedance $\hat{Z}_r$.
R_s	Secondary ESR.
R_{sL}	Adjusted load resistance. R_{sL} is the sum of R_s and R_L.
u	Normalized frequency.
u_{ai0}, u_{ai1}, u_{ai2}	Normalized IAB frequencies. u_{ai} describes the initial Z minimum, while u_{ai0} and u_{ai2} describe the Z maximum and Z minimum, respectively, which emerge after IAB occurs.
u_{ao0}, u_{ao} , u_{ao}	Normalized OAB frequencies. u_{ao} describes the initial P_{out} maximum, while u_{ao0} and u_{ao2} describe the P_{out} minimum and P_{out} maximum, respectively, which emerge after OAB occurs.
$u_{\varphi 0}$, $u_{\varphi 1}$, $u_{\varphi 2}$	Normalized PB frequencies. $u_{\varphi 0}$ describes the initial ZPA frequency, while $u_{\varphi 1}$ and $u_{\varphi 2}$ describe the additional ZPA frequencies emerging after PB occurs.
$\hat{V}_{CCP}$	Primary side compensation capacity voltage. V_{CCP} marks its amplitude.
$\hat{V}_{CCS}$	Secondary side compensation capacity voltage. V_{CCS} marks its amplitude.
$\hat{V}_{CoilP}$	Primary coil voltage. V_{CoilP} marks its amplitude.
$\hat{V}_{CoilS}$	Secondary coil voltage. V_{CoilS} marks its amplitude.
$\hat{V}_{CS}$	Current shunt voltage. V_{CS} marks its amplitude.
$\hat{V}_{in}$	Input voltage. Used as reference. V_{in} marks its amplitude.
$\hat{V}_{ip}$	Induced voltage in the primary. V_{ip} marks its amplitude.
$\hat{V}_{is}$	Induced voltage in the secondary. V_{is} marks its amplitude.
$\hat{V}_{out}$	Output voltage. V_{out} marks its amplitude.
X_p	Primary side reactance.
X_r	Reflected reactance. Imaginary part of the reflected impedance $\hat{Z}_r$.
X_s	Secondary side reactance.
$\hat{Z}$	Input impedance. Z marks its amplitude.
$\hat{Z}_p$	Primary side impedance. Z_p marks its amplitude.

$\hat{Z}_r$	Reflected impedance. Z_r marks its amplitude.
$\hat{Z}_s$	Secondary impedance. Z_s marks its amplitude.
φ_{in}	Input phase (phase angle from $\hat{I}_{in}$ to $\hat{V}_{in}$).
φ_{io}	Phase angle from $\hat{I}_{in}$ to $\hat{I}_{out}$.
η_p	Primary side efficiency.
η_s	Secondary side efficiency.
η_{tr}	IPT transformer efficiency
ω	Operating angular frequency.
ω_0	Common resonance angular frequency.
ω_{0p}	Primary resonance angular frequency.
ω_{0s}	Secondary resonance angular frequency.

1 Introduction

Inductively coupled power transfer (ICPT) is a method to transfer power by magnetic field between two coils instead of wired connection. In the rest of the thesis the more common name inductive power transfer (IPT) is used instead of ICPT. The origins of IPT [1]–[3] can be traced to Nikola Tesla, who at the beginning of the 20th century proposed the first systems for wireless power transfer [4]. However, it was not until the 1990s that the first industrial applications of the technology were developed, based on the research of A. W. Green, J. T. Boys and others (e.g. [5]) from the University of Auckland. Nowadays, thanks to its ease of use, increased safety, increased durability and improved aesthetics [2], [6], IPT is an emerging technology finding its applications in many fields: material handling systems such as cranes or factory transport systems [2], [7], electric vehicle (EV) charging [6], consumer electronics [1], [8], biomedical applications [9], [10], etc. Several standards were developed to ensure interoperability of devices produced by different manufacturers, e.g. Qi [11]–[13] or AirFuel [14] for consumer electronics and SAE J2954 [15] or IEC 61980 [16] for electric vehicle charging.

The typical system for inductive power transfer is formed by a single transmitter and single receiver, which are both based on resonant circuits [1], [6]. The alternating current flows through the transmitter coil and generates the magnetic field. Part of the magnetic flux closes through the receiver coil, where it induces voltage. The coil inductance in combination with the compensation capacity determines the resonance frequency of each side. If the resonance frequencies of the transmitter and receiver are the same and the power source operates at this frequency, the impedance of the coupled circuits is only resistive and the power transfer is maximal [2].

The IPT operation is affected by two closely related phenomena: bifurcation [17] and frequency splitting [18], [19]. In inductive power transfer systems, “bifurcation” refers to splitting of the frequency in which the phase of the input impedance equals zero, while “frequency splitting” refers to the splitting of the output power maxima. While these two important phenomena are related, they are commonly analyzed separately without examining an underlying principle or mechanism that links them together.

The thesis is aimed to examine the bifurcation and its control methods. However, it is necessary to consider the frequency splitting in the analysis due to its similarity to bifurcation. The analysis of frequency splitting (i.e., splitting of the output power maxima) also requires mathematical description of the splitting of the input impedance amplitude minima. The analysis results presented in this thesis show that all three phenomena (bifurcation, frequency splitting, splitting of the input impedance amplitude minima) are results of growing reflected impedance, i.e., growing secondary side influence on the primary. These findings cause a shift of perspective: there are not three separate phenomena, but only three manifestations of a single phenomenon, which is a growing secondary side influence (i.e., reflected impedance) impacting the primary side.

To reflect these results and improve the comprehensiveness of the thesis, novel nomenclature is proposed, which can be summarized as follows. Bifurcation is a process of growing secondary side influence (represented by an increasing reflected impedance) on the primary side, which manifests as the phase bifurcation (splitting of ZPA frequency), the input amplitude bifurcation (splitting of the input impedance amplitude minima) and the output amplitude bifurcation (splitting of the output power maxima). The phenomenon and its three manifestations are further referred as bifurcation phenomena [20].

Due to these findings, the scope of the thesis is extended to all three manifestations of bifurcation, which are examined in the two-coil IPT system with series-series compensation for EV charging applications.

1.1 Motivation

During my master’s studies I have focused on EVs. When I was offered to study IPT in my PhD, I saw it as an interesting alternative to conductive chargers thanks to its advantages, such as improved safety, durability, and ease of use. However, when I began examining the IPT system I learned that the familiar approaches for analysis of the common transformers unusable, even though the equivalent circuit of IPT is very similar to the common transformer. On the contrary to common transformers the IPT systems are impacted by the bifurcation (of input phase) and frequency splitting (of output power maxima). Initially, the research presented in this thesis was originally focused only on bifurcation. Nevertheless, the analysis results showed the close relationship between bifurcation and frequency splitting. For this reason, the scope of the analysis was expanded to cover both phenomena. However, in the literature these phenomena are studied separately and typically in the context of different circuit parameters, i.e., bifurcation was studied in the context of equivalent load resistance R_L [17], while the frequency splitting in the context of coupling coefficient k [21]. Also, while the bifurcation description uses the mathematical model based on general parameters (loaded quality factors and normalized frequency) [17], the description of frequency splitting uses the regular circuit parameters (inductances, capacitances, resistances, etc.).

For this reason, I have decided to develop a unified mathematical model for both phenomena and use it for the common analysis. To improve the analysis process, I have developed novel visual tools, which are easy to use, improve comprehension of system operation. These diagrams are inspired by diagrams used to analyze thermodynamic processes. The unified mathematical model and the visual tools are presented in the first part of the thesis.

In the second part of the thesis, the analysis of bifurcation and frequency splitting is performed under the framework of the unified mathematical model. Examination of the frequency splitting required including the splitting of the input amplitude minima in the analysis. The analysis showed, that both bifurcation and frequency splitting are not two separate phenomena but two manifestations of a single phenomenon, which is growing reflected impedance, which represents the secondary side influence on the primary. To reflect this shift of perspective I also propose a novel nomenclature, which also improves comprehensiveness (terms "bifurcation" and "frequency splitting" are very similar).

The third part evaluates the impacts of the bifurcation phenomena on the selection of the operating area and the IPT system regulation.

The fourth part of the thesis examines methods to mitigate negative effects of the bifurcation phenomena or prevent their occurrence altogether.

1.2 State of Art

In this chapter, IPT is related to other means of wireless power transfer and the history of its development is outlined. Its principle is examined together with its advantages and disadvantages in comparison with the conductive connection. The main applications of IPT are presented together with standards ensuring interoperability between devices from different manufacturers. A brief overview of the important research institutions and companies is listed. The review is concluded with examination of literature on the bifurcation and frequency splitting phenomena. The IPT technology for charging applications (especially EV charging) is discussed in further detail in Chapter 2.

1.2.1 Classification of Wireless Power Transfer

IPT is not the only way to achieve contactless energy transfer (WPT), i.e., energy transfer between two or multiple objects without any contact which could transfer the energy. A relatively wide range of ways to achieve WPT exists, however, they all are based on the wave field and the resonance phenomenon. Energy is transferred from the transmitter by some type of an oscillating field or wave. Provided that the field generated by the transmitter has the same frequency as the resonance frequency of the receiver (i.e., transmitter is tuned to the receiver), the power transfer from transmitter to receiver is maximal. This allows selectivity of energy transfer. Types of WPT can be distinguished by a type of the field or wave which transfers the energy [7], [22], [23]:

Acoustic energy transfer (AET). The energy is transferred by sound waves [24] or by ultrasound waves [25]. This method can operate over longer distances in comparison with IPT. However, the transfer is dependent on the medium between transmitter and receiver. This technology is often used in medical implants [25], [26] and was successfully employed in energy harvesting [24].

The WPT concepts employing the electromagnetic field can be distinguished whether they operate in the far-field or near-field region. The distinction between the regions is whether the electromagnetic field has wave character (far field) or non-wave character (near field) [27], [28]. The boundary between the regions depends on the wavelength and the largest dimension of the transmitting element. The far-field transfer typically employs microwaves, while the near-field transfer can be divided between the capacitive and inductive power transfer.

Far-field power transfer. Microwave power transfer (MPT) or radio frequency (RF) power transfer operates in the far-field region and the energy is transferred by electromagnetic waves [29], [30]. The receiver typically uses a rectenna ("rectifying antenna") [31]. This method can be used for power transfer over longest distances – in [32] is discussed the use of MPT for space application, such as transfer of energy from potential orbital power plant to Earth surface.

Capacitive power transfer (CPT). CPT operates in the near-field region and employs the electric field to transfer energy [33]. While CPT operates in comparison with IPT at the similar power and efficiency levels, its air gap is generally smaller [34].

Inductive power transfer (IPT). IPT also operates in the near-field region, but the energy is transferred by the magnetic field. It is currently most widely used approach to achieve WPT. Because IPT is the focus of this thesis, it will be examined in further detail.

1.2.2 Important Overviews of IPT

Important overviews of IPT were compiled by Covic and Boys [2], [3] in 2013, Hui et al. [35] in 2014, Li and Mi [6] (focused on IPT in EVs) in 2015, Lu et al. [30] (more focused on the far-field technologies) in 2016, Foote and Onar [36] (review of high power IPT for EV applications) in 2017, Zhang et al. [1] (also examines CPT and metamaterials) in 2019 and Feng et al. [22] (review of high power IPT for EV applications) in 2020 .

1.2.3 History of IPT

First attempts to achieve IPT can be traced to Hutin and Le Blanc, who in 1984 proposed and apparatus and method to power wirelessly an EV using 3 kHz AC generator (U.S. Patent 527 857) [2]. In 1900s-1920s Nikola Tesla tried to develop wireless power distribution system called "World Wireless System" (U.S. patents 645 576 and 1 119 732). Even though, his effort ultimately failed, he laid foundations for IPT by developing coupled resonant circuits as means of WPT.

The attempts to employ IPT in the biomedical applications began in 1960s. B. K. Kusserow proposed a new way of powering the implanted blood pump based on magnetic field [37]. Pump mechanism was attached to a permanent magnet, which was propelled through rotating magnetic field excited by another permanent motor driven magnet. J. C. Schuder of University of Missouri-Columbia described in [38] "transcutaneous energy transformer" which was one of the first concepts of powering implantable devices by inductive coupling between transmitter and receiver coil.

In 1970s, researchers became interested in IPT as means to power roadway EVs. In 1972 Don Otto designed inductively powered EV (Provisional Patent NZ19720167422, JP49063111 (A)). According to [2], "his work proposed two spaced-apart circular cross-section conductors made of copper buried some 20 cm under the road, each carrying a current of 2000 A in opposing directions. The system had no controller; the pickup was series tuned, rectified, and connected directly to a dc drive motor. The work was abandoned, in 1974, but it did establish that power could be coupled to moving bodies." In late 1970s, Bolger et al. begun to publish a series of papers on electric highway systems (e.g. [39], [40]).

In 1980s, research of IPT applications kept examining its possibilities in the bio-implants and for roadway powered vehicles. The Partners for Advanced Transit and Highways (PATH) project in 1980s resulted in a roadway powered IPT vehicle with a variable air gap [41]. Kelly and Owens also proposed IPT supply for powering aircraft entertainment systems in 1986, which was further improved by Turner and Roth (U.S. patent 4 914 539) in 1990s [2].

In 1990s University of Auckland's group of scientists lead by A. W. Green and J. T. made significant contribution by developing an IPT system for industrial use (U.S. Patent 5 293 308, [5]). Results of their research were implemented in the cooperation with their Japanese partner company Daifuku in the material handling systems (where IPT replaces continuously strained supply cables, see Fig. 1) and other applications. This advancement begun current development of IPT technologies, which permeates in the growing number of fields.

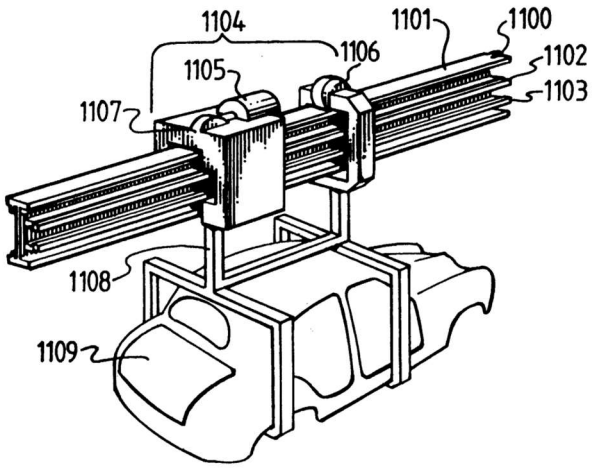

Fig. 1: Material handling system developed by University of Auckland and Daifuku. Source U.S. Patent 5 293 308.

In 2000s, IPT found its applications in consumer electronics [8], [42], biomedical implants [43], [44], commercial bus systems [36] and others. In 2007 a group of researchers led by Marin Soljačić at Massachusetts Institute of Technology (MIT) proposed a 4-coil topology to improve the range of operation. This arrangement

allowed them to light up a 60 W light bulb with receiver coil 2 m away from transmitter coil [45]. Consortiums begun to form to achieve interoperability via standardization, e.g., Wireless Power Consortium (WPC) [46], Power Matters Alliance (PMA) and Alliance for Wireless Power (A4WP). In 2015, PMA and W4PA merged in the AirFuel Alliance [47].

In 2010s the commercialization of the stationary IPT chargers for EVs was initiated by Plugless Power [48] and WiTricity (founded by Marin Soljačić) [49] and the concepts of dynamic EV charging were proposed [50], [51] and tested by Qualcomm Halo (Qualcomm Halo was in 2019 purchased by WiTricity).

1.2.4 Principle of IPT, Advantages and Disadvantages

The fundamental principle of IPT can be demonstrated on the basic 2-coil setup – see Fig. 2. The transmitter coil is connected to an AC source and the receiver coil to the load. AC current i_r flowing through the coil generates an oscillating magnetic field with total magnetic flux Φ_t. Part of the magnetic flux Φ_m closes through the receiver coil and the remaining is the leakage magnetic Φ_l. Because the magnetic field is oscillating, the voltage is induced in the secondary side. As the receiver circuit is closed, current i_r flows through it. Each of the coils is accompanied by a capacitive compensation, which together with the coil inductances set the resonance frequencies of the transmitter and the receiver. Under regular conditions, when the transmitter and receiver resonance frequencies match and the AC source operates also at this frequency, the power transfer between the transmitter and receiver is maximal.

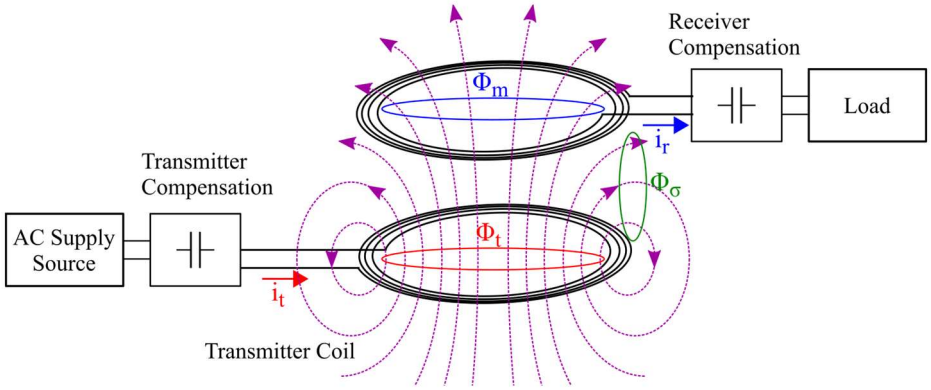

Fig. 2: Principle of IPT.

IPT has following advantages in comparison with the cable connection [2], [52].

Safety. Because the power is transferred by a magnetic field instead of a galvanic contact, both the transmitter and receiver can be covered by a seamless layer of insulation. Absence of contacts removes occurrence of sparks occurring when the galvanic contact is established, thus it is convenient for the dangerous environments. Also, such sparks create impurities, thus IPT is suitable for applications in the clean environments. In the biomedical implant applications, use of IPT removes the skin punctures for cables powering the heart pumps and similar high-power implants, thus it decreases the risk of infection.

Durability. Because the power between the transmitter and receiver is transferred by magnetic field, IPT is convenient for the applications where transmitter and receiver are in movement with respect to each other, such as in the case of the material handling systems – cables forming the galvanic connection suffer from increased strain. Replacement of galvanic connection by IPT also improves durability in the applications, where the repeated assemble and disassemble would decrease the lifespan of the contacts, especially in the harsh environments.

Ease of use. Use of IPT removes the necessity to correctly plug the charging connector and any other manipulation with the cables. Especially in the case of EVs this improves the charging process, as the charging cables capable of fast charging are rather heavy and bulky.

Aesthetically pleasing. Removal of cables improves visual presentation of the device. This is especially significant in the case of powering the EVs: Both the stationary charging stations for battery EVs and the trolley wires for the railway EVs can be placed completely underground.

Disadvantages. The main disadvantage of the IPT is that each system is designed for a certain range of the coupling coefficient [6]. If the coupling coefficient value leaves this range due to misalignment or air gap change, the efficiency and power transfer capability decreases.

1.2.5 Main Applications and Standards

Thanks to advantages described in the previous chapter, IPT technology replaced conductive connection in many applications.

Initially, IPT found its commercial use in the factory automation and clean factories [2], [7], [52]. Developed materials handling systems comprise of one elongated loop forming the track with multiple pickup coils such as in Fig. 1. In comparison with the conventional technology of trolley lines and collectors, IPT removes the collector wear, wear debris and sparks caused by line separation [2].

IPT systems are used for EV charging. Based on the movement of the vehicle, this application can be divided in dynamic, semi-dynamic or stationary charging. In dynamic charging, an EV is charged while it travels over an electrified road [53]. Multiple scenarios of the electrification track are possible: it can be formed by a single elongated primary coil (similar to materials handling systems), or by segmented track, where each segment powered or switched individually, or by a sequence of pads similar to those used for EV charging [22], [53].

Semi-dynamic charging is derived from the dynamic charging, but instead powering vehicles in-move, they are powered at the intersections, traffic lights or bus stops (electrified public transport vehicles), where the vehicles are temporary stationary [51].

Stationary IPT chargers replace conductive chargers and can be fully integrated in the parking space, so that no part of the charger is visible [52]. The modern IPT systems for EV charging achieve the similar levels of efficiency (> 90%) and transferred power (tens and hundreds of kW) as the conductive chargers [22].

IPT technology is also used in the harsh environments [54], consumer electronics [1], [8], biomedical applications [9], [10], etc.

Several standards were developed, e.g. Qi [11]–[13] or AirFuel [14] for consumer electronics and SAE J2954 [15] or IEC 61980 [16] for EV charging. To ensure interoperability of devices produced by different manufacturers, the standards specify operating frequency bands, power classes, distances, communication and other aspects of the system operation.

1.2.6 Important Research Institutions, Conferences and Companies

Probably the most important research institution in the development of IPT is the University of Auckland in New Zealand. The research of the Power Electronics Group [55], nowadays formed by John Boys, Grant Covic, Aiguo Patrick Hu, Dariusz Kacprzak, Duleepa Thrimawithana and others, begun the development and spread of IPT technology in last 30 years [2], [3], [5], [52]. Among their focus belongs the design of IPT systems for industrial and EV applications [56]–[59], theory of IPT [17], coil design for stationary and dynamic EV charging [60], [61], dynamic EV charging [50], [62], [63] and even CPT [64], [65].

Madhu S. Chinthavali, Omer C. Onar, Larry Seiber, Burak Ozpineci and others from the National Transportation Research Center [66] at Oak Ridge National Laboratory (ORNL) in USA contribute to the IPT development by a wide range research projects focused primarily for the IPT applications in EV charging [67]–[70], dynamic charging [67], [71], [72] high power IPT technology for EV stationary charging [70] (55 kW), [73] (100 kW).

The team of Chun-Taek Rim, Hoi R. Kim, Yun-Su Kim, and others at Korean Institute of Technology (KAIST) in South Korea also develops the dynamic EV charging (they call it online electric vehicle charging (OLEV)) [74]–[77]. They also examine unusual coil designs for ubiquitous IPT and other applications [78], [79] and metal object detection [80], which is an important issue for the safety of IPT charging.

Paul D. Mitcheson, David C. Yates, Juan M. Arteaga, and others from Wireless Power Lab [81] at the Imperial College London in the United Kingdom develop the high frequency IPT technology (6.78 MHz, 13.56 MHz) [82]–[84]. They also examine its applications for the charging of light EVs (600 W, 6.78 MHz [85]), and drones (10W, 13.56 MHz [86], 500 W, 13.56 MHz [87]). They also develop methods for the circuit parameter characterization [88], [89].

Also, Czech universities develop the IPT technologies, e.g., Vladimir Kindl, Roman Pechanek and Tomas Kavalir from the University of West Bohemia focus on the 4-coil IPT [90], [91].

In 2021, IEEE founded the Wireless Power Transfer Project (IEEE WPT) to connect the researchers from universities and companies and advance the WPT technology (here the term “WPT” includes IPT, CPT together with the far field power transfer) [92].

Between the most important conferences focused on WPT belongs the IEEE Workshop on Emerging Technologies: Wireless Power (WoW), which is organized by the IEEE Power Electronics Society (PELS) and focused primarily on IPT. It is accompanied by the IEEE Wireless Power Transfer Conference (WPTC), organized by the IEEE Microwave Theory & Technologies Society (MTT-S). WPTC is primary focus on the far-field power transfer. The conferences and organizing societies well illustrate two typical backgrounds of researchers developing the WPT (power electronics and electric drives on one hand, and RF engineering on the other). Since

2018, WoW and WPTC joined in a single conference called Wireless Power Week (WPW) with WoW and WPTC tracks.

The main companies commercializing the IPT technology in the industrial applications are Daifuku in Japan [93] and Conductix Wampfler in Germany [94]. In 1990s, Daifuku developed the suspended material handling systems based on a monorail such as in Fig. 1. They also produce the IPT based solutions from cleanroom applications. Conductix Wampfler produces suspended material handling systems similar to those produced by Daifuku, floor conveyors for assembly lines (IPT track and set of IPT powered carts) and also stationary charging stations for factory EVs (e.g., forklifts) and public transport applications (e.g., charging of electric buses).

The solutions for stationary charging of EVs are developed by Plugless Power [48] and WiTricity [49], both stationed in USA.

IPT found its application in a wide range of consumer electronics, such as cellular phones, tablets, wearables (headphones, smart watches, etc.), electric razors and other products provided by Samsung, Apple, Philips, Huawei, and other main electronics manufacturers.

1.2.7 Bifurcation and Frequency Splitting Phenomena

The phenomena of bifurcation [17] and frequency splitting [18], [19] impacting the IPT systems were examined in the literature. Bifurcation is connected to the phase of the input impedance φ_{in}. Namely, at the resonance frequency f_0, the phase shift between the input current and voltage – and thus the impedance phase – is equal to 0. Thus f_0 is called the zero-phase angle (ZPA) frequency. However, under certain conditions, this single ZPA frequency splits into three. Fig. 3 (a) depicts bifurcation as a consequence of decreasing equivalent load resistance R_L in the IPT system with series-series compensation. Wang et al. in [17] provides a detailed mathematical description of the bifurcation phenomena, including the calculation of ZPA frequencies and the condition for the bifurcation occurrence based on the primary and secondary loaded quality factors Q_{Lp}, Q_{Ls} and normalized frequency u.

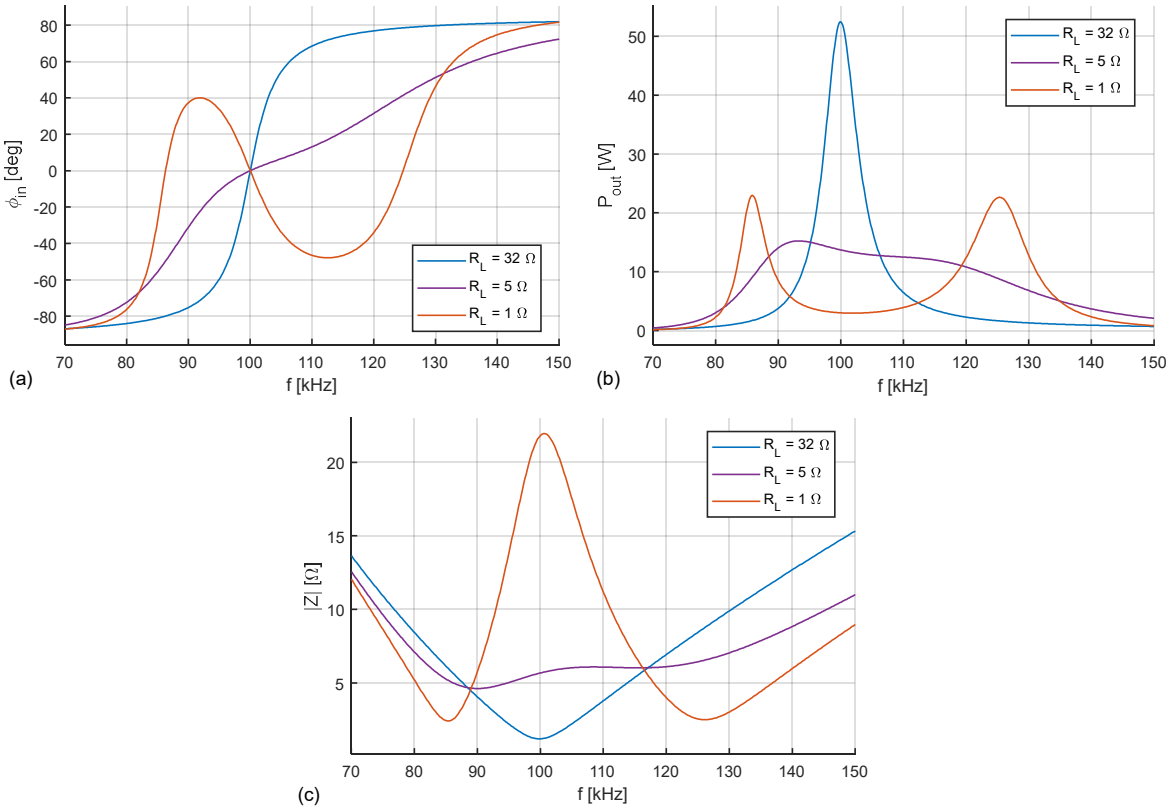

Fig. 3: (a) Bifurcation of the input phase φ_{in}. (b) Frequency splitting of the output power P_{out} maxima. (c) Splitting of input amplitude Z minima.

IPT systems advantageously employ inverters with ZVS [95], as it is easy to set their operating frequency above f_0, where $\hat{Z}$ is inductive. However, bifurcation causes $\hat{Z}$ to change from inductive to capacitive for $f > f_0$, which adversely affects ZVS and decreases the system efficiency [96]. This issue was examined from the practical

perspective for single phase [95], [97], [98] and multiple phase [99] IPT systems and design guidelines were developed to prevent the bifurcation occurrence [100].

Researchers paid more attention to frequency splitting in comparison with bifurcation, especially in the context of the coupling coefficient influence and critical coupling [18], [19], [21]. Frequency splitting is a phenomenon similar to bifurcation: under certain conditions the frequency of the output power P_{out} maximum splits into two, one moves under f_0 and second moves above f_0 [18], [19]. Fig. 3 (b) depicts the frequency splitting as a consequence of decreasing R_L in the IPT system with series-series compensation. Initial mathematical descriptions for the four-coil systems [45] described the frequency splitting by the coupled mode theory [101]. Then the circuit theory based descriptions were developed using the linear magnitude of scattering parameter S_{21} [18] or the output power P_{out} for 4-coil [102] and 2-coil systems [103]. The formulas for the frequencies of the P_{out} maxima were derived; however, these are limited primarily to symmetrical or otherwise specific systems [19], [21], as finding the roots for general unsymmetrical system analytically is difficult [21]. Based on these findings, methods to obtain uniform received power independent of the varying transfer distance (and consequent frequency splitting) were developed (e.g. [18], [104], [105]).

The splitting of input impedance amplitude Z minimum (see Fig. 3 (c)) was not examined in the literature at all, to the best of author's knowledge.

1.3 Thesis Objectives

The topic of this work is to analyze the bifurcation phenomena and examine methods to control it. As it was prefaced, the bifurcation phenomena include phase bifurcation, output amplitude bifurcation (frequency splitting), and the input amplitude bifurcation; thus, all of these phenomena are encompassed in both the analysis and control methods. Because the bifurcation phenomena were described using the different set of parameters in the literature, a unified model must be developed and verified. This model should allow a comprehensive and simple analysis of the bifurcation phenomena. This analysis should also consider the impacts on the selection of the operating area and the system regulation. Existing control methods should be examined in the perspective of the developed mathematical model and the results of the analysis and if necessary, novel methods should be developed. Selected methods, either existing or novel, should be verified.

The individual objectives were defined as follows:

1) Compose an overview of inductively coupled power transfer systems, existing descriptions of the bifurcation phenomena and the bifurcation control methods.
2) Choose a suitable mathematical model of a selected IPT system for the bifurcation analysis.
3) Specify and explain the term "bifurcation phenomena".
4) Assemble or derive the suitable mathematical description of the bifurcation phenomena for the analysis.
5) Verify the mathematical description by measurement and simulation.
6) Analyze the bifurcation mechanism and its impacts on device operation.
7) Examine the existing methods for bifurcation control or if necessary, develop new control methods.
8) Verify the selected bifurcation control methods by measurement and simulation.
9) Evaluate the obtained results of simulations and measurement.

1.4 Thesis Organization

The thesis is organized as follows. In the second chapter, the IPT technology for charging applications is examined with the focus on EV charging. The IPT systems are distinguished by their operating frequency and the used types of coils, compensation topologies and electronics are discussed.

The third chapter presents the equivalent circuit model and specifies the quantities such as voltages, currents, powers, and efficiency including their equations, which will be used in the rest of the thesis.

As the verification of both of the mathematical model and the control methods is required and the bifurcation analysis requires input data, the fourth chapter presents both the measurement setup and simulations employed to meet these tasks. Because no suitable measurement setup was available, it was necessary to build a new one.

In the fifth chapter, the bifurcation phenomena are summarized, and the novel nomenclature is presented. Also, the term "course of bifurcation", which is essential for the bifurcation analysis is specified.

Chapter 6 presents the novel general parameter model describing the bifurcation phenomena, which is based on the primary and secondary loaded quality factors Q_{Lp} and Q_{Ls}, and the normalized frequency u. In this chapter, the novel visual tools are presented.

The bifurcation analysis follows in Chapter 7. In its first part, the mechanism of the bifurcation phenomena is analyzed. Second part of the chapter examines the influence of individual circuit parameters (e.g., coil inductances L_p and L_s, resonance frequency f_0 or equivalent load resistance R_L) on the bifurcation phenomena occurrence.

Chapter 8 discusses the impacts of the bifurcation phenomena on the selection of the operating area from the viewpoints of efficiency and ways to achieve the required output power and the input phase. Also, the impacts on the system regulation are examined and the role of frequency splitting in the limits of stability for frequency regulation is analyzed.

The control methods of the bifurcation phenomena are presented in Chapter 9. These methods are divided between passive (design based) and active (measures adjusting the IPT system during operation). Selected methods are verified by measurements and simulations.

The thesis is closed by the conclusions together with references, list of author's publications in Chapters 10, 11, 12 and appendices.

2 IPT for Charging Applications

This chapter discusses an arrangement of IPT systems for battery charging, with the focus on the stationary EV charging. Fig. 4 depicts the general structure of such a system. The grid rectifier interfaces the grid, converts the AC voltage to DC, provides the power factor correction (PFC) and reduces the input harmonic distortions [22]. The inverter converts the DC voltage to AC, either at a constant or variable frequency. The AC voltage supplies the transmitter coil, which is compensated to form the primary resonant circuit. The magnetic flux generated by the coil closes through the receiver coil, which with its compensation forms the secondary resonant circuit. The coupled primary and secondary resonant circuits form the IPT transformer. The received power is rectified and supplied to the load, which is in this case a battery. DC/DC converters can be optionally added to the primary and secondary side DC links for power flow control or impedance matching [106]. The DC/DC converters in the transmitter and receiver DC links and the inverter with variable frequency control are used in the system regulation. The IPT charger structure is similar to the conductive charger, except the wireless stage. The IPT charger typically employs some form of wireless communication between the transmitter and receiver (not marked in Fig. 4).

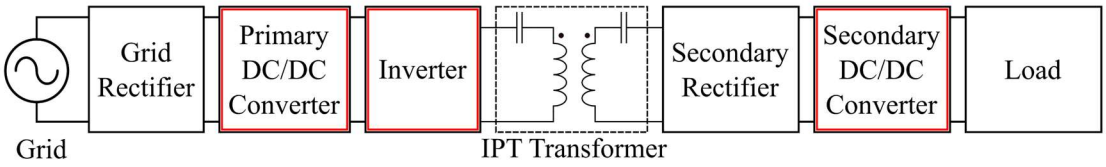

Fig. 4: System block diagram with the highlighted components typically used for regulation. Published by author in [20].

In the following text, the IPT systems are distinguished based on their operating frequency. Then, individual components specific for the IPT chargers such as pads, compensation topologies and electronics are discussed.

2.1 Operating Frequency

From the perspective of operating frequencies, the IPT systems can be divided between the low frequency (hundreds of kHz) and high frequency systems (typically 6.78 MHz or 13.56 kHz).

The low-frequency IPT is the most widespread and the most developed technology for IPT and WPT generally. The power rating of low-frequency charging systems varies from low power for consumer electronics (units of W) to high power for EV charging (up to hundreds of kW [36], [22]). High power at hundreds of kHz is achievable primarily thanks to the development of the wide bandgap semiconductors, as discussed further in Chapter 2.4.2. The Qi standard was developed for charging of consumer electronics (5 W – tens of W). The recommended setup consists of a single transmitter and single receiver and operates in the frequency range typically between 100 – 200 kHz [13]. The standard SAE J2954 was developed for stationary EV charging. It sets the nominal operating frequency to 85 kHz. SAE J2954 also specifies multiple power classes (WPT1 3.7 kVA, WPT2 7.7 kVA, WPT3 11.1 kVA, WPT4 22 kVA), air gap classes (Z1 110-150 mm, Z2 140-210 mm, 170-250 mm) and interoperability requirements between them [15].

High frequency IPT systems typically operate at the frequencies of 6.78 MHz and 13.56 MHz. These frequencies were selected for IPT because they correspond with the ISM radio band frequencies, which are reserved for industrial, scientific and medical (ISM) purposes [1]. The high frequency IPT systems are typically used for the low power (units of W) and mid power (units of kW [107]) applications, such as charging of consumer electronics and the charging of light EVs [85]. The transferred power is limited by the current state of art of the power electronics devices [6]. The AirFuel standard was developed for consumer electronics applications. It specifies the operation at 6.87 MHz for transferred power up to 50 W in PRU category 7, and it allows multiple receivers for a single transmitter [14].

2.2 Pads

There is a large quantity of various coil arrangements for the IPT. As this thesis is primarily focused on IPT for EV stationary charging, the examination of coils also limits to this scope. In EV charging, the whole coil arrangement is typically referred as “pad”, due to its planar design. Overview of pad designs for EV charging can be found in [23], [52]. An inductive pad for EV charging typically consists of a winding, magnetic core, and a shielding, as depicted in Fig. 5.

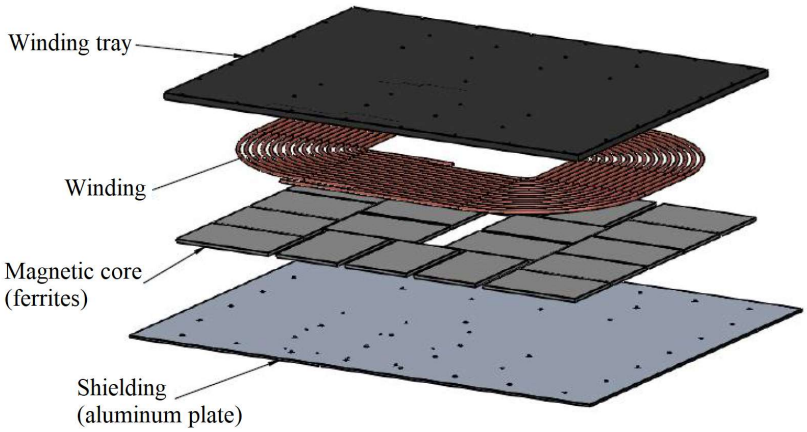

Fig. 5: Typical arrangement of a low frequency inductive pad for EV charging. Source [115] (adjusted).

2.2.1 Winding

The winding carries currents that generate oscillating magnetic field (transmitter) or voltage is induced at its terminal as magnetic flux closes through it (receiver). The winding is usually placed in a tray which maintains the winding shape under the forces resulting from the interaction between the current flowing through the winding and the magnetic field. Special conductors such as litz wire, tubular conductors, etc. are required to achieve low AC loses at the operating frequencies

Litz wire is formed by a large number of insulated copper strands of small cross-section (tens of micrometers) twisted in bundles, which are further twisted to create a round or planar wire. Minimizing the cross-section of each strand reduces the skin effect, decreasing the AC resistance. Correct twisting pattern is important as it equalizes the length and consequently the current distribution between the individual strands [108]. Litz wire is convenient for the low frequency IPT with frequencies in hundreds of kHz, as its AC resistance significantly increases with increasing frequency around 1 MHz [109], [110].

AC resistance of the litz wire at higher frequencies can be reduced by adding a thin magnetic film between the copper and insulation of each strand. The proximity effect is reduced [111], [112].

Tubular conductor is formed by a hollow copper tube are an alternative for litz wire, as they have a low skin-effect resistance, they are easy to manufacture and allow easy implementation of active cooling. They are suitable for high frequency IPT systems [85], [113].

The conductor technologies for high frequencies are further developed, e.g., superconductive REBCO wire structure [114].

2.2.2 Magnetic Core

Also, in the matter of the magnetic core the low and high frequency IPT differs. This can be explained on their approaches to achieve the high efficiency. Maximal possible efficiency of the IPT system for optimized load impedance can be calculated as [6]:

$$\eta_{max} = \frac{k^2 Q_p Q_s}{\left(1 + \sqrt{1 + k^2 Q_p Q_s}\right)^2} \tag{1}$$

where Q_p and Q_s stand for primary and secondary coil quality factors, respectively, both of which are calculated as:

$$Q = \frac{\omega L}{R} \tag{2}$$

where R is the equivalent series resistance (ESR) of each coil. To achieve high efficiency, the IPT system must have either high coupling between the coils or the coils with high quality factors.

Due to frequencies in tens or hundreds of kHz, the windings for low frequency IPT have lower Q. Thus, a magnetic core is added to them. The impact is twofold: First, adding a magnetic core increases inductance of the coils (typically in tens of μH [115]) and consequently Q, which is then typically 300-400 for EV charging pads [115]. Second, magnetic cores significantly boost coupling between the coils. While the coils for high frequency IPT, which are air-core, have coupling coefficient k typically under 0.1 [83], [85], the low frequency IPT coils have k typically between 0.1 and 0.4 [115].

On the other hand, the high frequency IPT achieves high efficiency due to high values of Q. Even though the coil inductances are low, operating frequency of 6.78 MHz or 13.56 MHz achieves high Q. For example, in [85] the coil has 2.76 μH and Q of 1685.

Besides improving k and Q, the magnetic core directs the magnetic flux in the system and minimizes the leakage flux, which improves the system compatibility with EMF standards [23].

The magnetic core for the low frequency IPT pads is typically formed by ferrites. Ferrite is a material manufactured by mixing and sintering iron(III) oxide (Fe_2O_3) with a small portion one or more additional metallic element, such as manganese (Mn), nickel (Ni) or zinc (Zn) (U.S. patent 3027327A). The magnetically soft ferrites have low coercivity; thus, they are used as magnetic cores or magnetic conductors [116]. Typically, Mn-Zn and Ni-Zn ferrites are used due to their low losses at 100 kHz frequencies [23].

While the magnetic core for low power charging applications (customer electronics) typically consists of a single block of ferrite, the magnetic cores for EV charger pads are typically assembled from multiple ferrite blocks, due to the significantly larger size of the pads. As the pads for EV charging are typically planar (see Chapter 2.2.4), the ferrite blocks also planar – I shape, square or rectangular [117]. Resulting shape of magnetic core corresponds with the coil type.

However, the magnetic core comprised of ferrites is rather expensive and it increases the weight, which is an issue especially for the receiver. Also, it ferrites are rather brittle – if a robust protective cover is not used, ferrites can be exposed to elements and its performance deteriorates [118]. In addition, the losses in the ferrites and shielding can be significant [119] and consequently a thermal runaway may occur, especially in high-power systems [118].

For these reasons, ferrite-less coil designs are developed even for low frequency IPT [118], [120]. However, because the ferrite directing the magnetic flux is missing, the resulting magnetic field may not meet the limits required by standards, e.g. [121]. For this reason, ferrite-less coil designs are accompanied by the cancellation coils, which are further described in the following chapter.

2.2.3 Shielding

IPT systems for EV can transfer very high power (up to hundreds of kW [36]) over a relatively large air gap (up to 250 mm in Z3 class in [115] via magnetic field. Therefore, it is necessary to ensure that the magnetic field is contained between the transmitter and receiver even at the allowed misalignment of the coils to prevent any harm to passengers. In order to meet the EMC requirements, i.e., the magnetic flux density must be lower than 27 μT_{rms} [121] outside the specified operating area (i.e., outside the space underneath the vehicle) [115], both the transmitter and receiver pads are equipped with shielding [122].

In the typical pad design (Fig. 5), the shielding is formed by the ferrites and the aluminum plate. The ferrites, besides serving as the magnetic core and enhancing the coupling between the pads, also directs the magnetic flux, thus it does not enter the vehicle interior. Any exceeding electromagnetic field is then absorbed by the aluminum plate which serves as a conductive shielding [122], [123]. Design procedure for passive shielding with aluminum plate is described for example in [124].

However, adding the passive shielding introduces additional losses in the system and increases weight and price of the pads [118], [119]. For this reason, both ferrite and shielding are replaced by an additional cancellation coil (or coils), which is either reactive (closed loop) or active (directly connected at the end of the transmitter winding but wound in the opposite direction).

In the reactive coil, the voltage is induced by the magnetic flux generated by the transmitter and because the coil is closed, the current flows through it. Induced voltage and consequently the current has polarity that the resulting field is opposite to the field generated by the transmitter winding and thus cancels it [122], [125]. Examples of design can be found in [118] and [120] for the circular and DD pad, respectively. (Both pad types are examined in the following chapter.)

In the case of the active cancellation coil, the same current flows through the active coil as through the transmitter winding, but because the cancellation coil is wound in the opposite direction, the current and consequently the magnetic field has the opposite polarity with respect to the transmitter winding which field is canceled [126].

2.2.4 Pad Types

Pads (or coils) for IPT are very different from the commonly used coils. They are designed primarily to maximize coupling between the coils while keeping the quality factor high. IPT pads have typically a planar design. The IPT pads can be distinguished between the non-polarized and polarized pads based on the magnetic flux pattern. In the non-polarized pads, the magnetic flux pattern is symmetrical around the pad center, while in the polarized coils it is not symmetrical [127]. Fig. 6 depicts the most important pad types for EV charging [23], [128].

Circular pad (CP). CP depicted in Fig. 6 (a) without its shielding aluminum plate is a typical non-polarized pad. It was the initial coupler design for the EV charging, essentially derived from the gapped pot core [52]. To optimize the pad design for required diameter (e.g., 700mm [52]) radially placed I cores were used. The optimization procedure is described in [61]. Magnetic flux generated by this pad design is marked in Fig. 6 (a) by dashed lines. The relationship between the pad dimensions and its ability to throw flux to the receiver pad can described by the concept of the fundamental flux path height [129]. The fundamental flux path height for the CP is proportional only to the quarter of the pad diameter (given by the end points of the ferrites) [130], which is the main disadvantage of this design. Another disadvantage is the existence of a null point for receiver offset by 38% of the pad diameter [61]. Rectangular pad (Fig. 5) is a variant of the CP with the same principle of operation, only the winding shape and magnetic core is adjusted.

Flux pipe pad (FPP). To remove the disadvantages of the circular pad design, especially the null point inconvenient for the dynamic EV charging, FPP (Fig. 6 (b)) was developed [129]. This design is a single pad type which does not use planar windings, but it is based on the solenoid. FPP is a polarized pad. It consists of a ferrite body comprising of two poles connected by a midsection. At the ends if the midsection two coils are placed. The coils are connected in parallel, thus from the flux pipe requires a single inverter or rectifier. The fundamental flux path height for FPP is one half of its length, thus its required dimensions are reduced by half in comparison with the circular path [129]. However, this design without a shielding plate has a symmetrical magnetic field above and below the pad. For this reason, aluminum plate is added under the pad and even on the top of the pad covering the coils to achieve the required flux pattern. Consequently, due to the losses in the shielding it is difficult to achieve high efficiency [52].

Double D pad (DDP). The DDP (Fig. 6 (c)) was developed as the improvement of the FPP design [130]. The pad is called double D, because it is formed by two coils, which should ideally have D shape. The coils are placed back-to-back on a ferrite base. The ferrite channels the main flux behind coils while forcing the flux to radiate on one side [130]. Therefore, aluminum shielding contains only the stray fields, thus the losses are negligible in comparison with the flux path. The DD coils form a single winding; thus, a single inverter or rectifier is needed. Fig. 6 (c) depicts the flux pattern of the pad. The coils a and b in the shaded area create a "flux pipe". Width (y coordinate) of flux pipe controls the height of the intra-pad flux Φ_{ip}. The portion of flux Φ_{ip} which closes through the receiver pad is the mutual flux Φ_{M}. To maximize Φ_{M}, the length of the flux pipe should be also maximized. Remaining sections of the coil should minimized to reduce material demands and reduce the pad's ESR [130]. The influence of the coil length and width with the coupling coefficient k and output current and voltage is discussed in [60]. The fundamental flux path height h_z is proportional to a half of the pad length.

Double D – quadrature pad (DDQP). The issue of the DDP is that it has a null point for offset by 34% of the pad length in the x-axis. At this position, no voltage is induced, because the flux enters and exits the same coil [60]. The offset tolerance in the x-axis can be significantly improved by adding a quadrature coil to the DDP receiver. This results in the DDQP design (see Fig. 6 (d)). The quadrature coil is decoupled from the DD coils and it couples the flux only when the receiver is offset in the x-axis. The quadrature coil requires its own rectifier [60].

Bipolar pad (BPP). The DDQP improves the offset tolerance, however, it consists of three coils, thus a large quantity of copper is required. BPP was developed [131] to reduce this amount. Bipolar pad is formed by two coils which are partially overlapping (see Fig. 6 (f)). BP pad has similar offset tolerance as DDQP, but it requires about 25% to 30% less copper [131]. The coils forming the winding of the BP pad are controlled separately, which improves the interoperability [131].

Tripolar pad (TPP). Depicted in Fig. 6 (f), TPP is formed by three coils, which are mutually decoupled [132], [133]. Each of the coils is driven independently by a single-phase inverter. Driving of the coils determines, whether the magnetic field generated by the pad is polarized or not [132]. TPP improves the tolerance to the rotational misalignment. [132], [133] describes the approach to maximize the effective coupling coefficient by controlling the voltage magnitude and phase of each coil. This decreases the transmitter VA rating by 45% in comparison with the circular pad over an airgap of 150 mm [133]. However, use of three inverters requires complex regulation and increases the cost.

Tree-phase bipolar pad (TPBP). Pries et al. presented a TPBP (see Fig. 6 (g)) in [70]. This design utilizes rotating magnetic field to improve power density (kW/m^2) and specific power (kW/kg) for high power EV charging (50 kW in [70]). On the contrary to the TPP, TPBP is powered by the three-phase inverter instead three single-phase inverters.

Three-phase systems allow such manipulation of the magnetic field orientation, which strengthens the flux coupled to the receiver and simultaneously reduces the leakage flux. Thus, both position tolerance and leakage field performance are improved. However, the main issue is the cross-coupling between the phases, which alters the impedance of each phase. Consequently, reactive power increases and current is unevenly distributed between phases, which may result in the loss of ZVS. Receiver misalignment aggravates these issues [22].

As the pads for EV charging are very different, the interoperability between them was examined for example in [127], [134], [135].

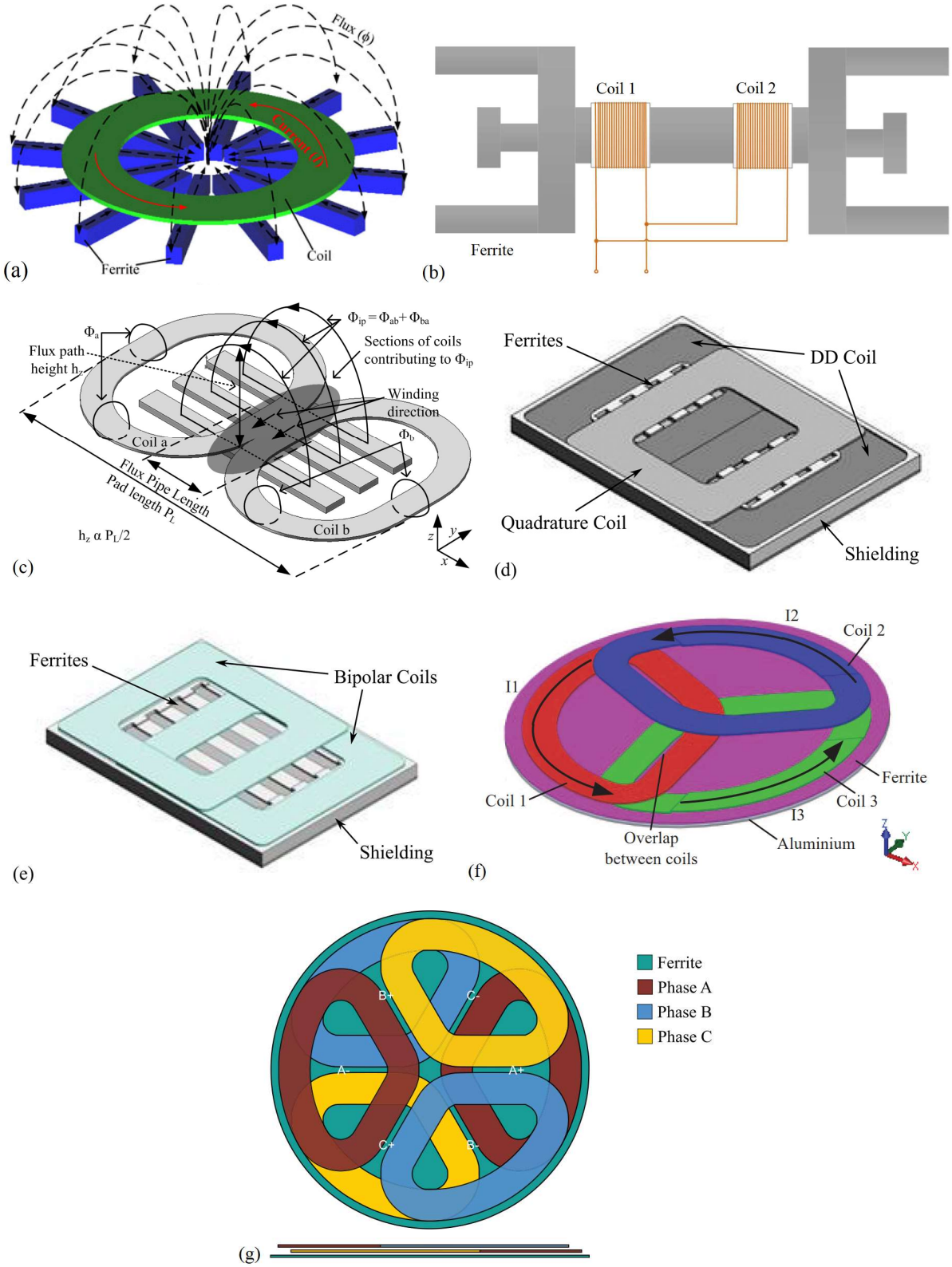

Fig. 6: Pads for EV charging. (a) Circular pad. Source [127]. (b) Flux pipe pad. Source [128] (adjusted). (c) Double D (DD) pad. Source [127]. (d) Double D – quadrature pad. Source [115] (adjusted). (e) Bipolar pad. Source [115] (adjusted). (f) Tripolar pad. Source [132]. (g) Tree-phase bipolar pad. Source [70] (adjusted).

2.3 Compensation Topologies

Transfer coils of the IPT systems are loosely coupled (coupling coefficient k typically from 0.1 to 0.4 for low frequency IPT [115] and below 0.1 for high frequency IPT [83], [85]) which results in large leakage inductances. To reduce the VA rating of the power supply necessary to provide the required output power, compensation networks are applied. This examination is focused on the main compensation topologies for 2-coil IPT. These topologies are used both in the low and high frequency IPT. At first, the single-phase compensation topologies are examined, followed by the three-phase.

Single-sided compensation. In the early IPT designs, a single-sided compensation was used, in the form of a capacitor placed either is series or parallel with either the transmitter or receiver coil [136], [137]. However, when the k gets smaller than 0.3, single-sided compensation becomes insufficient and double-sided compensation becomes necessary [6].

The four basic compensation topologies. The basic double-sided compensation topologies are formed by a single capacitor placed to each side – see Fig. 7. The capacitor can be added to the coil either in series or in parallel. This results in four basic compensation topologies: series-series (SS), series-parallel (SP), parallel-series (PS) and parallel-parallel (PP).

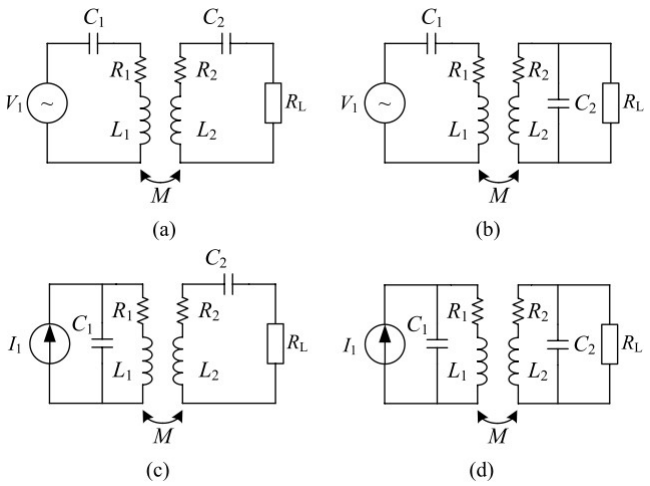

Fig. 7: Basic compensation topologies. (a) SS. (b) SP. (c) PS. (d) PP. Source [6].

If the primary side is compensated by a capacitor placed in series, it can be powered directly by the voltage converter. However, if the primary compensation capacitor is placed in parallel, either a current source is necessary, or an inductor is inserted to change the voltage converter into a current source [6]. When the primary side current is constant, series compensated secondary operates as a voltage source from the perspective of the output, while the parallel compensated secondary operates as the current source [57].

The calculation of the secondary compensation is the same for all four basic compensation topologies:

$$C_s = \frac{1}{\omega_0^2 L_s} \tag{3}$$

where ω_0 is the selected resonance frequency and L_s is the inductance of the secondary coil. On the other hand, compensation of the primary compensation capacity depends on the selected topology – calculations for primary tuned at the same frequency as secondary are listed in Table 1 [6], [57]. In these calculations, primary and secondary ESR describing the losses in each circuit are neglected and Q_{Ls} stands for the secondary loaded quality factor, which is calculated as $Q_{Ls} = \omega_0 L_s / R_L$ for the PS topology and as $Q_{Ls} = R_L / \omega_0 L_s$ for PP topology.

The C_p calculations in Table 1 show that only the SS topology is independent both on the coupling k and the load resistance R_L, i.e., even if both k (M changes, L_p and L_s remain constant) and R_L change, primary remains tuned to the secondary. On the other hand, the primary tuning is in the SP topology is affected by k and in PS and PP topologies by both k and R_L.

Table 1: Calculation of the primary side compensation capacity.

Topology	Primary capacity C_p
SS	$C_p = \frac{1}{\omega_0^2 L_p}$
SP	$C_p = \frac{1}{\omega_0^2 L_p} \frac{1}{1-k^2}$
PS	$C_p = \frac{1}{\omega_0^2 L_p} \frac{1}{Q_{Ls}^2 k^4 + 1}$
PP	$C_p = \frac{1}{\omega_0^2 L_p} \frac{1-k^2}{Q_{Ls}^2 k^4 + (1-k^2)^2}$

Both the primary and secondary compensations are typically tuned to the same resonance frequency ω_0 for the specific coupling and load value – zero-phase angle (ZPA) tuning. This reduces the required VA rating of the power supply to its minimal value. Furthermore, to improve converter efficiency, the soft switching is often employed [6]. Primary side compensation is then mildly detuned, thanks to which the impedance loading the converter gains a slight reactive component. This is necessary to achieve the zero-voltage switching (ZVS) or zero-current switching (ZCS) [95], [97], [98]. Because the reactive component necessary for soft switching is typically small, resulting primary resonance frequency remains close to the secondary resonance frequency.

As its tuning is independent on k and R_L, the SS topology may seem as the most convenient compensation topology. However, it is also necessary to examine the reflected impedance $\hat{Z}_r$:

$$\hat{Z}_r = \frac{\omega^2 M^2}{\hat{Z}_s} \tag{4}$$

The calculation is the same for all four basic topologies [17]. As coupling or R_L decreases, according to (4), $\hat{Z}_r$ drops, which may result in a spike of primary current for SS or SP topologies powered from the voltage source. On the other hand, in the PS and PP topologies powered from the current source, the drop of $\hat{Z}_r$ causes unloading. The four basic topologies are further examined in [137].

SP-S topology. To provide high-misalignment tolerant compensation topology, SS and PS compensations were combined into SP-S topology – see Fig. 8 (a) [138]. The SP-S is powered from a voltage inverter with a relatively large inductor (700 μH) placed at its output, which allows to transfer the nominal power even in the misaligned position. SP-S topology could be powered from a current source instead of using an additional inductor, but then the nominal power could not be transferred in misaligned position [138].

LCL topology. Another approach to create a topology which can be supplied by voltage inverter independently on the misalignment and output load is the LCL topology was presented by Wang et al. in [139] – see Fig. 8 (b) . Resonant converters with LCL compensation were initially used for inductive heating [140]. The LCL topology is composed of an inductor and capacitor, which are placed in series and in parallel, respectively, with the primary coil [139]. At resonance, LCL topology operates as a current source. Also, by tuning parameters of LCL, the reactive power can by fully compensated, which reduces the VA rating of the input voltage source [6]. However, the required inductance of the series inductor is usually quite large, which results in higher primary ESR R_L and consequently in lower system efficiency [141].

In [58], [142], LCL topology was applied as the compensation for secondary in order to reduce the circulating current in the secondary and achieve the unity power factor pickup by compensating the reactive power at the secondary side.

LCC compensation. By adding a capacitor in series with the primary coil, the LC compensation network of the LCL topology is transformed into the LCC compensation (see Fig. 8 (c)). LC and the additional capacitor form a T-type compensation network. The LCC topology for the primary side was examined by Pantic et al. [143]. LCC compensation allows the reduction of the additional inductor resulting in its lower size and cost. By tuning of LCC compensation parameters, ZCS can be achieved [143]. Application of the LCC to the secondary side results in unity power factor pickup [58].

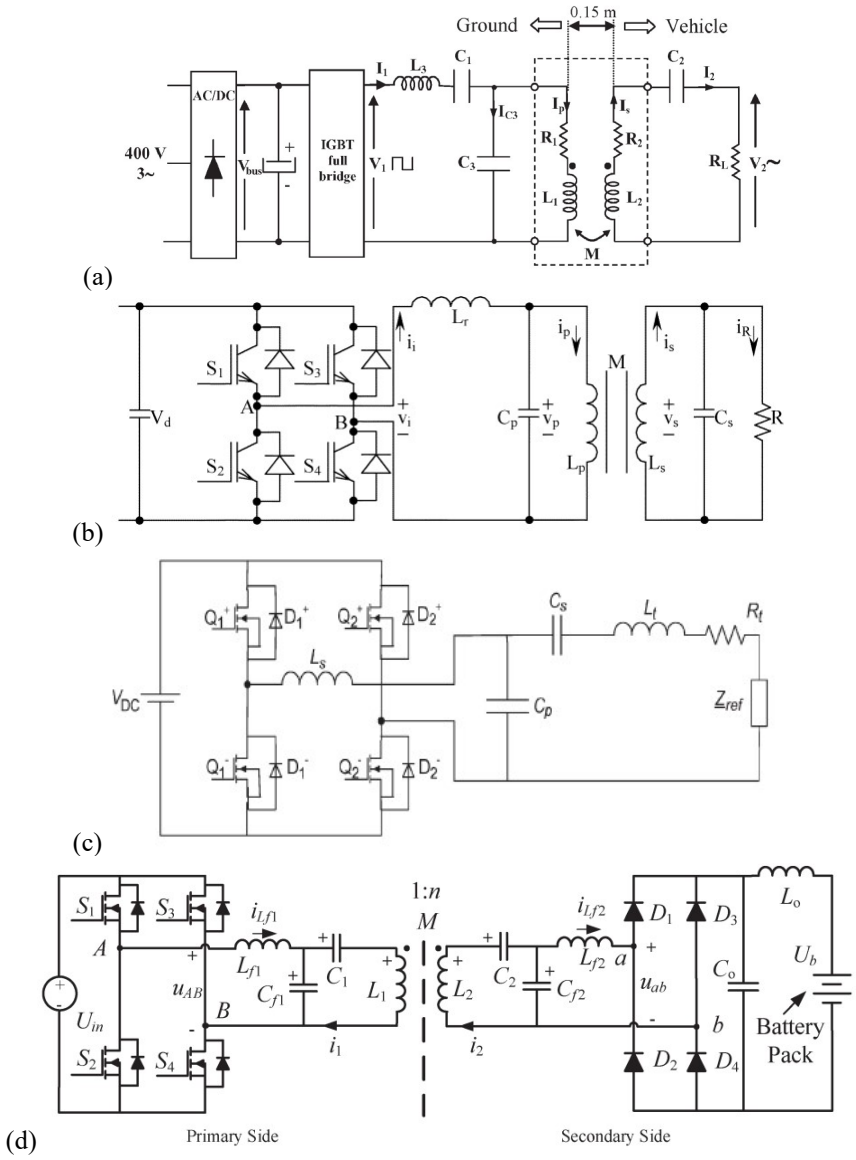

Fig. 8: (a) SP-S compensation topology. Source [138]. (b) LCL topology. Source [139]. (c) LCC compensation topology. Source [143]. (d) DLCC compensation topology. Source [184].

A lot of effort is focused on the issue of the IPT compensation up to today, existing topologies are further developed, and novel compensation topologies are presented, e.g., LCC-SP [141], LC-S [144], S-CLC [145], etc. Besides fixed compensation topologies, the variable compensation topologies were developed, which allow controlling of the compensation capacity during the operation. For example, Waters et al. presented adaptive impedance matching networks (low pass π-match networks formed by a fixed inductor and two variable capacitors) in [146] and Lim et al. introduced adaptive impedance matching based on the switched capacitor matrix [147].

Three-phase compensation. The three-phase pads such as TPBP require three-phase compensation topology. Topologies similar to the single-phase compensation, such as the SS can be used; however, it is necessary to consider whether the branches are connected in wye (Y) or delta (Δ). Fig. 9 shows the four possible implementations of the series compensation. The tuning methodology using the Clarke transformation is described in [70].

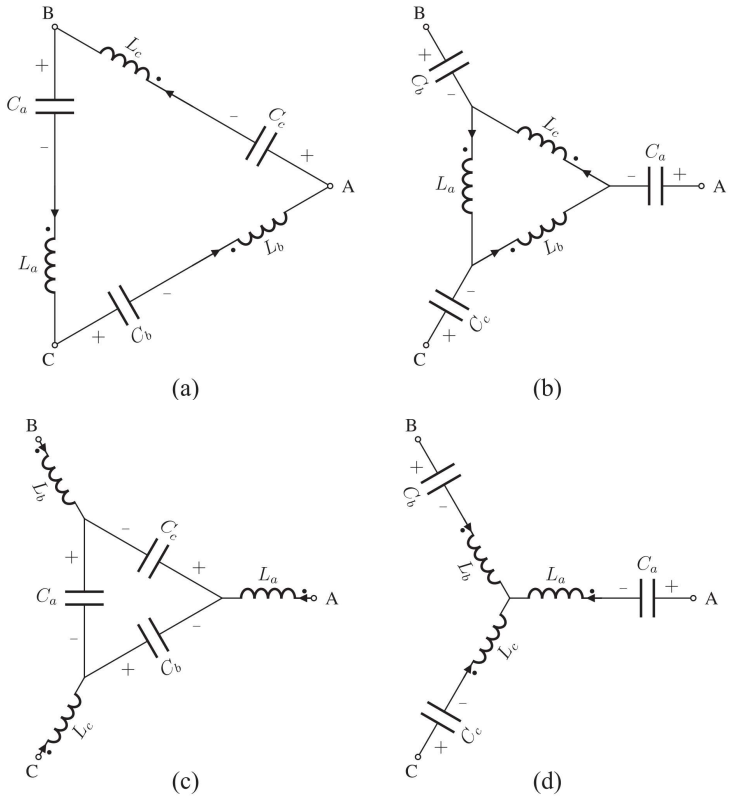

Fig. 9: Possible implementations of series compensation in three-phase systems. (a) Series ΔC-ΔL. (b) Series YC- ΔL. (c) Series ΔC-YL. (d) Series YC-YL.Source [70].

2.4 Electronics

Power electronics significantly impacts the system efficiency, reliability, and its power density. Likewise the conductive chargers, IPT chargers require an AC-DC conversion, which interfaces with the grid, ensures the power factor correction (PFC) and reduces the input harmonics distortions to meet the power quality standards for the grid connection [22]. Optionally, the primary and secondary side DC-DC converters are added for power flow control or impedance matching [106]. Because of their similarity conductive chargers, these electronic components are not examined here. Instead of that, this chapter primarily focuses on the electronics for the wireless of the IPT charger – the DC-AC converter at the primary side (transmitter) and the AC-DC converter at the secondary side (receiver). The semiconductor devices used for IPT and the control methods are also discussed. Relevant overviews of electronics used in IPT systems for EV charging can be found in [6], [22].

2.4.1 Topologies

The main role of the primary side DC-AC converter is to generate a high-frequency current for the transmitter pad. On the receiver side, the rectifier converts the AC current to DC current. A large number of possible topologies for exists for both the primary and secondary converters [6], [22]. They can be distinguished by number of phases, direction of power transfer (single direction or bidirectional) power level, operating frequency, and other criteria.

Single-phase topologies. In the low-frequency IPT, the single-phase systems are the most common in EV charging. They can accommodate most of the power range required for EV charging, but the high-power EV charging requires the three-phase connection at the grid rectifier, because the single-phase grid is limited in maximum power [22]. Single-phase systems are also preferred because of their simple structure and regulation.

The selection of the type the primary DC-AC converter type is given by two considerations: (A) whether the compensation topology requires a voltage source (e.g., SS, SP or LCC) or current source (e.g., PS, PP or SP-S), (B) whether the converter itself requires a voltage source (voltage-source driven converter) or current source (current-fed converter). In all cases, the resonant topologies are usually employed in order to increase efficiency [22]. The resonant part is typically provided by the IPT transformer as it is formed by the pad inductance and compensation capacity.

The current-fed converters (Fig. 10 (b)) provide lower current stress and inherent short-circuit protection [148], [149]. However, a DC inductor is required at the inverter input to form the current source. In addition,

compensation must be designed to match the current source characteristics. For these reasons, the application of current-fed converters is limited in high-power IPT systems [22]. Similarly, because the converters with the current source output [149] require a bulky inductor (Fig. 10 (b)), the compensation topologies requiring current source are less favored. Thus, the IPT systems typically employ the full bridge voltage source resonant converters [6].

The main type of the primary DC-AC converters for IPT chargers are voltage-source driven inverter with the voltage source output. Typically, full-bridge or half-bridge is employed (see Fig. 10 (c) and (d), respectively), depending on the requested power. For example, WiTricity developed an EV charger providing 11 kW at 91-93% efficiency [22], [150], which employs an SiC based full-bridge inverter and rectifier together with a single-phase bridgeless PFC. The Fraunhofer Institute presented in [151] an 11 kW bidirectional IPT charger with SiC devices, and Bosch developed a 7 kW prototype using the single-phase semiactive bridge topology as a rectifier [152].

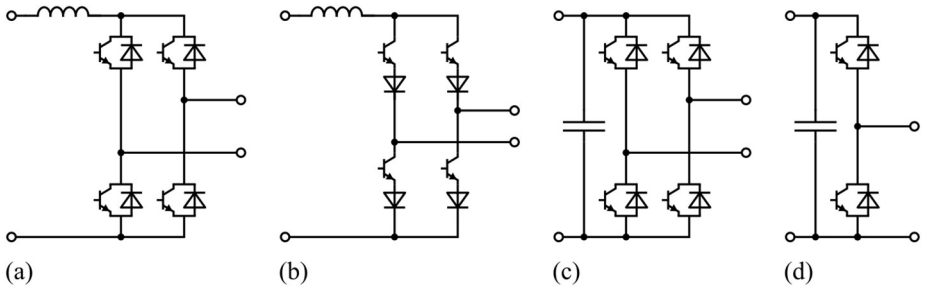

Fig. 10: Single-phase inverter topologies: (a) Current-fed inverter [148]. (b) Current-source inverter [149]. (c) Full-bridge voltage-source driven inverter. (d) Half-bridge voltage-source driven inverter.

Three-phase topologies. In comparison with the single-phase systems, the three-phase systems provide the higher power rating and higher power density, using the semiconductor devices with the same current rating. The high power density is achieved through system integration of couplers and lower filer requirements because of interleaving operation [22]. Pries et al. presented in [70] a 50kW 3-phase system for TPBP pad with very high power density of 195 kW/m^2 and specific power of 3.65 kW/kg per pad. Three-phase systems are used to power three-phase pads such as TPBP, which allows advanced control of the magnetic flux, in comparison with the single-phase systems. Initial designs of three-phase resonant inverter (see Fig. 11 (a)) can be traced to [62], where it was proposed to broaden the operating zone of a roadway vehicle charging system. Research effort focuses on the three-phase systems, because they can generate rotary magnetic field similar to the one in electric machines. [153] presents such systems, which cancel the magnetic field outside the specified operating area to improve EMC performance.

Three-phase inverter can be used to supply high power for single-winding pads (see Fig. 11 (b)). Each of the phase half-bridges are connected in parallel via coupled inductors, which suppress the circulating currents [154].

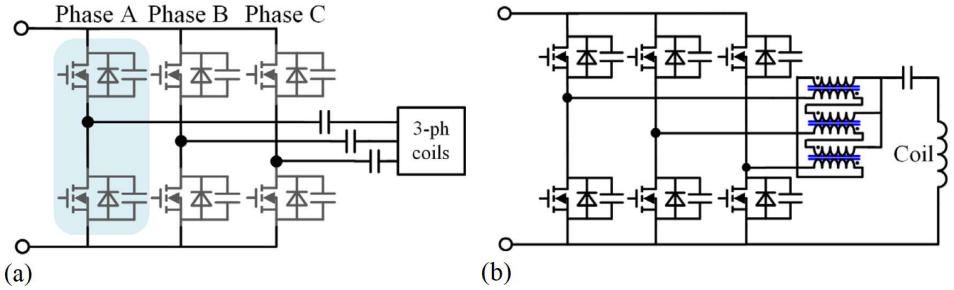

Fig. 11: Three-phase inverter. (a) Basic topology for pads with three-phase winding. (b) Three-phase inverter interleaved by a coupled inductor for a pad with a single-phase winding. Source [22].

Multi-module topologies. Another way to increase power rating of the primary converter is to use multiple parallel modules as in Fig. 12 (a). However, the circulating currents among the modules must be suppressed [155]. In some systems, multiple primary windings are coupled to a single secondary winding (see Fig. 12 (b)). This typical for the BPP and TPP pads [131], [133]. Similarly, because the DDQ pad has two windings (DD and quadrature), it requires two rectifiers when used in the secondary [60] - see Fig. 12 (c). Some systems increase the power transfer capabilities by using two parallel branches of both primary and secondary [156] as in Fig. 12 (b). However, the cross-coupling between the branches must be either considered or eliminated.

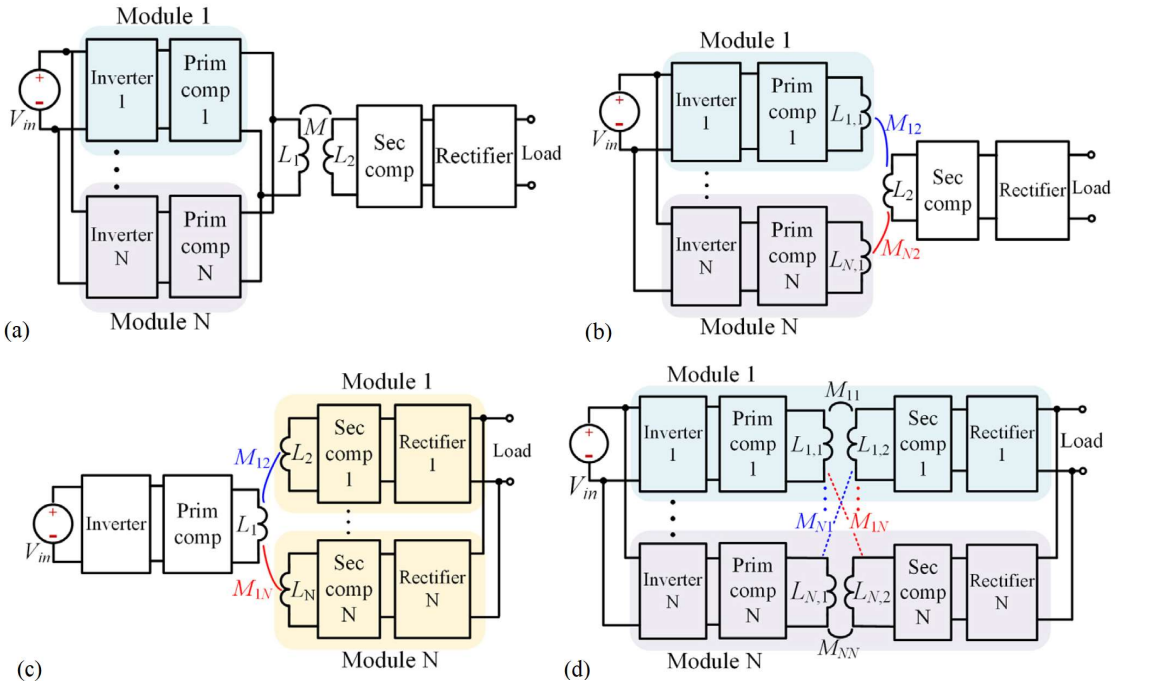

Fig. 12: Multi-module topologies. (a) Primary converter paralelization to increase tranmitter power rating. (b) Mutliple primary winding with separate inverters supplying a single secondary winding (e.g., BBP and CP). (c) Single primary winding supplying mutliple secondary windings with separate rectifiers (e.g., CP and DDQP). (d) System with multiple parallel branches [156]. Source [22].

Matrix converters. An alternative to the to the previous topologies is provided by the matrix converter, which replaces all of the primary side electronics (grid rectifier with PFC, DC-DC converter, and inverter). The main idea behind the use of the matrix inverter is to reduce the number of conversion stages. This improves the system efficiency and reliability and reduce the cost and volume [157]. However, because the matrix converter plays so many roles (convert low frequency AC current to required frequency, PFC, and control of power transfer), complex regulation methods are required which are consequently very demanding on the computational performance of the controller. Also, the operating frequency of the system is limited – matrix converters are unsuitable for high-frequency IPT.

Matrix converter topology is given by the number of phases of the grid, to which it is connected, and by the number of phases of the pad, which it powers. For example, [157] presents a matrix converter with three input phases and a single output phase (Fig. 13 (a)), while [158] presents a matrix converter with single phase both at its input and output (Fig. 13 (b)). Because the second topology is supplied from a single phase and there is no DC link capacitor, the power provided to the primary pad pulsates at the twofold frequency as the grid [158]. Thus, to achieve a DC voltage after the secondary rectifier, a larger compensation capacity is required.

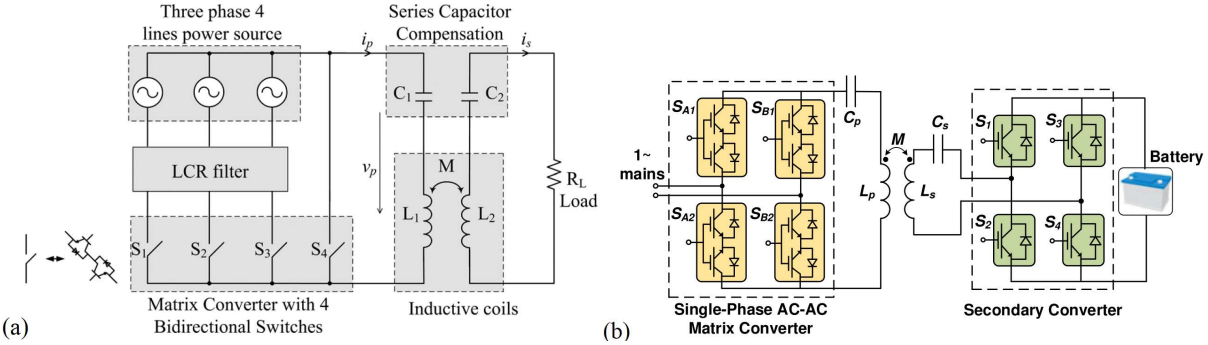

Fig. 13: Matrix converter (a) Topology with three input phases and single output phase. Source [157]. (b) Topology with single input phase and single output phase. Source [158].

Rectifiers. Depending on the output voltage level and required controllability, the secondary side uses full diode rectifier (Fig. 14 (a)), voltage doubler (Fig. 14 (b)), semiactive bridge (Fig. 14 (c)) or active bridge (Fig. 14

(d)) [22], [152], [159]. Three-phase secondary pads (e.g., TPBP) require three-phase rectifiers. Their topology is similar to the single-phase rectifiers, only additional branch is added.

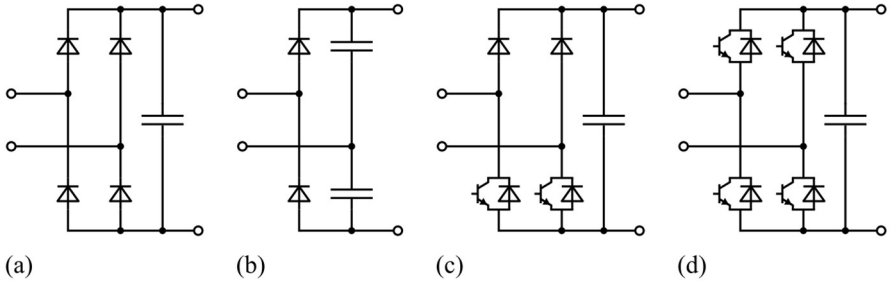

Fig. 14: Single phase rectifier topologies. (a) Full diode rectifier. (b) Voltage doubler. (c) Semiactive bridge. (d) Active bridge.

Amplifiers. The high-frequency IPT systems typically use the class E amplifiers at the primary side [160] – see Fig. 15 (a). Resistance *R* in Fig. 15 (a) represents the load, i.e., in the IPT system it is replaced with the primary pad with the compensation capacity. This topology is further elaborated, for example push-pull class EF topology in [85] (see Fig. 15 (b)), class EF_2 topology in [82] (see Fig. 15 (c)) and similar.

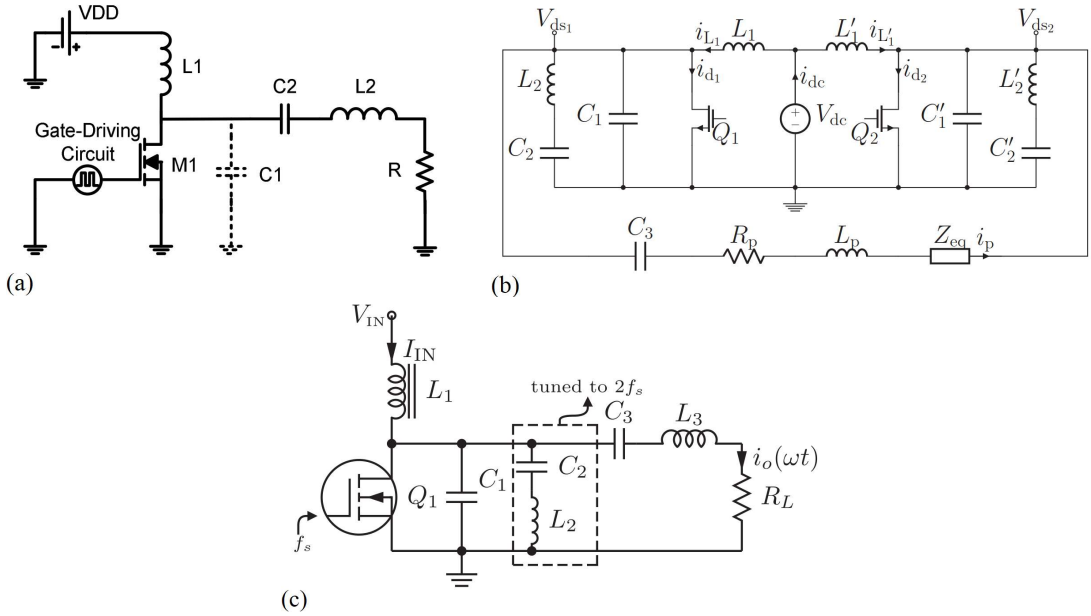

Fig. 15: Amplifier topologies for high-frequency IPT. (a) Class E topology. R represents the load, i.e., in the IPT system it is replaced with the primary pad with the compensation capacity. Source [160]. (b) Push-pull class EF topology. Source [85]. (c) Class EF_2 topology. Source [82].

2.4.2 Semiconductors

In the initial IPT systems, silicone-based devices such as IGBT were used [52]. However, because of the IPT system require both the high power and high operating frequencies (in comparison with the regular converters, e.g., for electric drives), Si devices are replaced by the wide bandgap semiconductors, such as silicon carbide (SiC) or gallium nitride (GaN). Comparison of SiC and GaN with Si devices can be found in [161].

SiC devices are typically used in the high-power low-frequency IPT systems for EV charging [70], [150], [151]. However, as the operating frequency of the SiC devices is typically limited up to 1 MHz [162], high-frequency IPT systems require the GaN devices [85], [107], [160]. Because the typical power rating of the GaN devices is smaller than of the SiC devices, power capability of high-frequency IPT system is limited [161]. Because the gating voltage threshold of both SiC and GaN devices is limited and they are sensitive to parasitic parameters, particular attention to the design procedure is required [22].

In order to increase power rating of a converter, multiple devices can be placed in parallel to share the current stress and reduce the equivalent ON-state resistance. Note that the proper selection of the gate driver

scheme and the design of communication loop is necessary to guarantee even sharing of the current among the devices and consequently the reliability of the system [22], [163].

2.4.3 Control Methods

The main goal of the system control is to regulate the output voltage, current or power, depending on the load requirements. In addition, another control loop can be added to maximize efficiency. In the literature, large number of control methods was proposed. They can be distinguished by the side at which they are applied as the primary side control methods [69], [164]–[166], secondary side control methods [58], [159], [167], [168], and dual side control methods [169], [170]. Mechanism of these methods is discussed further in Chapter 8.2 together with their relationship to the bifurcation phenomena.

Primary side control methods. The primary side control methods include the change of DC-link voltage (performed by the primary DC-DC converter), change of the operating frequency, duty cycle or phase between two legs (performed by the inverter). The variable frequency control is the main control method used by the Qi standard for consumer electronics charging [11], [13]. For EV charging it is employed e.g. in [166]. Frequency control employs wider frequency range, which may increase the risk of electromagnetic interference [6]. In designing the frequency control scheme, it is necessary to consider the bifurcation phenomena, as examined in Chapter 8.2.1.

In the systems with the fixed frequency, the duty cycle or phase shift can be employed for regulation [171]. However, these methods may result in a high circulating current in the converter and in the loss of the ZVS or ZVC condition [6]. These issues can be avoided by controlling the input DC-link voltage instead [172]. However, this introduces another converter, which losses may decrease the overall efficiency of the system.

More advanced control methods can be applied at inverter by altering its switching pattern. For example, the asymmetrical voltage cancellation method uses an alternative way to change the duty cycle, which increases the ZVS region [173]. ZCS and the lower switching frequency at light load conditions can be achieved by the discrete energy injection method [164].

The pulse density control method also uses the inverter, but instead of altering its duty cycle or the phase shift, the inverter is switched off for a number of periods [151]. By controlling the number of the switched-off periods with respect to the total number of periods in the cycle, amount of power transferred to the secondary is controlled.

Secondary side control methods. The secondary side control is typically performed by an additional converter. If the secondary regulation is performed by the DC-DC converter, the series compensation requires the buck converter, while the parallel compensation requires the boost converter. When the DC-DC is used for regulation, an additional DC inductor together with a diode on the current control path is typically added [6].

When the controller is moved to the AC side, the additional DC inductor and diode is not necessary. Also, thanks to the resonance, ZVS or ZCS can be achieved. This control method is presented in [167] and [168] together with the design of series and LCL compensation, respectively.

Dual side control methods. Dual side control is a combination of the primary side and secondary side control methods [169], [170]. The second control loop is typically used to increase the efficiency. However, use of the dual side control may increase the cost and complexity of the system in comparison with the single side control.

2.5 IPT Technology for Charging Applications Summary

IPT chargers can be divided by their operating frequency between the low-frequency systems (lower hundreds of kHz) or high-frequency system (6.78 MHz, 13.56 MHz). Stationary systems for EV charging achieve comparable levels of transferred power and efficiency as the conductive chargers [22], from which they differ by the wireless stage comprising of pads, compensation topology and electronics. Various pad geometries (CP, DDP, DDQP, BP, TPP, TPBP, etc.) were developed to achieve wide air gap and high misalignment tolerance required for EV applications. To improve the power transfer capability by operation at resonance, pads are compensated by compensation topologies such as SS, SP, SP-S, LCL, LCC and others. Electronics ensure the conversion between DC-AC at the transmitter and AC-DC by employing various single and three phase topologies of inverters and rectifiers, respectively.

3 Equivalent Circuit Model

All analyses in this work are performed for the two-coil IPT system with series-series compensation. Because its mathematical description is the simplest, it is a good starting point for the complex topic of the bifurcation phenomena analysis and the outlined approaches and obtained insights are transferable for other, more intricate topologies. The IPT system will be operated at low frequencies (tens or hundreds of kHz) to match the measurement setup for verification, which was designed for nominal operating frequency of 100 kHz. However, the findings presented in this thesis are valid for any frequency range (i.e., for high-frequency IPT systems).

In the first part chapter, the equivalent AC circuit model for such a two-coil IPT system with series-series compensation is presented. The quantities such as voltages, currents, powers, and efficiency including their equations, which will be used in the rest of the thesis are specified in the second part of the chapter.

3.1 Equivalent AC Circuit Model

The device setup from Fig. 4 can be characterized by the equivalent circuit model presented in Fig. 16. The model represents the series-series (SS) compensation and single transmitter-receiver arrangement. The transmitter voltage source (grid, rectifier, optional DC/DC converter and inverter) is described by the input voltage v_{in} [174]–[176], which is considered sinusoidal (first harmonic approximation). Therefore, all the voltages and currents are represented by phasors, which are marked as $\hat{X}$. The symbol X without this marking refers to phasor amplitude. The input voltage $\hat{V}_{in}$ is described by its amplitude V_{in}, its frequency f (equal to the operating frequency) and its phase φ_{in} with respect to the input current $\hat{I}_{in}$, which is taken as the reference. V_{in} is considered constant.

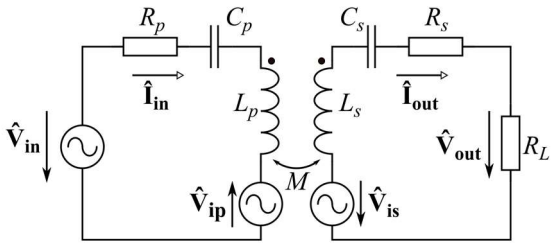

Fig. 16: Equivalent AC circuit schematics for the series-series compensated IPT system. Phasors are marked by bold symbols. Published by author in [20].

The IPT transformer coils are described by the inductances L_p, L_s, which are coupled by the mutual inductance M. The inductances are compensated by capacities C_p, C_s calculated as (5), which set the primary (f_{0p}) and secondary (f_{0s}) resonant frequencies:

$$C_p = \frac{1}{\omega_{0p}^2 L_p},\ C_s = \frac{1}{\omega_{0s}^2 L_s} \tag{5}$$

In the following analysis, it is assumed that both primary and secondary perfectly are perfectly tuned to the common resonance frequency f_0. The operating frequency f is tuned to the value for optimal power transfer, usually equal or close to the common resonance frequency f_0. The resistances R_p, R_s represent the sum of all the equivalent series resistances (ESR) in the circuit (i.e., coils, compensation capacities, connecting cables, etc.), which cause the loses. $\hat{V}_{ip}$ and $\hat{V}_{is}$ are the voltages induced in the primary (6)) and secondary (7)), respectively:

$$\hat{V}_{ip} = -j\omega M \hat{I}_{out} \tag{6}$$

$$\hat{V}_{is} = j\omega M \hat{I}_{in} \tag{7}$$

$\hat{V}_{ip}$ and $\hat{V}_{is}$ are plotted in the schematics in Fig. 16 to show their orientation with respect to other circuit voltages and currents.

The circuit load comprising of a rectifier, optional DC/DC converter, and a battery, is represented by the equivalent load resistance R_L. Ways to represent various rectifiers and DC/DC converters in R_L can be found for example in [174]–[176] and the battery model for example in [177]. Current and voltage at R_L are labelled as the output current $\hat{I}_{out}$ and voltage $\hat{V}_{out}$.

The circuit in Fig. 16 is described by following voltage equations:

$$\hat{V}_{in} = R_p \hat{I}_{in} + j\left(\omega L_p - \frac{1}{\omega C_p}\right)\hat{I}_{in} - j\omega M \hat{I}_{out} \tag{8}$$

$$j\omega M \hat{I}_{in} = (R_s + R_L)\hat{I}_{out} + j\left(\omega L_s - \frac{1}{\omega C_s}\right)\hat{I}_{out} \tag{9}$$

3.2 Quantities of Equivalent Circuit Model

The impedance, currents, voltages, powers, and efficiency of the equivalent AC circuit model in in Fig. 16 from the following equations.

3.2.1 Impedances

In this work, the influence of the secondary side on the primary side is examined as the cause of the bifurcation phenomena. One way to describe this influence is to use the induced voltage in the primary $\hat{V}_{ip}$ given by (6). However, in this case it is more practical to describe the secondary side influence by the reflected impedance $\hat{Z}_r$ [17]. This quantity describes how the secondary side impedance $\hat{Z}_s$ (10) is transferred via the coupling (described by the mutual inductance M) to the primary (11):

$$\hat{Z}_s = R_s + R_L + j\left(\omega L_s - \frac{1}{\omega C_s}\right) \tag{10}$$

$$\hat{Z}_r = \frac{\omega^2 M^2}{\hat{Z}_s} = \frac{\omega^2 M^2}{R_s + R_L + j\left(\omega L_s - \frac{1}{\omega C_s}\right)} \tag{11}$$

The secondary side reactance can be calculated as:

$$X_s = \omega L_s - \frac{1}{\omega C_s} \tag{12}$$

The reflected impedance can be divided in the real (i.e., resistance) and imaginary (i.e., reactance) component:

$$R_r = Re\{\hat{Z}_r\} = \frac{\omega^2 M^2 (R_s + R_L)}{(R_s + R_L)^2 + \left(\omega L_s - \frac{1}{\omega C_s}\right)^2} \tag{13}$$

$$X_r = Im\{\hat{Z}_r\} = -\frac{\omega^2 M^2 \left(\omega L_s - \frac{1}{\omega C_s}\right)}{(R_s + R_L)^2 + \left(\omega L_s - \frac{1}{\omega C_s}\right)^2} \tag{14}$$

The reflected impedance at resonance Z_{r0} has only a real component (15) and it is used in the normalization process of the general parameter model (which assumes a lossless system, i.e., $R_s = 0$) which is described in more detail in Chapter 6:

$$Z_{r0} = \frac{\omega_0^2 M^2}{R_L} \tag{15}$$

The primary side impedance $\hat{Z}_p$ is calculated as:

$$\hat{Z}_p = R_p + j\left(\omega L_p - \frac{1}{\omega C_p}\right) \tag{16}$$

As described in Chapter 5, when the reflected impedance $\hat{Z}_r$ increases, the bifurcation phenomena occur. Interactions between the primary side impedance $\hat{Z}_p$ (16) and $\hat{Z}_r$ (15) resulting in the bifurcation phenomena are examined in Chapter 7.4 Mechanism of Bifurcation.

The side reactance X_p is calculated as:

$$X_p = \omega L_p - \frac{1}{\omega C_p} \tag{17}$$

The input impedance $\hat{Z}$ which is often also labelled as the impedance seen by the source (e.g. in [17]) is calculated as the sum of $\hat{Z}_p$ and $\hat{Z}_r$ (18)):

$$\hat{Z} = \hat{Z}_p + \hat{Z}_r = R_p + j\left(\omega L_p - \frac{1}{\omega C_p}\right) + \frac{\omega^2 M^2}{R_s + R_L + j\left(\omega L_s - \frac{1}{\omega C_s}\right)} \tag{18}$$

The relationship between the induced voltage and reflected impedance is described by:

$$\hat{V}_{ip} = \hat{Z}_r \hat{I}_{in} \tag{19}$$

3.2.2 Voltages and Currents

The input current $\hat{I}_{in}$ can be calculated as the ratio of the input voltage $\hat{V}_{in}$ and the input impedance $\hat{Z}$:

$$\hat{I}_{in} = \frac{\hat{V}_{in}}{\hat{Z}} = \frac{\mathrm{V}_{in}\left(R_s + R_L + j\left(\omega L_s - \frac{1}{\omega C_s}\right)\right)}{\left(R_p + \left(\omega L_p - \frac{1}{\omega C_p}\right)\right)\left(R_s + R_L + j\left(\omega L_s - \frac{1}{\omega C_s}\right)\right) + X_M^2} \tag{20}$$

The output current $\hat{I}_{out}$ can be calculated as a ratio of the voltage induced in the secondary $\hat{V}_{is}$ and the secondary impedance $\hat{Z}_s$:

$$\hat{I}_{out} = \frac{\hat{V}_{is}}{\hat{Z}_s} = \frac{j\omega M \hat{I}_{in}}{R_s + R_L + j\left(\omega L_s - \frac{1}{\omega C_s}\right)} \tag{21}$$

The output voltage is calculated as a product of the output current $\hat{I}_{out}$ and equivalent load resistance R_L:

$$\hat{V}_{out} = R_L \hat{I}_{out} = \frac{j\omega M R_L \hat{I}_{in}}{R_s + R_L + j\left(\omega L_s - \frac{1}{\omega C_s}\right)} \tag{22}$$

In SS compensated IPT systems it is necessary to consider the phase shift between the primary and secondary side, especially in the calculation of the output power P_{out}. This phase shift is given by the polarity of the mutual inductance M (in Fig. 16 marked by the dots at the input terminal of each coil) and the direction of the current flowing through the coils, as they determine the polarity of the voltages induced both in the primary and in the secondary ($\hat{V}_{ip}$ and $\hat{V}_{is}$, respectively). If the current polarity is considered as given in Fig. 16, then if both beginning terminals of both coils are at the same side (either up or down), then the induced voltages have polarity depicted in Fig. 16. However, if they are alternating (if one beginning terminal is up and the second is down or vice versa), then the induced voltage polarities would be reversed.

In the following analysis, the same side position is considered – this results in the phase shift from $\hat{I}_{in}$ to $\hat{I}_{out}$ at f_0 of 90° (positive coupling). If the position is alternating, the phase shift is -90° (negative coupling). Outside resonance the phase shift depends both on difference between f, f_0 and on R_L value and it gains values between 0° and 180° for the same side coil orientation or -180° and 0° for the alternating coil orientation.

The voltages at coils and compensation capacitors calculated according to Table 2 are used in evaluation of bifurcation influence on the device operation in Chapter 8.1.3 Achieving the Required Output Power. The ESRs of the capacitors and coils is not considered in the calculation.

Table 2: Voltages at coils and compensation capacitors.

Primary inductance voltage $\hat{V}_{CoilP}$ [V]	$\hat{V}_{CoilP} = j\omega L_p \hat{I}_{in}$
Primary capacitance voltage $\hat{V}_{CCP}$ [V]	$\hat{V}_{CCP} = -\frac{j}{\omega C_p}\hat{I}_{in}$
Secondary inductance voltage $\hat{V}_{CoilS}$ [V]	$\hat{V}_{CoilS} = j\omega L_s \hat{I}_{out}$
Secondary capacitance voltage $\hat{V}_{CCS}$ [V]	$\hat{V}_{CCS} = -\frac{j}{\omega C_s}\hat{I}_{out}$

3.2.3 Input and Output Power, Efficiency

The input active power is calculated as the product of input current $\hat{I}_{in}$ and voltage $\hat{V}_{in}$ considering the phase shift φ_{in} between them:

$$P_{in} = \frac{1}{2} I_{in} V_{in} cos\varphi_{in} \tag{23}$$

The power transferred by the primary is depends on the input current amplitude I_{in} and the reflected impedance $\hat{Z}_r$. The amplitude Z_r determines the apparent power S_{tr}, the reflected reactance X_r determines the reactive power VA_{tr} and the reflected resistance R_r describes the active power P_{tr}:

$$P_{tr} = \frac{1}{2} R_r I_{in}^2 \tag{24}$$

The primary side efficiency η_p is then calculated as a ratio of P_{tr} (24) and the active input power P_{in} (23):

$$\eta_p = \frac{P_{tr}}{P_{in}} \tag{25}$$

When P_{tr} and P_{in} are substituted in (25), an equation for η_p is found solely in terms of R_r (13) and R_p:

$$\eta_p = \frac{R_r}{R_r + R_p} \tag{26}$$

As the IPT system is loaded only by a pure resistance represented by R_L, the phase shift between the output voltage and current is always zero. Thus, the output power has only an active component, calculated as:

$$P_{out} = \frac{1}{2} V_{out} I_{out} = \frac{1}{2} R_L I_{out}^2 \tag{27}$$

However, the calculation of the output power must consider the phase shift between the output variables ($\hat{V}_{out}$ and $\hat{I}_{out}$) and the input current $\hat{I}_{in}$, which is the reference, i.e., the current amplitude I_{out} must be used in (27).

The power received in the secondary is determined by the output current amplitude I_{in} and the secondary side impedance $\hat{Z}_s$. Again, the apparent power S_{rc} is given by the amplitude Z_s, the reactive power VA_{rc} by the reactance X_s and finally the active power P_{rc} by the sum of R_L and R_s:

$$P_{rc} = \frac{1}{2} (R_s + R_L) I_{out}^2 \tag{28}$$

The secondary side efficiency is then a ratio of the output power P_{out} (27) and P_{rc} (28):

$$\eta_s = \frac{P_{out}}{P_{rc}} \tag{29}$$

which after substituting P_{out} and P_{rc}, yields an expression for η_s solely in terms of R_L and R_s:

$$\eta_s = \frac{R_L}{R_L + R_s} \tag{30}$$

The losses in the coil ferrites are included in the coil ESRs R_p and R_s [178] and the transfer between the primary and secondary coil is considered lossless, thus the transferred and received active power P_{rc} and P_{tr} are equal.

The efficiency of the IPT transformer η_{tr} is defined as the ratio of the input active power P_{in} (23) and output power P_{out} (27):

$$\eta_{tr} = \frac{P_{in}}{P_{out}} \tag{31}$$

It can be expressed as the product of the primary and secondary efficiencies η_p and η_s, respectively:

$$\eta_{tr} = \eta_p \eta_s \tag{32}$$

When η_p (26) and η_s (30) are substituted, (32) is transformed into:

$$\eta_{tr} = \frac{R_r}{R_r + R_p}\frac{R_L}{R_L + R_s} \tag{33}$$

When the real part of reflected impedance R_r (13) is substituted, η_{tr} can be calculated from the circuit parameters as:

$$\eta_{tr} = \frac{\omega^4 M^2 C_s^2 R_L}{R_p(1 - 2\omega^2 L_s C_s) + C_s^2\left(\omega^4 M^2(R_s + R_L) + \omega^2 R_p(\omega^2 L_s + (R_s + R_L)^2)\right)} \tag{34}$$

4 Verification Instruments

This chapter briefly outlines the instruments used for verification of the general parameter model in Chapter 6, the bifurcation analysis in Chapters 7 and 8, and the bifurcation control methods in Chapter 9. The first part of this chapter provides an overview of the measurement setup and the methodology for data acquisition and processing. The second part outlines the implementation of the AC circuit model in MATLAB Simulink and the third a finite element method (FEM) model in ANSYS Maxwell, used for pad design.

4.1 Measurement Setup

Data for this thesis were measured using the setup displayed in Fig. 17 (schematics) and in Fig. 18 (photographs). There was no measurement setup available at the department, thus it was necessary to build a new one. However, thanks to this it was possible to tailor it specifically for the purpose of the bifurcation phenomena analysis. The setup was designed to closely represent the equivalent circuit model and allow a change of each of the circuit parameters (except R_p and R_s) as independently on others as possible in order to measure their influence on the bifurcation occurrence. Also, the setup was designed to allow precise and especially the repeatable measurements – to evaluate bifurcation phenomena, it is necessary to measure a frequency response, consisting of up to 70 measurement points.

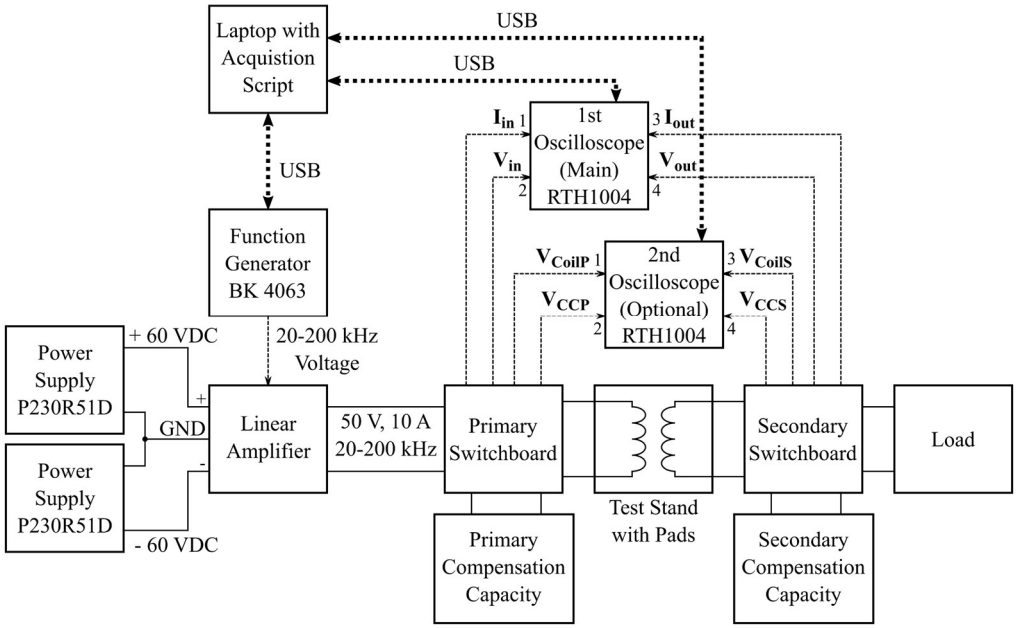

Fig. 17: Measurement setup block diagram.

The circuit is powered by a linear amplifier driven by the function generator BK Precision 4063 which generates a sinusoidal voltage. The linear amplifier is supplied by power sources Diametral P230R51D. Both the primary and the secondary use DD pads (double D pads [60]). Each coil inductance is compensated by a capacitive decade to provide control over f_{0p} and f_{0s}. Nominal resonance frequency was selected as 100 kHz (85 kHz could not be selected, because frequency range of LRC bridge used to measure the system parameters was limited to selected discrete points.

The output is loaded by a custom-built resistive decade, designed for high frequency operation. However, for lower values of R_L it has a slight inductive character, but this is considered in L_s and the calculation of C_s, which compensates it. The currents are calculated from the measured voltages at current shunts. Two oscilloscopes Rohde & Schwarz RTH1004 measure the component voltages with RT-ZI10 probes and the shunt voltages with P2220 probes set to 1:1 attenuation. The voltages are measured at designated points at the switchboards. For efficient measurement of frequency responses, the measurement procedure was automated – the function generator and the oscilloscopes are controlled by acquisition MATLAB script running on the laptop. The setup was designed with a focus on the IPT transformer operation and the bifurcation phenomena; thus, the linear amplifier and the resistor decade are used in place of an inverter and output rectifier, respectively. The component parameter values were measured with the LRC bridge Hameg HM8118 with Kelvin probe.

Many of the design issues connected with high frequency (HF) operation were solved thanks to prof. Vaclav Papež advice. The first subchapter describes the individual components of the measurement setup in further detail. It is followed with closer look at the data acquisition and data processing.

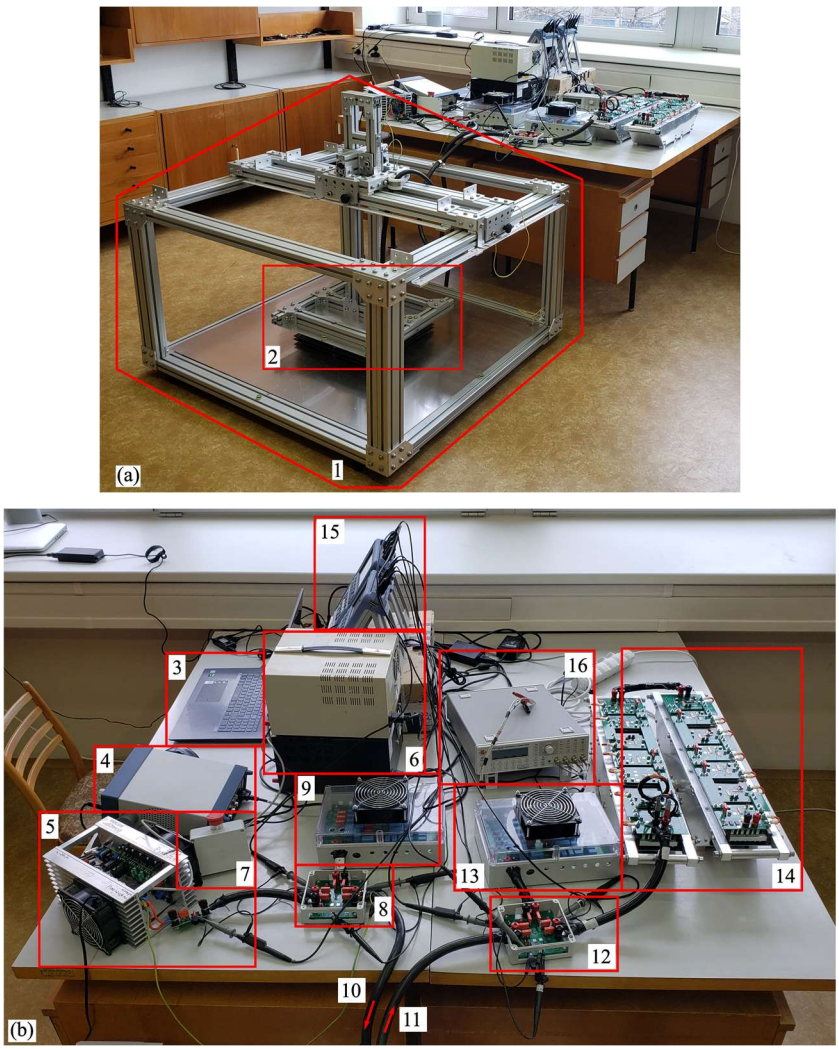

Fig. 18: Measurement setup. (a) Test stand for coil positioning. 1 - Test stand. 2 – Pads in the aligned position. (b) Setup without the test stand. 3 – Laptop. 4 – Function generator. 5 – Linear amplifier. 6 – Laboratory power sources. 7 – Total stop. 8 – Primary switchboard. 9 – Capacitive decade used as the primary compensation. 10 – Cable connecting the primary pad. 11 – Cable connecting the secondary pad. 12 – Secondary switchboard. 13 – Capacitive decade used as the secondary compensation. 14 – Resistive decade used as the load. 15 – Oscilloscopes. 16 – LRC bridge. Published by author in [20] (adjusted).

4.1.1 Components of Measurement Setup

Voltage source. The sinusoidal voltage powering the circuit is generated by a linear amplifier, which is driven by a function generator and powered from laboratory sources. The custom-built linear amplifier was designed and built by Ing. Pavel Skarolek. It comprises of two identical modules, which can be connected in series to double the output voltage. One module amplifies the voltage up to 50 V and can provide up to effective 10 A of current. The operating frequency range is 20-200 kHz. Circuit schematics of the module can be found in Fig. 105 in Appendix A1. Only one module was used in the presented analysis.

The linear amplifier is symmetrically powered from two laboratory sources Diametral P230R51D. These sources have two channels with controllable voltage in range 0-30 V, and maximal current 4 A. When the channels are connected in series, they provide 60 V required by the amplifier. The power supplies have current protection, which limits the current in the case of a short circuit. The laboratory sources are connected to the amplifier via a total stop, which allows safe disconnection of the laboratory sources in case of emergency.

Function generator BK Precision 4063 generates the source wave which is amplified. Thus, the function generator controls both the input voltage amplitude V_{in} and the operating frequency f. The generator is connected to laptop via USB and controlled by acquisition script in MATLAB

Test stand. The test stand for positioning of the transmitter and receiver pads was inspired by test stand developed by Qualcomm Halo and used for example in [179]. It is assembled from aluminum profiles and aluminum shielding plates at the sockets for transmitter and receiver pads. The transmitter pad is stationary, while the receiver pad can be manually positioned with respect to it in x, y, z coordinates with precision of approximately 1 mm. Positioning space is 1000 mm for x and y coordinates and 500 mm for z coordinate.

Pads. The DD pads described in Chapter 2.2.4 are used as the couplers between the primary and secondary side. The pads were inspired by examples provided in SAE J2954 [115]. The specific parameters of the magnetic core and winding such as dimensions, number of turns, etc. were selected based on the finite element method (FEM) simulation in ANSYS MAXWELL. The pads were optimized for high inductance value while keeping low amount of ferrite and wire used.

The pad construction was specifically designed to allow easy testing of various combinations. While the shielding is a part of the sockets for the transmitter and receiver pads, magnetic core and winding are placed attached to plastic sheets, which allows easy disassembly. In this way a single sheet with magnetic core and three sheets with windings which differ only by number of turns create three pads with different values of inductance. The magnetic core and winding sheets are assembled in the way which minimizes the gap between them (plastic sheets are on the outside).

The winding is made of copper litz wire STÄUBLI FLEXI-2V, 60.7032-22, (core section 2.5 mm^2, 651 strands of 0.07 mm diameter, rated current 32A, rated voltage 1.5 kV). The high insulation value was required, because for 100 kHz, 20A and 30 µH, the voltage between the input and output terminals is 377 V. The magnetic core is assembled of separate ferrite tiles Laird 33P2098-0M0. 2mm aluminum plate is used as the shielding. The magnetic core and winding of the transmitter and receiver pads are depicted in Fig. 106 in Appendix A1.

Originally, the winding was attached to the plastic sheet by a double-sided tape. However, due to forces connected with switching of relatively high current (>10 A) the mutual position of winding turns was changing resulting in changes of pad inductance significant to affect measurement precision. To prevent this, the winding had to be sealed by epoxide coat.

Capacitive decades. The pads are compensated by custom-built capacitive decades. They are identical for both the primary and secondary side. Decades are designed for 500 V and 30 A. Voltage rating corresponds with the pads – when compensating 30 µH pad at 100 kHz, 30A, the voltage between capacity terminals is also 377 V. Each decade consists of a capacitor assembly allowing parallel connection which achieves capacitance values in range 0.25-1999 nF with step of 0.25nF. Film capacitors with double metallized propylene from Kemet were used. They are listed in Table 3 together with their parameters. Capacitor values has tolerance of ±5%. The blade fuses were used instead of switches or jumpers to connect capacitors in the circuit. They are low cost, simple, can conduct required current of 20 A and introduce minimal parasitic parameters into the circuit. To improve safety, 1.1 MΩ discharge resistor added to deplete any remaining charge after turn-off. The capacitive decade is depicted in Fig. 107 in Appendix A1.

Table 3: Capacitors for capacitive decades.

	Capacity [nF]	Voltage [VDC]	Voltage [VAC]	Max. dV/dt [V/µs]	Inductance [nH/m]	Dissipation factor @100kHz
PHE450PF6470JF13R06L2	470	1000	600	1300	6	0.06%@10kHz
PHE450SD6100JR06L2	100	2000	700	1800	6	0.15%
PHE450TB5100JB16R17	10	2500	900	2500	6	0.15%
PHE450SB4100JR06	1	2000	700	2500	6	0.15%

Resistive Decade. The measurement setup is loaded by a custom-built resistive decade designed for 500 V and 30 A. The decade is comprised of thick film resistors from TELPOD RTS-02 series with tolerance of ±5%, each of which can burn up to 600 W if placed on a heatsink. The load resistance can be selected in range of 0-163 Ω with step 0.5 Ω. Decade is divided into two blocks of seven resistors to ease manipulation. The connection of resistors into the circuit is again controlled by blade fuses. The selection of resistors can be found in Table 37 in Appendix A1 together with the depiction of the decade in Fig. 108.

In designing the resistive decade, following measures adopted to adjust the design for high frequency (HF) operation:

- Each resistor has own heatsink.
- Heat sink is connected to potential of its resistor's output terminal.

- The heat sinks are spaced by 10 mm from each other and divided from the aluminum support structure by 10 mm of pertinax insulation in order to ensure galvanic insulation and to reduce capacitive coupling between the heat sinks.
- Each cell is tuned to have phase shift lower than 0.75 degree at 200 kHz.
- The cells interconnected by PCB to reduce parasitic inductance.

The combination yielding 32 Ω has non-measurable phase shift at 200 kHz. Otherwise, slight inductive character. Parasitic load inductance is considered in the calculations by adding to the secondary pad inductance L_s and only the resistive component is considered as the load.

Switchboards. As the connecting points between the components on each side (i.e., amplifier, compensation, and pad on the primary side and pad, compensation, and load on the secondary side) serve the switchboards. They are also used as the defined measurement points for the oscilloscope and LRC bridge. Each switchboard has designated test points for measurement of voltage across the components and a current shunt to measure current. To improve measurement of individual component parameters (e.g., pad inductance) by LRC bridge, the components can be disconnected from the circuit by removal of blade fuses and its parameters can be measured at a dedicated test point – it is not necessary to physically disassemble the circuit. The current shunt consists of three 10 mΩ 2W resistors WSR2R0100FEA from VISHAY with tolerance ±1%. The switchboard is depicted in Fig. 109 in Appendix A1.

Switchboards also define whether the compensation capacity will be connected in series or in parallel as two versions were designed. Thus, replacement of switchboards allows switching between four basic compensation topologies (SS, SP, PS, PP) described in Chapter 2.3.

Connecting cables. In the regular systems, the components placed as close as possible to minimize the length of connectors and thus to reduce resulting parasitic parameters. However, in the case of this measurement setup it is not possible. Long cables are necessary especially for connecting the pads placed in the test stand to the rest of the circuit placed on the adjacent tables (see Fig. 18 (a)). The connecting cables should be suitable for high frequencies and allow repeatability of measurement – current loops formed by connecting cables should be minimal and unchanging. The cables should also be able to transfer currents up to 30 A. It is not possible to use same wire as for windings of the pads. Even though they are designed for HF operation, the current loops are not minimal and could change due to manipulation. Due to required current it is not possible to use regular coaxial cables. High-power coaxial cables would meet all requirements, but they are difficult to obtain and expensive (especially at the required lengths).

However, these issues can be circumvented by using a regular cable with multiple cores such as Helukabel 10640. Coaxial cable has the characteristic impedance of 50 Ω. However, multicore cable where half of the cores conducts one direction and the remainder the opposite direction and the cores with opposite direction are interleaved, has the characteristic impedance of 100 Ω/n_p, where n_p stands for the number of core pairs. Helukabel 10640 has 25 insulated cores, 12 is used for one direction, 12 for the opposite and one is unused. Thus, its characteristic impedance is approximately 8.3 Ω. Outer sheath also holds the cores in place; thus, the inductive loop does not change when the position of the receiver pad changes in the test stand. Thanks to this, it is possible to connect the pads placed in the test stand further away from the rest of the circuit. without any significant impacts on the measurement precision. The resistance and inductance of connecting cables are included to the pad ESR and inductance.

Oscilloscopes. Two oscilloscopes Rohde & Schwartz Scope Rider RTH1004 were used to measure the currents and voltages. The Rohde & Schwartz probes RT-ZI10 with attenuation 10:1 were used to measure voltages and the probes Tektronix P2220 with attenuation 1:1 were used to measure the shunt voltages corresponding with the currents. The main oscilloscope measured the input current $\hat{I}_{in}$ and voltage $\hat{V}_{in}$ and also the output current $\hat{I}_{out}$ and voltage $\hat{V}_{out}$. The second optional oscilloscope could be added to measure voltages at the coils $\hat{V}_{CoilP}$, $\hat{V}_{CoilS}$ and compensation capacities $\hat{V}_{CCP}$, $\hat{V}_{CCS}$. The oscilloscopes were connected to laptop via USB and controlled by acquisition script in MATLAB

LRC Meter. Hameg HM8118 with Kelvin probe HZ184 was used to measure the component parameters for turned-off state and for preliminary tuning of the sides. HM8118 with probe HZ184 uses the four terminal method to measure the component parameters. HM8118 allows a compensation of the test leads; however, this compensation is only valid for the position of test leads at which it was performed. Thus, any manipulation will alter the position of the test leads and invalidate the compensation. Therefore, to improve measurement precision, it was necessary to tape together the HZ184 test leads to stabilize the inductance loops.

4.1.2 Data Acquisition for Bifurcation Analysis

Here will be discussed some of the issues of data measurement for the bifurcation analysis and measures to mitigate them. Analysis of bifurcation requires precise measurement of the input phase φ_{in} to evaluate its zero crossings (phase bifurcation (PB)), and of the voltage and currents to precisely locate the position of input impedance amplitude Z minima (input amplitude bifurcation (IAB)) and output power P_{out} maxima (output amplitude bifurcation (OAB)). Also, the circuit parameters must be measured accurately to achieve a good match between the measured data and calculations.

To resolve these issues, the current shunt inductance was considered, both sides were tuned actively (in operation instead of turned-off state) and the acquisition was automated. Also, the pad windings were sealed with epoxide, to remove small, but gradual changes caused by shifts due to forces produced by switching of high currents, as described in previous chapter.

Considering the current shunt inductance. As visible from Fig. 3 (a) there is a region where the transition of the input phase φ_{in} is relatively slow (5 Ω) thus any error in phase measurement will result in large error of the ZPA frequency. The input phase φ_{in} is calculated as a phase shift between the input current $\hat{I}_{in}$ (reference) and the input voltage $\hat{V}_{in}$. The current is calculated from the voltage measured at the current shunt in the primary switchboard. However, in this calculation is not enough to use the shunt resistance value R_{CS} of approximately 30 mΩ but also its inductance L_{CS} of approximately 12 nH must be also considered (measurement procedure described in Appendix A2). Even though the inductance value seems small, it causes phase shift of 13.9 degrees at 100 kHz (nominal operating frequency) and of 26.3 degrees at 200 kHz (upper limit of operating frequency).This phase shift appears to be capacitive (negative) – in a tuned system $\hat{I}_{in}$ and $\hat{V}_{in}$ are in phase, but the voltage at the current shunt $\hat{V}_{CS}$ is before them (inductance causes delay of current after voltage – see Fig. 19). The error of phase shift measurement renders the data unusable.

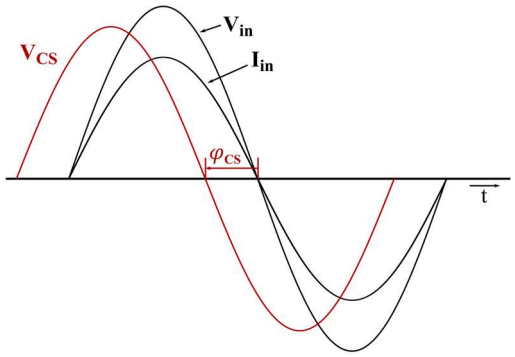

Fig. 19: Phase shift of the current shunt voltage $\hat{V}_{CS}$.

The input current amplitude I_{in} and phase φ_{in} is calculated from $\hat{V}_{CS}$ and models of R_{CS} and L_{CS} as follows. Model of both inductance and resistance of the shunt was obtained (their values slightly vary with frequency) according to Appendix A2. From R_{CS}, L_{CS} and operating frequency f, the correction phase shift is calculated, which is then subtracted from the phase of $\hat{V}_{CS}$, resulting in φ_{in}:

$$\varphi_{in} = \varphi_{CS} - atan\frac{\omega L_{CS}}{R_{CS}} \tag{35}$$

The amplitude I_{in} is calculated from V_{CS} and R_{CS}:

$$I_{in} = \frac{V_{CS}}{R_{CS}} \tag{36}$$

Output current $\hat{I}_{out}$ amplitude and phase are calculated in the similar fashion.

Active tuning method. The magnetic core of the coils is made of ferrites, thus the pad inductances are dependent on the currents through the coils and ferrite non-linearity [178]. This is influence causes detuning of the circuit with increasing current, i.e., system tuned in turned-off state becomes detuned as the current grows. The effect of detuning is especially significant for the operating points where the transition of φ_{in} is sharp and the peak of P_{out} is well pronounced. To compensate for detuning due to the ferrite influence, the IPT system must be tuned for the specific current in active state (i.e., during operation).

The frequency responses of the detuned systems were examined in order to find a suitable active tuning method. The results showed, that when measured at the target resonance frequency f_0, the input phase shift φ_{in}

between $\hat{I}_{in}$ and $\hat{V}_{in}$ is equal to zero, and it depends on the tuning of both the primary and the secondary (i.e., on f_{0p} and f_{0s}). On the other hand, the phase shift φ_{io} between $\hat{I}_{in}$ and $\hat{I}_{out}$ is equal to 90 degrees (for the same side orientation of the coils, see 3.2.2) depends only on the secondary side tuning (i.e., f_{0s}). Thus, if accurate measurement of phase is available, the secondary side is tuned with use of φ_{io} ($f_{0s} = f_0 \rightarrow \varphi_{io} = 90°$) in the first step and in the second step the secondary side with use of φ_{in} ($f_{0p} = f_0, f_{0s} = f_0 \rightarrow \varphi_{in} = 0°$).

To improve match between the measured and calculated values, newly tuned values of C_p and C_s should be used together with new values of L_p and L_s calculated from C_p, C_s and phase shifts φ_{in} and φ_{in}. Measurement showed, that coupling coefficient k is independent on the high current effects on ferrite cores, thus new value of M can be calculated from new values of L_p, L_s and unchanged k.

However, not even the active tuning removes the negative effects of ferrites – it only changes which part of the frequency response is affected. The IPT system will be tuned in the frequency range corresponding with the selected current level; however, outside this range the tuning will decay as current changes.

Automated acquisition script. Typical measurement for bifurcation analysis is a measurement of a frequency response, which can consist of up to 70 measurement points. Performing such a measurement takes a rather long time (if one point takes 1 minute, whole measurement takes 1 hour and 10 minutes) and is prone to errors during reading and saving of the data. Additionally, during such a period, the IPT system will heat up, which will decrease the match between measured and calculated values, especially in the case of the system with ferrites as their heating up changes the coil inductance.

To prevent these issues, automated acquisition script was developed in MATLAB. The script controls the function generator BK Precision 4063 and the one or two oscilloscopes R&S RTH1004 to measure the frequency response for selected set of frequency points. For the instrument control the script employs resources from the Instrument Toolbox. Communication with the function generator is based on NI VISA, while the communication with the oscilloscopes uses IVI VISA.

In the initialization phase the output folders for saved data are created. The function generator and the oscilloscopes are identified, and the communication is established. Initial frequency value and voltage is loaded to the function generator. The measurement itself is performed in a cycle, which steps through the selected measurement points. At first, the horizontal range is set based on selected frequency. The vertical ranges of oscilloscopes to match them to the measured voltages. Then, the main measurement of the all the voltages is performed and the data are saved for further processing.

The function generator and thus the voltage source is turned only during the calibration of vertical ranges, then it is paused (i.e., its channel is turned off) for 5 seconds, and then it is turned on again only for duration main measurement (including time necessary for transients to diminish). Otherwise, it is paused. Thus, while the one step of measurement cycle takes approximately 12 s, the function generator is turned on only for approximately 5 s. By this measure the heating of the IPT system is significantly reduced. Also, the measurement time is significantly reduced (measurement of 70 points takes about 15 minutes).

4.1.3 Data Processing

The data processing consists of two steps. At first, it is necessary to obtain the parameters of the first harmonic, corresponding with the voltages and currents in 3.2.2. From these, the impedances, powers, and efficiency can be calculated according to equations presented in 3.2.1 and 3.2.3. In this chapter, the obtaining of the voltages and currents will be described.

A MATLAB script was developed to process the measured data, as any other form of processing would be rather difficult. The waveform data saved from the oscilloscope contain 5-6 periods of 15,000 samples per trace. The script is aimed to obtain the obtain the amplitude and phase with respect to the input current $\hat{I}_{in}$ and calculate the currents from the shunt voltages consider the current shunt parameters R_{CS} and L_{CS}.

Because the circuit is powered from the sinusoidal voltage source, all the measured voltages are also sinusoidal. Thus, aforementioned parameters were obtained by fitting the data. For this purpose, robust sineFit function developed by Peter Seibold was used [180].

The sine wave is described by four parameters (see Fig. 20): frequency (or period), amplitude, phase (horizontal shift with respect to certain time) and offset (vertical shift with respect to certain level). The sineFit function returns these four parameters, phase with respect to $t = 0$ and offset as the mean of all values [180]. The actual phase shifts are calculated by subtracting the phase shift for voltage corresponding with $\hat{I}_{in}$ from the rest and the phase shift for $\hat{I}_{in}$. As the circuit is powered from an AC circuit, the offsets (which would correspond with DC component, but here are result of fitting of incomplete periods) are neglected. By this, the required voltage parameters (i.e., amplitude, frequency and phase) are obtained. Consequently, the currents $\hat{I}_{in}$ and $\hat{I}_{out}$ are calculated from the shunt voltage amplitude and phase and shunt R_{CS}, L_{CS} according to (35) and (36).

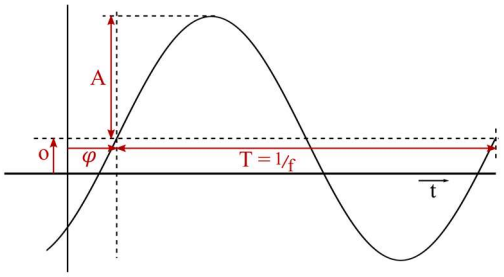

Fig. 20: Parameters describing the sine wave: period T, frequency f, amplitude A, phase φ and offset o.

4.2 AC Circuit Model in Simulink

Model of the AC circuit described in Chapter 3 implemented in MATLAB was used as another verification tool. Similarly, as in the case of the measurement setup, its typical task is to measure the frequency response in a specific range. Model is simulated in the time domain – the sine waveforms of voltages and currents are evaluated. It is too tedious to run the simulation of each frequency point manually, thus the simulation has two parts: a model in Simulink and a control script in MATLAB, which controls the simulation.

The time domain Simulink model is depicted Fig. 21. The input variables are loaded from the workspace, where they are defined by the control script. The model simulates a single frequency point of the frequency response. Because the frequency differs in each simulation run, both the simulation stop time and step is variable. The stop time is set to 150 periods and the variable step maximum was set to 1 µs. The main circuit is comprised of Simscape blocks. It is powered by controlled voltage source, which is directed by a Sine Wave block. Blocks PS->Amp,Phi obtain the amplitude and phase values from the measured sinusoidal voltages and currents by using PS Harmonic Estimator. They also convert the phase in radians into degrees. Last 100 samples of the amplitude and phase is then exported back in the workspace, where they are further processed by the control script.

The MATLAB script controls the whole simulation. The simulation of the frequency response is controlled by a cycle, which gradually simulates each frequency point. In each step, the input variables are loaded to the workspace and the simulation is started. When it is done, an average is calculated from the obtained amplitudes and phases. The results are saved in the same format as the outputs of the processing scrip for the measurement data described in Chapter 4.1.3. Thanks to this compatibility, any following scripts can use the data obtained from measurement or simulation interchangeably. Because the bifurcation phenomena are typically evaluated for a change of single or multiple circuit parameters, it is convenient to define additional cycle, which would step through the values of the evaluated circuit parameters, and thus fully automate the simulation.

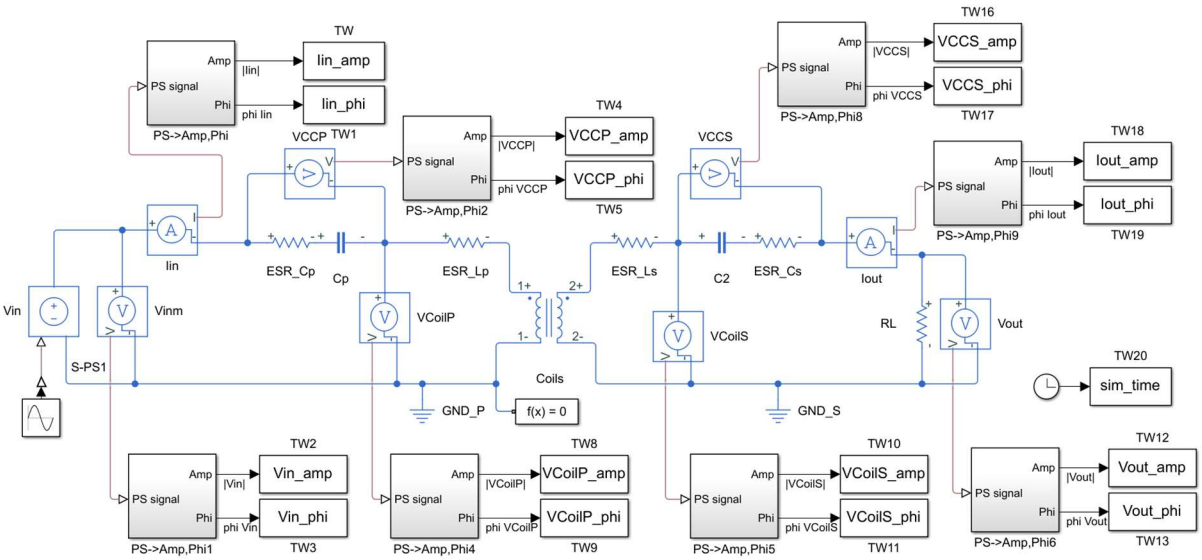

Fig. 21: Simulation of AC circuit model from Chapter 3 in MATLAB Simulink.

4.3 FEM Model in ANSYS Maxwell

A 3D model of the pad arrangement was developed to design the pads with the suitable parameters (see Fig. 22). Model was developed in ANSYS Maxwell 2019 R1.The solution is selected as Eddy Current.

The modelled pads consist of shielding, magnetic core, and winding. Winding and magnetic core materials are adjusted to match the parameters of litz wire and ferrites used in pads described in Chapter 4.1.1. Instead of modeling the individual turns, the winding is modeled as a single loop. Its width corresponds with the width of winding (without the insulation). To achieve relevant values of the coil ESR, its thickness is calculated so that the cross-section of the loop matches the cross-section of the winding.

To ease testing of different geometries, a control script written in VBScript was developed. Multiple geometries are defined via a CSV file containing defining parameters. For each arrangement the script creates the geometry, assigns boundaries, mesh, and excitations. It sets the parameters of analysis and runs it for selected frequencies. When finished, the results are exported to CSV for further processing.

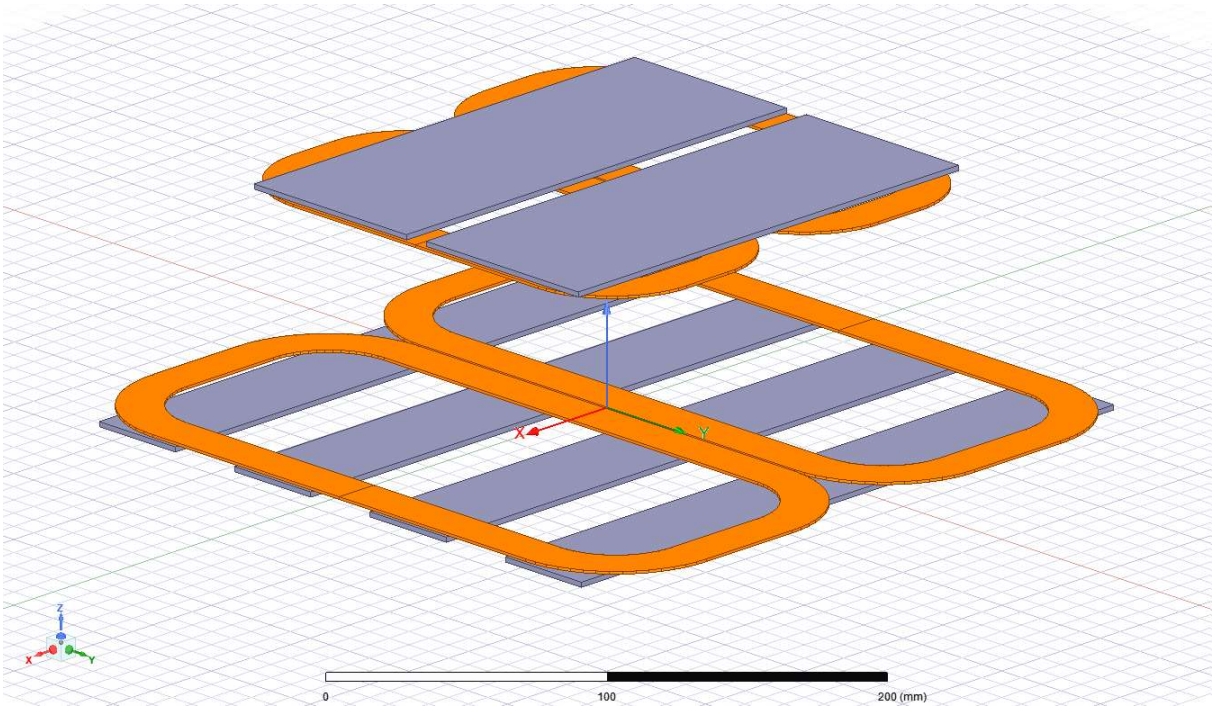

Fig. 22: Model of pad arrangement in ANSYS Maxwell. Both the transmitter and receiver shielding are hidden.

5 Overview of Bifurcation Phenomena

This thesis focuses on the analysis and control methods of bifurcation. As it was prefaced in the introduction, for the full understanding it is not sufficient to focus only on the bifurcation of the input phase φ_{in} as presented in [17], but also on the frequency splitting of the output power P_{out} maxima (e.g. in [21]) and the splitting of the input impedance amplitude Z minima. The analysis presented in the following chapters resulted in a shift of perspective – these are not three separate phenomena but three manifestations of single phenomenon of growing secondary side. Thus, in this chapter the new perspective is discussed in further detail together with the novel nomenclature as it is the basis for the rest analysis.

In the first part of the chapter, a closer look will be given to the bifurcation phenomena – phase bifurcation (PB), output amplitude bifurcation (OAB) and the input amplitude bifurcation (IAB). The link between these phenomena is outlined in the next part of the chapter, followed by the discussion of the novel nomenclature. The chapter is closed by the definition of term "course of bifurcation", which is essential for the further analysis.

5.1 Manifestations of Bifurcation Phenomena

As the first step, let's examine the splitting of ZPA frequency (PB), output power P_{out} (OAB) and input impedance amplitude Z (IAB) for decreasing equivalent load resistance R_L, while the other circuit parameters remain constant. Fig. 23 (a), (b) and (c), respectively, depict the frequency responses of φ_{in}, output power P_{out}, and input impedance amplitude Z for different values of R_L. For each R_L value, Fig. 23 presents the frequency responses measured at the test stand described in the previous chapter and that calculated from the equivalent circuit model, which show good agreement.

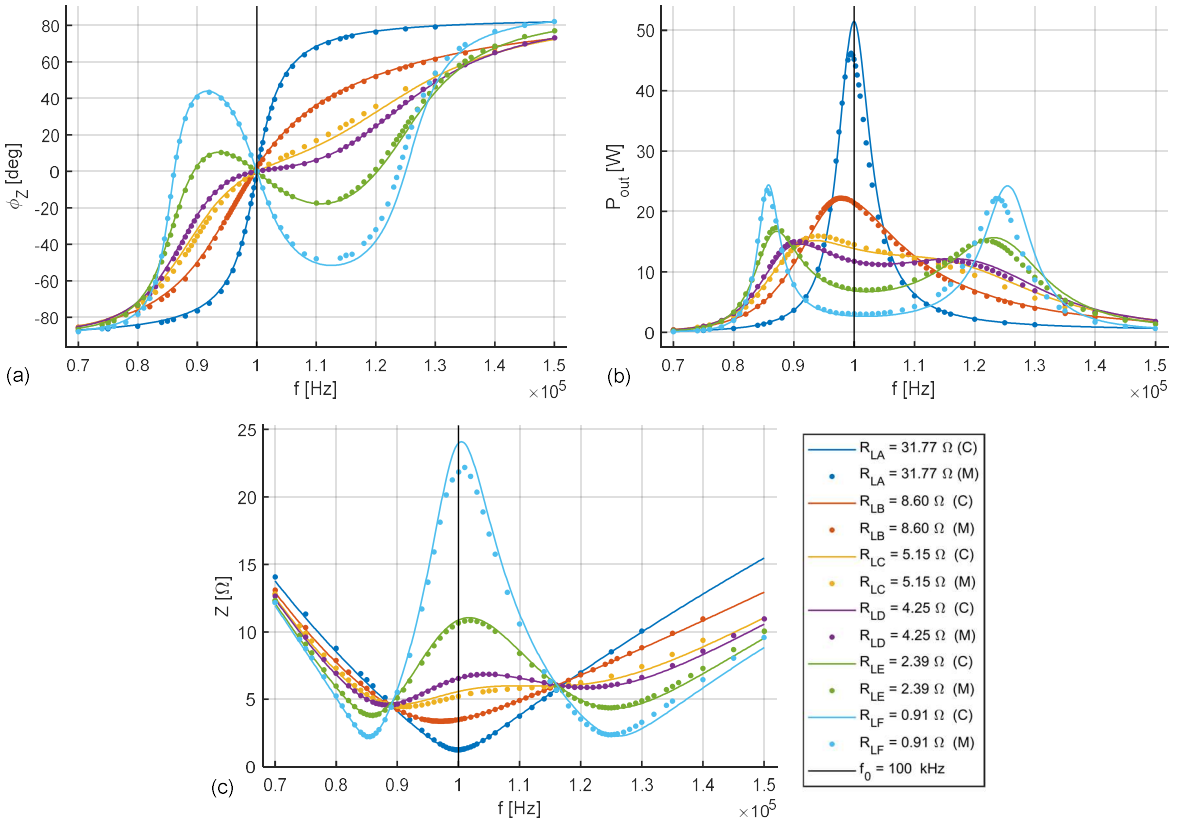

Fig. 23: (a) The phase shift between the input current and voltage φ_{in}, (b) the output power P_{out} and (b) input impedance amplitude Z for decreasing load resistance R_L. Labels (C) and (M) mark the calculated and measured frequency responses, respectively.

The differences between the calculated and measured frequency responses are caused by the dependance of the coil inductances on the currents through the coils and ferrite non-linearity [178], despite using the active tuning described in Chapter 4.1.2. This is especially significant for R_{LA} and R_{LE}, at which the I_{in} or I_{out} current amplitudes are the highest. Also, the limitation of active tuning to a specific current level becomes apparent as the bifurcation phenomena deepens (R_{LE} and R_{LF}). The difference between the I_{in} and I_{out} values at f_0 and their

maxima which are away from f_0 increase and the IPT transformer becomes detuned outside f_0. This results in mismatch between the measured data and the model, which views the circuit parameters as constant.

The circuit parameters of the used measurement setup are summarized in Table 4. The input voltage amplitude V_{in} was limited only to 13.26 V due to the 10 A current limit of the linear amplifier. High values of R_p, R_s and consequently rather low primary and secondary quality factors Q_p = 57.6 and Q_s = 34.9 are caused by the experimental nature of the setup (e.g., long interconnecting cables, etc.) described in Chapter 4.1. The coils themselves have ESRs of 122 mΩ (primary) and 98 mΩ (secondary), which correspond with quality factors of 154.5 and 112.84 respectively. 4-turn coils were used both in primary and secondary.

Table 4: Equivalent circuit model parameters.

Parameter	Symbol	Value
Input voltage amplitude	V_{in}	13.26 V
Operating frequency range	f	70-150 kHz
Primary inductance	L_p	30.0 µH
Secondary inductance	L_s	17.6 µH
Primary capacitance	C_p	84.60 nF
Secondary capacitance	C_s	143.97 nF
Mutual inductance	M	8.5 µH
Load resistance range	R_L	0.91-31.77 Ω
Resonance frequency	f_0	100 kHz
Primary ESR	R_p	0.33 Ω
Secondary ESR	R_s	0.32 Ω

One could consider frequency responses for R_{LA} = 31.77 Ω, i.e., single peak of P_{out} (Fig. 23 (b)), a single minimum of impedance amplitude Z (Fig. 23 (c)) and a single zero crossing of the input phase φ_{in} at the resonance frequency f_0 (Fig. 23 (a)), as the typical frequency responses of the output power P_{out} described by (27), and the input impedance $\hat{Z}$ described by (18). However, this is valid only over a small portion of possible operating points, when R_L is high and no bifurcation phenomena occurs.

As R_L decreases (e.g., R_{LB} = 8.60 Ω and R_{LC} = 5.15 Ω in Fig. 23), the single peak of P_{out} flattens, widens and its maximum moves away from the resonance frequency f_0. Similarly, the Z minimum becomes less pronounced and moves away from f_0.The sharp phase φ_{in} transition becomes less steep (Fig. 23 (a)).

With further decrease of R_L both IAB and OAB occur (e.g., R_{LD} = 4.25 Ω in Fig. 23). In this case, both the P_{out} maximum and Z minimum splits into two. As examined further in Chapter 6.4, IAB occurs at slightly higher values of R_L than OAB. The input phase φ_{in} increasingly flattens in a band around f_0. Finally, PB occurs as R_L is further decreased (e.g., R_{LE} = 2.39 Ω in Fig. 23). As the decrease of R_L continues towards zero, the frequencies of φ_{in} zero crossings and the local maxima of P_{out} and local minima Z stabilize at certain values (e.g., 85.44 kHz and 125.99 kHz for R_{LF} = 0.91 Ω in Fig. 23).

5.2 Cause of Bifurcation Phenomena

In the literature, PB (bifurcation) and OAB (frequency splitting) were previously compared from the perspective of their frequencies, boundary conditions or whether they relate to the system input (bifurcation) or output (frequency splitting) [21], [181]. However, the similarities and differences between PB and OAB raise the following questions: What is the origin of PB and OAB? Do the correlations between the course of PB and OAB imply that they are both caused by the same underlying phenomena? Investigation of these issues is essential for a deeper understanding of the inductive power transfer.

Insight into these questions is provided by the description of the PB mechanism in [17]. According to Wang et al., PB is caused by the reflected impedance $\hat{Z}_r$ (11) of the secondary into the primary side. However, splitting of the ZPA frequency of the input impedance $\hat{Z}$ is only one of the effects which the reflected impedance has – it also affects the input impedance amplitude Z, causing a splitting of its minimum. Consequently, as examined in Chapter 7.4.2, the splitting of Z minimum impacts the input current $\hat{I}_{in}$ and both output voltage $\hat{V}_{out}$ and current $\hat{I}_{out}$, resulting in the output power P_{out} frequency splitting.

The influence of reflected impedance $\hat{Z}_r$ is visible from frequency responses Fig. 23. As the equivalent load resistance R_L decreases, $\hat{Z}_r$ grows according to (11) – see Table 5 containing values of Z_{r0}. When the ratio of $\hat{Z}_r$ with respect to $\hat{Z}_p$ (which does not change with R_L) reaches specific thresholds, specific bifurcation phenomena begin to occur. The relationship between the reflected impedance and PB, IAB and OAB is in detail examined in Chapter 7.4 Mechanism of Bifurcation, which further confirms the assumption of $\hat{Z}_r$ as the cause of bifurcation phenomena.

Due to the findings presented in Chapter 7.4, it is necessary to change the perspective on bifurcation as splitting of input phase φ_{in} and frequency splitting as splitting of the output power P_{out} together with the input impedance amplitude Z: They are not three separate phenomena, but only three manifestations of a single phenomenon, which is a growing secondary side influence (i.e., reflected impedance) impacting the primary side.

The examination in Chapter 7.4 also shows that the splitting of the input current amplitude I_{in} corresponds to the input impedance amplitude Z splitting and the splitting of the output voltage and current amplitudes V_{out} and I_{out} and the input active power P_{in} maximum corresponds with the frequency splitting of P_{out}.

Table 5: Reflected impedance at resonance Z_{r0} for frequency responses in Fig. 23.

R_L [Ω]	31.77	8.60	5.15	4.25	2.39	0.91
Z_{r0} [Ω]	0.90	3.32	5.54	6.71	11.93	29.71

5.3 Novel Nomenclature

To reflect all these outcomes and make the presented analysis more comprehensive, the following labelling was used. First, the main phenomenon of growing secondary side influence on the primary side is denoted as "bifurcation". Its manifestations are called as follows:

(A) Splitting of the ZPA frequency (bifurcation according to [17]) is labelled as "phase bifurcation" (PB).

(B) Splitting of the input impedance or current amplitudes Z and I_{in} is labelled as the "input amplitude bifurcation" (IAB).

(C) Splitting of the output power P_{out} maximum (frequency splitting according to [19], [21]) together with splitting of the input power P_{in} maximum and output voltage and current amplitudes V_{out} and I_{out} is labelled as the "output amplitude bifurcation" (OAB).

This adjustment can be summarized as: bifurcation is a process of growing secondary side influence (represented by the increasing reflected impedance $\hat{Z}_r$) on the primary side, which manifests as the phase bifurcation (splitting of ZPA frequency), the input amplitude bifurcation (splitting of the input impedance amplitude minima) and the output amplitude bifurcation (splitting of the output power maxima). This nomenclature is used in in the rest of the thesis.

The described nomenclature was presented in [20].

5.4 Course of Bifurcation

It can be seen from the previous description and Fig. 23, as R_L is decreased, the secondary side influence and thus the bifurcation phenomena intensify. The process of growing secondary side influence during which the manifestations of bifurcation (IAB, OAB, PB) gradually occur is labelled as the "course of the bifurcation". More specifically, the course of bifurcation can be viewed as a trajectory of the system operating point, along which the reflected impedance $\hat{Z}_r$ grows and consequently the frequencies of Z minimum, P_{out} maximum and $\varphi_{in} = 0$ progressively split. The degree of secondary side influence of a specific operating point then is expressed by the reflected impedance amplitude at resonance Z_{r0} given by (15). The value for f_0 is used because Z_r changes with operating frequency. Z_{r0} is used for normalization in the general parameter model.

6 General Parameter Model

The frequency responses and the description based on the circuit parameters are insufficient for the further analysis of bifurcation phenomena (e.g., description of bifurcation frequencies and boundaries). Thus, general parameter model was developed including a novel visual tool called the Q_L state diagram. The model unifies the description of phase bifurcation (PB), input amplitude bifurcation (IAB) and output amplitude bifurcation (OAB).

In the literature, the mathematical descriptions of PB (labeled as "bifurcation") and OAB (labeled as "frequency splitting") are based on different approaches. While in the description of PB by Wang et al. in [17] the IPT system is represented by only three generalized parameters (loaded quality factors Q_{Lp}, Q_{Ls} and normalized frequency u), the description of OAB provided by Niu et al in [21] is based on the circuit parameters (L_p, M, R_L, ω, etc.). The IAB was not yet described in the literature.

The general parameter model uses as its starting point the description of PB, because it uses the general parameters Q_{Lp}, Q_{Ls} and u. In this manner, the resulting descriptions of bifurcation phenomena are significantly simplified. This generalization also provides a common metric for description and comparison of bifurcation phenomena very different systems (e.g., phone charger vs electric vehicle charger) – occurrence of the bifurcation phenomena depends only on Q_{Lp} and Q_{Ls} (u only specifies the operating point position in the frequency sweep). Thus, similar normalized descriptions based on Q_{Lp}, Q_{Ls} and u are developed for IAB or OAB.

From these descriptions, the frequencies describing the individual phenomena are calculated (e.g., frequencies describing the splitting of the output power P_{out} maxima). Based on these frequencies, generalized boundary conditions for the bifurcation phenomena occurrence are developed. The main advantage of the generalized boundary conditions is that they are expressed only in terms of Q_{Lp} and Q_{Ls}. Thanks to this, they apply to any trajectory of the operating point, no matter whether it is given by a single or multiple circuit parameter change (e.g., change of equivalent load resistance R_L or change of the primary, secondary, and mutual inductances due to misalignment).

The description of bifurcation phenomena is summarized in a novel analytical tool called the Q_L state diagram. Its 2D version allow easy visual evaluation of bifurcation or frequency splitting at the specific operating point, trajectory, or area. The sections of its 3D version are useful tools for better understanding of the bifurcation phenomena in the IPT system (see Chapter 7) and also for the comprehensive evaluation of system regulation (see Chapter 8), impacts of disturbances (e.g., change of load) and other phenomena. This tool also is used for evaluation of the bifurcation control methods in Chapter 9.

The first section presents the methodology used to develop the general parameter model. The following three chapters examine the mathematical description of PB, OAB (i.e., frequency splitting) and IAB. Based on them, the different regions with the typical behavior of the bifurcation phenomena are delimited by obtained boundaries in the course of bifurcation, followed by a discussion of the Q_L state diagram. The following description of the general parameter model was presented in [20].

6.1 Methodology

As discussed in the introduction, it is advantageous to base the resulting model on the generalized parameters (loaded quality factors Q_{Lp}, Q_{Ls} and normalized frequency u), i.e. keep the description of PB as presented in [17], and develop a corresponding description for OAB. IAB is based on the amplitude of the normalized impedance $\hat{Z}_n$, also presented in [17]. This section provides an overview of the approach used to develop the general parameter model, which will be fully expanded upon in further sections.

The resulting general parameter model is based on the following set of assumptions:

- The normalization approach from [17] requires the lossless circuit, thus the resistances R_p and R_s are neglected.
- The IPT transformer is powered from an ideal sinusoidal source. Thus, the analysis assumes the first order harmonic approximation.
- The load impedance is real and draws only active power.
- Both the primary and secondary sides are synchronously tuned to have the same resonance frequency f_0.

After applying these assumptions, the device is described by seven circuit parameters: V_{in}, L_p, L_s, M, f_0, R_L and f.

The mathematical description presented in the following section can be outlined as follows: Each of the bifurcation phenomena (PB, OAB, IOB) is described by its governing equation, e.g., PB is described by $Im\{Z\} = 0$, which is another way to express that the phase shift between the input voltage $\hat{V}_{in}$ and current $\hat{I}_{in}$ is equal to 0.

These equations are normalized as in [17] in order to be expressed by the loaded quality factors $Q_{L\mathrm{p}}$ and Q_{Ls} and normalized frequency u instead of the equivalent circuit parameters:

$$Q_{L\mathrm{p}} = \frac{R_L L_\mathrm{p}}{\omega_0 M^2},\ Q_{Ls} = \frac{\omega_0 L_\mathrm{s}}{R_L} \tag{37}$$

$$u = \frac{\omega}{\omega_0} \tag{38}$$

The $Q_{L\mathrm{p}}$, Q_{Ls} are linked together with the coupling k coefficient by (39):

$$k = \frac{1}{\sqrt{Q_{Lp} Q_{Ls}}} \tag{39}$$

The general parameter model is based on the normalization from [17], which assumes a lossless circuit. However, as shown in Chapter 7.5, the influence of R_p is minimal and can be neglected, while R_s can be simply handled by lumping this term together with R_L to form the adjusted load resistance R_{sL}:

$$R_{sL} = R_L + R_s \tag{40}$$

In this work, R_{sL} is further used instead of R_L and the defining equations for $Q_{L\mathrm{p}}$, Q_{Ls} (37) are adjusted in a simple manner by replacing R_L with R_{sL}:

$$Q_{L\mathrm{p}} = \frac{R_{sL} L_\mathrm{p}}{\omega_0 M^2},\ Q_{Ls} = \frac{\omega_0 L_\mathrm{s}}{R_{sL}} \tag{41}$$

The adjusted formulas (41) for $Q_{L\mathrm{p}}$, Q_{Ls} are considered in the rest of the analysis. The relationship between $Q_{L\mathrm{p}}$, Q_{Ls} and k given by (39) remains unchanged.

In the next step, the normalized equations are solved for u. The resulting roots describe the frequencies, at which the input phase φ_{in} crosses 0 (zero-phase angle frequencies, ZPA) for PB, and the frequencies of the local extrema of Z and P_{out} for IAB and OAB, respectively. These frequencies are further denoted by the respective phenomenon they describe (e.g., PB frequencies) and as the bifurcation frequencies as a whole.

The equations of the bifurcation frequencies are then compared with the measurement and simulation results obtained with instruments described in Chapter 4. Specifically, the frequencies of the zero crossings of φ_{in} (PB), and local extrema of Z (IAB) and P_{out} (OAB) are examined which are obtained from the measured frequency responses in presented in Fig. 23 and from a Simulink model presented in Chapter 4.2, which uses the parameters in Table 4.

The conditions describing the bifurcation occurrence (e.g., whether PB occurs) are derived from the equations of the bifurcation frequencies. These conditions are general, given as $Q_{L\mathrm{p}} = f(Q_{Ls})$. Thanks to this, they may be applied to any evaluated trajectory, independently whether it is given by a single or multiple circuit parameter change (e.g., R_L change or L_p, L_s, M change due to misalignment). These conditions describe the boundaries in the course of bifurcation which divide it to regions with a specific behavior (see Chapter 6.6 Boundaries and Regions).

The bifurcation boundaries are given by equations for $Q_{L\mathrm{p}}$ in terms of Q_{Ls}, i.e., $Q_{L\mathrm{p}} = f(Q_{Ls})$. The procedure to obtain the values of the circuit parameters (i.e., L_p, L_s, M, f_0 and R_{sL}) for the boundaries is described in Chapter 6.6. As the examination is focused on bifurcation due to decreasing R_L, the bifurcation frequencies, the bifurcation boundaries, and the displayed quantities (e.g., φ_{in}) in the diagram sections are related to R_L, which is calculated from R_{sL} according to (40).

As it shall be shown later, all of these results can be summarized in a Q_L state diagram, which is a graphic representation of the general parameter model. It is a 3D diagram based on the $Q_{L\mathrm{p}}$, Q_{Ls} and u which both represent the graph coordinates and describe the system operating point. In this diagram, the bifurcation frequencies, boundaries, and the trajectory of the operating point (operating trajectory) are plotted.

However, such a 3D diagram is rather difficult to use as it is, but its sections along the operating trajectory are useful for evaluation of the course of bifurcation – see Fig. 24 (a). These sections are further called diagram sections. It is often useful to plot a quantity of interest (e.g., output voltage amplitude V_{out}) in the diagram section in addition to the bifurcation frequencies and boundaries to examine how it changes along the course of bifurcation. In this work, the quantities displayed in the diagram sections as colormaps are calculated from the equivalent circuit model, i.e., they are not normalized and consider both R_p and R_s.

A 2D version of the Q_L state diagram, is also a practical visual aid. Both the diagram coordinates and system operating point are given only by $Q_{L\mathrm{p}}$ and Q_{Ls} and u is not considered (see Fig. 24 (b)). This does not impact the

evaluation of the bifurcation occurrence, as that is given solely in terms of Q_{Lp} and Q_{Ls}. The 2D diagram displays only the bifurcation boundaries and the trajectory, which then can be illustrated further by a diagram section as in Fig. 24 (a). The 2D diagram is useful for evaluating of a single operating point, operating trajectory in which one or multiple parameters change or operating area (e.g., an IPT system with a variable load, which should operate with a variable air gap). A quantity may be plotted in the background, as in the case of the diagram sections.

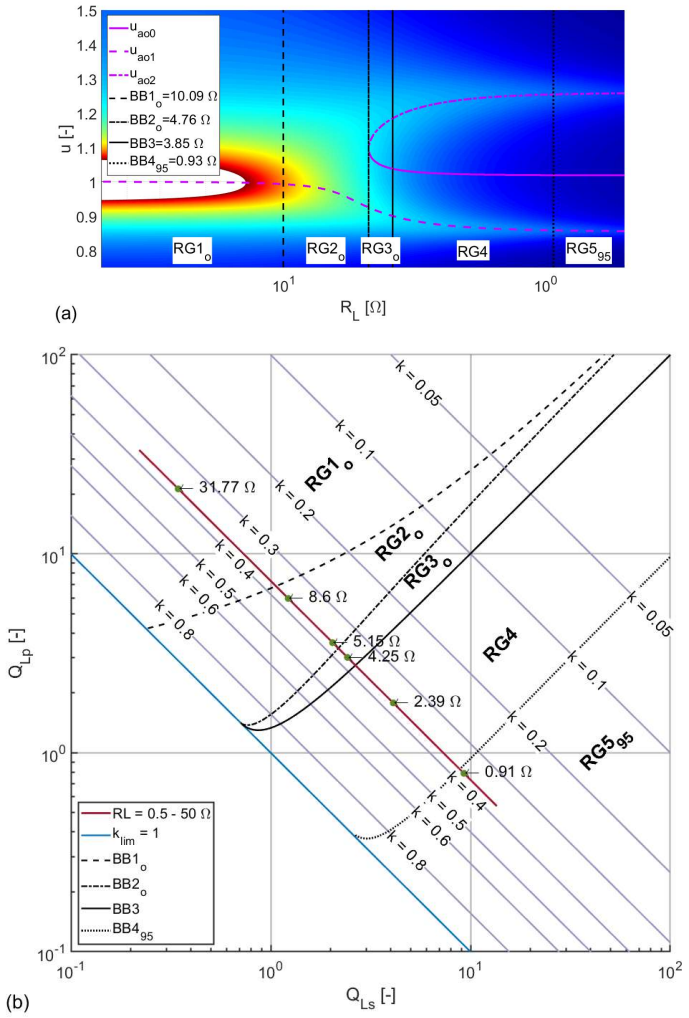

Fig. 24: (a) Example of a diagram section along a trajectory of decreasing R_L with marked OAB frequencies (purple), OAB and PB boundaries (black), regions ($RG1_o$, etc.) and a colormap of the output voltage amplitude V_{ou} in the background. (b) Example of a 2D Q_L state diagram with the same trajectory as in (a) (dark red), operating points of the frequency responses in Fig. 23, bifurcation boundaries (black) and limit value of coupling coefficient k (blue).

6.2 Phase Bifurcation

The zero-phase angle (ZPA) frequencies are defined as frequencies at which the input phase φ_{in} (the angle between the input current $\hat{I}_{in}$ and input voltage $\hat{V}_{in}$) is equal to 0. Phase bifurcation (PB) is a process in which a single ZPA frequency splits into three frequencies. For example, in Fig. 23 (a) the input phase φ_{in} crosses zero only at f_0 for the case corresponding to R_{LA} = 31.77 Ω. As the load is decreased, PB eventually occurs and the single zero crossing splits into three (e.g., see the frequency response for to R_{LE} = 2.39 Ω in Fig. 23 (a)).

The mathematical description of PB starts with the condition (42) describing the ZPA frequencies:

$$\varphi_{in} = 0 \tag{42}$$

As outlined by Wang et al. in [17], this condition is met, when the imaginary part of the input impedance $\hat{Z}$ (called the impedance seen by the source in [17]) is equal to 0:

$$Im\{\hat{Z}\} = 0 \tag{43}$$

Equation (43) is the governing equation for PB. The aim of its mathematical description is to obtain the formulas describing the ZPA frequencies and from them derive the condition for the PB occurrence.

6.2.1 Normalization Procedure

Wang et al. in [17] introduced the normalization process, which is the foundation of the general parameter model. The outcome of this process applied to (43) is a normalized equation, expressed in the terms of the primary and secondary loaded quality factors Q_{Lp}, Q_{Ls} (37) and normalized frequency u (38). Roots of this equation describe the ZPA frequencies including f_0. Based on them, it is possible to derive the general condition for PB.

The normalization procedure takes following steps. The operating angular frequency ω is normalized by resonant angular frequency ω_0 according to (38) resulting in u. The input impedance $\hat{Z}$ is normalized in terms of Z_{r0} obtained according to (15) as:

$$\hat{Z}_n = \frac{\hat{Z}}{Z_{r0}} = \frac{Re\{\hat{Z}\}}{Z_{r0}} + \frac{Im\{\hat{Z}\}}{Z_{r0}} = Re\{\hat{Z}_n\} + Im\{\hat{Z}_n\} \tag{44}$$

(Normalization in [17] uses the real part of the reflected impedance at resonance $Re\{\hat{Z}_{r0}\}$. Because it is the same as Z_{r0} for the SS compensation, Z_{r0} is used in order to simplify the description.)

By substituting $\hat{Z}$ given by (18) with neglected R_p and R_s, the equations for $Re\{\hat{Z}_n\}$ and $Im\{\hat{Z}_n\}$ are obtained as:

$$Re\{\hat{Z}_n\} = \frac{R_r}{Z_{r0}} \tag{45}$$

$$Im\{\hat{Z}_n\} = \frac{\omega L_p}{Z_{r0}} - \frac{1}{\omega C_p Z_{r0}} + \frac{X_r}{Z_{r0}} \tag{46}$$

When R_p and R_s are neglected, $Re\{\hat{Z}_n\}$ is equal to normalized R_r given by (13). On the other hand, $Im\{\hat{Z}_n\}$ depends on normalized primary reactance X_p (17) besides X_r (14). The equations (45) and (46) are further simplified when expressed in terms of u and the loaded quality factors Q_{Lp} and Q_{Ls} calculated according to (41). Individual terms comprising (45) and (46) then can be substituted with the terms in Table 6.

Table 6: Substitutions for normalization of input impedance $\hat{Z}$.

$\frac{R_r}{Z_{r0}}$	$\frac{u^4}{(u^2-1)^2 Q_{Ls}^2 + u^2}$
$\frac{\omega L_p}{Z_{r0}}$	$\frac{Q_{Lp}}{u}$
$\frac{1}{\omega C_p Z_{r0}}$	uQ_{Lp}
$\frac{X_r}{Z_{r0}}$	$-\frac{u^3(u^2-1)Q_{Ls}}{(u^2-1)^2 Q_{Ls}^2 + u^2}$

The real part of normalized impedance $\hat{Z}_n$ is then expressed as:

$$Re\{\hat{Z}_n\} = \frac{u^4}{(u^2-1)^2 Q_{Ls}^2 + u^2} \tag{47}$$

And its imaginary part as:

$$Im\{\hat{Z}_n\} = \frac{(u^2-1)\left((Q_{Lp}Q_{Ls}^2 - Q_{Ls})u^4 + (Q_{Lp} - 2Q_{Lp}Q_{Ls}^2)u^2 + Q_{Lp}Q_{Ls}^2\right)}{u(u^2-1)^2 Q_{Ls}^2 + u^3} \tag{48}$$

The normalized imaginary part $Im\{\hat{Z}_n\}$ is further used for the governing equation of PB – it is substituted into condition (43), which is then represented as:

$$\frac{(u^2-1)\left((Q_{Lp}Q_{Ls}^2 - Q_{Ls})u^4 + (Q_{Lp} - 2Q_{Lp}Q_{Ls}^2)u^2 + Q_{Lp}Q_{Ls}^2\right)}{u(u^2-1)^2 Q_{Ls}^2 + u^3} = 0 \tag{49}$$

6.2.2 Governing Equation of PB and its Solution

Equation (49) has six roots for u, but the three negative roots are neglected as u cannot be negative. The remaining three roots describe the PB frequencies (i.e., ZPA frequencies), from which the root $u_{\varphi 0} = 1$ describes the resonance frequency (index 0 was selected to match the established label for the resonance frequency f_0). As the other two roots $u_{\varphi 1}$ (50), $u_{\varphi 2}$ (51) transition from the complex to the real domain, PB occurs:

$$u_{\varphi 1} = \sqrt{\frac{2Q_{Lp}Q_{Ls}^2 - \sqrt{Q_{Lp}\left(4Q_{Ls}^3 - 4Q_{Lp}Q_{Ls}^2 + Q_{Lp}\right)} - Q_{Lp}}{2Q_{Ls}\left(Q_{Lp}Q_{Ls} - 1\right)}} \tag{50}$$

$$u_{\varphi 2} = \sqrt{\frac{2Q_{Lp}Q_{Ls}^2 + \sqrt{Q_{Lp}\left(4Q_{Ls}^3 - 4Q_{Lp}Q_{Ls}^2 + Q_{Lp}\right)} - Q_{Lp}}{2Q_{Ls}\left(Q_{Lp}Q_{Ls} - 1\right)}} \tag{51}$$

Fig. 25 presents a diagram section that compares the measured and simulated course of PB, in which the background is a colormap showing the simulated input phase φ_{in}. Because the secondary side influence grows with decreasing load resistance R_L, the horizontal R_L axis is reversed so that one can conveniently observe the course of bifurcation as one scans the diagram from left to right. The roots $u_{\varphi 1}$, $u_{\varphi 2}$ do not emerge with value of 1 (i.e., at $u_{\varphi 0}$) but above 1. The root $u_{\varphi 1}$ is lower than $u_{\varphi 0}$ except over a very narrow interval after it emerges. The root $u_{\varphi 2}$ is always higher than $u_{\varphi 0}$.

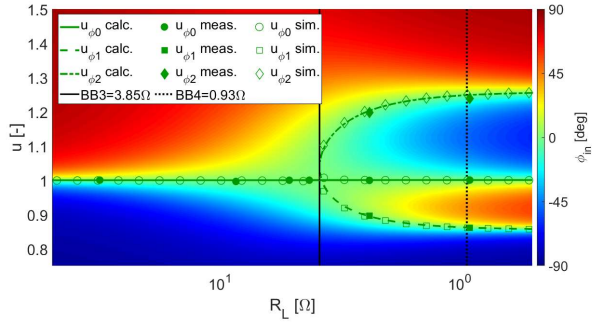

Fig. 25: Course of PB in a diagram section along a trajectory of decreasing R_L. Calculated PB frequencies $u_{\varphi 0}$, $u_{\varphi 1}$, and $u_{\varphi 2}$ (calc. in legend) are compared with the results of measurement (meas. in legend) and the simulation (sim. in legend) The background shows a colormap of the input phase φ_{in} and the boundaries BB3 and $\mathrm{BB4}_{95}$ are marked.

Analyzing equations (50) and (51) for the ZPA frequencies $u_{\varphi 1}$ and $u_{\varphi 2}$ shows that these frequencies are asymptotic and that the asymptotes depend solely on the coupling coefficient k. The asymptotic behavior is well visible for the examined case of the equivalent load resistance R_L decreasing towards zero – see Fig. 26.

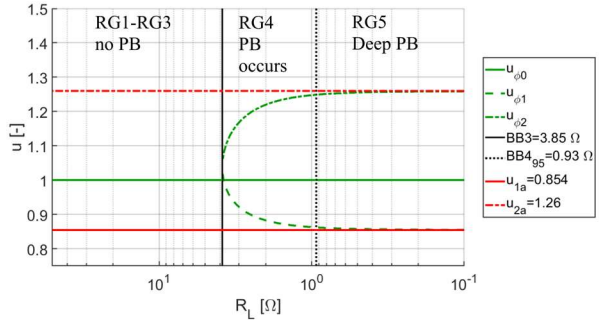

Fig. 26: The asymptotes u_{1a} and u_{2a} of phase bifurcation frequencies $u_{\varphi 1}$ and $u_{\varphi 2}$, respectively. $\mathrm{BB4}_{95}$ marks the boundary at which $u_{\varphi 1}$ and $u_{\varphi 2}$ makes 95 % of the transition to their respective asymptotes (i.e., $u_{\varphi 1}$ and $u_{\varphi 2}$ match their asymptotes u_{1a} and u_{2a}, respectively, with 5 % tolerance.

As it can be seen, the ZPA frequencies $u_{\varphi 1}$ and $u_{\varphi 2}$ begin close to the resonance frequency u_0. As R_L decreases further, $u_{\varphi 1}$ and $u_{\varphi 2}$ recede until they stabilize at the asymptotes. The deep bifurcation, i.e., very low

R_L, is required for the roots of the bifurcation equation approach the asymptotes closely. The boundary defining the deep bifurcation region is described in the next chapter. The easiest way to achieve this is to short-circuit the output of the IPT system.

The asymptote formulas can be obtained as follows. In the first step, the loaded quality factors Q_{Lp} and Q_{Ls} given by (41) are substituted in the roots $u_{\varphi 1}$ and $u_{\varphi 2}$ of the bifurcation equation, which are given by (50) and (51), respectively. Then their asymptotic values are calculated in the limit as R_L goes to zero. In the next step the coupling coefficient k (39) is substituted. The final results are the equations for the asymptotes u_{1a} and u_{2a}:

$$u_{1a} = \frac{1}{\sqrt{1+k}} \tag{52}$$

$$u_{2a} = \frac{1}{\sqrt{1-k}} \tag{53}$$

This result is interesting, because the asymptotes of the frequencies describing the OAB can be approximated by a similar set of formulas [21], [182]. The IAB frequencies also have similar asymptotes. The asymptotes of OAB and IAB are further discussed in Chapter 6.5.

6.2.3 PB Based Boundaries - BB3 and BB4

The black solid line in Fig. 25 marks the boundary BB3, at which PB occurs. The OAB or IAB boundaries are at the lower values of Z_{r0} (which correspond to higher values of R_L) describing the course of bifurcation, thus they have lower number (i.e. BB1 and BB2) as explained in the Chapter 6.6 Boundaries and Regions). The generalized boundary formula (54) is also derived in [17] from (49):

$$Q_{Lp,BB3} = \frac{4Q_{Ls}^3}{4Q_{Ls}^2 - 1} \tag{54}$$

However, the boundary calculated from (54) must be limited by an additional condition (55) as it would cut of some operating points, at which PB does not occur [183]:

$$Q_{Ls} > \frac{1}{\sqrt{2}} \tag{55}$$

The evaluation of PB occurrence for an operating point given by Q_{Lp}, Q_{Ls} is then twofold: In the first step, its Q_{Ls} is tested by condition (55), if it is not met, PB does not occur. If the operating point's Q_{Ls} meets the condition (55), the operating point's Q_{Lp} is compared with $Q_{Lp,BB3}$ calculated from (54). If it is higher than $Q_{Lp,BB}$, then PB occurs.

The boundary BB3 plotted in the Q_L state diagrams is calculated from the boundary formula (54), and the condition (55) limits the input values of Q_{Ls} for (54).

It is useful to introduce another boundary BB4, which describes a threshold after which the PB frequencies $u_{\varphi 1}$ and $u_{\varphi 2}$ are approximately stabilized at their respective asymptotes u_{1a} and u_{2a}. Similarly, as the boundary BB3 defined by (54), the equation of the boundary BB4 is expressed as $Q_{Lp} = f(Q_{Ls})$. The definition of BB4 is based on based on the course of bifurcation in the diagram section along the trajectory of decreasing R_L, as displayed in Fig. 26, which was used to obtain the asymptote equations (52) and (53). The boundary BB4 is a point at which the frequencies $u_{\varphi 1}$ and $u_{\varphi 2}$ make a certain percentage of their transition between their value at boundary BB3 (the point of emergence of $u_{\varphi 1}$ and $u_{\varphi 2}$) and their respective asymptotes u_{1a} and u_{2a}.

The R_L value at the boundary BB3 is calculated from (63). At this point, $u_{\varphi 1}$ has the same value as $u_{\varphi 2}$ ($u_{\varphi 1} = u_{\varphi 2} = u_{\varphi 12}$). From Fig. 26 it may seem that this u value is equal to $u_0 = 1$; however, that is not true. Value of $u_{\varphi 12}$ at the point of emergence is always above u_0, and it increases with the increasing coupling coefficient k – see Fig. 27.

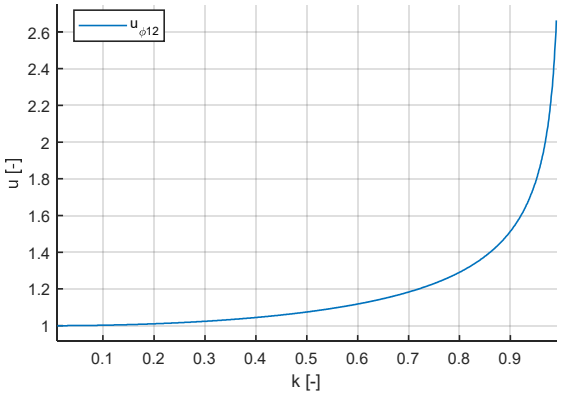

Fig. 27: Dependency of $u_{\varphi 12}$ (value of $u_{\varphi 1}$ and $u_{\varphi 2}$ at BB3) on the coupling coefficient k.

The dependency of $u_{\varphi 12}$ on k can be obtained as follows. In the first step, it is necessary to express the boundary BB3 solely in terms of k. Thus, equation (39) describing the relationship between k and Q_{Lp}, Q_{Ls} is substituted for Q_{Ls} in (54) and the resulting equation is solved for Q_{Lp}. This yields the desired equation for the boundary BB3:

$$Q_{Lp,BB3} = \sqrt{2\left(\frac{1}{k^4} - \frac{\sqrt{k^4(1-k^2)}}{k^6}\right)} \tag{56}$$

In the second step, equation (39) is also substituted for Q_{Ls} to the defining equations of $u_{\varphi 1}$ and $u_{\varphi 2}$ (50) and (51), respectively. In the third step, the adjusted definition of BB3 given by (65) is substituted in the adjusted equations of $u_{\varphi 1}$ and $u_{\varphi 2}$ obtained in the second step. After simplification, both equations give the same value, which corresponds with $u_{\varphi 12}$ at BB3:

$$u_{\varphi 12} = \frac{1}{\sqrt[4]{1-k^2}} \tag{57}$$

The boundary BB4 definition then can be selected from two possible equations, each based on one of the frequencies $u_{\varphi 1}$ and $u_{\varphi 2}$:

$$u'_{\mathrm{uBB4}} = u_{\varphi 12} - PX\left(u_{\varphi 12} - u_{1a}\right) \tag{58}$$

$$u''_{\mathrm{uBB4}} = u_{\varphi 12} + PX\left(u_{2a} - u_{\varphi 12}\right) \tag{59}$$

where PX is the required percentage of transition between $u_{\varphi 12}$ and u_{2a}. For general purposes, it is useful to set it to 95 %, which corresponds with error of 5 %. However, it is useful to set PX to higher value, e.g., 99 % (error of 1 %) when the asymptotes u_{1a} and u_{2a} are used for estimation of k, which is described in Chapter 8.3. The PX percentage used for defining BB4 is indicated as $\mathrm{BB4}_{95}$ for $PX = 95$ % or $\mathrm{BB4}_{99}$ for $PX = 99$ %.

The models of $\mathrm{BB4}_{95}$ and $\mathrm{BB4}_{99}$ were obtained numerically as follows. Both R_p and R_s were considered equal to zero and L_p, L_s and f_0 from Table 4 were used. The coupling coefficient k was varied in the range of 0.01 to 0.99 with 1000 samples evenly spaced. For each k, the frequencies u'_{uBB4} and u''_{uBB4} were calculated according to (58) and (59), and the value of R_L over the interval of 0.0001 to 100 Ω was searched to yield $R'_{L,BB4}$ where $u_{\varphi 1} = u'_{\mathrm{uBB}}$ and $R''_{L,BB4}$ where $u_{\varphi 2} = u''_{\mathrm{uBB4}}$. To approximate these intersections, an approach was used which is similar to the numerical method for obtaining the IAB frequencies described in Appendix A3. The circuit parameters in Table 4 were used. Frequencies $u_{\varphi 1}$ and $u_{\varphi 2}$ values were calculated according to (50) and (51). The $R'_{L,BB4}$ and $R''_{L,BB}$ values were obtained with the maximal allowed error of 10^{-9} Ω.

From the obtained values of $R'_{L,BB4}$ or $R''_{L,BB4}$, k and the remaining circuit parameters the loaded quality factors Q_{Lp}, Q_{Ls} were calculated which describe the boundary BB4.

Obtained values of $Q_{Lp,\mathrm{BB4}}$ differ, whether they are obtained from $R'_{L,BB4}$ $(u_{\varphi 1})$ or $R''_{L,BB4}$ $(u_{\varphi 2})$ and this difference increases with k (see Fig. 28). Obtained values of $Q_{Lp,\mathrm{BB4}}$ differ, whether they are obtained from $u_{\varphi 1}$ or $u_{\varphi 2}$ and this difference increases with k (see Fig. 28). Above the plotted $Q_{Lp,\mathrm{BB4}}$ the frequencies $u_{\varphi 1}$ and $u_{\varphi 2}$ are not yet stabilized, while below $Q_{Lp,\mathrm{BB4}}$ they passed the required threshold (either u'_{uBB4} or u''_{uBB4}) for

stabilization. Thus, $Q_{Lp,\mathrm{BB4}}$ obtained from $u_{\varphi 2}$ was selected as the boundary BB4 (i.e., boundary BB4 is described by (59)), because bellow this curve, both $u_{\varphi 1}$ and $u_{\varphi 2}$ are stabilized, while bellow $Q_{Lp,\mathrm{BB4}}$ obtained from $u_{\varphi 1}$, only $u_{\varphi 1}$ is stabilized. The definition based on $Q_{Lp,\mathrm{BB4}}$ obtained from $u_{\varphi 2}$ is used both for $\mathrm{BB4}_{95}$ (general use) and $\mathrm{BB4}_{99}$ (estimation of k in Chapter 8.3).

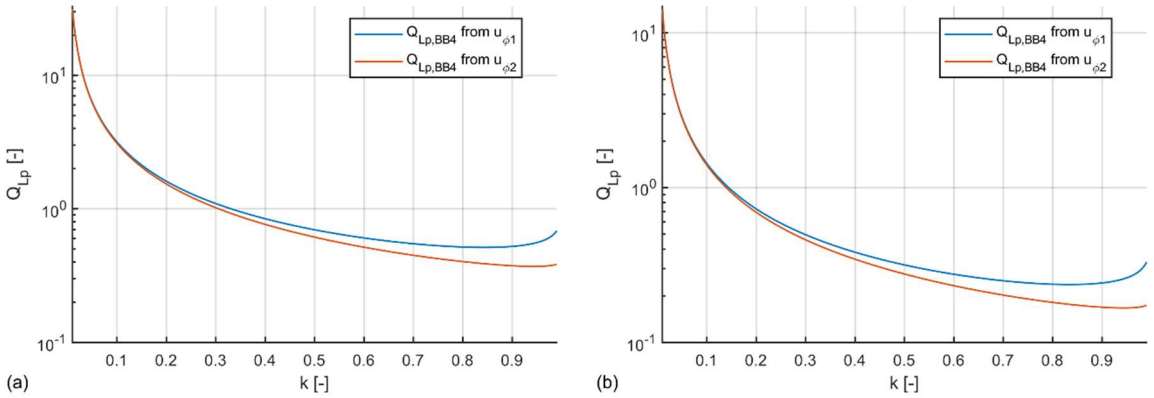

Fig. 28: BB4 boundary values obtained for threshold percentage PX (a) of 95 % ($\mathrm{BB4}_{95}$) and (b) of 99 % ($\mathrm{BB4}_{99}$). In both cases, the frequency $u_{\varphi 2}$ reaches PX at lower values of Q_{Lp} than $u_{\varphi 1}$.

The obtained Q_{Lp} and Q_{Ls} datapoints were fitted to obtain a model of the boundary BB4 with the use of MATLAB cftool. A Rat32 model (a fraction of polynomials with the leading coefficient of the denominator set to 1) was selected as a good compromise between the model complexity and the fit precision:

$$Q_{Lp,BB4} = \frac{p_3 Q_{Ls}^3 + p_2 Q_{Ls}^2 + p_1 Q_{Ls} + p_0}{Q_{Ls}^2 + q_1 Q_{Ls} + q_0} \tag{60}$$

The model coefficients are listed in Table 7.

Goodness of fits for k over the interval $\langle 0.01, 0.99\rangle$ of 1000 evenly spaced samples is summarized in the Table 8. When Q_{Lp} is higher than $Q_{Lp,BB4o}$ calculated from (60), the distance of both $u_{\varphi 1}$ and $u_{\varphi 2}$ to u_{1a} and u_{2a}, respectively is smaller than 5% of its possible maximum for $\mathrm{BB4}_{95}$ or smaller than 1 % for $\mathrm{BB4}_{99}$.

Table 7: Coefficients of the PB boundary BB4 models.

	p_3	p_2	p_1	p_0	q_1	q_0
$\mathrm{BB4}_{95}$	0.0975	0.01517	-0.1923	0.3419	0.9007	-4.866
$\mathrm{BB4}_{99}$	0.0199	0.008456	-0.2059	0.8474	2.18	-24.54

Table 8: Evaluation of the PB boundary BB4 models.

Boundary	$\mathrm{BB4}_{95}$	$\mathrm{BB4}_{99}$
Error sum of squares (SSE)	$9.3799 \cdot 10^{-6}$	$2.1471 \cdot 10^{-6}$
R-square	1	1
Adjusted R-square	1	1
Root mean squared error (RMSE)	$9.7044 \cdot 10^{-5}$	$4.643 \cdot 10^{-5}$

The obtained approximate formulas of $\mathrm{BB4}_{95}$ and $\mathrm{BB4}_{99}$ (i.e., mathematical models represented by (60)) must be limited to the Q_{Ls} intervals, at which these models were obtained – for different Q_{Ls} values they are not valid anymore. The boundary $\mathrm{BB4}_{95}$ is limited by condition (61) and boundary $\mathrm{BB4}_{99}$ by condition (62):

$$Q_{Ls} > 2.648 \tag{61}$$

$$Q_{Ls} > 5.877 \tag{62}$$

The boundary BB4 plotted in the Q_L state diagrams is calculated from the boundary formula (60) using the coefficients listed in Table 7 specific either to $BB4_{95}$ or $BB4_{99}$. The conditions (61) or (62) limits the input values of Q_{Ls} for (60).

6.3 Output Amplitude Bifurcation (Frequency Splitting)

The output amplitude bifurcation (OAB, frequency splitting) examines the local extrema of the output power P_{out} given by (27). Along the course of OAB (see Fig. 29), the P_{out} maximum u_{ao} moves below the resonance frequency u_0 ($u = 1$) and another P_{out} maximum u_{ao2} appears. The OAB frequencies are labeled to match the corresponding PB frequencies in which they are near. Specifically, as the course of bifurcation progresses (i.e., R_L decreases), the frequency u_{ao} nears $u_{\varphi 1}$ and u_{ao2} nears $u_{\varphi 2}$. The frequencies of the P_{out} maxima u_{ao1}, u_{ao2} are separated by a valley with a minimum described by u_{ao0}, which nears $u_{\varphi 0}$. The OAB frequencies is characterized by the following condition:

$$\frac{\partial P_{out}}{\partial \omega} = 0 \tag{63}$$

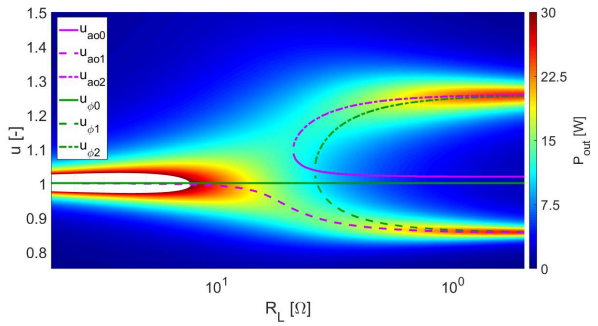

Fig. 29: Calculated OAB frequencies (purple) and PB frequencies (green) are shown for comparison in a diagram section along a trajectory of decreasing R_L. The background shows a colormap of the output power P_{out}.

The frequency splitting was examined in detail by Niu et al. in [21], where they discussed solutions for SSIPT system cases of increasing complexity: symmetrical systems ($L_p = L_s$, $C_p = C_s$, $R_p = R_s + R_L$), the special case of unsymmetrical systems ($\alpha R_p = R_s + R_L$, where $\alpha = \frac{L_s}{L_p}$ and $L_p \neq L_s$, $C_p \neq C_s$) and finally general unsymmetrical systems. In the first two cases, [21] provides the root equations describing the local extrema. However, due to the high complexity of the root formulas, they are not listed for the most interesting case of the general unsymmetrical system and [21] only explains the steps necessary for solving (63).

However, it is possible to apply a similar normalization process as in the case of PB. The local extrema of P_{out} are then described by $\frac{\partial P_{out,n}}{\partial u} = f(Q_{Lp}, Q_{Ls}, u)$ and the complexity of formulas is greatly reduced. Besides that, the frequency splitting phenomena becomes the part of the general parameter model, which allows deriving of general conditions, easy comparison with PB and evaluation via Q_L state diagram.

(Note that Niu et al. refers to IPT in [21] as "contactless power transfer" with acronym "CPT".)

6.3.1 Normalization Procedure

The normalization is inspired by the approach presented by Wang et al. in [17] and its goal is to normalize P_{out} as a function of Q_{Lp}, Q_{Ls} and u. Before the normalization itself starts, it is necessary to express P_{out} as a function of impedance. The deriving starts with the input impedance $\hat{Z}$ (64) and continues towards the P_{out} formula:

$$\hat{Z} = \frac{\omega^4 C_s^2 M^2 R_{sL}}{(\omega^2 C_s L_s - 1)^2 + \omega^2 C_s^2 R_{sL}^2} + j\left(\omega L_1 - \frac{1}{\omega C_p} - \frac{\omega^3 C_s M^2 (\omega^2 C_s L_s - 1)}{(\omega^2 C_s L_s - 1)^2 + \omega^2 C_s^2 R_{sL}^2}\right) \tag{64}$$

The input current $\hat{I}_{in}$ is calculated from the impedance $\hat{Z}$ as:

$$\hat{I}_{in} = \frac{V_{in}}{\hat{Z}} \tag{65}$$

According to the (7), the voltage induced in the secondary $\hat{V}_{is}$ is:

$$\hat{V}_{is} = j\omega M \hat{I}_{in} = \frac{j\omega M}{\hat{Z}} V_{in} \tag{66}$$

The output current $\hat{I}_{out}$ is calculated from $\hat{V}_{is}$ as:

$$\hat{I}_{out} = \frac{\hat{V}_{is}}{\hat{Z}_s} = \frac{j\omega M}{\hat{Z}\hat{Z}_s} V_{in} \tag{67}$$

The output voltage $\hat{V}_{out}$ from $\hat{I}_{out}$ as:

$$\hat{V}_{out} = R_L \hat{I}_{out} = \frac{j\omega M R_{sL}}{\hat{Z}\hat{Z}_s} V_{in} \tag{68}$$

The calculation of the output power P_{out} as the product of $\hat{I}_{out}$ and $\hat{V}_{out}$ given by (67) and (68), respectively, must consider the phase shift between $\hat{I}_{out}$ and $\hat{V}_{out}$ and the phase shift between $\hat{I}_{out}$ and the input current $\hat{I}_{in}$. The phase shift between $\hat{I}_{out}$ and $\hat{V}_{out}$ is equal to 0 as the IPT system is loaded by a pure resistance, thus the output power is only active. Due to the positive coupling between the primary and secondary coils, the phase shift between $\hat{I}_{out}$ and $\hat{I}_{in}$ is 90° for f_0. Outside resonance the phase shift depends both on difference between f and f_0 and on the R_L value. It gains values between 0° and 180° – see Chapter 3.2.2. The phase shift is considered in by the absolute value in output power calculation:

$$P_{out} = \frac{1}{2}\left|\hat{V}_{out}\hat{I}^*_{out}\right| = \frac{1}{2}\frac{\omega^2 M^2 R_{sL}}{\left|\hat{Z}\hat{Z}_s\right|^2} V_{in}^2 \tag{69}$$

Formula (69) is the input to the normalization procedure. The goal is to derive a normalized expression for P_{out} as a function of Q_{Lp}, Q_{Ls} and u that preserves the local extrema positions of P_{out}. The normalization is implemented in the following step-by-step process:

1. To normalize the P_{out} formula (69), it is necessary to normalize each impedance term (i.e., ωM, R_{sL}, $\hat{Z}$, $\hat{Z}_S$) separately and remove the dependance on V_{in}. Thus, (69) is multiplied by the normalization coefficient C_n:

$$C_n = \frac{Z_{r0}^4}{Z_{r0}^3}\frac{1}{V_{in}^2} \tag{70}$$

2. The input impedance $\hat{Z}$ (64) is normalized according to [17] – see Chapter 6.2.1. The resulting equation for the normalized impedance $\hat{Z}_n$, which is expressed in terms of the parameters Q_{Lp}, Q_{Ls} and u, is the sum of (47) and (48):

$$\hat{Z}_n = \frac{u^4}{(u^2-1)^2 Q_{Ls}^2 + u^2} + j\frac{(u^2-1)\left(\left(Q_{Lp}Q_{Ls}^2 - Q_{Ls}\right)u^4 + \left(Q_{Lp} - 2Q_{Lp}Q_{Ls}^2\right)u^2 + Q_{Lp}Q_{Ls}^2\right)}{u(u^2-1)^2 Q_{Ls}^2 + u^3} \tag{71}$$

3. The remaining terms in (69) (i.e., ωM, R_{sL}, $\hat{Z}_S$) are also divided by Z_{r0} provided by C_n. This allows the substitution of the normalized function from Table 9, where c_{LR} stands for the inductance ratio coefficient:

$$c_{LR} = \sqrt{\frac{L_s}{L_p}} \tag{72}$$

This coefficient is an equivalent to the turns ratio of the IPT transformer (e.g. [184]) and c_{LR}^2 corresponds with α in [21].

Table 9: Substitutions for normalization of input impedance P_{out}.

Mutual reactance	$\frac{\omega M}{Z_{r0}} = c_{LR}\frac{\sqrt{Q_{Lp}}}{\sqrt{Q_{Ls}}}u$
Real part of secondary impedance, adjusted load resistance	$\frac{Re\{Z_S\}}{Z_{r0}} = \frac{R_{sL}}{Z_{r0}} = c_{LR}^2\frac{Q_{Lp}}{Q_{Ls}}$
Imaginary part of secondary impedance	$\frac{Im\{Z_S\}}{Z_{r0}} = c_{LR}^2\frac{(u^2-1)Q_{Lp}}{u}$

4. The resulting equation is simplified. The c_{LR} terms in the numerator and denominator cancel out, leaving the equation for the normalized output power $P_{out,n}$ only in terms of Q_{Lp}, Q_{Ls} and u:

$$P_{out,n} = \frac{u^6}{(u^2-1)^2 {Q_{Lp}}^2 u^2 + \left((u^2-1)^2 Q_{Lp} Q_{Ls} - u^4\right)^2} \tag{73}$$

6.3.2 Governing Equation of OAB and Its Solution

Similarly, as in the case of obtaining the formulas of the OAB frequencies from the regular P_{out}, the normalized output power $P_{out,n}$ described by (73) is partially differentiated with respect to the normalized frequency u and set equal to 0:

$$\frac{\partial P_{out,n}}{\partial u} = 0 \tag{74}$$

The resulting equation may be simplified as:

$$-u^8 + 2Q_{Lp}Q_{Ls}u^4(u^4-1) - Q_{Lp}^2(u^2-1)\left(2u^2 + Q_{Ls}^2(u^2-1)^2(u^2+3)\right) = 0 \tag{75}$$

Equation (75) is a normalized equivalent of splitting equation (14) in [21], and the procedure for finding its roots corresponds with solving the aforementioned equation as described in [21]. Equation (75) may be expressed as a polynomial:

$$u^8 + a_3u^6 + a_2u^4 + a_1u^2 + a_0 = 0 \tag{76}$$

where:

$$a_3 = 0$$
$$a_2 = \frac{2Q_{Lp}(Q_{Lp}+Q_{Ls}-3Q_{Lp}Q_{Ls}^2)}{(Q_{Lp}Q_{Ls}-1)^2}$$
$$a_1 = \frac{2Q_{Lp}^2(4Q_{Ls}^2-1)}{(Q_{Lp}Q_{Ls}-1)^2}$$
$$a_0 = -\frac{3Q_{Lp}^2Q_{Ls}^2}{(Q_{Lp}Q_{Ls}-1)^2}$$

As [21] states, this is a bi-quartic equation, which may be solved using the approach described in [185]. If $a_0 < 0$, then (76) has at least one negative and one positive real root, based on the Vieta's formulas. This bi-quartic equation may be factorized into two bi-quadratic equations, the first corresponding with the through equation and the second with the ridge equation (see [21]). The substitutions $p = a_2$, $q = a_1$, $r = a_0$, and $z = u^2$ are applied to (76) which translates this 8th order polynomial in u into a quartic equation in z:

$$z^4 + pz^2 + qz + r = 0 \tag{77}$$

The quartic equation (77) is factorable as it may be written as a difference of two squared terms:

$$P^2 - Q^2 = (P+Q)(P-Q) = 0 \tag{78}$$

The resolvent cubic equation (79) must be solved to make (77) factorable.

$$(y-p)(y^2-4r) = q^2 \tag{79}$$

The resolvent cubic equation has three roots, from which y_1 is its only real root:

$$y_1 = \frac{p}{3} + \frac{2^{\frac{4}{3}}(p^2+12r)^3 + (2B)^{\frac{2}{3}}}{6B^{\frac{1}{3}}} \tag{80}$$

where

$$B = 2p^3 - 72pr + 27q^2 + \sqrt{(2p^3-72pr+27q^2)^2 - 4(p^2+12r)^3}$$

Considering y_1, the terms P, Q in (78) may be calculated as:

$$P = z^2 + \frac{1}{2}y_1 \tag{81}$$

$$Q = Dz - \frac{q}{2D},\ D = \sqrt{y_1 - p} \tag{82}$$

Equation (78) may be divided into the through equation (83) with roots r_{TE1}, r_{TE} and the ridge equation (84) with the roots r_{RE1}, r_{RE2}:

$$P + Q = 0 \tag{83}$$

$$P - Q = 0 \tag{84}$$

The root r_{TE2} is always complex and the remaining roots r_{TE1}, r_{RE1} and r_{RE2} describe the local extrema of the output power. All three roots can be calculated from the following formula:

$$r = \frac{N_1}{N_2 \sqrt[4]{B_1^2}} \left(\sqrt{S(1,i_r)\sqrt{B_2 - N_3 B_3 Q_{Lp} + B_4} + S(2,i_r)\sqrt{S(3,i_r)\frac{N_4 Q_{Lp}^2 \sqrt{3B_1^2}(4Q_{Ls}^2 - 1)}{\sqrt{B_2 - N_3 B_3 Q_{Lp} + B_4}} - N_5 B_3 Q_{Lp} - B_2 - B_4}} \right) \tag{85}$$

where symbols N_x stand for large numbers (when possible, the numbers were factored to their primes for easier handling):

$$N_1 = 2419716372272021$$
$$N_2 = 2^{65}$$
$$N_3 = 2^{54}$$
$$N_4 = 2^{80} \cdot 3$$
$$N_5 = 2^{55}$$
$$N_6 = 5674179970822795$$
$$N_7 = 14298037572263032$$

and symbols B_x stand for substitutions:

$$B_1 = Q_{Lp} Q_{Ls} - 1$$
$$B_2 = N_6 B_5 Q_{Lp}$$
$$B_3 = -3Q_{Lp} Q_{Ls}^2 + Q_{Lp} + Q_{Ls}$$
$$B_4 = \frac{N_7 B_6 Q_{Lp}}{B_5}$$
$$B_5 = \sqrt[3]{112Q_{Ls}^3 - B_7 + B_8 - 3B_9 Q_{Lp} + 3\sqrt{3B_1^2 T_C}}$$
$$B_6 = Q_{Lp}^2 + 2Q_{Lp} Q_{Ls} - 8Q_{Ls}^2 + 12Q_{Lp} Q_{Ls}^3 - 6Q_{Lp}^2 Q_{Ls}^2$$
$$B_7 = Q_{Lp}^3 (9Q_{Ls}^2 - 4)$$
$$B_8 = 6Q_{Lp}^2 Q_{Ls} (24Q_{Ls}^2 - 7)$$
$$B_9 = 48Q_{Ls}^4 + 32Q_{Ls}^2 - 9$$
$$B_{10} = Q_{Lp}^4 (128Q_{Ls}^4 - 61Q_{Ls}^2 + 8)$$
$$B_{11} = Q_{Lp}^3 Q_{Ls} (128Q_{Ls}^4 - 48Q_{Ls}^2 + 5)$$
$$B_{12} = Q_{Lp} Q_{Ls}^3 (32Q_{Ls}^4 + 32Q_{Ls}^2 - 7)$$
$$B_{13} = 512Q_{Ls}^6 + 32Q_{Ls}^4 - 64Q_{Ls}^2 + 9$$

The term T_C is distinguished because it gives the condition for the OAB boundary which is discussed later:

$$T_C = B_{10} - 6B_{11} - 32B_{12} + 3B_{13} Q_{Lp}^2 + 768Q_{Ls}^6 \tag{86}$$

The roots are distinguished by the signs $S(x, i_r)$ listed in the sign matrix S:

$$S = \begin{pmatrix} -1 & 1 & 1 \\ 1 & -1 & 1 \\ 1 & -1 & -1 \end{pmatrix}, \tag{87}$$

where the row index x corresponds with the sign position in the formula (85), while column index i_r is the root index: for $i_r = 1$ the equation describes r_{TE1}, for $i_r = 2$ it describes r_{RE1} and for $i_r = 3$ it describes r_{RE2}, e.g., the signs for root r_{RE1} are: $S(1, i_r) = 1$, $S(2, i_r) = -1$ and $S(3, i_r) = -1$.

The assignment of the roots to the frequencies describing the position of the P_{out} local extrema is not as straightforward as in the case of PB. The behavior of the roots r_{TE1} and r_{RE2} depends on the sign of q coefficient. The q sign depends solely on the value of Q_{Ls}, as it can be derived from (76) ($q = a_1$):

$$Q_{Ls} = \frac{1}{2} \rightarrow q = 0 \tag{88}$$

If $Q_{Ls} > \frac{1}{2}$, then $q > 0$ and vice versa. Along the course of bifurcation (i.e., as Z_{r0} increases) the condition $q = 0$ always occurs before the occurrence of OAB, thus there is only a single extremum (maximum) of $P_{out,n}$ described by the normalized frequency u_{ao1}. For $q < 0$, the root r_{TE} is complex and the root r_{RE2} describes u_{ao1}. As Z_{r0} increases, q becomes equal to 0. The root r_{RE} switches from real to complex and u_{ao1} is now described by the root r_{TE}, which becomes real. The transition between the roots r_{RE1} and r_{TE} at $q = 0$ is smooth and there is no abrupt change in the value of u_{ao1}, as the transition occurs. Note that the roots obtained from the Niu's splitting equation (14) in [21] based on regular P_{out}, display the same behavior at the same values of R_L.

As mentioned, the condition $q = 0$ is met before the onset of OAB, thus there is still a single maximum described by u_{ao}. Next, as Z_{r0} increases and OAB occurs, the root r_{TE1} continues to describe the main maximum u_{ao}, while the root r_{RE2} now describes the additional maximum u_{ao2}. Root r_{RE1} of the ridge equation always describes the minimum u_{ao} as OAB occurs. Root assignment to the OAB frequencies and to their equivalents in [21] is summarized in Table 10.

Table 10: Roots of (76) and the local extrema frequencies of OAB.

Local extremum	Niu 2013 [21] frequency	OAB frequency	Root
Main maximum	ω_o	u_{ao1}	$q < 0$: r_{RE2} $q > 0$: r_{TE1}
Additional maximum (in OAB)	ω_e	u_{ao2}	$q > 0$: r_{RE2}
Minimum between the maxima (in OAB)	ω_t	u_{ao0}	r_{RE1}

Fig. 30 presents the measured and simulated OAB frequencies which show a good agreement with the obtained roots of (76) as the description of OAB (frequency splitting) frequencies. To further validate the obtained roots of (76), Fig. 31 compares them with the roots of Niu's splitting equation (14) in [21], for the unsymmetrical system described in Table I in [21]. Here the coupling coefficient is varied between 0 and 0.6 (L_p, L_p are constant, thus only M changes). The curves in Fig. 31 show a very good match, and the two sets of frequencies are almost indistinguishable, even though the (76) based on the normalized $P_{out,n}$, which neglects R_p (in this case R_p = 1.23 Ω).

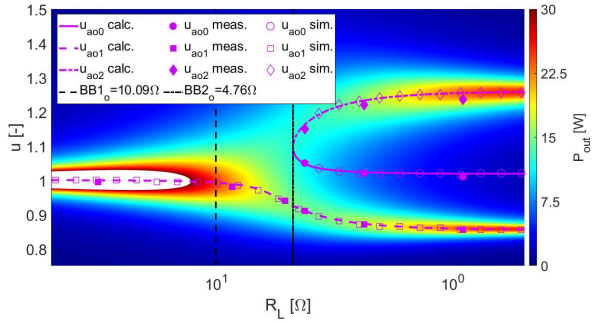

Fig. 30: Course of OAB in a diagram section along a trajectory of decreasing R_L. Calculated OAB frequencies u_{ao0}, u_{ao} and u_{ao2} (calc. in legend) are compared with the results of measurement (meas. in legend) and the simulation (sim. in legend) in a diagram section along a trajectory of decreasing R_L. The background shows a colormap of the output power P_{out} and the boundaries $BB1_o$ and $BB2_o$ are marked.

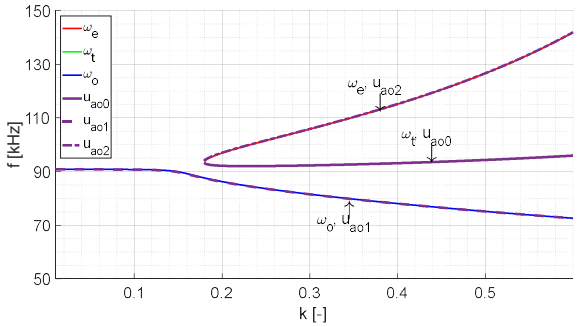

Fig. 31: Comparison of OAB (frequency splitting) frequencies calculated according to Niu et al. [21] (ω_e, ω_t and ω_o) and from the normalized output power $P_{out,n}$ (u_{ao0}, u_{ao1} and u_{ao2}) in a diagram section along increasing k. Published by author in [20].

6.3.3 OAB Based Boundaries $BB1_o$ and $BB2_o$

There are two possible phenomena, which may be used to establish the OAB boundary in the course of bifurcation. The first is when u_{ao1} leaves u_0, the second is the u_{ao} , u_{ao} emergence. To establish consistency with PB it was decided to define the second phenomenon as the basis for the OAB boundary, which is labeled $BB2_o$. However, the first phenomenon is also important; thus, it is the basis for boundary $BB1_o$. The boundaries are numbered in correspondence with the increasing values of reflected impedance Z_{r0} with which they are connected. The index "o" distinguishes the $BB1_o$ and $BB2_o$ boundaries as corresponding to OAB. As it will be discussed in the next chapter, $BB1_i$ and $BB1_i$ (note the index "i" in this notation) distinguish the similar boundaries for IAB.

The definition of boundary $BB1_o$ is based on the course of bifurcation in the diagram section along the trajectory of decreasing R_L, as displayed e.g., in Fig. 30. If the examination starts on the left side of the diagram section, the P_{out} maximum described by u_{ao} is at u_0. As R_L decreases (and Z_{r0} grows) at a certain value of R_L the transition of u_{ao1} to its second asymptote begins. The definition of $BB1_o$ is then the point at which u_{ao1} reaches 5% of the transition between the u_0 and u_{ao1L} (89), where u_{ao1L} is the u_{ao1} value for R_L going to 0 (90):

$$u_{BB1o} = u_0 - 0.05(u_0 - u_{\varphi 1L}) \tag{89}$$

$$u_{ao1L} = \lim_{R_{sL}\to 0} u_{ao1}(R_L) \tag{90}$$

Both R_p and R_s are considered equal to zero and L_p, L_s and f_0 from Table 4 were used. When $R_L \to 0$, then $Q_{Ls} \to +\infty$ and $q \to +\infty$. Thus, u_{ao1L} is based on the root r_{TE1}. Due to the complexity of root r_{TE} , attempts to derive the asymptote u_{ao1L} analytically in MATLAB R2020a or Wolfram Mathematica 12 failed. However, a numerical analysis presented in Chapter 6.5 shows, that for R_p and R_s equal to zero the asymptote u_{ao1L} matches u_{1a} given by (52), which is obtained from the PB frequency $u_{\varphi 1}$. This finding corresponds with the literature [21], [182]. Thus, u_{ao1L} was calculated according to (52).

The $BB1_o$ model was obtained numerically as follows. The coupling coefficient k was varied in the range of 0.01 to 0.99 with 1000 samples evenly spaced. For each k, the frequency u_{BB1o} was calculated according to (89) and (90), and the value of R_L over the interval of 0.0001 to 100 Ω was searched to yield $R_{L,BB1o}$ where $u_{ao1} = u_{BB1o}$.

To approximate this intersection, an approach was used which is similar to the numerical method for obtaining the IAB frequencies described in Appendix A3. The circuit parameters in Table 4 were used. Root u_{ao} values were calculated from roots r_{TE1} and r_{RE2} according to (85). The $R_{L,BB1o}$ values were obtained with the maximal allowed error of 10^{-7} Ω.

From the obtained values of $R_{L,BB1o}$, k and the remaining circuit parameters the loaded quality factors Q_{Lp}, Q_{Ls} were calculated. These generalized parameters describe the $BB1_o$ in the Q_L state diagram. The datapoints given by combinations of Q_{Lp} and Q_{Ls} were fitted with the use of MATLAB cftool. A Rat43 model (a fraction of polynomials with the leading coefficient of the denominator set to 1) was selected as a good compromise between the model complexity and the fit precision – the model equation is (91) and its coefficients are listed in Table 11:

$$Q_{Lp,BBxo} = \frac{p_4 Q_{Ls}^4 + p_3 Q_{Ls}^3 + p_2 Q_{Ls}^2 + p_1 Q_{Ls} + p_0}{Q_{Ls}^3 + q_2 Q_{Ls}^2 + q_1 Q_{Ls} + q_0} \tag{91}$$

Goodness of fit for k over the interval $\langle 0.01,0.99\rangle$ of 1000 evenly spaced samples is summarized in the Table 12. When Q_{Lp} is higher than $Q_{Lp,BB1}$ calculated from (91), the distance of u_{ao1} to u_{a0} is smaller than 5% of its possible maximum.

Table 11: Coefficients of the OAB boundary models.

	p_4	p_3	p_2	p_1	p_0	q_2	q_1	q_0
$\mathrm{BB1_o}$	1.995	19.79	51.46	34.26	3.638	6.421	7.840	1.322
$\mathrm{BB2_o}$	1.984	54.16	38.27	-31.09	6.239	29.57	43.77	-29.62

Table 12: Evaluation of the OAB boundary models.

Boundary	$\mathrm{BB1_o}$	$\mathrm{BB2_o}$
Error sum of squares (SSE)	$6.9937\cdot10^{-4}$	$1.2909\cdot10^{-3}$
R-square	1	1
Adjusted R-square	1	1
Root mean squared error (RMSE)	$8.3838\cdot10^{-3}$	$1.1390\cdot10^{-3}$

The boundary $\mathrm{BB2_o}$ is defined as the point in which the frequencies u_{ao} and u_{ao2} emerge and OAB occurs. On the contrary to $\mathrm{BB1_o}$, the condition for $\mathrm{BB2_o}$ can be derived from the root formula (85). Its constituent term T_C (86) was found as the simplest term corresponding with OAB – when the sign of T_C changes from positive to negative, OAB occurs. Thus, from $T_C = 0$ it is possible to calculate the condition for boundary $\mathrm{BB2_o}$ as a function $Q_{Lp} = f(Q_{Ls})$ to match the other boundary conditions. Equation $T_C = 0$ has four roots for Q_{Lp}, two are always complex. The third root describes such a combination of Q_{Lp} and Q_{Ls} such that their resulting coupling coefficient k is above 1, thus it cannot occur in a real device. Finally, the fourth root describes $\mathrm{BB2_o}$; however, its formula is rather complicated:

$$Q_{Lp} = \frac{1}{D_1}\left(15\,Q_{Ls} - D_2 - 144\,Q_{Ls}^3 + 384\,Q_{Ls}^5 + \sqrt{18\,D_3 - (512\,Q_{Ls}^4 - 244\,Q_{Ls}^2 + 32)\,D_4 - D_5\,D_6 - D_7 + \frac{D_8}{D_2}}\right) \tag{92}$$

where:

$$D_1 = 256\,Q_{Ls}^4 - 122\,Q_{Ls}^2 + 16$$

$$D_2 = \sqrt{D_5\,D_6 - D_1\,D_4 + 9\,D_3 + D_7}$$

$$D_3 = (128\,Q_{Ls}^5 - 48\,Q_{Ls}^3 + 5\,Q_{Ls})^2$$

$$D_4 = 512\,Q_{Ls}^6 + 32\,Q_{Ls}^4 - 64\,Q_{Ls}^2 + 9$$

$$D_5 = 384\,Q_{Ls}^4 - 183\,Q_{Ls}^2 + 24$$

$$D_6 = \left(5504\,Q_{Ls}^4 - 576\,Q_{Ls}^2 - 33792\,Q_{Ls}^6 + 148480\,Q_{Ls}^8 - 2^{16}7\,Q_{Ls}^{10} + 2^{17}7\,Q_{Ls}^{12} - 2^{20}\,Q_{Ls}^{14} + 2^{19}\,Q_{Ls}^{16} + 512 D_9 Q_{Ls}^3 \sqrt{(16\,Q_{Ls}^6 - 16\,Q_{Ls}^4 + 6\,Q_{Ls}^2 - 1)^3} + 27\right)^{\frac{1}{3}}$$

$$D_7 = \frac{D_5\,(2048\,Q_{Ls}^8 - 2048 Q_{Ls}^6 + 768\,Q_{Ls}^4 - 128\,Q_{Ls}^2 + 9)}{D_6}$$

$$D_8 = 16\,D_9 Q_{Ls}\,(16384\,Q_{Ls}^{10} + 34304\,Q_{Ls}^8 - 54696\,Q_{Ls}^6 + 25724\,Q_{Ls}^4 - 5246\,Q_{Ls}^2 + 405)$$

$$D_9 = (4\,Q_{Ls}^2 - 1)^2$$

The resulting condition was tested against the R_L values obtained in the similar fashion as the data for the $\mathrm{BB1_o}$ model (except in this case the change of roots u_{ao} and u_{ao2} from real to complex was evaluated) and the results showed an exact match.

The $\mathrm{BB2_o}$ equation (95) is rather complicated. For this reason, the $\mathrm{BB2_o}$ values were fitted to obtain a model similar to $\mathrm{BB1_o}$, which would be easier to use. The result is again a Rat43 model, its formula is (91) and coefficients are listed in Table 11. Goodness of fit for k over the interval $\langle 0.01,0.99\rangle$ with 1000 evenly spaced

samples is evaluated in the Table 12. When Q_{Lp} of the operating point is higher than $Q_{Lp,BB2o}$ calculated from (91), OAB does not occur.

The obtained approximate formulas of $BB1_o$ and $BB2_o$ (i.e., mathematical models represented by (91)) must be limited to the Q_{Ls} intervals, at which these models were obtained – for different Q_{Ls} values they are not valid anymore. The boundary $BB1_o$ is limited by condition (93) and boundary $BB2_o$ by condition (94):

$$Q_{Ls} > 0.2419 \tag{93}$$

$$Q_{Ls} > 0.7370 \tag{94}$$

The evaluation of the OAB occurrence for a specific operating point and the construction of the OAB boundaries in the Q_L state diagrams is similar as for the PB boundary BB4 described at the end of Chapter 6.2.3.

6.4 Input Amplitude Bifurcation

To explain the mechanism of output amplitude bifurcation (OAB) in Chapter 7, it is necessary to understand behavior of the input impedance $\hat{Z}$, because $\hat{Z}$ is an input to the OAB's governing equation (69). Phase bifurcation (PB) describes the behavior of the input phase φ_{in}. However, it is also necessary to evaluate the behavior of the impedance amplitude Z splitting. Comparison in Fig. 32 shows that the frequencies of the local extrema of Z are different than the frequencies of P_{out} extrema, which are described by OAB. Thus, a separate description was developed for the bifurcation impacts on the input impedance amplitude. For distinction from OAB, it was labeled the input amplitude bifurcation (IAB).

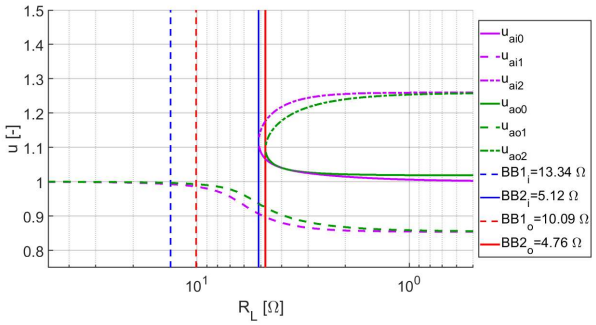

Fig. 32: Comparison of IAB (purple) and OAB (green) frequencies and boundaries in a diagram section along a trajectory of decreasing R_L.

6.4.1 Governing Equation of IAB and its Solution

The mathematical description is based on the normalized impedance $\hat{Z}_n$ (71) which was obtained in [17]. Similarly, as in the case of OAB, to goal is to obtain the functions, that describe the frequencies of the local amplitude extrema. Based on these formulas, the condition for IAB occurrence is derived . Similarly, as in the case of the OAB governing equation, the Z_n amplitude (95) is differentiated with respect to the normalized frequency u (96):

$$Z_n = \sqrt{\frac{u^8 - 2Q_{Lp}Q_{Ls}u^4(u^2-1)^2 + Q_{Lp}^2(u^2-1)^2(u^2 + Q_{Ls}^2(u^2-1)^2)}{u^2(u^2 + Q_{Ls}^2(u^2-1)^2)}} \tag{95}$$

$$\frac{\partial Z_n}{\partial u} = 0 \tag{96}$$

After substituting (95) into (96), calculating the derivative and simplifying, the equation (97) was obtained, which is the governing equation for IAB.

$$\begin{aligned} 2u^{10} + Q_{Ls}^2u^8(3 - 4u^2 + u^4) + Q_{Lp}^2(u^4-1)(u^2 + Q_{Ls}^2(u^2-1)^2)^2 \\ - 2Q_{Lp}Q_{Ls}u^4(u^2-1)(2u^4 + Q_{Ls}^2(u^2-1)^3) = 0 \end{aligned} \tag{97}$$

Similar to the OAB governing equation (76), the governing equation (97) can be expressed as a polynomial in u:

$$u^{12} + a_5u^{10} + a_4u^8 + a_3u^6 + a_2u^4 + a_1u^2 + a_0 = 0 \tag{98}$$

where:

$$a_5 = -4 + \frac{2}{Q_{Ls}^2}$$

$$a_4 = \frac{3Q_{Ls}^2+4Q_{Lp}(Q_{Ls}-3Q_{Ls}^3)+Q_{Lp}^2(1-4Q_{Ls}^2+5Q_{Ls}^4)}{Q_{Ls}^2(Q_{Lp}Q_{Ls}-1)^2}$$

$$a_3 = \frac{8Q_{Lp}Q_{Ls}}{(Q_{Lp}Q_{Ls}-1)^2}$$

$$a_2 = -\frac{Q_{Lp}^2-4Q_{Lp}^2Q_{Ls}^2+2Q_{Lp}Q_{Ls}^3+5Q_{Lp}^2Q_{Ls}^4}{Q_{Ls}^2(Q_{Lp}Q_{Ls}-1)^2}$$

$$a_1 = \frac{2Q_{Lp}^2(2Q_{Ls}^2-1)}{(Q_{Lp}Q_{Ls}-1)^2}$$

$$a_0 = -\frac{Q_{Lp}^2Q_{Ls}^2}{(Q_{Lp}Q_{Ls}-1)^2}$$

If the polynomial form of the OAB equation (76) was labelled as a bi-quartic equation, the IAB equation (98) could be labelled as a tri-quartic equation. This increase of complexity is inconvenient, as it is not possible to use the approach outlined by [21], [185] to solve the equation. In fact, (98) defied any effort of analytical solution including use of MATLAB R2020a and Wolfram Mathematica 12 solvers. Thus, the equation was solved numerically with the approach described in Appendix A3.

.The numerically obtained roots describe the IAB frequencies u_{ai0}, u_{ai1} and u_{ai2}. The naming of the IAB frequencies corresponds with the OAB frequencies – see Fig. 32. As it is visible from Fig. 32, the IAB and OAB frequencies are very similar, but not identical. IAB occurs at higher values of R_L, thus earlier in the course of bifurcation. The cause of this behavior is later explained in Chapter 7.4. Obtained values of the IAB frequencies are compared with measurement and simulation results in Fig. 33.

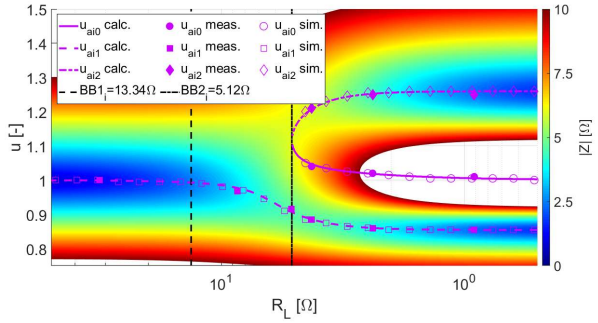

Fig. 33: Course of IAB in a diagram section along a trajectory of decreasing R_L. Calculated IAB frequencies u_{ai0}, u_{ao1} and u_{ai2} (calc. in legend) are compared with the results of measurement (meas. in legend) and the simulation (sim. in legend) in a diagram section along a trajectory of decreasing R_L. The background shows a colormap of the input impedance amplitude Z and the boundaries $BB1_i$ and $BB2_i$ are marked.

It is possible to fit the obtained numerical values to gain approximate formulas of the roots. However, the fit is specific for the operating trajectory in the Q_L state diagram, which is given by all of the circuit parameters, not only the changing ones [183]. If any of these parameters are changed, the trajectory would shift, and the root models would become invalid. Thus, it is better to use the numerical approach in Appendix A3, as it is applicable for any trajectory.

6.4.2 IAB Based Boundaries $BB1_i$ and $BB2_i$

Because the curves of the IAB and OAB frequencies are very similar (see Fig. 32), the IAB boundaries are based on the same phenomena as the OAB boundaries. The boundary $BB1_i$ describes the point at which u_{a1i} leaves u_0 and $BB2_i$ describes the u_{ai2}, u_{ai0} emergence. Similarly, as in the case of OAB, the boundary $BB2_i$ delimits the occurrence of IAB. As it is shown in Fig. 32, the IAB boundaries have higher R_L and thus smaller Z_{R0} values than corresponding OAB boundaries.

The defining equations (99) and (100) for $BB1_i$ as the point at which u_{ai1} leaves u_0 correspond to the similar set of equations for $BB1_o$ (89), (90):

$$u_{BB1i} = u_0 - 0.05(u_0 - u_{ai1L}) \tag{99}$$

$$u_{ai1L} = \lim_{R_L \to 0} u_{ai1}(R_L) \tag{100}$$

Due to lack of an equation for root u_{ai1}, it was necessary to obtain u_{ai1L} numerically. The numerical analysis presented in Chapter 6.5 shows, that for R_p and R_s equal to zero the asymptote u_{ai1L} matches u_{1a} given by (52), which is obtained from the PB frequency $u_{\varphi 1}$.

The boundary function was obtained by the identical numerical approach as for $BB1_o$, except the values of the u_{ai1} root were approximated by the approach according to Appendix A3 instead of an analytical calculation. A resulting Rat32 model was selected as a good compromise between the model complexity and the fit precision – model formula is (101) and coefficients are listed in Table 13:

$$Q_{Lp,BBxi} = \frac{p_3 Q_{Ls}^3 + p_2 Q_{Ls}^2 + p_1 Q_{Ls} + p_0}{q_2 Q_{Ls}^2 + q_1 Q_{Ls} + q_0} \tag{101}$$

The goodness of fit for k over the interval $\langle 0.01,0.99\rangle$ with 1000 evenly spaced samples is summarized in Table 14.

Table 13: Coefficients of the IAB boundary models.

	p_3	p_2	p_1	p_0	q_1	q_0
$BB1_i$	2.411	18.2	23.68	3.667	3.055	0.8676
$BB2_i$	2.382	17.8	-10.82	5.279	9.272	-1.573

Table 14: Evaluation of the IAB boundary models.

Boundary	$BB1_i$	$BB2_i$
Error sum of squares (SSE)	$4.2117 \cdot 10^{-3}$	$5.3933 \cdot 10^{-2}$
R-square	1	1
Adjusted R-square	1	1
Root mean squared error (RMSE)	$2.0891 \cdot 10^{-3}$	$7.3697 \cdot 10^{-2}$

On the contrary to $BB2_o$, the boundary condition for $BB2_i$ cannot be obtained analytically. Thus, a similar approach was used to calculate the boundary as in the case of $BB1_i$ or $BB1_o$. However, in the case of $BB2_i$, the search is performed to obtain such a R_L value, at which the roots u_{ai0} and u_{ai2} (and thus the local extrema they represent) appear. This value is marked as $R_{L,BB2i}$. The numerical method similar to the one described in Appendix A3, was used to find such a R_L interval, that at its lower limit the u_{ai0}, u_{ai} existed, but at its upper limit did not. (u_{ai0}, u_{ai} always become real in the same interval.) As the roots u_{ai} , u_{ai} have the same u at their emergence, their match (difference below 10^{-5}) was a condition in the $R_{L,BB}$ approximation process, besides maximal allowed error for R_L of 10^{-7} Ω and maximal allowed error of the u_{ai0}, u_{ai2} approximation of 10^{-8}. Obtained data for k over the interval $\langle 0.01,0.99\rangle$ with 1000 evenly spaced samples were again fitted with cftool and the resulting Rat32 model is described by (101) with the coefficients listed in Table 13. The boundary model is evaluated for the specified k interval in Table 14.

Similarly, as in the case of the OAB boundaries, the obtained mathematical models of the IAB boundaries $BB1_i$ and $BB2_i$ must be limited to the Q_{Ls} intervals, at which these models were obtained – for different Q_{Ls} values they are not valid anymore. Boundary $BB1_i$ is then limited by condition (102) and boundary $BB2_i$ by (103):

$$Q_{Ls} > 0.1746 \tag{102}$$

$$Q_{Ls} > 0.7317 \tag{103}$$

The evaluation of the OAB occurrence for a specific operating point and the construction of the OAB boundaries in the Q_L state diagrams is similar as for the PB boundary BB4 described at the end of Chapter 6.2.3.

6.5 Asymptotes of OAB and IAB

The asymptotes of OAB and IAB are necessary for defining of the boundary BB1 and they also provide an interesting information about the system. However, due to the complexity of OAB roots and lack of root equations for IAB, the asymptotes had to be obtained numerically.

The asymptote values were obtained as follows. Both R_p and R_s were set to 0, R_L was set to a very small value ($R_L = 0.1$ mΩ) and L_p, L_s and f_0 from Table 4 were used. Thanks to this, the operating point is always in

very deep bifurcation region and all nine bifurcation frequencies are stabilized at their respective asymptotes. The coupling coefficient k was varied in the range of 0.01 to 0.99 with 1000 samples evenly spaced. For each k, the PB frequency asymptotes u_{1a} and u_{2a} were calculated according to (52) and (53), respectively, for selected R_L and u_{0a} is equal to 1 as $u_{\varphi 0}$ is always equal to 1. OAB frequencies were calculated according to (85) and IAB frequencies were obtained numerically with the approach described in Appendix A3.

Fig. 34 depicts all three asymptotes for PB, IAB, and OAB in dependency on the coupling coefficient k. Fig. 34 show that the OAB asymptotes u_{ao1L} for u_{ao1} and u_{ao2L} for u_{ao2} together with the IAB asymptotes u_{ai1L} for u_{ai1} and u_{ai2L} for u_{ai2} match the PB asymptotes u_{1a} and u_{2a}, respectively, with an error of u smaller than 10^{-9}. On the other hand, while IAB asymptote u_{ai0L} for u_{ai0} matches the PB asymptote $u_{0a} = 1$, the OAB asymptote u_{ao0L} for u_{ao0} is different and it varies with k. The same values of u_{ao0L} were obtained, even when R_L was set to 1 μΩ, thus the difference between u_{ao0L} and u_{0a} is not caused by slower stabilization of OAB frequency u_{ao0} at its asymptote u_{ao0L}.

Therefore, the asymptotes u_{ao1L} and u_{ai1L} can be calculated as u_{1a} given by (52) and the asymptotes u_{ao2} and u_{ai2L} can be calculated as u_{2a} given by (53). Hence the labeling of asymptotes u_{1a} and u_{2a} – they are common for all three bifurcation phenomena. The calculation OAB asymptotes u_{ao1L} and u_{ao2L} according to (52) and (53) match their approximate equations already presented in literature [21], [182].

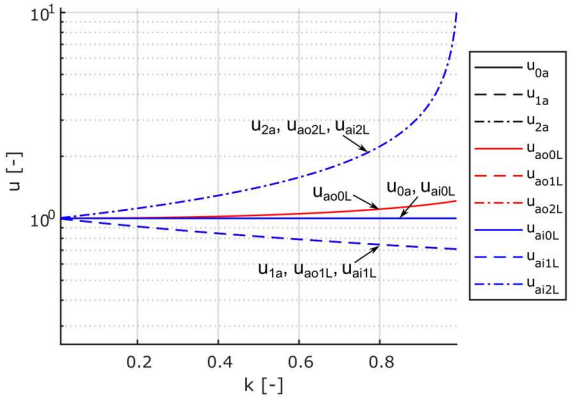

Fig. 34: Asymptotes of bifurcation phenomena frequencies.

The asymptote equations (52) and (53) can be used for the calculation of the coupling coefficient k. A novel coupling coefficient estimation method based on the asymptotes of the bifurcation frequencies is presented in Chapter 8.3.

6.6 Boundaries and Regions in the Course of Bifurcation

In this chapter, the findings from the previous chapters are combined into a description of the course of bifurcation (see Chapter 5.4). Obtained frequencies describing the bifurcation phenomena are summarized in Table 15 and Fig. 35. The input amplitude bifurcation (IAB) is characterized by the frequencies u_{ai0}, u_{ai1} and u_{ai2} (Fig. 35 (a)), which correspond to the local extrema of Z: u_{ai1} and u_{ai2} describe the local minima of Z while u_{ai} describes the local maximum of Z. Similarly, output amplitude bifurcation (OAB) is characterized by u_{ao0}, u_{ao1} and u_{ao2} (Fig. 35 (b)), from which u_{ao1} and u_{ao2} describe the local maxima of P_{out} and u_{ao} the local minimum of P_{out}.

To examine which quantities are described by IAB and which by OAB, a numerical approach was applied which is similar to that used for obtaining the IAB frequencies (Appendix A3). The tested quantities were the input current amplitude I_{in}, input active power P_{in} and the output current and voltage amplitudes I_{out} and V_{out}. Local extrema were numerically approximated as the roots of the first derivative of the quantity with respect to ω (quantity formulas are not normalized), which was set equal to 0. The results show that IAB describes besides Z also I_{in}, while OAB describes besides P_{out} also I_{out}, V_{out} and P_{in}. The maximum of transformer efficiency does not follow either IAB nor OAB and is described in Chapter 8.1.1).

The phase bifurcation (PB) is characterized by the frequencies $u_{\varphi 0}$, $u_{\varphi 1}$ and $u_{\varphi 2}$. These correspond with the ZPA frequencies: $u_{\varphi 0}$ matches the resonance frequency f_0 after its normalization and $u_{\varphi 1}$, $u_{\varphi 2}$ describe the other ZPA frequencies emerging as PB occurs. The main difference between PB and the amplitude bifurcation (both IAB and OAB) is that while the frequency $u_{\varphi 0}$ remains constant at u_0, u_{ax1} moves out of u_0 and is gradually replaced with u_{ax} emerging as IAB or OAB occurs.

Table 15: Overview of bifurcation frequencies.

	Symbol	Description
IAB	u_{ai0}	Additional Z maximum
	u_{ai1}	Main Z minimum
	u_{ai2}	Additional Z maximum
OAB	u_{ao0}	Additional P_{out} minimum
	u_{ao1}	Main P_{out} maximum
	u_{ao2}	Additional P_{out} minimum
PB	$u_{\varphi 0}$	Original ZPA frequency, $f_{\varphi 0} = f_0$
	$u_{\varphi 1}$	Additional ZPA frequency, bellow f_0
	$u_{\varphi 2}$	Additional ZPA frequency, above f_0

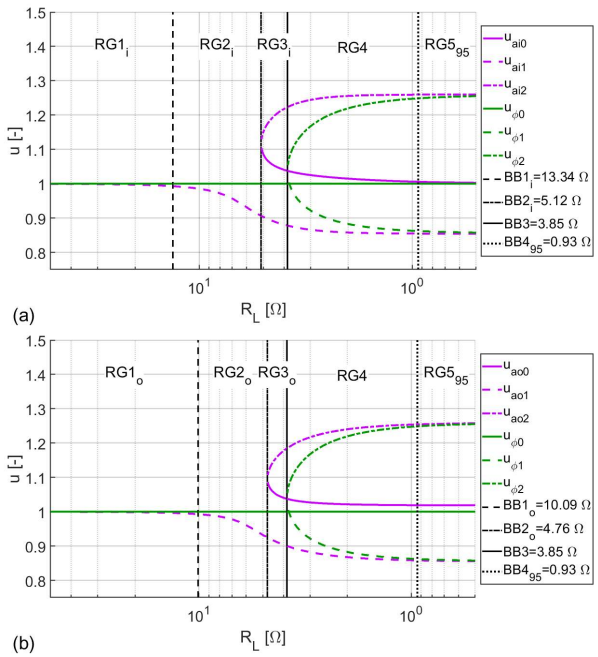

Fig. 35: Comparison of (a) the IAB, (b) the OAB with the PB. The regions and boundaries are marked.

As it is visible from Fig. 35 or R_L values of boundaries summarized in the Table 16, OAB occurs first (at smaller Z_r, respective higher R_L), followed by OAB and finally PB.

Table 16: Boundaries in the course of bifurcation.

Symbol	Event connected with the boundary	R_L value
BB1	Single local extremum leaves the resonance frequency.	13.34 Ω (IOB), 10.09 Ω (OAB)
BB2	Amplitude bifurcation emerges.	5.12 Ω (IOB), 4.76 Ω (OAB)
BB3	Phase bifurcation emerges.	3.85 Ω
BB4	PB frequencies $u_{\varphi 1}$ and $u_{\varphi 2}$ stabilize at asymptotes u_{a1} and u_{a2}	0.93 Ω ($PX = 95$ %)* 0.25 Ω ($PX = 99$ %)**

* Note that $R_{sL} = R_s + R_L$ is 1.25 Ω for $BB4_{95}$.
** Note that $R_{sL} = R_s + R_L$ is 0.57 Ω for $BB4_{99}$.

Using the boundaries BB1, BB2, BB3 and BB4 obtained from the amplitude and PB, regions with a specific bifurcation behavior can be delimited – see Fig. 35 and Table 17. The boundaries $BB1_i$, $BB2_i$ and $BB1_o$, $BB2_o$ describe the same type of phenomena only from a different perspective (input or output), i.e., at BB1 frequency u_{ai1} or u_{ao1} leaves u_0 and at BB2 the input or output amplitude bifurcation occurs. Thus, they are not viewed as four different boundaries, but as two boundaries, specific to whether the input or output quantities are examined. This was indicated by using the same label and differentiation by index "o" or "i". Thus, if the bifurcation phenomena are examined for the input quantities Z and I_{in}, IAB with boundaries $BB1_i$ and $BB2_i$ are used and the course of bifurcation corresponds to Fig. 35 (a). Similarly, OAB with boundaries $BB1_o$ and $BB2_o$ describe the output quantities I_{out}, V_{out}, P_{out} and P_{in} and the course of bifurcation corresponds to Fig. 35 (b).

The boundaries $BB4_{95}$ and $BB4_{99}$ also describe the same boundary BB4, which indicates that all bifurcation frequencies (PB, OAB and IAB) were stabilized at their respective asymptotes. They only differ by the threshold value for this stabilization – $PX = 95$ % for $BB4_{95}$ and $PX = 99$ % for $BB4_{99}$. While $BB4_{95}$ is for the general use (its threshold value matches both $BB1_i$ and $BB1_o$), the $BB4_{99}$ is recommended for the proposed coupling coefficient k estimation method presented in Chapter 8.3.

Table 17: Regions of the course of bifurcation.

Symbol	Region name	Frequency response in Fig. 23
RG1	Bifurcation-free region	R_{LA}
RG2	Region of growing secondary side influence	R_{LB}
RG3	Region of only amplitude bifurcation (IOB / OAB)	R_{LD}
RG4	Region of both bifurcations (IOB / OAB and PB)	R_{LE}
RG5	Region of deep bifurcation	R_{LF}

To delimit the regions in the course of bifurcation, the examination starts on the left side of the diagram section in the Fig. 35 (a) for IAB ((b) for OAB) and scans the graph in the direction of decreasing R_L (from left to right). The regions are labelled "RGx". The numbering of both the regions and boundaries corresponds to increasing reflected impedance Z_{R0}, which characterizes growing secondary side influence. For further distinction, the regions can be associated with IAB or OAB by using index "i" or "o", similar to the notation used for designating the bifurcation boundaries. Likewise, the region RG5 is distinguished for $BB4_{95}$ or $BB4_{99}$ by adding the corresponding threshold level in its index (i.e., $RG5_{95}$ or $RG5_{99}$).

The course of bifurcation starts with the bifurcation-free region $RG1_i$ ($RG1_o$). Both u_{ai1} which describes the Z minimum (u_{ao1} which describes the P_{out} maximum) and the ZPA frequency $u_{\varphi 0}$ match the resonance frequency u_0. After reaching the boundary $BB1_i$ ($BB1_o$), u_{ai1} (u_{ao}) leaves u_0 but $u_{\varphi 0}$ remains at u_0 and the operating point transitions into $RG2_i$ ($RG2_o$), which is a region of growing secondary side influence. Here u_{ai1} (u_{ao}) distances itself further away from u_0.

With the further progress from left to right along the diagram section, the operating point eventually reaches the boundary $BB2_i$ ($BB2_o$), the amplitude bifurcation occurs, and an additional Z local minimum u_{ai2} (P_{out} local maximum u_{ao}) appears accompanied by Z_n local maximum u_{ai0} (P_{out} local minimum u_{ao0}) between u_{ai1} and u_{ai2} (u_{ao1} and u_{ao2}).

When the operating point moves further in the region $RG3_i$ ($RG3_o$), which is a region where only amplitude bifurcation occurs, the u_{ai0} and u_{ai2} (u_{ao0} and u_{ao}) move further away from each other and local extrema connected with them become more pronounced.

When the operating point reaches BB3, PB occurs and the additional ZPA frequencies $u_{\varphi 1}$, $u_{\varphi 2}$ accompany $u_{\varphi 0}$. With a further decrease of R_L the operating point moves through the region RG4 (region of both bifurcations) and the amplitude bifurcation frequencies u_{ai}, u_{ai} and u_{ai2} (u_{ao}, u_{ao1} and u_{ao2}) near their respective PB counterparts $u_{\varphi 0}$, $u_{\varphi 1}$ and $u_{\varphi 2}$.

At the boundary BB4, all bifurcation frequencies approach their respective asymptotes with required threshold. The asymptotes are u_{1a} for $u_{\varphi 1}$, u_{ai} and u_{ao1} and u_{1a} for $u_{\varphi 2}$, u_{ai2} and u_{ao2}. This pattern is broken for u_{0a} which is the asymptote only for $u_{\varphi 0}$ and u_{ai0}, while u_{ao} has its own asymptote u_{ao2L}. After passing the boundary BB4, the bifurcation frequencies enter RG5 (deep bifurcation region), in which all the frequencies are considered to be stabilized at their respective asymptotes.

The frequency responses in Fig. 23 were specifically selected to display the curves of φ_{in}, P_{out} and Z typical for each region. The frequency responses are linked with their corresponding regions in Table 17.

The formulas of the bifurcation boundaries are expressed as a function $Q_{Lp} = f(Q_{Ls})$ (i.e., BB3 as (54)). Thanks to the use of the generalized parameters, their calculation is independent of the operating trajectory. Boundary value for a specific parameter (e.g. R_L, M or k) may be calculated either by substituting the loaded quality factor Q_{Lp}, Q_{Ls} formulas (41) for circuit parameters or (39) for the coupling coefficient k, or from the intersection of the trajectory with the boundary in the Q_L state diagram.

The analytical approach (substitution of Q_{Lp}, Q_{Ls}) is useful for calculating BB3 as its basic formula (54) is fairly simple. If R_s and R_L are incorporated in R_{sL} in the calculation of Q_{Lp} and Q_{Ls}, the BB3 value for R_L is calculated as (104):

$$R_{L,\mathrm{BB3}} = \sqrt{\frac{2L_\mathrm{s}^3 M^2 \omega_0^2}{\sqrt{L_\mathrm{p} L_\mathrm{s}^3 \left(L_p L_s - M^2\right)} + L_p L_\mathrm{s}^2}} - R_s \tag{104}$$

However, for the other boundaries, the analytical approach leads to significantly complicated formulas or is impossible at all. The analytical approach is also not applicable for trajectory given by change of multiple equivalent circuit parameters.

For these reasons, it is preferable to calculate the boundary value of circuit parameters from the intersection between the boundary and the operating trajectory. An operating trajectory is a sequence of circuit parameters of which some are variable, and some are constant, resulting in a sequence of $Q_{Lp,OT}$, $Q_{Ls,OT}$:

$$\left[Q_{Lp,OT}, Q_{Ls,OT}\right] = f\left(\left[L_p, L_s, M, f_0, R_{sL}\right]\right) \tag{105}$$

where f corresponds with the equations of Q_{Lp}, Q_{Ls} (41). The values of $Q_{Lp,B}$ for the boundary are calculated from the $Q_{Ls,OT}$ based on the boundary equations (e.g. (91) for $\mathrm{BB2_o}$), after the $Q_{Ls,OT}$ is limited by the additional condition specific for each boundary (e.g. (94) for $\mathrm{BB2_o}$). Resulting boundary is then described by a sequence $Q_{Lp,B}$, $Q_{Ls,OT}$.

In the next step, the intersection of the trajectory sequence $Q_{Lp,OT}, Q_{Ls,OT}$ and the boundary sequence $Q_{Lp,B}, Q_{Ls,OT}$ is found. However, the goal is not to find the specific values of Q_{Lp}, Q_{Ls} at the intersection, but the intersection position in the sequence forming the operating trajectory. This position is the same, whether the operating trajectory is expressed as a sequence of $Q_{Lp,OT}, Q_{Ls,OT}$ or a sequence of the circuit parameters L_p, L_s, M, f_0, R_{sL} and the combination of circuit parameters at this position gives the circuit parameter values for the boundary.

This approach is independent of the number of non-constant circuit parameters describing the trajectory. (It would be possible to calculate Q_{Lp}, Q_{Ls} of the intersection, and then the circuit parameters from (41), but only for up to two changing parameters.) The respective R_L values obtained by this method for the boundaries are listed in Table 16.

The influence of R_p and R_s (which is considered in R_{sL}) on the boundary values for R_L is evaluated in Chapter 7.5.

6.7 Q_L State Diagram

The mathematical description in the previous chapters can be advantageously summarized in the Q_L state diagram, which relates the system operating point with the bifurcation frequencies and boundaries. The initial concepts of the Q_L state diagram were examined and called as Q_L-maps in [183].

6.7.1 3D Q_L State Diagram

As it was outlined in the introduction of this chapter, there are two versions of the Q_L state diagram – 3D and 2D. The full 3D Q_L state diagram fully represents the general parameter model. Coordinates in this 3D space are given by the loaded quality factors Q_{Lp}, Q_{Ls} and the normalized frequency u. It contains the bifurcation frequencies, which are in fact 3D surfaces given by $u = \left(Q_{Lp}, Q_{Ls}\right)$ and bifurcation boundaries, which are also 3D surfaces, but they given $Q_{Lp} = f(Q_{Ls})$ across all u (i.e., the boundaries do not change along u, on the contrary to the bifurcation frequencies).

The IPT system is represented by its operating point, operating trajectory (sequence of operating points) or operating area (array of operating points). The construction of operating trajectories and operating areas for 3D and 2D Q_L State Diagram is described in Chapter 7.2 and Chapter 7.3, respectively. The 3D diagram contains all information about the general parameter model; however, it is rather inconvenient to use. It should be viewed more

as a defining space for further 2D visual tools (diagram sections, 2D Q_L state diagram) and a model for deeper understanding the bifurcation phenomena, than an evaluation tool itself.

The 3D Q_L state diagram is a space of all possible normalized frequency responses. A trajectory (e.g., along a decreasing R_L) is plotted in the Q_L state diagram (for its visualization in 2D Q_L state diagram see the dark red curve in Fig. 36 (a)). A diagram section is created along this trajectory and a quantity is placed in the background (e.g., input impedance phase φ_{in} – see Fig. 25). This diagram section is a sequence of frequency responses. For example, each frequency response curve in Fig. 23 (a) is a cross-section of Fig. 25 for a specific value of R_L (e.g., R_{LA}, R_{LB}, etc.).

6.7.2 Diagram Sections

The inconvenience of using the 3D Q_L state diagram directly is overcome by examining its sections, including diagram sections (sections along an operating trajectory) and a section for u = 1, which becomes the 2D Q_L state diagram. A diagram section along a trajectory (e.g., Fig. 25 or Fig. 30) depicts a surface given by Q_{Lp}, Q_{Ls} of the trajectory and the full u dimension. It is aimed to display the frequency dimension u (vertical axis) along a trajectory given by a single or multiple circuit parameter change (horizontal axis). It is useful for evaluating the movement of an operating point along the trajectory and in the frequency dimension u. The diagram sections display the selected the bifurcation frequencies and boundaries (as in Fig. 35) and can also display a superimposed colormap of a quantity of interest, e.g. the input phase φ_{in} in Fig. 25.

When these diagram sections depict the course of bifurcation (e.g., due to a decrease in R_L), the diagram section is oriented such that the reflected impedance Z_{r0} grows towards the right side. A diagram section can be also created for any arbitrary trajectory, e.g., for a regulation action (e.g., change of R_L by a controller in response to change of k). The trajectory may cross a single bifurcation boundary multiple times or not at all. In such a case, the orientation of the resulting diagram section is also arbitrary.

6.7.3 2D Q_L State Diagram

The 2D Q_L state diagram (such as in Fig. 36 (a) with OAB boundaries plotted) is described only in terms of Q_{Lp} and Q_{Ls}. It is approached as a top-down view on the 3D Q_L state diagram. This simplification allows an easy evaluation of the bifurcation phenomena as their occurrence is dependent solely on Q_{Lp} and Q_{Ls}. A section of the 3D Q_L state diagram for a specific value of the normalized frequency u can be displayed as a color map in the 2D diagram. This normalized frequency u can be set either as constant (flat section of 3D diagram) or as function of Q_{Lp} and Q_{Ls} (curved section of 3D diagram).

Besides Q_{Lp} and Q_{Ls} the 2D Q_L state diagram also displays the coupling coefficient k, as Q_{Lp} and Q_{Ls} are linked together to k by (39). If the Q_{Lp} and Q_{Ls} axes are set as logarithmic, constant contours of k form diagonal lines. Only the bifurcation boundaries and the maximal value of k = 1 (k_{lim} in Fig. 36), which limits the possible combinations of Q_{Lp} and Q_{Ls}, are depicted in the 2D diagram, not the bifurcation frequencies. The boundary line styles in Fig. 36 (a) correspond with the diagram sections in Fig. 35.

Similarly, as in the case of the course of bifurcation discussed in the previous chapter, it is necessary to decide whether the IAB boundaries ($BB1_i$, $BB2_i$) or the OAB boundaries ($BB1_o$, $BB2_o$) will be plotted together with the PB boundary BB3. Fig. 36 (b) depicts the comparison of the IAB and OAB boundaries – the IAB boundaries always have higher values of Q_{Lp} than the corresponding OAB for the same value of k. It is recommend using the Q_L state diagram with $BB1_o$, $BB2_o$ as default, as OAB describes the quantities of the main interest: P_{in}, P_{out}, and I_{out}, V_{out} amplitudes.

The 2D diagram is practical for evaluating the bifurcation occurrence of a single operating point, operating trajectory of single or multiple parameters change or an operating area (e.g., IPT system with variable load, which should operate with a variable air gap), by plotting their position with respect to the bifurcation boundaries.

The system operating point is characterized by Q_{Lp}, Q_{Ls} and u for 3D and by Q_{Lp} and Q_{Ls} for the 2D Q_L state diagram, respectively. This simplification for 2D the diagram does not impact the evaluation of the bifurcation occurrence, as that is given solely by Q_{Lp} and Q_{Ls} and u specifies only the position of operating point in the normalized frequency sweep. Because the circuit parameters L_p, L_s, M, f_0, R_{sL} are the inputs for the calculation of Q_{Lp}, Q_{Ls} (41), they do impact bifurcation. Their change moves the system operating point in the Q_L state diagram with respect to the bifurcation boundaries, as examined in [183]. Similar to the operating frequency f (equivalent to u), the input voltage amplitude V_{in} does not affect the bifurcation occurrence.

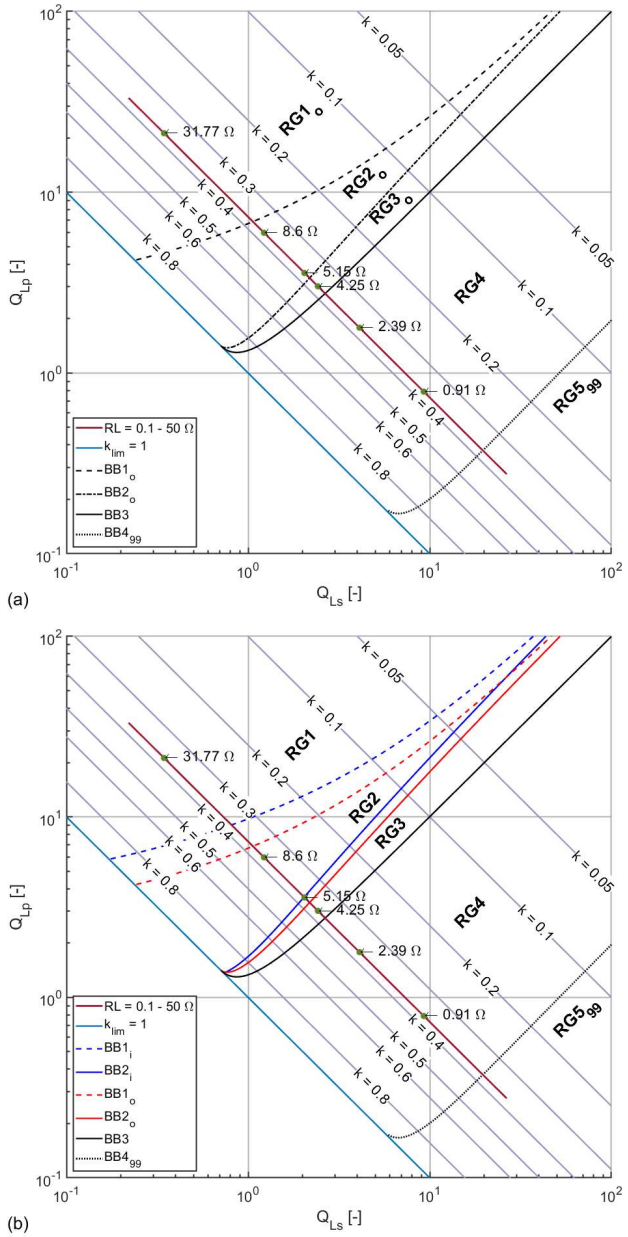

Fig. 36: (a) 2D Q_L state diagram for OAB, PB with marked operating trajectory (dark red), operating points of the frequency responses in Fig. 23, bifurcation boundaries (black) and limit value of coupling coefficient k (blue). (b) The comparison of OAB and IAB boundaries in the 2D Q_L state diagram. Published by author in [20].

The 2D diagram can also conveniently display a superimposed colormap of a quantity of interest (e.g., V_{out}); however, it is necessary to understand following. The bifurcation boundaries and regions are universal, their position is independent on the operating point, trajectory, or area. But the plotted quantity is connected with an operating area, which is given by ranges of at least two parameters (e.g., R_L from 5 to 10 Ω and k from 0.1 to 0.4 for the previously discussed example of operating area), thus the quantity's absolute values depend on the parameters defining the area. Therefore, if another operating area was defined using a different pair of parameters (e.g., f_0 and L_p), the quantity absolute values would be different even in the intersection with the initial operating area.

The general parameter model is not designed for efficiency analysis, because it neglects R_p while R_s is incorporated with R_L by (14). In this manner, the efficiency is always equal to 1. However, both the 2D diagram and the diagram sections are still useful for efficiency evaluation as it is demonstrated in Chapter 8.1.1. Any further references to the Q_L state diagram in this work aim primarily to the 2D diagram.

6.8 General Parameter Model Summary

The generalized model represents a comprehensive mathematical description of the phase bifurcation (PB), the output amplitude bifurcation (OAB, frequency splitting) and input amplitude bifurcation (IAB). For PB and OAB it provides formulas of bifurcation frequencies. The conditions describing bifurcation boundaries are provided for all three bifurcation phenomena. Based on the boundaries, the course of bifurcation is divided into regions with specific behavior from the perspective of bifurcation. All this information is summarized in the Q_L state diagram.

This model provides a unified description based on the normalization employing the loaded quality factors Q_{Lp}, Q_{Ls} and the normalized frequency u, which simplifies the equations (especially for OAB) and provides a common metric to conveniently describe and compare bifurcation phenomena in different systems (e.g., phone charger, EV charger, etc.) – the bifurcation occurrence depends only on generalized parameters Q_{Lp} and Q_{Ls}.

However, these advantages come at a price given by the initial assumptions of the model. Because the system considers perfectly tuned primary and secondary LC resonators, i.e., it does not describe the bifurcation phenomena in the detuned systems. Also, because R_p, R_s are not considered, the model cannot be applied to evaluate efficiency. However, the efficiency evaluation is not the aim of the model and the provided instruments (2D Q_L state diagram and diagram sections) are still useful for efficiency evaluation as shown in Chapter 8.1.1.

7 Bifurcation Analysis

Exploring the mathematical descriptions of phase bifurcation (PB), input amplitude bifurcation (IAB) and output amplitude bifurcation (OAB) in the previous chapter prepared the framework for the analysis of the bifurcation phenomena. At first, all nine bifurcation frequencies are examined in the 2D Q_L state diagram. In the second part, the influence of the circuit parameters figuring in the loaded quality factor equations (37) is evaluated by examining their influence on the movement of an operating point. Based on this, the construction of operating trajectories and operating areas, which are also useful for evaluating the bifurcation control methods in Chapter 9 is discussed in the third part of the chapter. The fourth part analyses the mechanism of bifurcation – the process of PB, IAB and OAB emergence. In last part, the validity of the general parameter model is examined by analyzing the influence of the primary and secondary coil ESRs, because the general parameter model is based on a lossless circuit. The impacts of the bifurcation phenomena on the device design and operation are discussed in the following chapter.

7.1 Examination of Bifurcation Frequencies in the 2D Q_L State Diagram

Fig. 37 depicts all nine bifurcation frequencies as color maps in the 2D Q_L state diagram. They are organized as follows. The rows are arranged according to bifurcation phenomena occurrence in the course of bifurcation: the first row depicts the IAB frequencies, the second row the OAB frequencies and the third row the PB frequencies. The columns are organized according to the bifurcation asymptotes: the first column depicts the u_{x0} frequencies, the second the u_{x1} frequencies and finally the third row the u_{x2} frequencies. The normalized frequency range u is set from 0.7 to 2 as default, but it was adjusted for u_{ai1} and u_{ao1} to 0.7 to 1 in order to make the frequency changes more visible.

The graphs well illustrate the behavior of bifurcation frequencies described in the previous chapter such as the emergence of bifurcation phenomena at their respective boundaries, stabilization of the frequencies at their asymptotes in the region $\mathrm{RG5}_{95}$ and increase of these asymptotes with growing k, as depicted in Fig. 34. Fig. 37 also shows that frequencies u_{ai} , u_{ao0} and $u_{\varphi 1}$ emerge above u_0 and this difference increases with k. Their counterparts which also emerge in bifurcation, i.e., u_{ai2}, u_{ao2} and $u_{\varphi 2}$, respectively, emerge at the same values of u.

7.2 Influence of Circuit Parameters Figuring in Loaded Quality Factor Calculation

The general parameter model presented in Chapter 6 is based on the loaded quality factors Q_{Lp} and Q_{Ls} given by (41). They are calculated from the primary inductance L_p, secondary inductance L_s, mutual inductance M, resonance frequency f_0 which is common for both primary and secondary and the adjusted load resistance R_{sL}. This examination is focused on the influence of the main parameters L_p, L_s, M, f_0 and R_L. Both ESRs R_p and R_s are considered equal to zero, thus $R_{sL} = R_L$ and the calculations of Q_{Lp} and Q_{Ls} match (37). The influence of R_p, R_s is discussed separately in Chapter 7.5. At first, the influence of each of five main parameters is examined individually, then the influence of the coupled parameters is examined. Coupled parameters refers to multiple parameters, which do not change independently on each other, but their change is proportional to some other variable, e.g., change of L_p, L_s and M due to displacement of the coils or change of the air gap.

The change of the single or coupled parameters moves the system operating point. The operating point movement creates an operating trajectory which may cross bifurcation boundaries, resulting in bifurcation phenomena occurrence. This trajectory is called the operating trajectory; thus, the examination of the circuit parameter influence also describes the construction of operating trajectory. The operating trajectory of decreasing R_L was used in the previous chapter to construct the general parameter model.

In the first part of the chapter, the influence of single parameters is examined. In order to examine the coupled parameters, it is necessary to examine the influence of multiple independent parameters on the operating point movement. This is the focus of the third part of this chapter. Finally, the third part of the chapter discusses the influence of the coupled parameters. Parts of this examination were published in [183], [186].

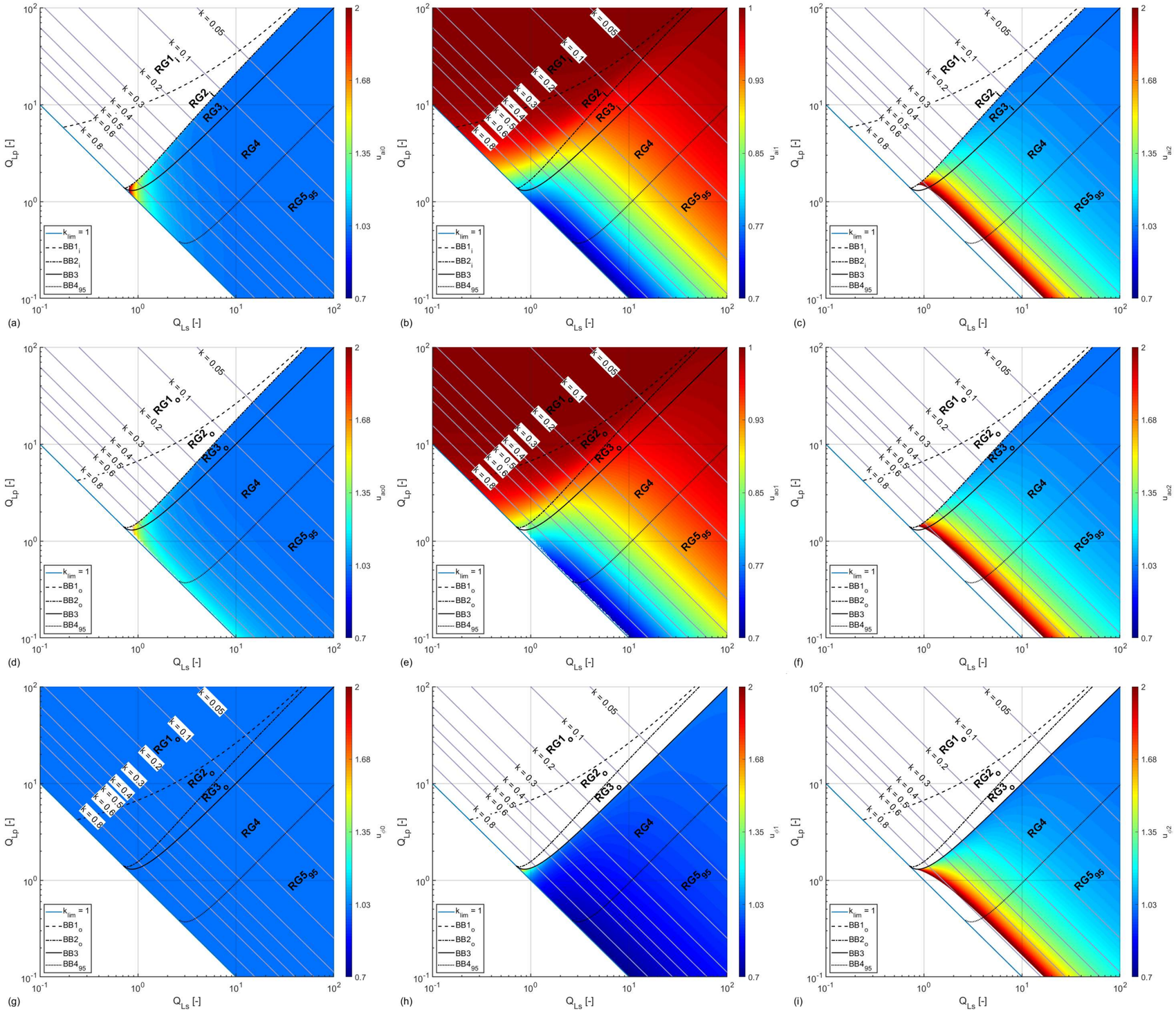

Fig. 37: Bifurcation frequencies in the 2D Q_L state diagram. IAB frequencies (a) u_{ai0}, (b) u_{ai} and (c) u_{ai} . OAB frequencies (d) u_{ao} , (e) u_{ao1} and (f) u_{ao} . PB frequencies (g) $u_{\varphi 0}$, (b) $u_{\varphi 1}$ and (c) $u_{\varphi 2}$. The figures (b) and (e) have different ranges of their colormaps than the rest.

7.2.1 Influence of Single Parameters

Fig. 38 depicts the movement of an operating point due to change of individual circuit parameters (i.e., only one of the parameters changes and the rest remain constant). The trajectories are independent on the rate of parameter change.

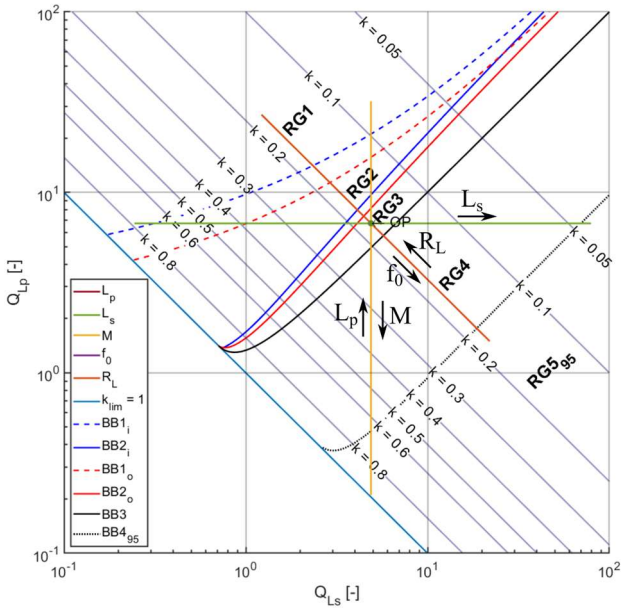

Fig. 38: Operating point movement in dependence on a single parameter change. Arrows point in the direction of the operating point movement with the circuit parameter growth. L_p and M have the same trajectory as well as f_0 and R_L.

Default position of the operating point is marked by OP in the figure. Its initial circuit parameters are listed in Table 18. Changes of the operating parameters determine operating trajectories. As it is visible form Fig. 38, there are only three distinctive trajectories - L_p has the same trajectory as M and f_0 the same as R_L. These three distinctive trajectories can be distinguished by the general parameter, which remains constant – see Table 19. Thus, these trajectories can be described as isolines. Isoline is a curve which connects the points at which the examined quantity gains the same value. For example, k-isoline connects all the points of 2D Q_L state diagram, at which k gains the selected value.

Table 18: Circuit parameters of the default operating point.

Parameter	Symbol	Value
Primary inductance	L_p	45.0 µH
Secondary inductance	L_s	40.0 µH
Mutual inductance	M	7.4 µH
Resonance frequency	f_0	100.0 kHz
Load resistance range	R_L	5.15 Ω

Table 19: Single parameter operating trajectories.

Parameter	Q_{Lp}	Q_{Ls}	k	Isoline	Direction
L_p	↗	–	↘	Q_{Ls}-isoline	Negative
L_s	–	↗	↘	Q_{Lp}-isoline	Positive
M	↘	–	↗	Q_{Ls}-isoline	Positive
f_0	↘	↗	–	k-isoline	Positive
R_L	↗	↘	–	k-isoline	Negative

The direction of the operating point movement with the increase of the parameter is indicated by the arrow in Fig. 38. This direction can be distinguished by the change of Z_{r0} with increase of the parameter – it is positive if Z_{r0} increases with the parameter (the operating point moves towards the bifurcation, e.g., M) and negative if Z_{r0} decreases while the parameter increases (the operating point moves away from the bifurcation, e.g., R_L). The parameters following the same isolines have opposite directions – while change of L_p is negative, the change of M is positive. The ranges in which the circuit parameters vary, are summarized in Table 20. Note that these ranges do not represent any real device, they were selected that the resulting operating trajectories would stretch from the region RG1 to region $\mathrm{RG5}_{95}$. Also, the ranges for L_p and f_0 were selected that they would match M and R_L, respectively.

Table 20: Circuit parameter ranges for the analysis of a single parameter on bifurcation.

Parameter	Symbol	Range
Primary inductance	L_p	1.4 – 213.8 µH
Secondary inductance	L_s	2.0 – 650.0 µH
Mutual inductance	M	3.4 – 41.9 µH
Resonance frequency	f_0	25.0 – 450.0 kHz
Load resistance range	R_L	1.14 – 20.6 Ω

Fig. 38 shows, that the operating point moves deeper in bifurcation with the growth of L_s, f_0 and M. On the other hand, the bifurcation phenomena decrease with the growth of L_p and R_L. Corresponding diagram sections to illustrate the course of bifurcation along the trajectories given by the change of these parameters are depicted in Fig. 39. Change of any of these parameters may result in the bifurcation phenomena occurrence. However, he bifurcation occurrence does not depend on a single circuit parameter but on the ratios of all of them (in the case of general parameter model these ratios correspond with the loaded quality factors Q_{Lp} and Q_{Ls}.

The parameters can be divided into independent or coupled, based on the actual device behavior. The independent parameters can be changed individually, while the coupled parameters cannot. The first independent parameter is the equivalent load resistance R_L which represents active power drawn from the IPT system. The second one is the resonance frequency f_0, which is implemented to the circuit through the compensation capacities C_p, C_s. To change the f_0, only the capacities change, and no other circuit element is affected. In the systems using the coils without the magnetic cores, the mutual inductance M is also independent. When the coils without a magnetic circuit change their mutual position, it affects only M and not the other parameters.

The behavior of the inductances L_p and L_s is more complicated. When there are no additional inductances, they represent the coil inductances, they are the coupled parameters. Even in the systems where the coils have no magnetic core, they cannot be changed without impacting M and if the respective compensation capacity remains constant, also the resonance frequency of the respective side. (For example, change of number of turns of the primary coil affects both L_p and M. If C_p is not adjusted, it also impacts f_{0p} resulting in detuning of the circuit). In the systems using the coils with magnetic cores, also the mutual inductance M is a coupled parameter. Any change of mutual position of the coils affects not only M, but also the coil inductances L_p and L_s. The magnetic cores of both coils also form a magnetic core of each single coil (i.e., the inductance of a coil is increased when the second coil is added). Thus, any mutual movement of the coils affects the resulting magnetic core of the single coil and thus L_p or L_s. Similarly, any change of magnetic core geometry results in change of both L_p and L_s, and it also affects M and f_0 if C_p and C_s remain constant.

When the inductances L_p and L_s comprise of the coil inductances and additional inductances (e.g., added reactors to the coupling coils) and the additional inductances are varied, then L_p and L_s are independent parameters.

For the purposes of the analysis, all parameters L_p, L_s, M, f_0 and R_L were considered independent in Fig. 38. To examine the influence of the coupled parameters on bifurcation, it is necessary to examine how multiple individual parameters affect the movement of the operating point.

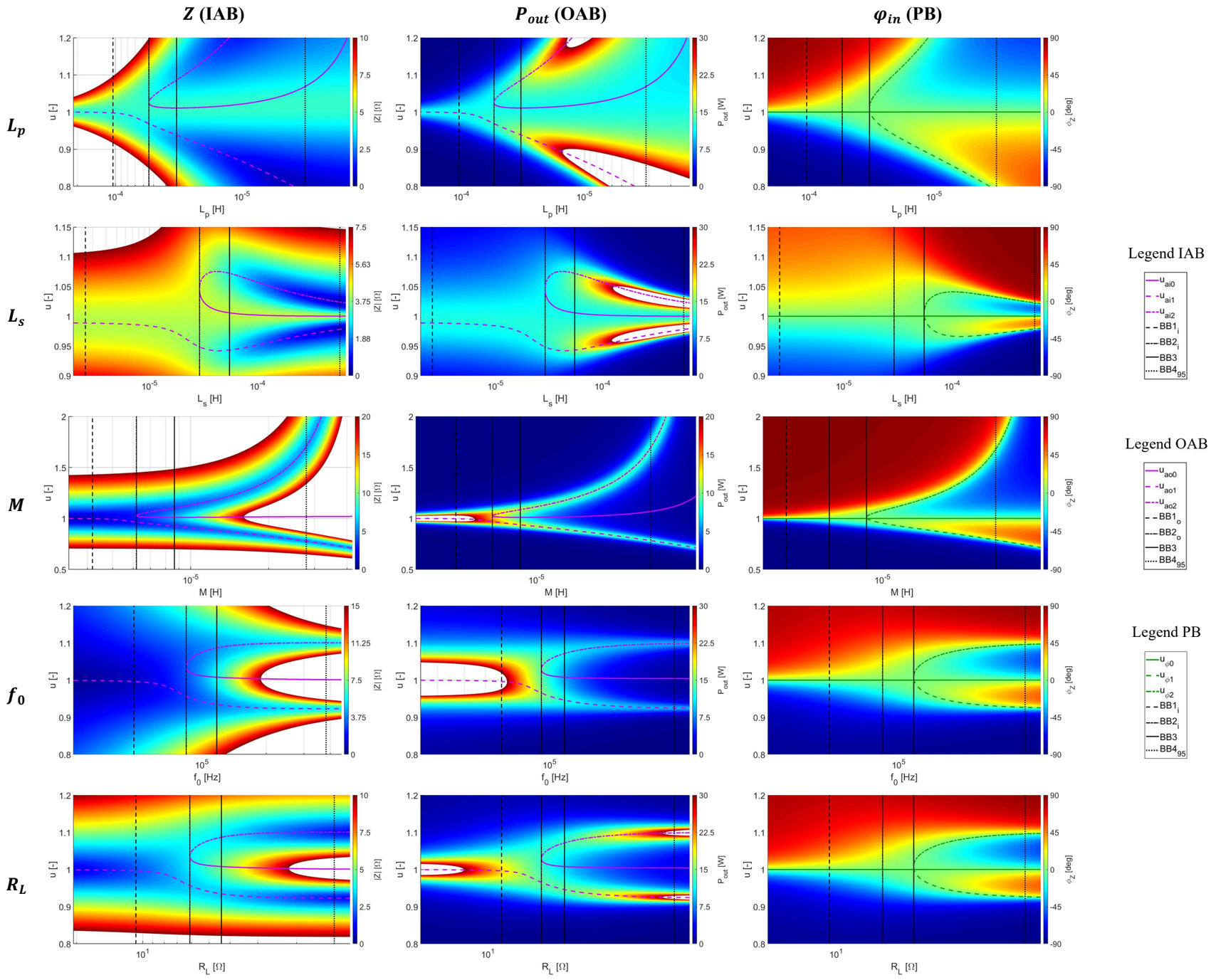

Fig. 39: Diagram sections along the trajectories of , L_s, M, f_0 and R_L in 2D Q_L state diagram in Fig. 38. Colormaps in the background displays (left to right) the input impedance amplitude Z, output power P_{out} and input phase φ_{in}, which correspond with IAB, OAB and PB phenomena.

7.2.2 Operating Trajectory of Multiple Parameters

Operating trajectory of the multiple parameter change is a composition of trajectories of single parameter changes. On the contrary to the trajectories of the single parameter, the trajectory of multiple parameters is determined by the growth rates of individual parameters composing the resulting trajectory.

The construction of the multiple parameter trajectory can be divided into obtaining the end point and obtaining the trajectory itself. The end point is independent on the growth rates of the individual parameters, but the trajectory itself between the beginning and end point is dependent on the parameter growth rates with respect of each other.

This can be demonstrated on the following example – see Fig. 40. The IPT system has at the beginning point the same parameters as in Table 18. The two parameters which change are the mutual inductance M, which varies in range of 7.4 to 24 μH and the equivalent load resistance R_L with range of 5.15 to 30 Ω. The trajectories A, B and C in figure are given by different growth rates of M and R_L. Trajectories cannot gain any values, but they are limited by trajectories of single parameter change (green – M, dark red – R_L in Fig. 40) which for a quadrilateral. In some sense, these single parameter trajectories demark an operating area - see Chapter 7.3, which describes the describes the construction of the operating area.

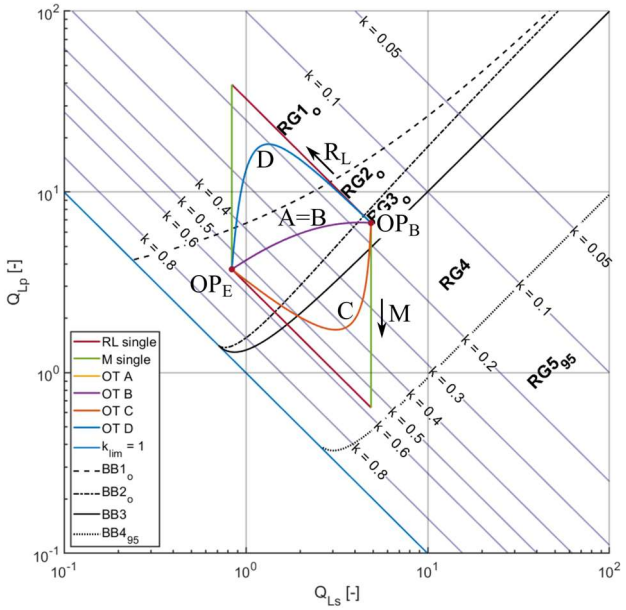

Fig. 40: Influence of differing growth rates on the operating trajectories for multiple parameters. Parameters M and R_L change while the rest remains constant. The growth rates are of M and R_L are different between points OP_B and OP_E, which mark the beginning and end operating points. That results in trajectories A, B, C, D. All the possible trajectories are bordered by quadrilateral, which sides are determined by single parameter operating trajectories (green - M, dark red R_L). Arrows point in the direction of the parameter growth.

The trajectory depends on the ratio of growth rates, but not on the growth rates itself, i.e., two parameters growing exponentially will result in the same trajectory as two parameters growing linearly (matching trajectories A and B in Fig. 40). If one parameter will grow exponentially and other will grow logarithmically, then the resulting trajectory will be different (trajectory CB: M grows logarithmically and R_L grows exponentially, trajectory D: M grows exponentially and R_L grows logarithmically).

Thus, in the case of the trajectory of a multiple parameter change, there is a single end point, which is given solely by the difference in the circuit parameters and infinite number of trajectories connecting the end point with the default position of the operating point, in dependence on the ratio of parameter growth rates.

7.2.3 Influence of Coupled Parameters

As it was explained in Chapter 7.2.1, in an actual device there are parameters, which do not change independently, but they are coupled together by a certain phenomenon, e.g., change of the mutual position of the coils. This phenomenon can be described by another parameter, e.g., width of an air gap between the coils, and the affected equivalent circuit parameters change proportionally to this additional parameter. Therefore, the growth

rates with respect to each other of such coupled parameters are given, thus there is a single operating trajectory between the beginning and end point.

This can be demonstrated on the following example of the secondary coil displacement in the system with ferrite-core coils. The secondary pad is horizontally moved in the x-axis (see Fig. 41) in the 10 mm steps from the initial position of 0 mm to 200 mm. The step is decreased to 5 mm near the DD pads null position ([60], Fig. 9 (c)).

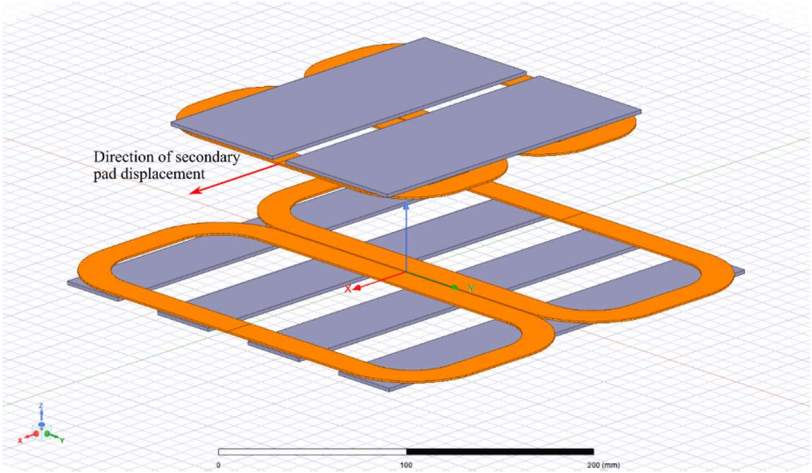

Fig. 41: Secondary pad displacement in x axis. Presented by author in [187].

Due to this displacement, inductances L_p, L_s and M change as shown in Fig. 42. The inductance values were obtained by a method described in Chapter 8.3.2.1. The values for the initial position (x = 0 mm) are shown in Table 21. For simplicity, the resonance frequency f_0 is considered independent on the change of L_p and L_s, i.e., it remains constant at 100 kHz.

Table 21: System parameters in the position x = 0 mm.

Parameter	Symbol	Value
Primary inductance	L_p	29.4 µH
Secondary inductance	L_s	17.1 µH
Mutual inductance	M	7.9 µH
Resonance frequency	f_0	100 kHz
Equivalent load resistance	R_L	0.5 Ω

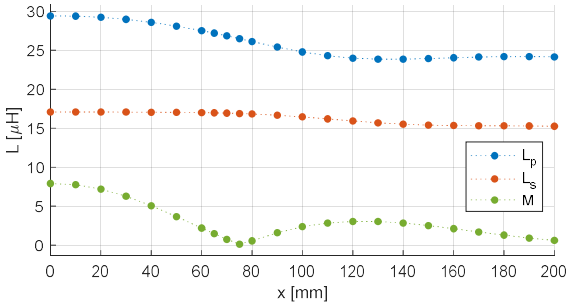

Fig. 42: Change of the inductances L_p, L_s and M due to the coil displacement in x axis.

Fig. 43 shows the resulting trajectory of the displacement in the x axis. When compared with Fig. 42 displaying the inductances, in the first part of the displacement trajectory until the null point, the OP moves due to the change of L_p and M as L_s remains approximately constant. Because the change of both L_p and M moves the OP on the same isoline (Q_{Lp}-isoline), as explained in Chapter 7.2.1, the resulting trajectory of coupled L_p, L_s and M is visually indistinguishable from the trajectories of L_p or M. The driving parameter of the OP movement is M and change of L_p works against it because it has the opposite direction (see Fig. 38). Due to the small value of M at the null point, the operating trajectory briefly moves outside the range of the Q_L state diagram. After passing the

null point, L_s begins to decrease until it stabilizes at 15 µH. This results in the shift of the operating trajectory from the original Q_{Lp}-isoline and stabilization at the new one as shown in Fig. 43.

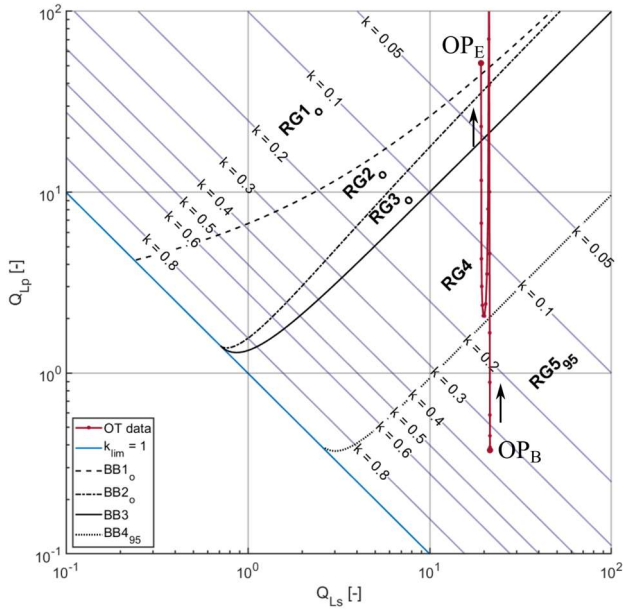

Fig. 43: Operating point movement due to the displacement in x axis. Operating point OP_B marks the beginning of the trajectory and OP_E marks the end of the trajectory.

7.3 Construction of Operating Area

Operating areas are used for evaluation of the bifurcation phenomena for circuit parameter ranges in the 2D Q_L state diagram. An operating area is a set of operating points, which represents all the possible combinations of the given circuit parameter ranges. They can be applied for design evaluation, e.g., they can be used to examine what bifurcation phenomena occur for any combination of R_L range representing the varying load and ranges of coupled L_p, L_s and M representing the change in mutual position of coils. Or the operating areas can be also viewed as total sum of all possible trajectories between two points given by the multiple parameter change. Then they could be used to evaluate IPT system regulation.

Operating areas are given by ranges of two circuit parameters following the different isolines (see Table 19). Both of these parameters are either independent or one is replaced by a set of coupled parameters. The other parameters remain constant. Consequently, any point (i.e., combination of Q_{Lp} and Q_{Ls}) in the operating area is given solely by one combination of the circuit parameters defining the operating area, which is a condition necessary to construct the color map of an evaluated quantity. (The operating area could be given by three circuit parameters – see [186], but then some of the points could be given by multiple combinations. Due to that, the quantity value varies depending on the combination of the circuit parameters, unless the quantity is normalized.)

The operating area is delimited by its boundary forming a quadrilateral comprising of segments which are obtained as the single or coupled parameter trajectories (see Chapter 7.2.1 and Chapter 7.2.3, respectively). Generalized description of the operating area boundary of two independent parameters is summarized in Table 22. T stands for the first varying parameter and U for the second one. Other circuit parameters remain constant.

Table 22: General description of two parameter operating area boundary.

Corner	Parameter Values	Side	Parameter Values
A	T_{max}, U_{max}	AB	$T_{max}, U \in \langle U_{min}, U_{max} \rangle$
B	T_{max}, U_{min}	BC	$U_{min}, T \in \langle T_{min}, T_{max} \rangle$
C	T_{min}, U_{min}	CD	$T_{min}, U \in \langle U_{min}, U_{max} \rangle$
D	T_{min}, U_{max}	DA	$U_{max}, T \in \langle T_{min}, T_{max} \rangle$

Each varying parameter creates two boundary segments; each segment has 2 endpoints defining the boundary corners A, B, C and D. The segment is an operating trajectory of one parameter varying from its

minimum to its maximum, while the other varying parameters defining the operating area are constant at their limit values (minimum or maximum).

Example of such an operating area is depicted in Fig. 44, for R_L range of 5.15 to 30 Ω and M range of 7.4 to 24 μ (e.g., examination of varying load and coil position of an IPT system with air-core coils). Remaining parameters are given by Table 18. Varying parameters R_L corresponds with U and M with T.

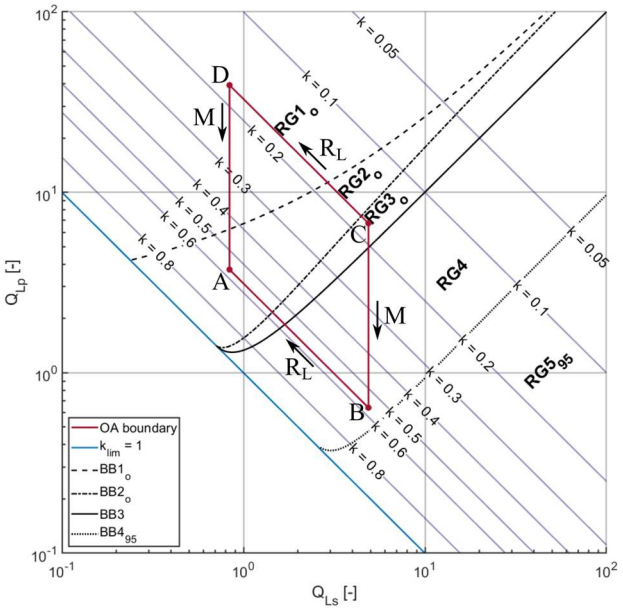

Fig. 44: Construction of operating area given by two independent parameters R_L and M. The arrows mark the direction of the parameter growth.

One of the parameters T and V in Table 22 can be replaced by a set of coupled parameters. As described in Chapter 7.2.3, the coupled parameters act as a single variable. Resulting boundary segment does not follow any parameter's isoline, but a trajectory is given by all of them. Fig. 45 shows an example of such operating area. It is given by R_L range of 0.5 to 1.5 Ω and by the secondary coil displacement in the x axis according to Fig. 42, which results in coupling coefficient k range 0.1 to 0.35 (corresponds with displacement in range of 0 to 60 mm). The resonance frequency is 200 kHz. The ESRs R_p and R_s are neglected.

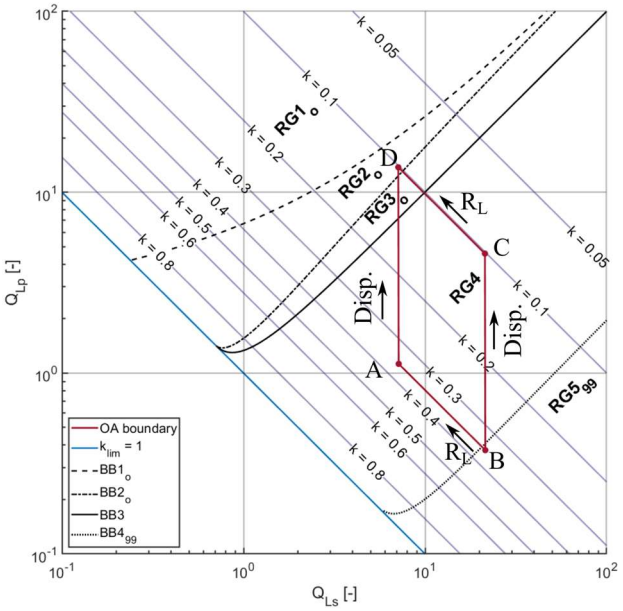

Fig. 45: Construction of operating area independent parameter R_L and coupled L_p, L_s and M, which are given by the secondary coil displacement in x axis (marked as Disp. in the figure). The arrows mark the direction of the parameter growth.

The influence of another independent or another set of coupled parameters can be evaluating by examining the movement of an operating area in the 2D Q_L state diagram. Fig. 46 shows the movement of the operating area $A_1B_1C_1D_1$ from Fig. 45 into the new position $A_2B_2C_2D_2$ by the change of the resonance frequency f_0 from 200 kHz to 40 kHz. In this movement, the operating area is viewed as a set of individual operating points. Movement of these operating points follow the same rules as the movement of a single OP – they move on an isoline or a trajectory depending whether the movement is controlled by an independent parameter or a set of coupled parameters. The yellow lines are the movement trajectories for the operating area corners – all of them follow k-isolines. Length of the movement trajectories is given by the point parameter values. Isolines or trajectories defining the object boundary segments keep their type, but their value may change.

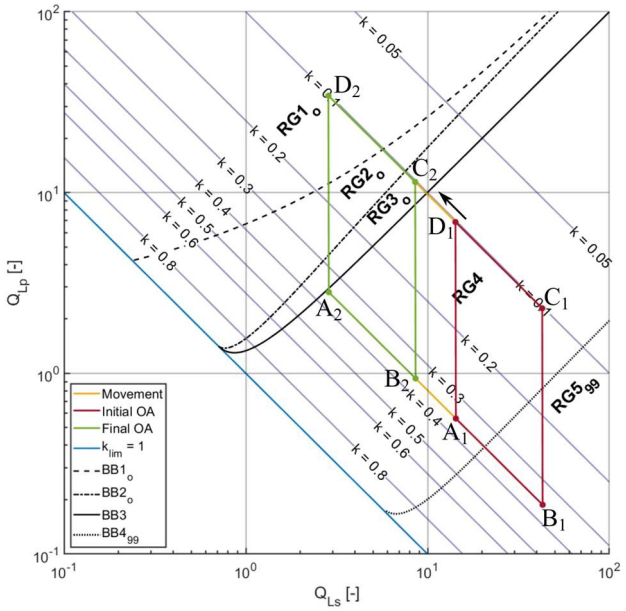

Fig. 46: Movement of the operating area due to a change of an independent parameter. Initial operating area $A_1B_1C_1D_1$ is moved into the position $A_2B_2C_2D_2$ by change of the resonance frequency f_0 from 200 kHz to 40 kHz. Yellow lines mark the trajectories along which the boundary of the operating area is moved.

The influence of two parameters, if they follow the same isoline, can be examined as follows. One of the parameters is plotted as an operating trajectory in the 2D Q_L state diagram. The influence of the other parameter is shown by the movement of the operating trajectory, which follows the similar rules as the movement of the operating area described in the previous paragraph.

7.4 Mechanism of Bifurcation

The mechanism of bifurcation is examined for the trajectory of R_L change. In brief, bifurcation is the result of interactions of between the primary side impedance $\hat{Z}_p$ and reflected impedance $\hat{Z}_r$, which represents the influence of the secondary side. As this influence grows the bifurcation phenomena gradually occur.

The first part of the chapter discusses the interactions of the primary side impedance $\hat{Z}_p$ and reflected impedance $\hat{Z}_r$ resulting in the bifurcation phenomena connected with the input impedance $\hat{Z}$ – PB and IAB. The bifurcation mechanism for the other parameters in Q_{Lp}, Q_{Ls} formulas (37) besides R_L is outlined at the end of this part. Then, in order to explain the difference between IAB and OAB, the analysis follows the process of expressing the P_{out} formula from (63) into a function of impedance (69). Both of these analyses are performed for the equivalent circuit model considering the losses (i.e., $R_p \neq 0$, $R_s \neq 0$). The analyses were presented in [20].

7.4.1 IAB and PB Mechanism – R_L Trajectory

To underline the influence of the reflected impedance, the equivalent circuit schematics in Fig. 16 can be adjusted to Fig. 47. The primary impedance $\hat{Z}_p$ is represented by the resistance R_p and reactance X_p (17), while the reflected impedance $\hat{Z}_r$ by the reflected resistance R_r and reactance X_r, which are calculated from (13) and (14), respectively.

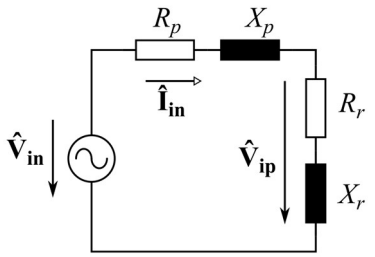

Fig. 47: Division of the reflected impedance and the induced voltage into the real and imaginary part. Phasors are marked by bold symbols. Published by author in [20].

The reflected impedance $\hat{Z}_r$ impacts the input phase φ_{in}, which can be calculated from (106):

$$\varphi_{in} = arctan\frac{X_p + X_r}{R_p + R_r} \tag{106}$$

Since R_r is always positive, it adds to R_p and decreases the resulting angle. As both the primary and secondary sides are tuned to the same resonance frequency f_0, their respective reactances X_p and X_s have the same sign for the whole frequency sweep. However, X_r as given by (14) has opposite polarity in comparison with X_p. Thus, it works against X_p resulting in the appearance of ZPA frequencies, as PB occurs in region RG4 of Fig. 35 (a).

Similarly, the secondary side influence affects the input impedance amplitude Z. Thanks to the series compensation of the primary, the impedance amplitude Z is calculated from (107), which shows how the reflected impedance causes amplitude bifurcation:

$$Z = \sqrt{\left(R_p + R_r\right)^2 + \left(X_p + X_r\right)^2} \tag{107}$$

However, these descriptions of both the phase and amplitude bifurcation are too general, thus this chapter discusses the interactions leading to bifurcation phenomena in detail. To understand how the reflected impedance $\hat{Z}_r$ causes bifurcation, it is necessary to analyze individual components forming $\hat{Z}_r$ according to (11) and then examine its interactions with the primary side impedance $\hat{Z}_p$, with which it forms the input impedance $\hat{Z}$.

Fig. 48 through Fig. 51 illustrate this analysis along the R_L diagram section. Red highlights mark the frequencies of interest, such as maxima (solid line), minima (dashed line) or zero-crossings (dot-dashed line). The values of local extrema and zero crossings were obtained numerically from functions based on the equivalent circuit model with the parameters in Table 4. To be consistent with the general parameter model, the normalized operating frequency u is used in the figures and description. The course of bifurcation is marked by the IAB and PB boundaries.

The analysis starts with examining the primary and secondary impedances $\hat{Z}_p$ and $\hat{Z}_s$, given by (16) and (10). $\hat{Z}_p$ is independent of R_L. Its impedance Z_p is equal to R_p at u_0. Outside u_0, the primary reactance (17) is dominant.

On the contrary, the secondary side impedance $\hat{Z}_s$ is strongly dependent on R_L near the resonance frequency u_0. Its amplitude Z_s value is approximately equal to R_L in region $\mathrm{RG1_i}$, but as R_L decreases, the secondary side reactance $\omega L_s - \frac{1}{\omega C_s}$ becomes more significant (Fig. 48 (a). Also as shown in Fig. 48 (b), the transition of the $\hat{Z}_s$ phase φ_s between -90° for $u \to 0^+$ and 90° for $u \to +\infty$ is at first significantly damped by R_L in the area near u_0. However, as R_L decreases, the transition gradually becomes sharper.

The secondary side impedance $\hat{Z}_s$ is reflected to the primary side according to (11), i.e., $\hat{Z}_s$ is inverted and multiplied by $\omega^2 M^2$. The amplitude of the inverted $\hat{Z}_s$ has its maximum at u_0 and goes to 0 for $u \to 0^+$, $u \to +\infty$. The real part of $\hat{Z}_s$ forms an approximately symmetrical peak with its maximum at u_0 (Fig. 49 (a)). As R_L decreases, the maximum value grows, but the peak also narrows. The imaginary part of the inverted $\hat{Z}_s$ has an inductive peak near u_0 for $u < u_0$, and a capacitive peak near u_0 for $u > u_0$ (Fig. 49 (b)), thus its polarity is opposite to X_p. Its peaks become pronounced with decreasing R_L. X_r also crosses 0 at u_0, and for $\to 0^+$, $u \to +\infty$ it goes to 0.

To achieve the reflected impedance $\hat{Z}_r$, the inverted $\hat{Z}_s$ is multiplied by $\omega^2 M^2$. Thus, both $Re\{\hat{Z}_s\}$ and $Im\{\hat{Z}_s\}$ are amplified proportionally to the square of u. This means the maximum along u of the resulting R_r (13) is initially shifted above u_0, but it moves towards to u_0 as R_L decreases (see Fig. 50 (a)), and in $\mathrm{RG3_i}$ it matches

u_{ai1}. The R_r curve below its maximum have higher gradient than above its maximum. Similarly, the inductive peak of X_r (14) is smaller than the capacitive one (see Fig. 50 (b)).

The input impedance $\hat{Z}$ is the sum of primary side impedance $\hat{Z}_p$ and the reflected impedance $\hat{Z}_r$. Its amplitude Z is a geometrical sum of $R_p + R_r$ and of $X_p + X_r$ (107). While R_r adds up to R_p, X_r has always the opposite polarity than X_p, thus it decreases Z. From the perspective of R_L, R_r becomes impactful before X_r (compare Fig. 50 (a) and (b)). Due to this, R_r asymmetry caused by uneven amplification by $\omega^2 M^2$ pushes the u_{ai1} under u_0 after $\mathrm{BB1_i}$ – Fig. 50 (a) and Fig. 51 (a).

With the further decrease of R_L, X_r begins to compensate X_p. Impedance amplitude Z decreases in the corresponding bands above and below u_0 while at u_0 Z increases due to growing R_r. This results in emergence of u_{ai2} (local maximum) and u_{ai0} (local minimum) at $\mathrm{BB2_i}$. When X_r fully compensates X_p at $\mathrm{BB3_i}$, $u_{\varphi 1}$ and $u_{\varphi 2}$ appears as PB occurs. As R_L decreases further, X_r amplitude grows higher than X_p in the bands between $u_{\varphi 1}$, u_0 and between u_0, $u_{\varphi 2}$, the changing the character of input impedance $\hat{Z}$ from capacitive to inductive and vice versa (see Fig. 51 (b)).

If the course of bifurcation is examined along the trajectories given by other circuit parameters, which appear in the loaded quality factor formulas (41) – see Chapter 7.2.1, following insights can be found:

- Primary side inductance L_p: The reflected impedance $\hat{Z}_r$ and R_p are constant, but X_p changes (C_p changes with L_p to keep the primary resonance frequency f_{0p} same as f_0). The change of X_p has the similar impacts on impedance amplitude Z and phase of φ_{in} as the change of $\hat{Z}_r$.
- Secondary side inductance L_s: The primary impedance, $\omega^2 M^2$, R_L and R_s are constant, but X_s changes (C_s changes with L_s to keep the secondary resonance frequency f_{0s} same as f_0). This results in the change of X_s and $R_L + R_s$ resulting in the similar change of the secondary impedance amplitude Z_s as in Fig. 48 (a) and consequently in the change of $\hat{Z}_r$.
- Mutual inductance M: Both $\hat{Z}_p$ and $\hat{Z}_s$ remain constant, but the coupling $\omega^2 M^2$ changes. This results in the change of $\hat{Z}_r$.
- Resonance frequency f_0: Change of f_0 impacts X_p, X_s and $\omega^2 M^2$. Both reactances change with the same rate, thus their ratio would remain constant. But $\omega^2 M^2$ in the definition of $\hat{Z}_r$ (11) changes faster than X_p, resulting in change of $\hat{Z}_r$ and causes bifurcation. If the trajectory of the changing f_0 is analyzed from the perspective of the general parameter model – then the normalized frequencies have the similar course along the increasing f_0 as along the decreasing R_L [183], if operating frequency is normalized.

  The influence of R_p and R_s is examined in Chapter 7.5.

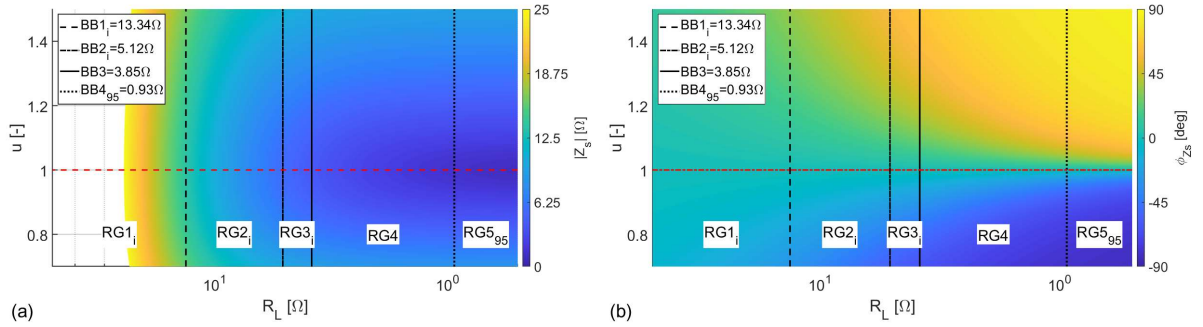

Fig. 48: Secondary side impedance $\hat{Z}_s$ in the diagram section along a trajectory of decreasing R_L. (a) Colormap of its amplitude Z_s with the minimum marked by red dashed line. (b) Colormap of its phase φ_s with the zero-crossing marked by red dot-dashed line.

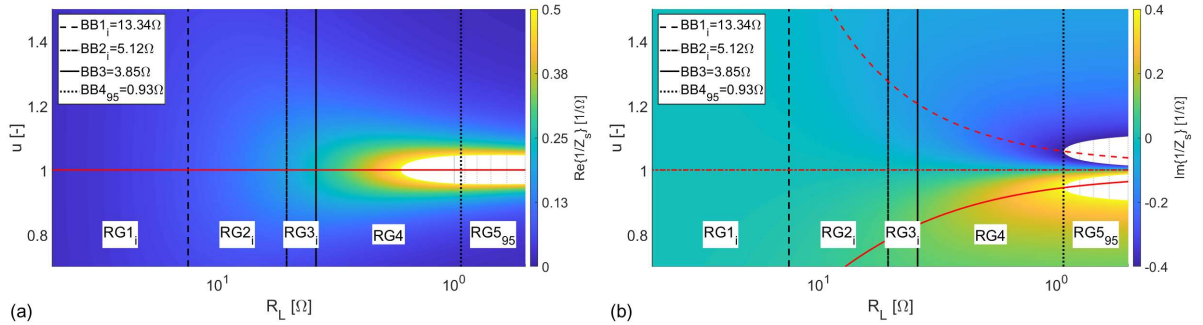

Fig. 49: Inverted secondary impedance $\hat{Z}_s$ in the diagram section along a trajectory of decreasing R_L. (a) Colormap of its real part with maximum marked by solid red line. (b) Colormap of its imaginary part with marked maximum (solid line), zero crossing (dot-dashed line) and minimum (dashed line) in red.

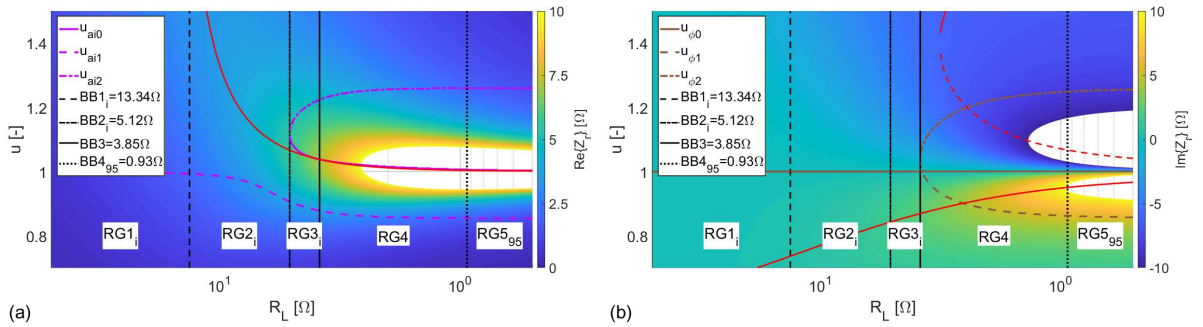

Fig. 50: Reflected impedance $\hat{Z}_r$ in the diagram section along a trajectory of decreasing R_L. (a) Comparison of its real part R_r maximum (solid red line) with the IAB frequencies (purple). The background shows a colormap of R_r. (b.) Comparison of its imaginary part X_r maximum (solid line) and minimum (dashed line) in red with the PB frequencies in brown. The background shows a colormap of X_r.

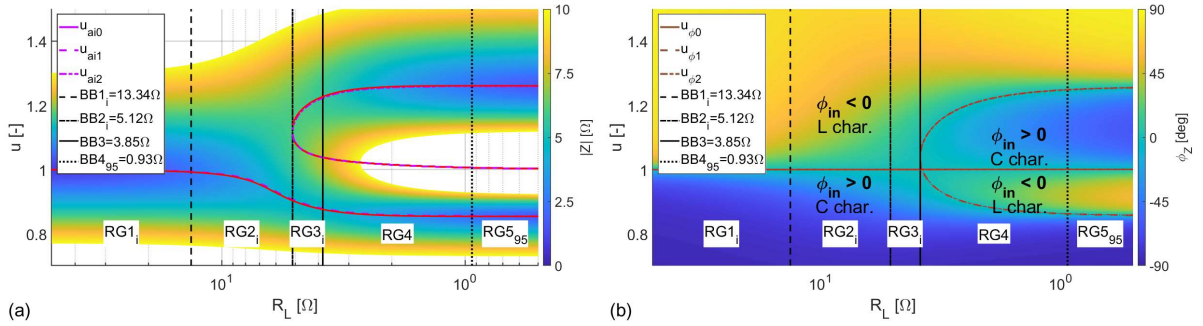

Fig. 51: Input impedance $\hat{Z}$ in the diagram section along a trajectory of decreasing R_L. a) Comparison of its amplitude Z local extrema obtained numerically (red) with IAB frequencies from general parameter model (purple). The background shows a colormap of Z. (b) Comparison of its phase φ_{in} zero-crossing frequencies obtained numerically (red) with PB frequencies from general parameter model (brown). The background shows a colormap of φ_{in} with marked inductive (L char.) and capacitive regions (C char.).

7.4.2 OAB Mechanism

Similarly, as the interactions resulting in IAB and PB were examined, also the interactions resulting in OAB can be examined. The aim is to explain the OAB mechanism and the shift between the IAB and OAB frequencies depicted in Fig. 32. The analysis follows the process of expressing the output power P_{out} as a function of impedance (69) described in Chapter 6.3.1 Normalization Procedure.

The analysis is illustrated by Fig. 52 and Fig. 53, which besides the evaluated quantity (e.g., I_{in}) depict its maxima (solid line) or minima (dashed line). The positions of local extrema were obtained numerically from the equivalent circuit model summarized in Table 4. The transition from IAB to OAB is illustrated by the changing position of each quantity's local extrema with respect to the boundaries $BB1_i$, $BB2_i$ (purple) and $BB1_o$, $BB2_o$ (black) boundaries.

The process starts with the calculation of the input current $\hat{I}_{in}$ from input impedance $\hat{Z}$ as $\frac{V_{in}}{\hat{Z}}$ (65). The frequencies of its amplitude local extrema remain unchanged with respect to the IAB frequencies (see Fig. 52).

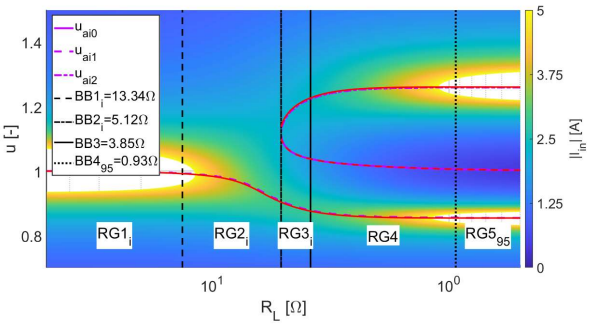

Fig. 52: Input current amplitude I_{in} in the diagram section along a trajectory of decreasing R_L. Comparison of its local extrema obtained numerically (red) with IAB frequencies from general parameter model (purple). The background shows a colormap of I_{in}.

The induced voltage in the secondary $\hat{V}_{is}$ is calculated as a product of $\hat{I}_{in}$ with $j\omega M$ (66)). Because ωM is not constant along the normalized frequency u, the $\hat{I}_{in}$ is amplified unevenly and the local extrema of its amplitude I_{in} shift with respect to the IAB frequencies (see Fig. 53 (a)). As the $\hat{I}_{in}$ is the reference, the phase shift of $\hat{V}_{is}$ is given by j and thus it is equal to a constant 90°.

The output current $\hat{I}_{out}$ is obtained as a ratio of $\hat{V}_{is}$ and $\hat{Z}_s$ (67). When two complex numbers are multiplied their magnitudes are multiplied and arguments added. Thus, its amplitude I_{out} is calculated as a product of V_{is} and inverted Z_s. Because inverted Z_s is not constant along the normalized frequency, resulting I_{out} is amplified unevenly and its local extrema shift with respect to V_{is} – they match the OAB frequencies (see Fig. 53 (b)). The phase of $\hat{I}_{out}$ is the sum of 90° of the $\hat{V}_{is}$ argument and value in range of -90° to 90° of the inverted $\hat{Z}_s$. This is the phase shift between the primary and secondary side due to the coil orientation, which is described in the Chapter 3.2.2 Voltages and Currents.

The output voltage $\hat{V}_{out}$ is a product of $\hat{I}_{out}$ and R_L (68). Because R_L changes only along the observed trajectory and it remains constant along the frequency sweep, the values of its amplitude V_{out} local extrema remain constant. The difference between I_{out} and V_{out} is that while I_{out} gains high absolute values for small R_L as inverted Z_s grows with decreasing R_L, the behavior of V_{out} is the opposite – its absolute values grow with R_L.

Since the load impedance is real, the output power P_{out} can be expressed as the magnitude of the product of I_{out} and V_{out} amplitudes (69), as both I_{out} and V_{out} have the same phase. Even though I_{out} and V_{out} change along the frequency sweep, the position of their local extrema is the same. Therefore, the local extrema of resulting P_{out} remains unchanged, forming the OAB frequencies (see Fig. 53 (c)).

Also, the input power P_{in} was examined, which is calculated as a product of the input current amplitude I_{in} and the sum of reflected resistance R_r (real part of $\hat{Z}_r$) and constant R_p (108):

$$P_{in} = \frac{1}{2} I_{in}^2 (R_r + R_p) \tag{108}$$

Over a frequency sweep, the values of R_r and I_{in} vary such that the resulting P_{in} local extrema match the OAB frequencies (not the IAB frequencies), as it can be seen in Fig. 53 (d).

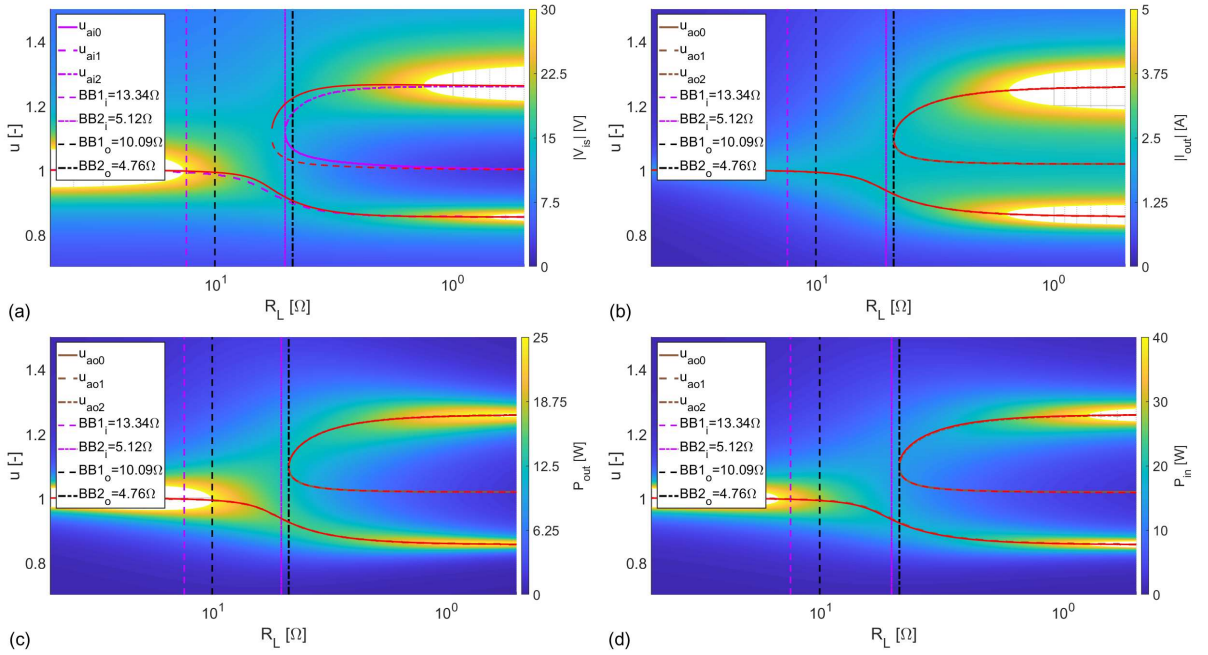

Fig. 53: OAB mechanism analysis shown in diagram sections along a trajectory of decreasing R_L. Numerically obtained local extrema (red) are compared with IAB (purple) or OAB (brown) frequencies calculated from general parameter model for: a) amplitude of the induced voltage in the secondary V_{is} (compared with IAB), (b) output current amplitude I_{out} (OAB), (c) output power P_{out} (OAB), and (d) input active power P_{in} (IAB). Each diagram contains a colormap of an evaluated quantity in the background.

7.5 Influence of Primary and Secondary ESRs

The general parameter model is based on the normalization presented in [17], which assumes a lossless IPT system (the ESRs R_p and R_s are not considered). In this section, the general parameter model (lossless) is compared with the circuit parameter model (with loss included) to examine how accurately the general parameter model predicts the boundary values of bifurcation. This analysis was presented in [20].

The influence of R_p and R_s is evaluated on the bifurcation boundaries of IAB ($BB1_i$, $BB2_i$), OAB ($BB1_o$, $BB2_o$) and PB (BB3) for R_p and R_s for the trajectory of decreasing R_L. The R_L values are examined, at which the trajectory crosses the boundaries. The analysis is performed for the measured system with parameters in Table 4 except R_p, R_s and M. The boundary values of R_L calculated from the general parameter model for lossless system (i.e., $R_p = 0$ and $R_s = 0$) are compared with the numerically obtained boundary values of R_L for R_p of 0.327 Ω, 1 Ω, 2 Ω and R_s of 0.317 Ω, 1 Ω, 2 Ω (first two values correspond with R_p, R_s of the measured system). These correspond with the coil quality factors Q of 57.6, 18.8 and 9.4 for the primary side and 34.9, 11.1 and 5.5 for the secondary side. The coupling coefficient k (L_p and L_s remain constant, while M changes) is varied over an interval from 0.01 to 0.99 and R_L values of the boundaries are plotted in Fig. 54 and Fig. 55. The black line $k_{meas} = 0.37$ in the figures marks k of the measured system in Table 4, and thus the trajectory at which PB, OAB and IAB was evaluated in previous chapters. The influence R_p and R_s is examined separately, if one is examined, the other is equal to 0.

The influence of R_s is clear from the defining equation of the reflected impedance $\hat{Z}_r$ (11) – R_s is added to the equivalent load resistance R_L. From the perspective of bifurcation, it is not important whether the specific $\hat{Z}_r$ value is obtained by high value of R_L and the small R_s, or vice versa – the resulting $\hat{Z}_r$ influence is the same in both cases. Thus, the boundary value of R_L is decreased by presence of R_s (see Fig. 54 for the OAB and PB boundaries) – if $R_s + R_L$ calculated from the general parameter model is 4.76 Ω for $BB2_o$ and R_s is 1 Ω, the actual value of R_L at which OAB occurs is 3.76 Ω.

Because R_s directly impacts $\hat{Z}_r$, it affects all of the IAB, OAB and PB boundaries, in such a way that it decreases the R_L value of the boundary. This is especially significant for $BB2_o$, BB3 and $BB4_{95}$, as they correspond with smaller R_L values. If the R_s value is high enough, and the coupling coefficient low enough, it may prevent some of the bifurcation phenomena to occur (e.g., PB described by BB3 for $k < 0.1$ and $R_s = 1\Omega$) – even if R_L goes to zero, the operating point following the trajectory does not reach the boundary.

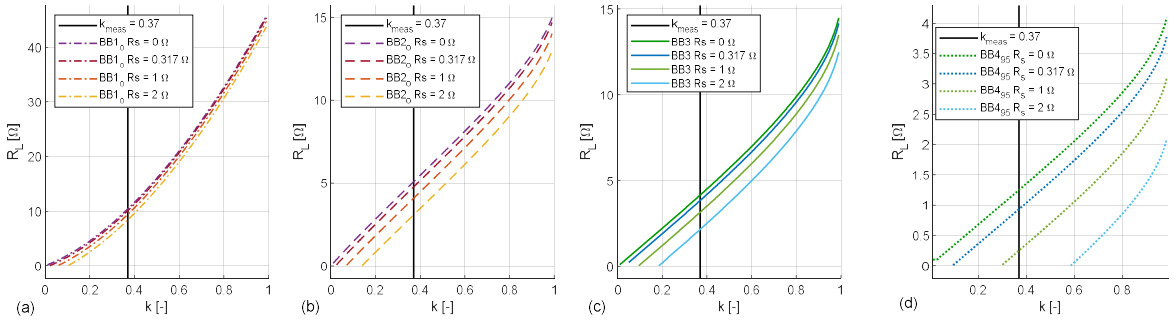

Fig. 54: Influence of R_s on the R_L value of the bifurcation boundaries (a) $BB1_o$, (b) $BB2_o$, (c) BB3 and $BB4_{95}$. Black line marks the k value of the trajectory examined in the previous sections. Published by author in [20].

For these reasons, R_s was incorporated by lumping it with R_L in $R_{sL} = R_L + R_s$ (40) in the Q_{Lp} and Q_{Ls} calculations in Chapter 6.1 describing the methodology of the general parameter model. Consequently, Q_{Lp} and Q_{Ls} calculations then shift from (37) to (41).

The influence of R_p on bifurcation is more complicated. It impacts the input phase value according to (106), but it does not affect the position of the zero crossing of the phase – this is solely given by the sum of X_p and X_r, in which X_r always has the opposite polarity to X_p. Thus, R_p does not impact PB boundaries BB3 or BB4.

However, R_p does affect the local extrema of the input impedance amplitude Z. The amplitude Z is given by (107), where R_p affects the term $(R_p + R_r)^2$, where R_r is the reflected resistance calculated as (13). If $R_p = 0$, then this term equals R_r^2 and the positions of the local extrema of Z are given by the IAB frequencies calculated from the general parameter model. However, for $R_p > 0$, the term is given by $R_p^2 + 2R_pR_r + R_r^2$. The additional R_p^2 is constant, thus it does not affect the position of local extrema, but $2R_pR_r$ varies with $\hat{Z}_r$, and thus it shifts the position of the local extrema of Z and consequently of P_{out} with respect to the case of $R_p = 0$.

Fig. 55 shows the impacts of R_p on the IAB and OAB frequencies, respectively. R_p has almost no impact on $BB2_i$ and $BB2_o$ (except for low k), but it has a significant impact on both $BB1_i$ and $BB1_o$, which intensifies with increasing k. In the case of $BB1_i$, R_p increases the R_L value of the boundary, but on the contrary, it decreases the R_L value for $BB1_o$. The high impact of R_p on $BB1_i$, smaller impact on $BB1_o$ and minimal impact on $BB2_i$ and $BB2_o$ is due to the fact that R_p is compared to the reflected resistance R_r in (107): Both $BB1_i$ and $BB1_o$ are connected with the small values of $\hat{Z}_r$ and thus small values R_r (e.g. 2.09 Ω and 2.74 Ω, respectively for k = 0.37 and $f = f_0$), thus R_p influence is more pronounced. On the other hand, the value of R_r is higher at $BB2_i$ and $BB2_o$ (e.g., 5.25 Ω and 6.85 Ω, respectively for k = 0.37 and $f = f_0$), consequently the influence of R_p is much smaller.

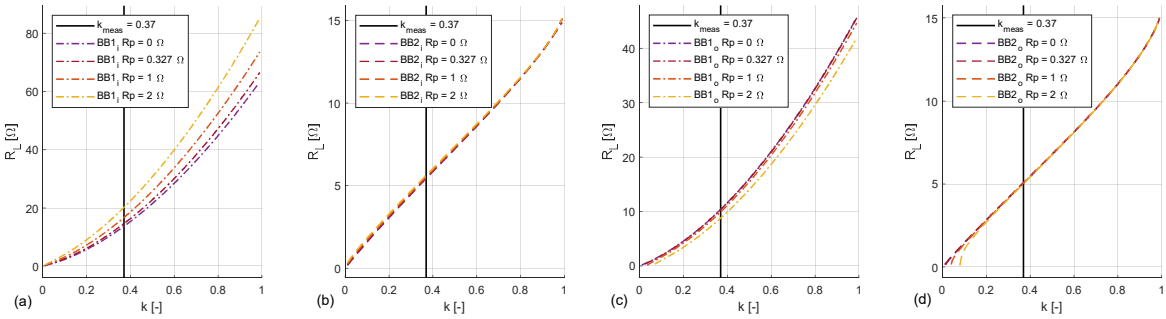

Fig. 55: Influence of R_p on the R_L value of the bifurcation boundaries (a) $BB1_i$, (b) $BB2_i$, (c) $BB1_o$ and (d) $BB2_o$. Black line marks the k value of the trajectory examined in the previous sections. Published by author in [20].

As it is explained in the following chapter, the optimal operating area is near the $BB2_o$ boundary. Therefore, R_s must be considered, as it has the same effects on all of the boundaries and thus it impacts the area of interest near $BB2_o$. On the other hand, R_p impacts primarily the boundaries $BB1_i$ and $BB1_o$, only slightly $BB2_i$ and $BB2_o$ and not at all BB3, thus it can be neglected. This is contributed by fact the coils used for IPT are required to have high quality factor [128], thus only the low-loss case of $R_p = 0.327$ Ω ($Q = 57.6$) corresponds to a coil that would be used in realistic, commercial application.

7.6 Bifurcation Analysis Summary

In this chapter, the bifurcation phenomena were analyzed. The discussion of the bifurcation frequencies in the 2D Q_L state diagram illustrated their behavior outlined in Chapter 6, such as emergence of bifurcation phenomena at their respective boundaries, stabilization of the frequencies at their asymptotes in the region $\mathrm{RG5}_{95}$ and other.

Analysis of the influence of the circuit parameters L_p, L_s, M, f_0 and R_L showed that change of any of these parameters may cause bifurcation. While growing L_s, M or f_0 move the operating point in direction of the increasing bifurcation phenomena, growth of R_L or L_p moves the operating point in the opposite direction. The distinction between the independent and coupled parameters was discussed, with ways to evaluate the influence of a set of coupled parameters on the operating point movement.

Based on these findings, the rules for construction of the operating trajectories and operating areas were developed, together with examining their movement due to a parameter change. Both operating trajectories and areas are useful for evaluating the system regulation and the bifurcation control methods. Operating areas can be also employed in evaluating the design tolerances (e.g., variable coupling between the coils and variable load).

The mechanism of bifurcation was examined for the R_L trajectory. At first, it was analyzed how the change of R_L causes PB and IAB and then how these changes result in OAB.

In the last part of the chapter, the influence of ESRs R_p and R_s on the bifurcation boundaries was discussed. The results showed that R_s impacts all the boundaries and for BB3 and $\mathrm{BB4}_{95}$ it can become significant, thus it is lumped with R_L into the adjusted load resistance R_{sL}. On the other hand, R_p can be neglected, because it does not impact the PB boundaries and its influence on IAB or OAB is small.

The presented findings were published in [20], [183], [186].

8 Impacts of Bifurcation on Device Design and Operation

The bifurcation phenomena must be always considered in system operation and either avoided or, in some cases, used advantageously for the device regulation or parameter estimation. In the first part of this chapter, the selection of the operating area is analyzed in the context of the course of bifurcation and in the second part the bifurcation impacts on the device regulation are examined. This is not an exhaustive summary, but only an outline of the main points. Both of these analyses were presented in [20]. The frequency response of an IPT system operating in the region $RG5_{99}$ (deep bifurcation) can be used to estimate the coupling coefficient k, as described in the third part of the chapter. This estimation method was published in [187].

8.1 Selecting the Operating Area

The operating area is examined, because the typical IPT system employs some form of regulation and consequently, its operating point is not constant. There are guidelines to select the optimal operating area (e.g. [188] focusing on maximizing the output power and efficiency), but they do not explicitly focus on its connection with PB or OAB.

The operating area selection is evaluated from the perspective of the transformer efficiency η_{tr}, the input phase φ_{in} due to its importance to zero-voltage switching (ZVS) and of the output power P_{out}. Resulting operating area is general; however, it is always necessary to consider the specific requirements of the IPT system and its regulation, due to which a different part of the course of bifurcation may be more convenient. All the figures in this chapter depict the quantities calculated from the circuit parameters in Table 4, if not stated otherwise.

8.1.1 Efficiency of IPT Transformer

High efficiency is the priority of the modern device design. To understand its connection with bifurcation, the efficiencies of the primary and secondary sides of the IPT transformer must be examined separately at first, and then the outcomes can be combined to calculate the overall efficiency of the IPT transformer, which was derived in Chapter 3.2.3.

To examine the influence of bifurcation let us look at the primary efficiency η_p (25), the secondary efficiency η_s (28), and the overall transformer efficiency η_{tr} (34) along the R_L trajectory. Table 23 contains their calculated and measured values for the R_L values of the measured frequency responses (FR) in Fig. 23. The values are for the resonance frequency f_0. As R_L decreases, the primary efficiency η_p grows due to increasing R_R (see Fig. 50 (a), (26)). However, decreasing R_L diminishes the secondary efficiency η_s (30). As the transformer efficiency η_{tr} is the product of η_p, η_s, it gains its highest value in the $RG2_o$ region near the boundary $BB2_o$ (see Fig. 56), where both η_p and η_s are relatively high and then η_{tr} decreases in both directions. In the case of the trajectories of the other circuit parameters (e.g., mutual inductance M, which corresponds with k for L_p, L_s = const.), the efficiency η_{tr} only grows with increasing R_r, as constant R_L results in constant η_s.

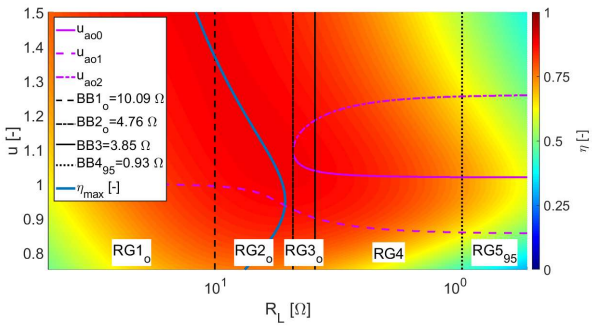

Fig. 56: IPT transformer efficiency η_{tr} in the diagram section along a trajectory of decreasing R_L. Thick blue line marks the R_L position of the efficiency maximum for given normalized frequency u. OAB frequencies (purple) are shown for comparison.

Table 23: Primary (η_p), secondary (η_s), and overall transformer (η_{tr}) efficiency at f_0 for frequency responses in Fig. 23.

		Calculated			Measured		
FR	R_L [Ω]	η_p [%]	η_s [%]	η_{tr} [%]	η_p [%]	η_s [%]	η_{tr} [%]
R_{LA}	31.77	73.3	98.7	72.4	76.6	97.6	74.8
R_{LB}	8.60	90.7	96.7	87.7	92.7	96.8	89.8
R_{LC}	5.15	94.2	94.5	89.0	95.4	95.0	90.6
R_{LD}	4.25	95.0	93.4	88.7	95.7	93.3	89.3
R_{LE}	2.39	97.0	88.8	86.1	95.5	88.0	84.0
R_{LF}	0.91	98.6	75.3	74.2	92.1	72.4	66.6

The R_L value at which the transformer efficiency η_{tr} is maximal, can be calculated from the 1st derivative of η_{tr} (34) with respect to R_L, set equal to 0 (109):

$$\frac{\partial \eta_{tr}}{\partial R_L} = 0 \tag{109}$$

If the other circuit parameters are constant, the resulting root $R_{L,\eta}$ (110) is a function of the operating frequency f, as the blue line shows in the Fig. 56:

$$R_{L,\eta} = \frac{\sqrt{\omega^4 C_S^2 (R_p L_S^2 + R_S M^2) + \omega^2 C_S R_p (C_S R_S^2 - 2L_S) + R_p}}{\omega C_S \sqrt{R_p}} \tag{110}$$

Thus, from the perspective of the maximal efficiency, the region $\mathrm{RG2_o}$ near the boundary $\mathrm{BB2_o}$ is optimal for the IPT system operation close to u_0 ($R_{L,\eta}$ = 5.27 Ω for u_0). In the measured frequency responses, R_{LC} = 5.15 Ω approximately corresponds with the ideal $R_{L,\eta}$ for f_0. Its calculated transformer efficiency η_{tr} for f_0 is 89 % and measured is 90.6 %. The lower efficiency η_{tr} is caused by the rather low coil quality factors (primary Q is 57.6 and secondary Q is 34.9) due to the measurement setup specifics described in Chapter 4. (Note that the existing IPT systems have similar efficiencies (e.g., tables I. and II. in [128]); however, these are efficiencies of the whole system, not only the IPT transformer.)

This analysis shows that reflected impedance $\hat{Z}_r$ impacts the efficiency η_{tr}. For the efficient power transfer, there must be a significant value of R_r, such that the primary efficiency η_p is high. However, R_r cannot be increased at will because PB could occur with its adverse effects on the input phase (discussed in the following chapter) and if R_r grows due to decreasing R_L, the secondary efficiency η_s would drop.

8.1.2 Input Impedance Phase

Many IPT systems employ a zero-voltage switching (ZVS) inverter to power the primary side [95], [97], [98]. ZVS requires a load with a slight inductive character [95], [189], thus tuned IPT systems with fixed frequency are typically operated slightly above the resonance frequency f_0. Therefore, besides η_{tr} a designer must evaluate the input phase φ_{in}. Fig. 57 illustrates with a diagram section how R_L impacts the input phase φ_{in}. Fig. 57 shows that over the course of bifurcation of decreasing R_L the phase transition between the capacitive and inductive regions is very sharp in the region $\mathrm{RG1_o}$, but the transition rate gradually decreases and flattens near f_0 ($u = 1$) as R_L moves towards the PB boundary BB3. This flattening is especially significant in the region $\mathrm{RG3_o}$ until R_L reaches BB3 – this is also illustrated by the frequency response for R_{LD} = 4.25 Ω in Fig. 23 (a).

IPT systems typically operate slightly above f_0 to achieve ZVS [190]. If the operating point of such a system crosses the boundary BB3, then the input impedance $\hat{Z}$ changes its character from the inductive to capacitive, which results in additional switching losses. This could be avoided by increasing the operating frequency f, thus the operating point would move above but close to $u_{\varphi 2}$ (where the input phase φ_{in} still has an inductive character). However, this requires a variable frequency controller with input phase feedback. Thus, it is more convenient to select an operating point with some margin from the boundary BB3 to prevent such a change in φ_{in}.

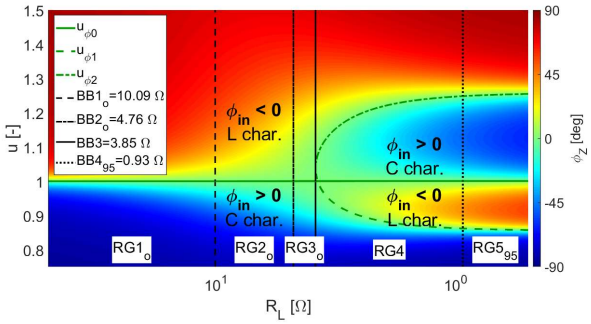

Fig. 57: Input phase φ_{in} in the diagram section along a trajectory of decreasing R_L. The areas with inductive (L char.) and capacitive (C char.) character of input impedance are marked in the colormap.

8.1.3 Achieving the Required Output Power

In the contradiction to the transformer efficiency η_{tr}, the output power P_{out} (see Fig. 58 (a)) is maximal in region $\mathrm{RG1_o}$ at u_{ao1} and in region RG4 at u_{ao1}, u_{ao2}. The higher P_{out} is caused by higher input current amplitude I_{in} (see Fig. 58 (b)) in these regions. The comparison of diagram sections for P_{out} and I_{in} shows, that there are multiple ways to achieve the required value of P_{out}. It can be achieved either by high I_{in} (regions $\mathrm{RG1_o}$, RG4) or by high V_{in} (regions $\mathrm{RG2_o}$, $\mathrm{RG3_o}$). This is illustrated on the following example:

Let us say that the IPT transformer of the measurement setup in Chapter 4 is supposed to supply P_{out} = 1 kW to the load, either by operation in the region $\mathrm{RG1_o}$ at R_{LA} = 31.77 Ω, near boundary $\mathrm{BB2_o}$ at R_{LC} = 5.15 Ω or in region $\mathrm{RG5_{95}}$ at R_{LF} = 0.91 Ω. At 31.77 Ω the system works at high I_{in} and V_{out}, while V_{in} and I_{out} are relatively small (see Table 24 with listed effective values of voltages and currents, the efficiencies are listed in Table 23). In the case of 5.15 Ω, the voltages and currents are more evenly distributed between both sides of the IPT system. The IPT transformer has rated current of 15A and rated voltage of 500 V for the coils. Thus, as it is visible from Table 24 and Table 25 (again effective values), operation at R_{LA} would exceed the current and voltage ratings of the primary side, while the operation at R_{LC} utilizes the IPT transformer well, without exceeding its ratings. Situation at 0.91 Ω is the opposite to R_{LA} = 31.77 Ω: I_{in} and V_{out} are small, while V_{in} and I_{out} are high and total losses are increased in comparison with R_{LC}. Accordingly to I_{out}, the voltages at the secondary resonant tank are increased, even though they do not exceed their rating. But I_{out} value coil exceeds the current rating.

Generally, the high current and resulting increased capacitor and coil voltages have impact on the selection of cables for the coils (cross-section, insulation rating) or compensation capacitors (dissipation factor, maximal dV/dt). Thus, besides higher losses the selection of 31.77 Ω as the operating point may result in more expensive and bulkier transmitter.

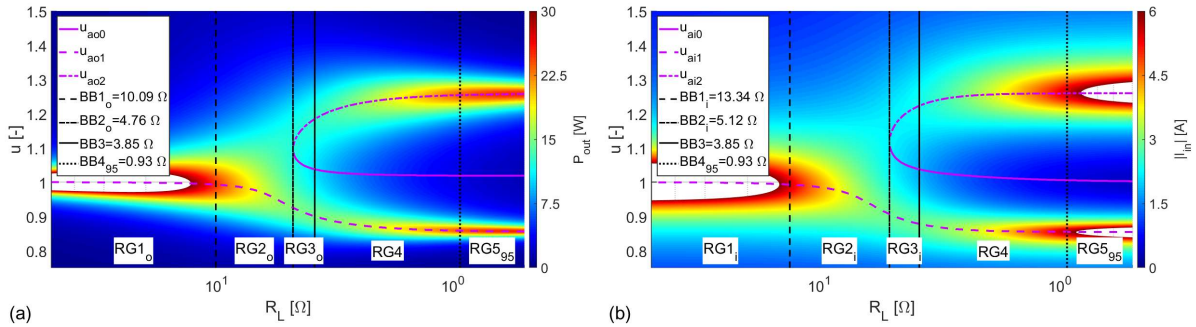

Fig. 58: Output power P_{out} and (b) input current amplitude I_{in} in the diagram section along a trajectory of decreasing R_L.

Table 24: Examples of 1kW output.

		Primary side			Secondary side		Losses		
FR	R_L [Ω]	V_{in} [V]	I_{in} [A]	P_{in} [W]	I_{out} [A]	V_{out} [V]	ΔP_p [W]	ΔP_s [W]	ΔP [W]
R_{LA}	31.77	40.99	33.71	1382	5.61	178.24	372	10	382
R_{LB}	8.60	63.48	18.00	1143	10.78	92.74	106	38	144
R_{LC}	5.15	79.09	14.26	1128	13.93	71.76	67	63	130
R_{LD}	4.25	86.21	13.12	1131	15.34	65.19	56	77	133
R_{LE}	2.39	112.63	10.37	1168	20.46	48.89	35	137	172
R_{LF}	0.91	179.53	7.62	1367	33.15	30.17	19	359	378

Table 25: Capacitor (V_{CCP}, V_{CCS}) and coil (V_{CoilP}, V_{CoilS}) voltages for 1kW output.

		Primary side		Secondary side	
FR	R_L [Ω]	V_{CCP} [V]	V_{CoilP} [V]	V_{CCS} [V]	V_{CoilS} [V]
R_{LA}	31.77	635.15	635.86	62.04	190.41
R_{LB}	8.60	339.26	344.11	119.25	153.18
R_{LC}	5.15	268.78	278.90	154.10	171.90
R_{LD}	4.25	247.17	260.39	169.63	183.52
R_{LE}	2.39	195.37	223.83	226.20	232.88
R_{LF}	0.91	143.51	227.90	366.58	368.83

8.1.4 Selecting the Operating Area Summary

Based on the overall evaluation of η_{tr}, P_{out}, and φ_{in} it is possible to determine the section of the region $\mathrm{RG2_o}$ near the boundary $\mathrm{BB2_o}$ as the optimal area for operation near f_0. Here, the transformer efficiency η_{tr} is maximal. As the required P_{out} level is achieved by higher input voltage and lower current, the requirements laid on the components are lower. However, the input phase φ_{in} is more convenient in region $\mathrm{RG3_o}$, as it is flatter. But near boundary $\mathrm{BB2_o}$ the φ_{in} behavior is still more convenient for ZVS than in the 1st half of region $\mathrm{RG2_o}$ or $\mathrm{RG1_o}$. Also, the position of operating point in region $\mathrm{RG2_o}$ near boundary $\mathrm{BB2_o}$ is more resilient to disturbances in the value of R_L), connected with the movement of operating point across the boundary BB3 resulting in $\varphi_{in} < 0$.

In conclusion, it is necessary to balance the reflected impedance $\hat{Z}_r$ with the primary side impedance $\hat{Z}_p$ to achieve high efficiency η_{tr}, while preventing PB. If the course of bifurcation due to decreasing R_L is examined, it is necessary to balance R_L to achieve high values of both η_p and η_s, as η_p and η_s have the opposite trends with respect to each other. Due to this, the optimal operating area is near the boundary $\mathrm{BB2_o}$ of OAB (its exact position depends on the specific values of R_p, R_s).

8.2 Bifurcation and Regulation

Dynamic variations in the load and mutual inductance can significantly impact the efficiency and output power of an unregulated IPT system without control. Therefore, practical IPT systems employ power control electronics that regulate by dynamically adjusting control variables to meet desired objectives against disturbances [1], [13], [191], [192]. Defining the control problem involves specifying the following electrical quantities.

- **Regulated variables:** Variables that the control system strives to maintain or control in the face of disturbances over the operation of the system. Typical regulated variables include the amplitudes of the output voltage V_{out}, current I_{out}, or power P_{out}, in which the system aims to keep constant. Another example is efficiency η_{tr}, in which the system aims to maximize. Regulated variables are typically monitored to ensure performance objectives are met.
- **System constants:** Fixed system quantities that are constant by design. Typical examples include the self-inductances of the coils (i.e., L_p and L_s), the resistances of the resonators (i.e., R_p and R_s), and the primary and secondary resonant frequencies (i.e., f_{0p} and f_{0s}).

- **System variables:** Dynamic system quantities that can vary over the course of operation. Typical examples include the load impedance (load in Fig. 4), and the mutual coupling (i.e., M for constant L_p and L_s).
- **Control variables:** Circuit parameters, that are continuously adjusted by the control system to meet performance objectives. Typical control variables include the input voltage V_{in} (usually controlled by the DC-DC converter between the grid rectifier and the inverter – see Fig. 4), the AC effective load resistance R_L (usually controlled by an active rectifier or DC-DC converter after the rectifier), the inverter's switching frequency f and the inverter's duty cycle D – see Chapter 2.4.3 Control Methods. The rest of the description is primarily focused on R_L, f and V_{in}.

Typical IPT systems contain a control loop that regulates one of the output quantities: V_{out}, I_{out} or P_{out}. In addition, there can be a second control loop that maximizes the transformer efficiency η_{tr}. Any of the control variables V_{in}, f or R_L may be used in any of the control loops. However, some implementations of the control loop may be more demanding on the regulation infrastructure. For example, high communication speed may be required – especially if the primary side parameters V_{in} or f are used to control the regulated output quantity. If R_L controls the output regulated quantity (V_{out}, I_{out} or P_{out}) and V_{in} or f controls efficiency, communication across the air gap may not be necessary [191].

The diagram sections can be used to conveniently visualize how the individual regulated quantity (I_{out}, V_{out}, or P_{out}) is linked to the transformer efficiency η_{tr} and course of bifurcation, which is useful for design and specifying the valid operational range. This is accomplished by plotting a contour line corresponding to the regulated quantity at the constant rated value on the diagram section. Such diagram section maps for I_{out}, V_{out}, and P_{out} are presented in Fig. 59. The diagram section maps are constructed based on the circuit parameters listed in Table 4 over a range of practical values for R_L and f (or R_L and u, if the operating frequency is normalized). Fig. 59 clearly shows that the regulated output quantities V_{out}, I_{out} or P_{out} are affected not only by decreasing R_L, but also by the bifurcation phenomena. Otherwise shapes of V_{out}, I_{out} or P_{out} curves would correspond with the Z_s amplitude in Fig. 48 (a). The connection between the efficiency η_{tr} and bifurcation was discussed in Chapter 8.1.1 and the η_{tr} maximum corresponding to a given R_L trajectory can be determined using (110).

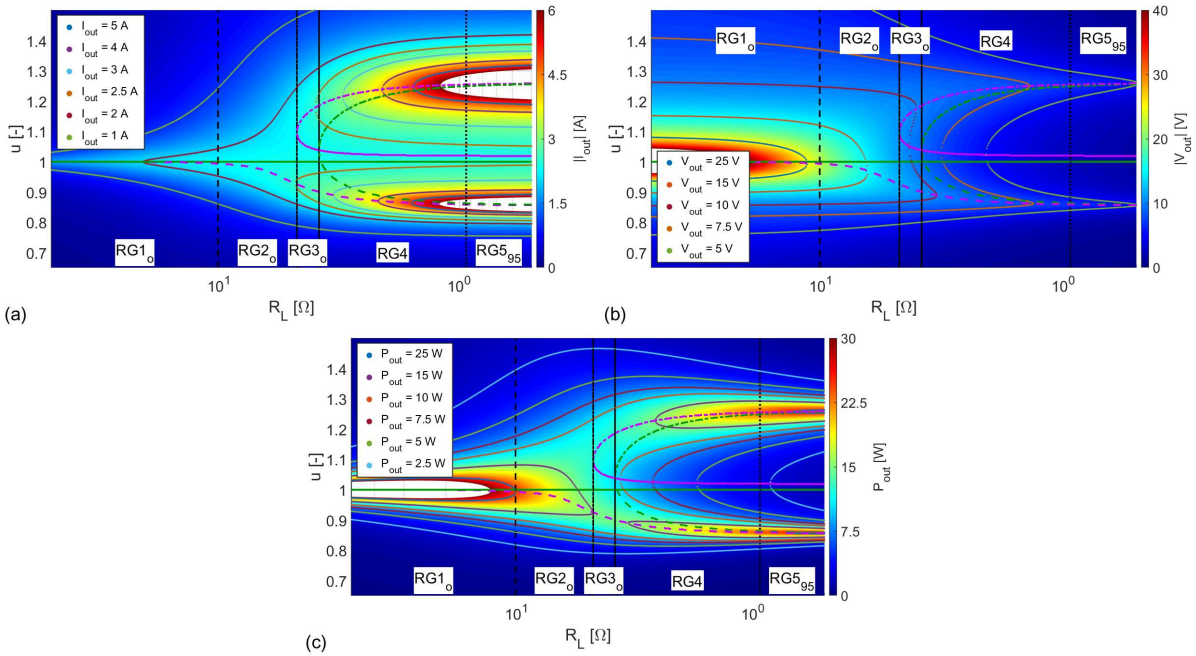

Fig. 59: (a) Output current amplitude I_{out}, (b) output voltage amplitude V_{out} and (c) output power P_{out} with marked amplitude levels in a diagram sections along a trajectory of decreasing R_L. The boundaries $BB1_o$ (dashed), $BB2_o$ (dot-dashed), BB3 (solid) and $BB4_{95}$ (dotted) are marked in black, OAB frequencies u_{ao} (solid), u_{ao1} (dashed) and u_{ao2} (dot-dashed) in purple and PB frequencies $u_{\varphi 0}$ (solid), $u_{\varphi 1}$ (dashed) and $u_{\varphi 2}$ (dot-dashed) in green.

The system is described by the operating point given by R_L and f (or u). Consider the case in which the input voltage amplitude V_{in} is used as the sole control variable. Here, varying V_{in} does not change the position of operating point but scales the amplitude of the whole map (but not the relative amplitudes or gradients). Thus, as the operating point does not move, η_{tr} is unaffected. On the contrary, regulation by f or R_L moves the operating point along a gradient while keeping the amplitude constant. For example, when the operating point moves closer

to u_{ao1}, the output power increases, but this movement also affects the η_{tr}. However, when the coupling coefficient k is high, there seems to be less emphasis on maximizing efficiency since the efficiency is relatively high over a wider range of operating points [12].

8.2.1 Regulation by Frequency Control

Regulation by frequency control is discussed extensively in the Qi standard [12] as a means to regulate the output voltage. The system operating point is typically set above resonance so that decreasing the operating frequency f increases the output voltage V_{out}. As an example, consider the IPT system with parameters listed in Table 26. In this example, there is one control loop that regulates the output voltage V_{out} to be a constant 10 V by adjusting f (control variable) against changes in R_L corresponding with power demands by the load. Fig. 60 presents a plot of P_{out} and R_L versus u for a constant output voltage $V_{out} = 10$ V. The corresponding regulation trajectory is depicted on a diagram section along R_L for V_{out} and P_{out} in Fig. 61 (a) and (b), respectively.

Table 26: Circuit parameters of IPT system for frequency regulation example. Based on system in Table 7 in [12], k set as 0.5 and V_{in} as 10 V

Parameter	Symbol	Value
Input voltage amplitude	V_{in}	10 V
Operating frequency range	f	100-200 kHz
Primary inductance	L_p	25.0 µH
Secondary inductance	L_s	35.0 µH
Load resistance range	R_L	0.1-1000 Ω
Primary resonance frequency	f_{0p}	100 kHz
Secondary resonance frequency	f_{0s}	100 kHz
Coupling coefficient	k	0.5
Primary coil quality factor	Q_p	100
Secondary coil quality factor	Q_s	40

The initial position of the operating point is f = 152 kHz (u = 1.52) and R_L = 24.81 Ω, corresponding to P_{out} = 2 W. To draw more power, the load begins to decrease R_L. As R_L decreases, the controller reacts by decreasing f to keep V_{out} = 10 V. When f crosses f_{ao2} at f = 140.1 kHz (u = 1.401), R_L = 3.953 Ω, P_{out} = 12.65 W, the power required by the load exceeds the P_{out} which the IPT system can supply. The regulation becomes unstable, because under f_{ao} , the output voltage V_{out} decreases with f. According to the control strategy described in [12], the regulator should detect this condition and reset f to its original value. However, after such resetting of f, the regulator again decreases f to increase V_{out} but as V_{out} does not reach its target value, the cycle repeats.

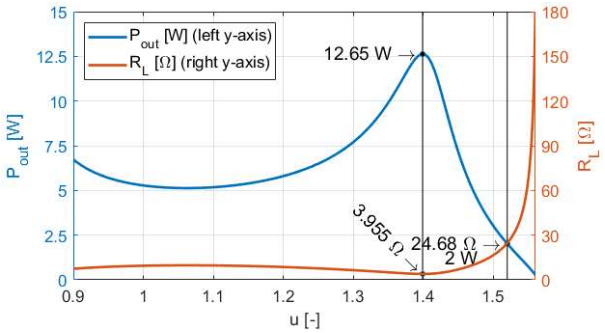

Fig. 60: Output power P_{out} and equivalent load resistance in dependance on the normalized frequency u. Published by author in [20].

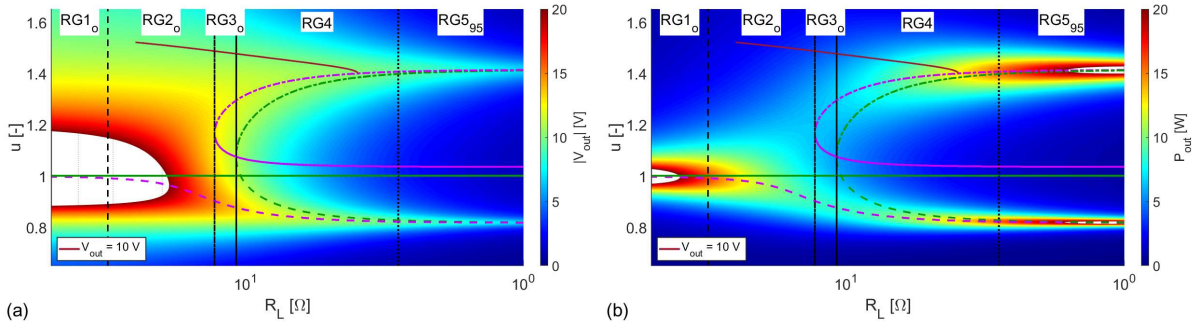

Fig. 61: Trajectory of frequency regulation of CV load. (a) Output voltage amplitude V_{out}, (b) output power P_{out}. Rest of the marked lines corresponds with Fig. 59.

For this example, frequencies f_{ao} (u_{ao1}) and f_{ao2} (u_{ao2}) of the OAB maxima define the limits of stability for frequency regulation. For $f > f_{ao2}$ and $f > f_{ao1}$ the quantities I_{out}, V_{out} and P_{out} grow with decreasing f except over the interval (f_{ao0}, f_{ao2}). In contrast, for frequencies in the interval (f_{ao0}, f_{ao2}) and for $f < f_{ao1}$ they decrease with decreasing f.

The diagram sections such as that shown in Fig. 61 are useful for the regulation analysis, due to the abundance of pertinent information they show. They conveniently depict both the control variable f and system variable R_L in the context of V_{out} which is relevant for the regulator and P_{out} which is relevant for the load power demand. The plots allow a designer to conveniently determine the usable ranges of R_L and P_{out} for a given V_{out} while keeping track of the limits of stability for f regulation (OAB frequencies) as well as the input phase φ_{in} bifurcation represented by the PB frequencies.

The operating range is determined by the choice of input voltage V_{in}, which is a system constant. The diagram sections allow the designer to select a suitable value of V_{in} that meets the frequency and load requirements. For example, Fig. 61 shows that the maximum attainable output power is 12.65 W for the example considered. If a higher output power is required, then the input voltage must be increased.

8.2.2 Regulation by Equivalent Load Resistance Control

Similarly, as with frequency regulation, the equivalent load resistance R_L can be used to regulate the output quantities V_{out}, I_{out} or P_{out} by moving the operating point along a gradient of the output quantity in the diagram section until the regulated quantity reaches its target value. In the following examination, both V_{in} and f are considered constant, while only R_L is employed by regulation. As R_L decreases, the output current amplitude I_{out} always increases (Fig. 59 (a)) while the output voltage amplitude V_{out} always decreases (Fig. 59 (b)). The output amplitude bifurcation (OAB) impacts the V_{out} and I_{out} amplitudes by splitting a single peak into two as $\hat{Z}_r$ grows.

However, as P_{out} is a product of V_{out} and I_{out}, its course along R_L is more complicated. If the evaluation the course of P_{out} starts from high R_L to low R_L outside resonance in Fig. 59 (c), at first, P_{out} grows with decreasing R_L. This is visible from the constant P_{out} lines moving away from each other (i.e., diverging) from the perspective of f (u axis). However, after reaching a certain R_L value, this trend reverses and P_{out} begins to decrease with decreasing R_L. The R_L value of the border between these two areas depends on f and it is heavily affected by bifurcation. This border is a limit of stability for P_{out} regulation by R_L. Selecting a stable operating area for the P_{out} regulation depends on the type of the load – whether it is voltage-driven (P_{out} decreases with growing R_L) or current-driven (P_{out} increase with growing R_L) – as neither of them is stable in the whole diagram section [193]. The P_{out} control is further described in [194].

Besides OAB and its impact on the limits of stability of the f and R_L regulation it is also necessary to consider the impacts of PB on the input phase φ_{in}. If the IPT system employs ZVS (see Chapter 8.1.2), the regulator must be set to avoid the negative φ_{in} regions (see Fig. 57), even though such regions would be convenient for the f or R_L regulation. Intentionally detuning the primary or secondary is another technique to prevent bifurcation for fixed frequency IPT systems and maintain ZVS despite disturbances [100].

8.2.3 Interactions Between Multiple Control Loops

When evaluating the regulation structure using the diagram sections for multiple control loops, it is necessary to consider the mutual interactions of the control loops. Consider V_{in} regulating the transformer efficiency η_{tr} and R_L regulating the P_{out} (voltage tuning in [194]). Even if V_{in} itself does not affect the operating point and thus cannot control η_{tr} directly, it does impact the value of P_{out} at the operating point. A change in P_{out} triggers the R_L regulator, which changes the position operating point to maintain constant P_{out}. The resulting

movement of operating point changes η_{tr}. This process iterates until both of the regulation loops reach their stable equilibriums, or their regulation limits.

8.3 Coupling Coefficient *k* Estimation Method

The bifurcation phenomena can be also advantageously used for the estimation of the coupling coefficient k, as the asymptotes u_{1a} and u_{2a} of the bifurcation frequencies in region RG5 are solely dependent on k. Following method was developed for estimation of k based on the frequency response of the input phase φ_{in}. This estimation method was presented in [187].

By substituting the normalized frequency given by (38), the asymptotesf_{1a} and f_{2a} are calculated from the normalized asymptotes u_{1a} and u_{2a} given by (52) and (53), respectively, as:

$$f_{1a} = \frac{f_0}{\sqrt{1+k}} \tag{111}$$

$$f_{2a} = \frac{f_0}{\sqrt{1-k}} \tag{112}$$

The coupling coefficient k is then obtained from (111) and f_{2a} (112) as:

$$k = \frac{f_{2a}^2 - f_{1a}^2}{f_{2a}^2 + f_{1a}^2} \tag{113}$$

The coupling coefficient k estimation is based on the bifurcation phenomena asymptotes u_{1a} and u_{2a}. However, these cannot be directly measured unlike the bifurcation frequencies (PB, IAB and OAB). Thus, it is necessary to select such an operating point, that these frequencies would approach their respective asymptotes with required tolerance.

For this purpose, the boundary $BB4_{99}$ was established in Chapter 6.2.3. When the operating point passes $BB4_{99}$ into region $RG5_{99}$ (see Fig. 62), all of the bifurcation frequencies match their respective asymptotes with maximal error of 1 % (i.e., real difference between the frequency and its asymptote is 1 % or less).

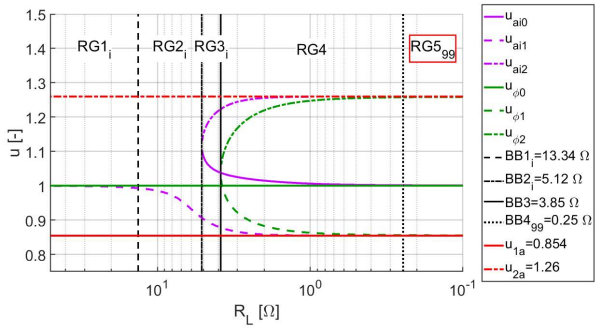

Fig. 62: Region $RG5_{99}$.

In order to use (113), it is necessary to achieve such values of Q_{Lp} and Q_{Ls} that the operating point would move into region $RG5_{99}$. While there are multiple ways to achieve such a change of Q_{Lp} and Q_{Ls} (see Chapter 7.2), minimizing of R_L by short-circuiting the output is the most practical. This limits the method use, as it cannot be employed during the operation. However, it can be employed in such applications where the preliminary or intermittent estimation of k is sufficient – e.g., in stationary charging of EVs. Here the method would be used to verify that the position of an EV with respect to the charging results in sufficiently high k enabling high efficiency of charging – see (1) in Chapter 2.2.2.). In practice, the load could be short circuited using an active rectifier (in which both of the bottom transistors are turned on), through the DC/DC converter between the rectifier and EV battery, or a dedicated switch at the DC side after the rectifier.

The asymptotes f_{1a} and f_{2a} given by (111) and (112), respectively, are common for PB, IAB and OAB frequencies – see Chapter 6.5. Thus, they can be approximated by different means, e.g., from the position of the zero crossings of the input phase φ_{in} (PB), input current amplitude I_{in} maxima (IAB) or output current amplitude I_{in} maxima (OAB). However, it is practical useful to use zero crossings of φ_{in}, because thanks to the known value of φ_{in} and linear character of φ_{in} curve near f_{1a} and f_{2a}, linear approximation can be employed to reduce number of measurement steps, resulting in decreased measurement time.

Note that the issue of coupling coefficient extraction is also important in distributed-element filter design; and, as discussed in [195], an equation identical to (106) is used to characterize coupled RF/microwave resonators based on the splitting of the scattering parameter S_{21}.

8.3.1 Procedure Outline

The method consists of following steps:

1) Short-circuit the output of the IPT system.
2) Find the approximate values of frequencies the f_{1a} and f_{2a} by searching for either zero crossings of φ_{in} or input current amplitude I_{in} maxima with a large step of f.
3) Measure φ_{in} with increased precision (smaller step of f) near the approximated values of f_{1a} and f_{2a}.
4) For each value of f_{1a} and f_{2a} select the frequency of $\varphi_{in} < 0$ and $\varphi_{in} > 0$ nearest to $\varphi_{in} = 0$. Use a linear approximation to calculate the zero-crossing frequency of φ_{in} ($\varphi_{in} = 0$) from the selected frequencies and phases. The obtained frequencies are approximately equal to f_{1a} and f_{2a}.
5) Apply (113) to calculate the coupling coefficient k from the approximated values of f_{1a} and f_{2a}.

The individual steps are examined in further detail in the following discussion.

Because the method is based on measuring the frequency response, a knowledge of a frequency range to examine is necessary. However, this range depends on an unknown k, which determines the values of asymptotes f_{1a} and f_{2a} according to (111) and (112). It is most convenient is to start at f_0, and then extend the search for f_{1a} and f_{2a} both above and below f_0. Therefore, an approximate value of f_0 is the only information about the IPT system required for the method. An IPT system with f_0 of 100 kHz was used for the method verification.

Measurement of the full frequency response with a small step of frequency is time consuming. This could render the method unusable for more dynamic applications. However, because only two frequency values (i.e., f_{1a} and f_{2a}) are required, it is also unnecessary. To reduce the number of steps, two measures were taken.

At first, a rough approximation of frequencies f_{1a} and f_{2a} is generated by employing a large measurement step – in testing of the method a step of 1 kHz was used. In this search, the positions of f_{1a} and f_{2a} in the frequency range can be evaluated based on multiple criteria. For example, if the evaluation is based on the input phase φ_{in}, the positions of f_{1a} and f_{2a} can be localized based on the change of sign of φ_{in}. Frequencies f_{1a} and f_{2a} can be also approximated by searching for the frequencies corresponding to maxima of the input current amplitude I_{in}, as these have the same asymptotes as the ZPA frequencies $f_{\varphi 1}$ and $f_{\varphi 2}$. Or, if the primary side DC link current is measured, the frequencies of its maxima can be used too, as they match I_{in} maxima. In the verification of the presented method, the frequencies of I_{in} maxima were used to generate a first approximation f_{1a} and f_{2a}.

The second measure is to use the linear approximation to find f_{1a} and f_{2a} with increased precision. Fig. 63 shows an example of the frequency response of the input phase φ_{in} for deep bifurcation (i.e., $f_{\varphi 1} \approx f_{1a}$ and $f_{\varphi 2} \approx f_{1a}$) with marked f_0, f_{1a} and f_{2a}. As the figure shows, in the near the ZPA frequencies f_{1a} and f_{2a}, the shape of frequency response φ_{in} is close to linear.

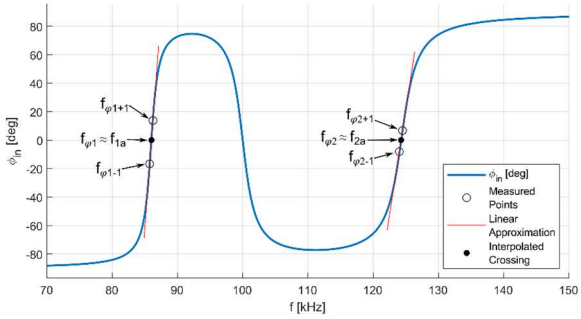

Fig. 63: Frequency response of input phase φ_{in} for the IPT system in deep bifurcation, with marked measured points, linear approximation and interpolated zero crossings. Based on the circuit parameters from Table 27. Presented by author in [187].

Thus, the values of φ_{in} are measured near the approximated values of f_{1a} and f_{2a} obtained in the first step with a smaller frequency step. In the verification of the method, the ±1 kHz surroundings of the approximated frequencies f_{1a} and f_{2a} were measured with a step of 0.5 kHz. From the resulting data series, the frequencies, and phases of the points nearest the zero crossing of φ_{in} are selected for each asymptote: the point f_{ia-1}, φ_{ia-1} with phase below zero and the point f_{ia+1}, φ_{ia+1} with phase above zero. Both points are marked by hollow circles in Fig. 63. From these two points, the values of asymptote frequencies are approximated by:

$$f_{ia} = f_{ia+1} - \frac{f_{ia-1} - f_{ia+1}}{\varphi_{ia-1} - \varphi_{ia+1}} \varphi_{ia+1} \tag{114}$$

The obtained values of f_{1a} and f_{2a} (full circles in Fig. 63) are then used to calculate the coupling coefficient according to (113).

The number of measured frequency points depends on k. For example, if $k = 0.3$ is measured and $f_0 = 100$ kHz, then $f_{1a} = 87.70$ kHz and $f_{2a} = 119.52$ kHz according to (111) and (112), respectively. The first approximation of f_{1a} and f_{2a} with a step of 1 kHz then requires measurement of 34 points and the second refining for the linear approximation requires 10 steps if the ±1 kHz surroundings of frequencies f_{1a} and f_{2a} are measured with a step of 0.5 kHz. In total, 44 points are measured. However, if the method is used to estimate k increasing from a small value (e.g., parking of an EV over a charging station), the number of points can be further reduced by using f_{1a} and f_{2a} estimated from the previous step in the first approximation instead of f_0.

8.3.2 Experimental Verification

The estimates of k provided bifurcation asymptotes method are evaluated with respect to a reference value measured with a calibrated LRC bridge and compared with the results of other active (based on the measurement of currents and voltages) estimation methods. A direct method based on Faraday's law (i.e., measuring the induced electromotive force (EMF)) and the method introduced by Jiwariyavej et al in [196] are used for comparison.

The measured sequence of coupling coefficients used for evaluation of all three estimation methods is described in first part of the chapter. Then, the procedures of the Faraday's law method and Jiwariyavej's method are outlined, and the estimation results are compared with the reference for all three selected methods. In the last part of the chapter, the match to the reference of all three methods is evaluated.

8.3.2.1 Measured Sequence Used for Method Evaluation

The experimental data were measured at the measurement setup described in Chapter 4.1. Only the main oscilloscope in Fig. 17 was used. System parameters are summarized in Table 27. On the contrary to the basic equivalent circuit presented in Chapter 3, the side inductances (e.g., L_p) are divided in the coil inductances (e.g., L_{coil1}) and additional inductances (L_{add1}), which represent the inductance of rest of the circuit for each side. Similarly, the ESRs are also divided between the coil ESRs (e.g., R_{coil1}) and the ESRs of capacitive compensation (e.g., R_{CC}). Resistances of the rest of the circuit are negligible. This division is necessary, because not all of the components of the measurement setup are used in measurement of each method and this has certain impacts on the obtained results, as discussed in the evaluation of the obtained results in Chapter 8.3.2.5.

Table 27: System parameters in the position x = 0 mm.

Parameter	Symbol	Value
Input voltage	V_{in}	5 V
Resonance frequency	f_0	100 kHz
Primary coil inductance	L_{coil1}	28.8 µH
Primary coil ESR	R_{coil1}	0.23 Ω
Primary additional inductance	L_{add1}	0.6 µH
Primary compensation capacitance	C_p	87.4 nF
Primary compensation ESR	R_{CC1}	0.08 Ω
Secondary coil inductance	L_{coil2}	16.7 µH
Secondary coil ESR	R_{coil2}	0.15 Ω
Secondary additional inductance	L_{add2}	0.4 µH
Secondary compensation capacitance	C_s	151.2 nF
Secondary compensation ESR	R_{CC2}	0.20 Ω

Presented method is evaluated together with selected existing methods by estimating the coupling coefficient k during the secondary pad displacement. The same sequence was used in the example for coupled parameters influence described in Chapter 7.2.3. The secondary pad is horizontally moved in the x-axis (see Fig. 41) in the 10 mm steps from the initial position of 0 mm to 200 mm. The step is decreased to 5 mm near the DD pads null position ([60], Fig. 9 (c)).

The coupling coefficient values used as a reference for method evaluation were measured by the following procedure using the calibrated LRC bridge.

1) Both pads are disconnected from the rest of the circuit.
2) The primary coil inductance L_{1a} is measured while the secondary coil is open.
3) The secondary coil is short circuited. The primary inductance is measured again and labeled as L_{1b}. L_{1b} is related to L_{1a} via:

$$L_{1b} = L_{1a}(1 - k^2) \tag{115}$$

4) The coupling coefficient k is then calculated from (115) as:

$$k = \sqrt{1 - \frac{L_{1b}}{L_{1a}}} \tag{116}$$

Fig. 64 depicts the resulting k values in (a) together with the primary and secondary inductances L_1 and L_2 in (b). The figure clearly shows the null point of the DD pads near x = 75 mm. The resulting sequence of k covers the interval of 0.08 to 0.35, which is an aggregated range of k, which the IPT systems presented in SAE J2954 as examples for EV stationary charging gain under displacement [115]. As Fig. 64 (b) shows, the movement of secondary coil changes the coil inductances, which in turn detunes primary and secondary circuits. Impacts of detuning will be discussed for each method individually.

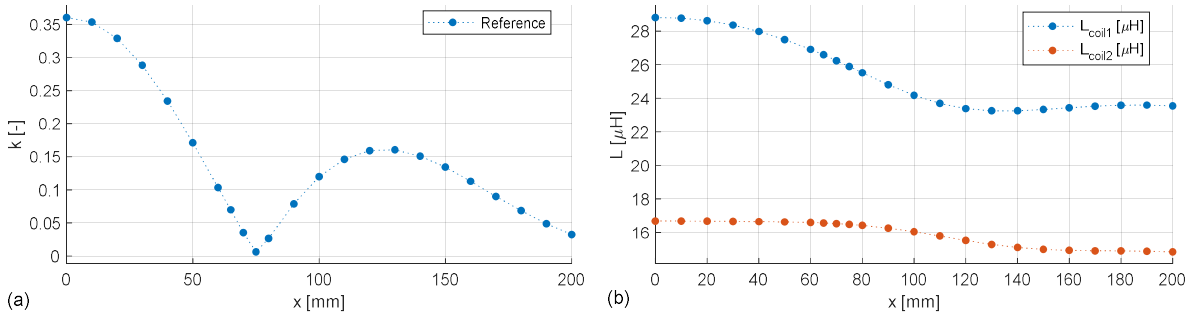

Fig. 64: Reference values for x-axis displacement. (a) Coupling coefficient k. (b) The primary and secondary inductances L_1 and L_2. Presented by author in [187].

The methods for estimating k will be compared with the reference measurement presented in Fig. 64 (a). For each displacement position, the relative error with respect to the reference value will be calculated according to:

$$\Delta k_r = \frac{k_M - k_{ref}}{k_{ref}}[\%] \tag{117}$$

where k_M is the value estimated by the method and k_{ref} is the reference value.

8.3.2.2 Bifurcation Asymptotes Method

The proposed method for estimating k was implemented and tested according to the procedure outlined in Chapter 8.3.1. The method employed the setup shown in Fig. 17 in Chapter 4.1, only the load was short-circuited at its connection point at the secondary switchboard. For each displacement position, the input current amplitude I_{in} was measured with a step size of 1 kHz to find the approximate values of f_{1a} and f_{2a}. These were then refined by measurement of the input phase φ_{in} measured with a step size of 0.5 kHz in interval ±1 kHz around the previously approximated frequencies f_{1a} and f_{2a}, and consequent linear interpolation. The obtained estimates of k "BA 0mm" and "BA AT" are compared in Fig. 65 (a) with the reference "ref". Label "BA 0mm" marks the measurement with the system tuned to $f_0 = 100$ kHz in the initial position x = 0 mm and "BA AT" refers to the measurement with the system was manually tuned by adjusting the primary and secondary capacitances for each misalignment position to $f_0 = 100$ kHz (AT stands for always tuned).

As k decreases less than $k = 0.17$, the relative error becomes positive, and its value increases up to 10%. For k smaller than approximately 0.08, the method fails altogether. However, for most practical systems [115], k is larger than 0.08 (typically, $k > 0.2$ is expected for high efficiency) so the method's breakdown at low values of k is not expected to pose a limitation in practice.

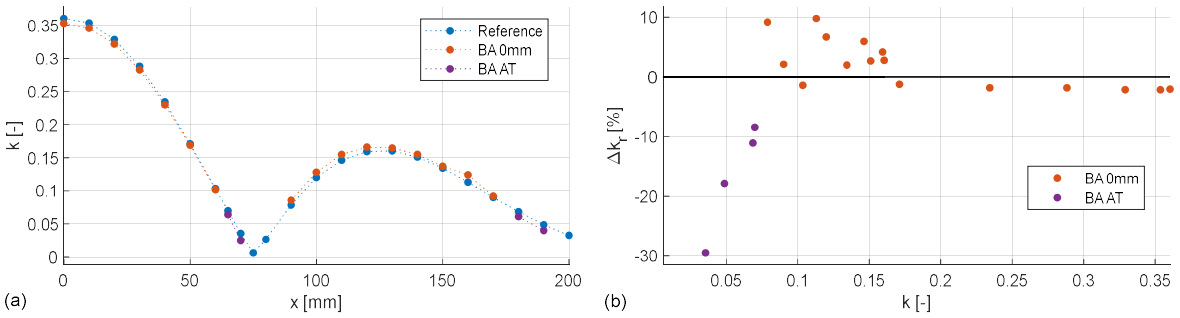

Fig. 65: Bifurcation asymptotes method. (a) Comparison with the reference measurement. (b) Relative error with respect to the reference over k. "BA 0mm" refers to system tuned for x = 0 mm. "BA AT" refers to system tuned for each misalignment position. Presented by author in [187].

The method's failure for low k is primarily caused by detuning. Fig. 66 shows that with increasing displacement the primary resonance frequency f_{0p} increases above the secondary resonance frequency f_{0s}. This detuning alters the frequency response of φ_{in}. Because $f_{0p} > f_{0s}$, the frequency response moves below zero in comparison with the case $f_{0p} = f_{0s}$ – see Fig. 67 (a) for the tuned system and Fig. 67 (b) for the detuned system.

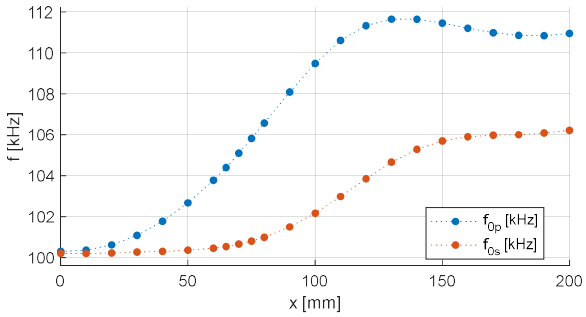

Fig. 66: Detuning of the primary and secondary side. Presented by author in [187].

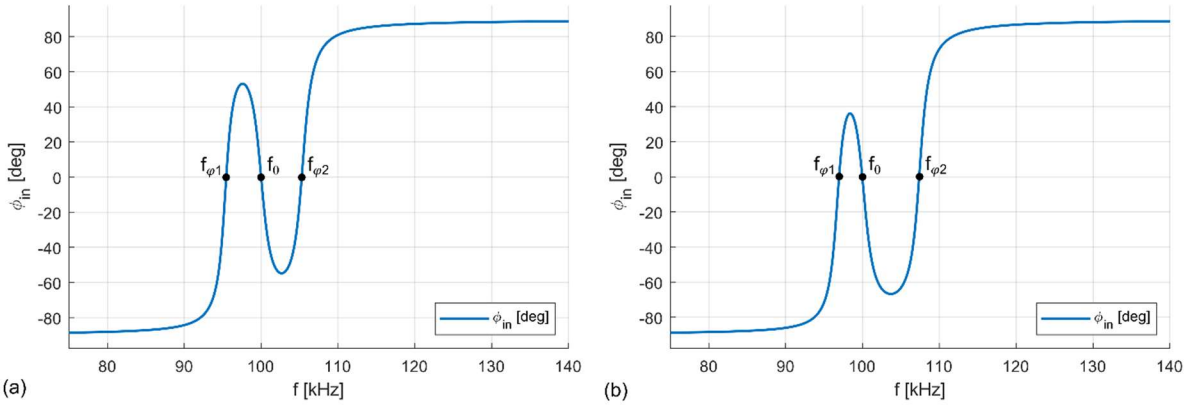

Fig. 67: Frequency response shift due to detuning, illustrated on displacement position of x = 60 mm. (a) Both sides are tuned to $f_0 = 100$ kHz. (b) The side resonance frequencies are given by Fig. 66, i.e., $f_{0p} = 103.27$ kHz and $f_{0s} = 100.13$ kHz. Presented by author in [187].

Under the displacement, the frequency responses change both with detuning and with changing k, as it is illustrated in Fig. 68. In deep bifurcation, the frequency response of φ_{in} is relatively sharp near the zero crossings and it approaches its limiting values of -90° and +90° between the crossings if k is sufficiently high (see Fig. 68 (a) and (b). Thus, the impacts of detuning are smaller for high k, as even with the shift the frequency response resembles a straight line at the zero crossing and can be approximated as a linear function there (see Fig. 68 (b)). However, as k decreases due to displacement, the frequency response curve becomes less pronounced, and it begins to cross zero near its peak, where it does not resemble a straight line (see Fig. 68 (c)). With a further decrease

of k and increase of detuning, former zero crossings are shifted below zero and only single zero crossing occurs – Fig. 68 (d). Thus, for low k and increased detuning, the method fails.

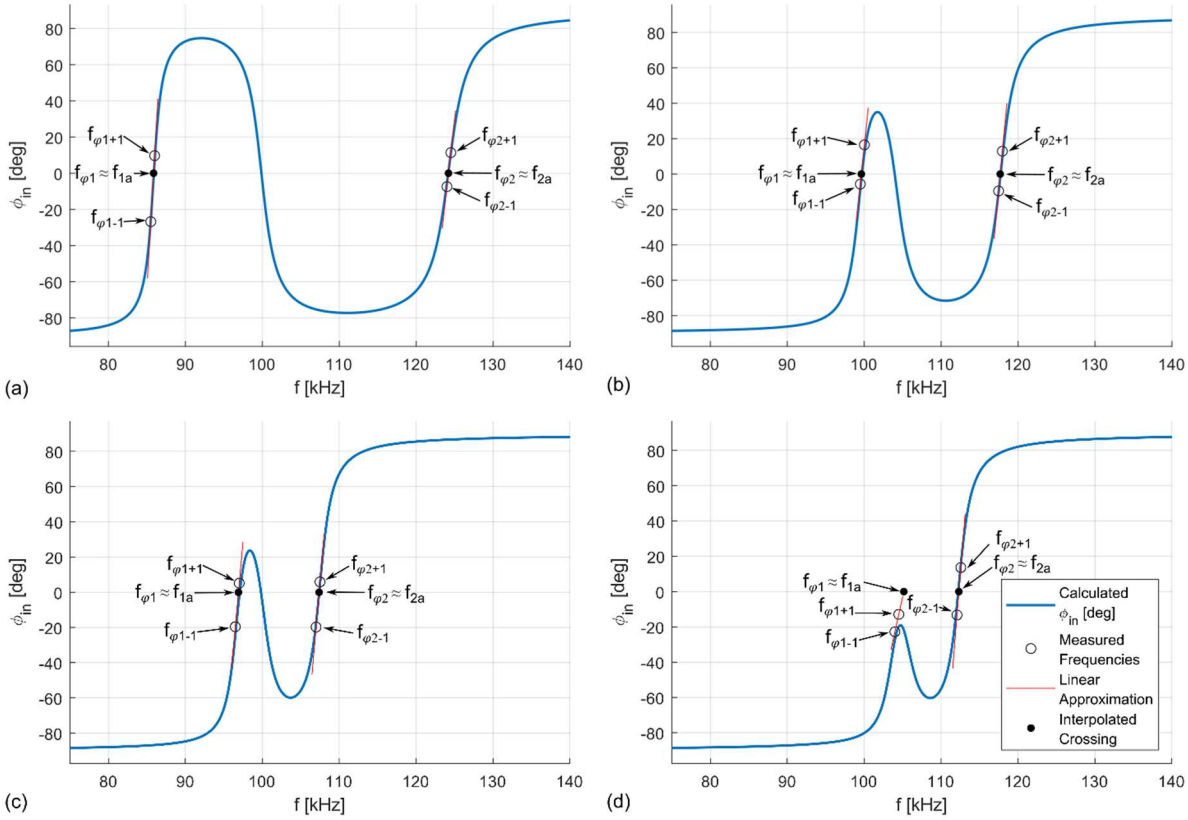

Fig. 68: Influence of detuning on the bifurcation asymptote method. (a) Tuned system (x = 0 mm). (b) Detuned system with medium coupling coefficient k (x = 130 mm). (c) Detuned system with small k (x = 60 mm). (d) Detuned system with very small k (x = 180 mm). The discrepancies between the measured data points and calculated frequency response (especially in (d)) are caused by high sensitivity of frequency responses for low k and influence of the ferrites. Presented by author in [187].

The method's performance for low k can be improved by maintaining the tuned system for specific inductance values under displacement by adjusting the primary and secondary compensation capacitances. The compensation adjustment can be done by e.g., switched capacity, or manually, as in the presented case. Thanks to removing the detuning, it was possible to obtain an approximate value of k in positions 65 mm, 70 mm, 180 mm, 190 mm – see "BA AT" in Fig. 65 (a). However, even though as k decreases the measurement error grows up to 30 %, as shown in Fig. 65 (b). The high error is caused by the fact, that the bifurcation is not deep enough such that frequencies $f_{\varphi1}$ and $f_{\varphi2}$ are not adequately meeting their asymptotes f_{1a} and f_{2a}, respectively. After k decreases under 0.04, not even tuning for specific displacement position could help to achieve any meaningful results.

In the remaining points (75 mm, 80 mm, 200 mm), only one zero crossing of the input phase was measured, even when the measurement step was decreased to 0.25 kHz. This may be caused either because the lack of bifurcation or the measurement step is still too coarse.

In applying the bifurcation asymptotes method, it is necessary to consider the impacts of bifurcation phenomena on the input impedance $\hat{Z}$. When short-circuiting the output, the input impedance is relatively high at f_0 (e.g., $Z = 99.3\ \Omega$ for x = 0 mm). However, near the ZPA frequencies $f_{\varphi1}$ and $f_{\varphi2}$ the impedance is very low (e.g., $Z = 0.73\ \Omega$), which is determined by the ESRs R_p and R_s. Thus, to limit the currents to 5 A to 7 A in the primary side corresponding with the regular operation, the input voltage V_{in} was decreased to 5V when applying the method.

8.3.2.3 Faraday's Law Method

For comparison, another common approach for extracting k was considered. The coupling coefficient k can be estimated by directly measuring the induced EMF in the secondary coil and solving for M using Faraday's law of electromagnetic induction. The adjusted measurement setup is depicted in Fig. 69. Both pads are placed in

their positions. The secondary coil is open, and the primary coil is in series with a resistor and a capacitor, which provide control of the coil current I_1. The primary coil current was limited between 5.8 A and 6.6 A during the measurement process.

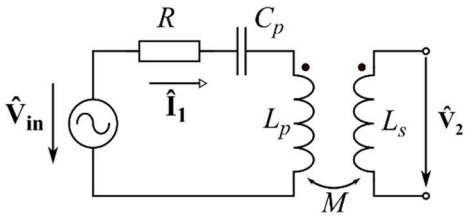

Fig. 69: Faraday's law method measurement setup. Presented by author in [187].

The primary coil is excited with current I_1, which is measured with a precision current shunt. The I_1 value is controlled with a resistor and a capacitor, which reduces the inductive character. The value of I_1 is adjusted to equal the value of I_{in} during regular operation, to consider ferrite saturation and similar effects. The voltage V_2 is measured across the secondary coil terminals, and the mutual inductance M is calculated as:

$$M = \frac{V_2}{\omega I_1} \tag{118}$$

The coupling coefficient k is calculated from M and the measured coil inductances L_1, L_2 according to (39).

The estimated values of k obtained by the Faraday's law method are compared with the reference measurements in Fig. 70 (a). The relative error depicted in Fig. 70 (b), is very low even for low k values. The distribution of error shows, that the method generally estimates k approximately by 1.55 % above the reference. The Faraday's law method is unaffected by detuning.

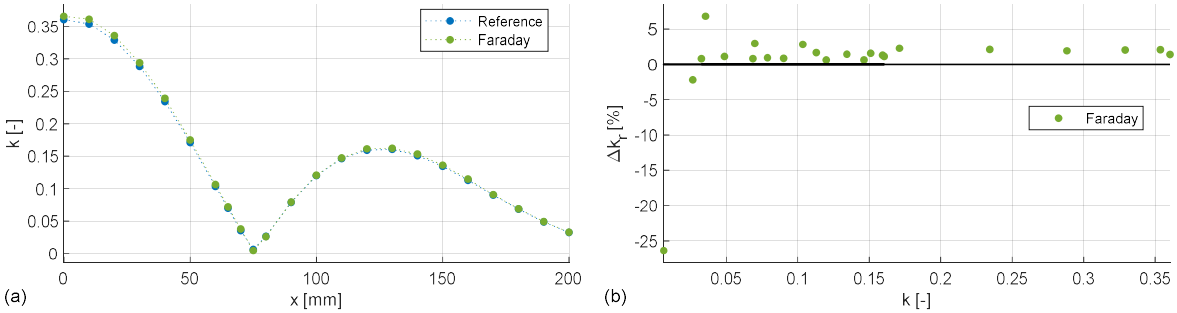

Fig. 70: Method based on the Faraday's law. (a) Comparison with the reference measurement. (b) Relative error with respect to the reference over k. Presented by author in [187].

8.3.2.4 Method of Jiwariyavej

The second method used for comparison was presented by Jiwariyavej et al in [196]. The variant for a single receiver was used. This method does not directly measure k but the mutual inductance M. The calculation of M is based on the equation for the real part of input impedance:

$$Re\{\hat{Z}\} = R_p + (\omega M)^2 \frac{R_L + R_s}{(R_L + R_s)^2 + X_s^2} \tag{119}$$

where X_s is the secondary side reactance:

$$X_s = \omega L_s - \frac{1}{\omega C_s} \tag{120}$$

The mutual inductance M is then calculated as:

$$M = \frac{1}{\omega}\sqrt{\frac{\left(Re\{Z_{in}\} - R_p\right)((R_L + R_s)^2 + X_s^2)}{R_L + R_s}} \tag{121}$$

The real part of input impedance $Re\{Z_{in}\}$ is calculated from the input current and voltage amplitudes I_{in} and V_{in}, respectively, and the input phase:

$$Re\{Z_{in}\} = \frac{V_{in}}{I_{in}} cos\varphi_{in} \tag{122}$$

The coupling coefficient k is then calculated according to (39). Obtaining the value of k according to this method requires preliminary measurement of R_L, R_p, R_s, L_p, L_s, and C_s.

The method was tested using the measurement setup shown in Fig. 17 in Chapter 4.1, with the resistive load set to 31.8 Ω. Due to the higher number of preliminary parameter measurements, the method was measured in reduced number of points. The primary and secondary capacitances were adjusted to keep the system tuned at resonance frequency $f_0 = 100$ kHz against variations in coil inductance that is illustrated in Fig. 64 (b). The specific values of the circuit parameters measured for each displacement position were used to calculate M according to (122) and consequently k according to (39).

Values of k obtained using the method of Jiwariyavej are compared to the reference values in Fig. 71 (a). Besides the plotted values, the method was also applied at displacement of 75 mm, 190 mm, and 200 mm, but did not provide any useful results. Thus, despite tuning for each displacement position, the method of Jiwariyavej suffers a similar limitation for small values of k as the bifurcation asymptote method, which was tuned only for x = 0 mm.

The relative error of the method of Jiwariyavej is depicted in Fig. 71 (b). For high k values (above approximately 0.23), this method exhibits good agreement with the reference. On the other hand, as k is decreased, the error grows significantly and reaches 19.3 % at $k = 0.08$.

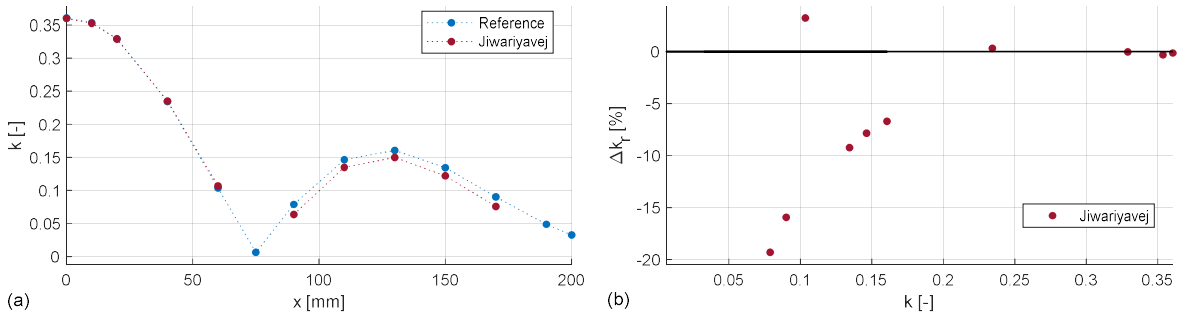

Fig. 71: Method presented by Jiwariyavej in [196]. (a) Comparison with the reference measurement. (b) Relative error with respect to the reference over k.

8.3.2.5 Measurement Comparison

A comparative evaluation of the methods for estimating k is summarized in Fig. 72. Fig. 72 (a) shows how the methods compare directly to the reference and Fig. 72 (b) shows their relative errors.

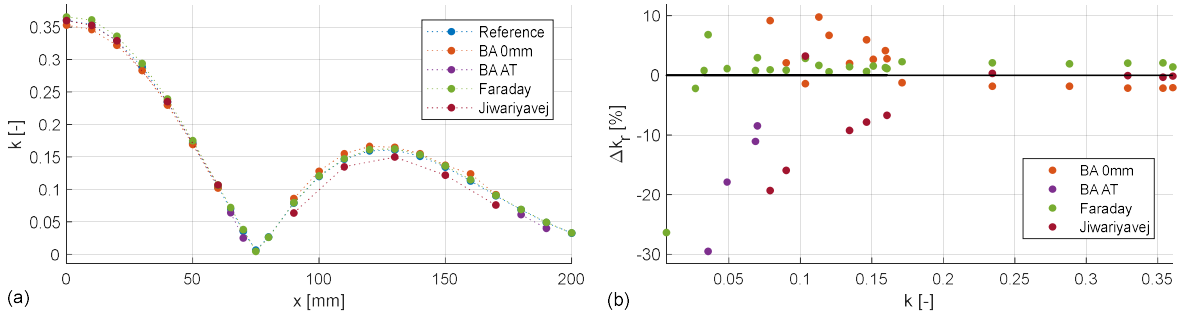

Fig. 72: a) Comparison of all tested estimation methods with the reference. (b) Relative error of the estimation methods with respect to the reference over k.

The evaluation of the methods is divided in two intervals $k \in \langle 0.08, 0.23)$ and $k \in \langle 0.23, 0.36\rangle$ based on the relative error results shown in Fig. 72 (b). The bottom limit of $k = 0.08$ was selected as the final value, at which all three methods yielded a result. Thus, only the bifurcation asymptote method with tuning at x = 0 mm

was evaluated. For each interval, the method is evaluated based on the average error $\overline{\Delta k}_r$ and average absolute error $\left|\overline{\Delta k}_r\right|$, which are calculated as:

$$\overline{\Delta k}_r = \frac{1}{n_M}\sum_{i=1}^{n_M}\Delta k_{r,i} = \frac{1}{n_M}\sum_{i=1}^{n_M}\frac{k_{M,i}-k_{ref,i}}{k_{ref,i}}\,[\%] \tag{123}$$

$$\overline{\Delta k}_r = \frac{1}{n_M}\sum_{i=1}^{n_M}\left|\Delta k_{r,i}\right| = \frac{1}{n_M}\sum_{i=1}^{n_M}\frac{\left|k_{M,i}-k_{ref,i}\right|}{k_{ref,i}}\,[\%] \tag{124}$$

While $\left|\overline{\Delta k}_r\right|$ quantifies the disagreement between the method's results from the reference in the selected interval, $\overline{\Delta k}_r$ describes the shift of the estimate with respect to the reference, i.e., if $\overline{\Delta k}_r \to 0$ then the values are distributed evenly around the reference. The results are summarized in Table 28.

Table 28: Overview of the average relative errors $\overline{\Delta k}_r$ and average absolute errors $\left|\overline{\Delta k}_r\right|$ of the evaluated methods.

Method	$k \in \langle 0.08, 0.23)$	$k \in \langle\, 0.23, 0.36\rangle$	$k \in \langle 0.08, 0.36\rangle$
Bifurcation asymptote method	$\overline{\Delta k}_r = 3.87$ % $\left\|\overline{\Delta k}_r\right\| = 4.36$ %	$\overline{\Delta k}_r = -2.01$ % $\left\|\overline{\Delta k}_r\right\| = 2.01$ %	$\overline{\Delta k}_r = 2.04$ % $\left\|\overline{\Delta k}_r\right\| = 3.62$ %
Faraday's law method	$\overline{\Delta k}_r = 1.39$ % $\left\|\overline{\Delta k}_r\right\| = 1.39$ %	$\overline{\Delta k}_r = 1.91$ % $\left\|\overline{\Delta k}_r\right\| = 1.91$ %	$\overline{\Delta k}_r = 1.55$ % $\left\|\overline{\Delta k}_r\right\| = 1.55$ %
Jiwariyavej's method	$\overline{\Delta k}_r = -9.30$ % $\left\|\overline{\Delta k}_r\right\| = 10.38$ %	$\overline{\Delta k}_r = -0.04$ % $\left\|\overline{\Delta k}_r\right\| = 0.20$ %	$\overline{\Delta k}_r = -5.6$ % $\left\|\overline{\Delta k}_r\right\| = 6.31$ %

All three estimation methods show a good match to the reference for k above 0.23. From these values it is visible, that the Jiwariyavej's method exhibits the best match to the reference ($\left|\overline{\Delta k}_r\right| = 0.20$ %), with the estimates which are distributed evenly around the reference ($\overline{\Delta k}_r = -0.04$ %). The estimates of the method based on the Faraday's law are shifted above the reference ($\overline{\Delta k}_r = 1.91$ %), while the estimates of the bifurcation asymptotes method are shifted below the reference ($\overline{\Delta k}_r = -2.01$ %).

However, with decreasing k all methods except the Faraday's law method decrease in precision (interval $k \in \langle 0.08, 0.23\rangle$). The Faraday's law method is the most accurate ($\left|\overline{\Delta k}_r\right| = 1.39$ %), but its estimates are again shifted above reference ($\overline{\Delta k}_r = 1.39$ %). The second-best method is the bifurcation asymptotes method ($\left|\overline{\Delta k}_r\right| = 4.36$ %) which is now shifted above the reference ($\overline{\Delta k}_r = 3.87$ %). The Jiwariyavej's method performs much worse ($\left|\overline{\Delta k}_r\right| = 10.38$ %) and its value begins to move further below the reference with decreasing k – see Fig. 72 (b), $\overline{\Delta k}_r = -9.30$ %.

Across the whole measured interval of $k \in \langle 0.08, 0.36\rangle$, the Faraday's law method is the most accurate ($\left|\overline{\Delta k}_r\right| = 1.55$ %), followed by the bifurcation asymptote method ($\left|\overline{\Delta k}_r\right| = 3.62$ %) and then Jiwariyavej's method ($\left|\overline{\Delta k}_r\right| = 6.31$ %). The estimates of two first methods are on average shifted above the reference ($\left|\overline{\Delta k}_r\right| = 1.55$ % and $\left|\overline{\Delta k}_r\right| = 3.62$ %, respectively), while the third is shifted below the reference ($\overline{\Delta k}_r = -5.6$ %).

The shifts of the estimates with respect to the reference could be partially explained by the different measurement currents used in each method (see Table 29) and the reference, which was measured with the LRC meter and thus with very small currents. The high currents could result in detuning caused by the dependance of the coil inductances on the currents through the coils and ferrite non-linearity [178], as the ferrites are used as the magnetic cores of the DD pads. This effect could impact especially the Jiwariyavej's method as the primary currents were significantly higher in the second interval.

Table 29: Currents used for the testing of the estimation methods.

Method	I_{in}	I_{out}
Bifurcation asymptote method	5 A to 7 A	5 to 10 A
Faraday's law method	5 A to 7 A	Open
Jiwariyavej's method	4.5 A to 6 A ($k \in \langle 0.23,0.36)$) 10.5 A ($k \in \langle 0.08, 0.23)$)	0.5 A to 1 A ($k \in \langle 0.23,0.36\rangle$) 0.5 A ($k \in \langle 0.08, 0.23)$)

The obtained results are also impacted by the selection of the circuit components used for the measurement of a specific method – whether the measurement used only the coils or the whole measurement setup. The reference measurement measured the coupling coefficient only between the coils, thus the coupling coefficient is given as $M/\sqrt{L_{coil1}L_{coi}}$, where L_{coil1} and L_{coil2} are the coil inductances. On the other hand, the bifurcation asymptotes used the whole circuit, thus also the additional inductances of each side L_{add1} and L_{add1} (i.e., inductances of connecting cables, switchboards, etc.) were included. These inductances do not impact the mutual inductance M, as they do not play any role in the coupling, but they increase inductances of each side ($L_p = L_{coil1} + L_{add1}$, $L_s = L_{coil2} + L_{add2}$) and thus change the position of the operating point in the 2D Q_L state diagram (see Chapter 7.2). Consequently, the obtained value of coupling coefficient is lower in comparison with the reference because it is calculated as $M/\sqrt{L_pL_s}$ instead of $M/\sqrt{L_{coi}\ L_{coil2}}$. The method based on Faraday's Law and Jiwariyavej's method) estimate M instead of k. Thus, the obtained values of M are not impacted by the additional inductances L_{add} or L_{add2}. If the coupling coefficient k is then calculated from the coil inductances L_{coi} and L_{coil}, it matches the reference.

Some of the differences could be also explained as a result of measurement errors due to limited instrument accuracy, loading effects, and environmental factors like temperature, etc.

8.3.3 Evaluation of the Estimation Methods

As evaluated in the previous chapter, the bifurcation asymptote method provides the relatively accurate estimates ($|\overline{\Delta k_r}| = 3.62\%$) across the interval of $k \in \langle 0.08, 0.36\rangle$. However, the estimate precision is not the only consideration for evaluating the usability of the method. Table 30 summarizes some of the practical aspects of all three evaluated methods, which should be also considered.

Table 30: Comparison of the practical aspects of the bifurcation asymptotes method with the selected estimation methods.

Method	Bifurcation Asymptotes Method	Faraday's Law Method	Jiwariyavej's Method [196]
Measured parameter	k	M	M
Use during operation	Intermittent	No	Yes, but only for air-core coils
Required active measurements	f, φ_{in}, I_{in} (optional)	f, I_1 (primary coil current amplitude), V_2 (secondary coil voltage amplitude)	f, I_{in}, V_{in}, φ_{in}
Number of frequency points required	Varies with k	1	1
Required preliminary measurements	None (general knowledge of f_0 to specify measurement range)	None to obtain M, L_p, L_s to obtain k	R_L, R_p, R_s, L_s, and C_s to obtain M, plus L_p to obtain k
Other requirements	Ability to short-circuit the load. Source with variable frequency Decreased source voltage	Open secondary coil	Air-core coils, or L_p and L_s has to be remeasured after displacement

While the method based on Faraday's law provides very accurate estimates, it requires the ability to disconnect the secondary coil from the rest of the circuit and measure the coil voltage across its open terminals. Thus, this method is more suitable for characterizing the coils in laboratory setting than performing real-time estimations of k for practical applications like EV charging.

Jiwariyavej's method for a single receiver also provide accurate estimates, but only for higher k values: $k \in \langle 0.08, 0.36 \rangle$. Another disadvantage is that it requires additional preliminary measurements including L_s to calculate the value of M. Due to this, use of Jiwariyavej's method during operation is limited to air-core coils in which the inductance does not vary with displacement. The method is not very useful for the coils with the magnetic cores, as their inductances change with displacement.

The main downside of the bifurcation asymptotes method is that it requires short- circuiting of the load; therefore, it cannot provide estimation of k during the operation of an IPT system. However, the method can be used to estimate k intermittently during a charging cycle and at critical times such as at start-up. In addition, the method involves the measuring the frequency response; thus, a variable frequency source is required, and a certain amount of time given by transients must be allotted for the extraction process to occur.

In return, however, the bifurcation asymptotes method provides significant advantages. Namely, the method requires no a-priori information of the system component values, it is based purely on primary-side measurements, it estimates k with good accuracy ($|\overline{\Delta k}_r| = 3.62\%$ for $k \in \langle 0.08, 0.36 \rangle$), and it is resilient to the detuning caused by the displacement of the coils with magnetic cores. Thanks to this, the bifurcation asymptotes method presents an interesting option for estimating k that can be readily employed by control strategies that require an accurate estimation of this variable. The method is especially suitable for implementation at the startup of stationary charging applications. For example, the method can be used to estimate k immediately after an EV is parked over a stationary wireless charger to determine if the EV is suitably positioned to allow for efficient wireless charging before high power is applied to the primary.

8.4 Impacts of Bifurcation Summary

This chapter examined the impacts of the bifurcation phenomena on device design and operation. In the first part, the selection of the suitable operating area was discussed. It was evaluated from the perspective of efficiency, the ways to achieve the required output power (whether is achieved by smaller input voltage and high input current or by higher input voltage and balanced input and output currents) and from the perspective of input phase.

The second part discussed the impacts of bifurcation on system regulation. Specifically, it was showed that the OAB frequencies form limits of stability for frequency regulation, which was demonstrated with an example using a Qi based regulation approach.

The bifurcation phenomena can be used for estimation of the coupling coefficient k. In the third part of this chapter, a novel bifurcation asymptotes method for accurately estimating k was presented. The method involves temporarily operating the system in bifurcation by short-circuiting the load and measuring the zero phase angle frequencies at the primary. The method can be used by control algorithms that require the value of k, and is especially suitable for implementation at the startup of certain applications such as EV stationary charging. A preliminary evaluation of the method was presented, which contains its connection to the general parameter model, the description of the method, experimental verification, and a comparison with existing k-estimation methods. The proposed method provides good estimates (average absolute error of 3.62 %) for wide range of coupling coefficients ($k \in \langle 0.08, 0.36 \rangle$).

9 Bifurcation Control Methods

The bifurcation phenomena occurrence corresponds with disturbances occurring during the device operation. The main causes of these disturbances are the change of load, which is represented in the equivalent circuit by varying equivalent load resistance R_L, and change of the mutual position of the coils, which is represented either by varying mutual inductance M (air core coils) or by varying set of coupled inductances L_p, L_s and M (coils with magnetic cores). Their influence on the operating point position was discussed in Chapter 7.2.

The regulation of the operating frequency plays a significant role in the way in which the system is impacted by the bifurcation phenomena as outlined in [100]. There are three types of frequency control schemes: Fixed frequency control, variable frequency control and self-oscillation control.

Fixed frequency control. The operating frequency f is set to a constant value, which is typically slightly above f_0 to make ZVS possible [197]. However, due to the decrease of R_L or increase of coupling, the operating point could move across the BB3 into bifurcation and the input impedance $\hat{Z}$ could become capacitive instead of inductive, resulting in the loss of soft switching as discussed in in Chapter 8.1.2. Also, to maintain the required power P_{out}, the input voltage $\hat{V}_{in}$ has to be increased (see Chapter 8.1.3), and the ratio of input and output currents I_{in} and I_{out} changes, resulting in the lower efficiency η_{tr} (see Chapter 8.1.1). Increased currents result in increased copper losses in the coils and conduction losses in the switches [100]. However, if the fixed frequency is set close to the primary side f_{0p}, low coupling or high R_L are also unfavorable – they may result in overcurrent at the primary side and consequently overvoltage at the primary resonant tank, as discussed in Chapter 8.1.3.

Variable frequency control. The duty cycle is typically kept constant at 50 % and the frequency is controlled to maintain the required value of the regulated quantity (P_{out}, I_{out} or V_{out}). To ensure ZVS in the bifurcation regions RG4 or RG5, the operating frequency must be set above all three OAB frequencies, otherwise the operation would not be stable – see the example in Chapter 8.2.1. According to [100], such a large deviation from the true resonance frequency f_0 results in a large current circulating in the resonant tank and thus large copper losses in the coils and the conductive losses in the switches.

Self-sustained oscillation control. Instead of externally setting the operating frequency f to a required value as in the case of the variable frequency control, f tracks a specific phase shift necessary for ZVS; thus, it changes (or oscillates) as the parameters of the IPT system change due to disturbances in the load or coupling. In such a case, a phase-locked-loop (PLL) controller is typically used to track the required phase shift between the input current $\hat{I}_{in}$ and voltage $\hat{V}_{in}$ [198]. However, the IPT system has three ZPA frequencies in phase bifurcation. Due to the disturbances, the controller may begin uncontrollably switching between all three ZPA frequencies, resulting in unstable and uncontrollable operation [100].

To prevent the negative impacts of bifurcation phenomena discussed in previous three paragraphs, multiple control methods were developed. The bifurcation control methods can be distinguished between passive and active. Passive methods are applied in the design phase of the IPT system, which is adjusted to mitigate the effects of bifurcation. They are discussed in the first part of the chapter. The active methods are based on implementation of such components in the system, which can actively change the parameters of the system during the operation in reaction on the bifurcation phenomena occurrence in order to remove or reduce the impacts of bifurcation. The active bifurcation control methods are discussed in the second part of the chapter.

9.1 Passive Bifurcation Control Methods

Passive methods for bifurcation control are based on hardware measures implemented in the design phase of the IPT device, which are intended to prevent the bifurcation occurrence completely or mitigate its effects on device operation. These measures are set in the design face and they do not adaptively react to the disturbances, such as in the case of the active methods for bifurcation control.

To prevent PB, the IPT system must operate in regions $\mathrm{RG1_o}$- RG3 (see Fig. 73). Thus, the operating point given by loaded quality factors Q_{Lp} and Q_{Ls} must be above the phase bifurcation boundary BB3, which is given by (54). Similarly, to prevent OAB (frequency splitting), the IPT system must operate in regions $\mathrm{RG1_o}$ or $\mathrm{RG2_o}$. Therefore, operating point must be above the boundary $\mathrm{BB2_o}$ given by (92). However, before selecting an operating point in $\mathrm{RG1_o}$, the value of operating frequency f of the transmitter must be considered, if fixed frequency control is selected. If the operating point is too deep in region $\mathrm{RG1_o}$ (i.e., too high above the boundary $\mathrm{BB1_o}$) and f is set close to the resonance frequency f_0, the primary side current may be too high, as it was described in the introduction.

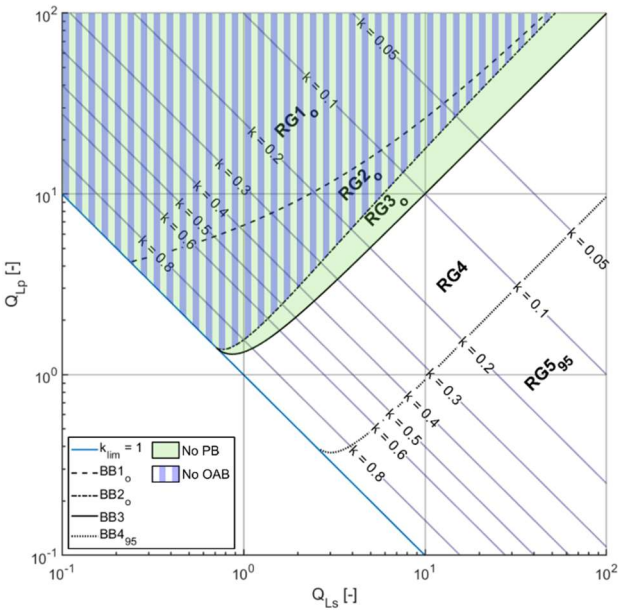

Fig. 73: 2D Q_L state diagram with highlighted regions without phase bifurcation (No PB) and without output amplitude bifurcation (No OAB).

The main passive control methods to remove or mitigate bifurcation include design for preventing the bifurcation occurrence [100], detuning (i.e., $f_{0p} \neq f_{0s}$) [100], use of antiparallel loops [104] and adding series inductances to both sides of the IPT system [199]. Description of listed methods follows.

Besides the existing control methods, two novel methods are presented in this chapter. The first proposed method is based on adding a series inductor only in the primary side and the second is based on the decrease of the resonance frequency f_0. Also, the guidelines based on the 2D Q_L state diagram are presented for evaluating bifurcation in multiple operating points given by variation of coupling or load.

9.1.1 Aditya, Williamson – Design Guidelines, Detuning

In [100], Aditya and Williamson present design guidelines to prevent bifurcation in IPT systems for EV charging. They address the PB occurrence due to the varying coupling coefficient k due to coil misalignment and change of the output power during the charging process, which is represented by change of R_L. The negative effects of PB on ZVS are mitigated by design guidelines based on the condition for PB occurrence and by detuning (i.e., $f_{0p} \neq f_{0s}$). The paper is primarily focused on avoidance of phase bifurcation.

Aditya and Williamson outline the design guidelines in [100] as follows. The IPT system topology in Fig. 74 is assumed. The primary side is powered from the voltage-sourced full bridge inverter. The inverter operates with the fixed frequency and ZVS, thus it is necessary to ensure inductive character of the input impedance $\hat{Z}$ for entire coupling and load variations.

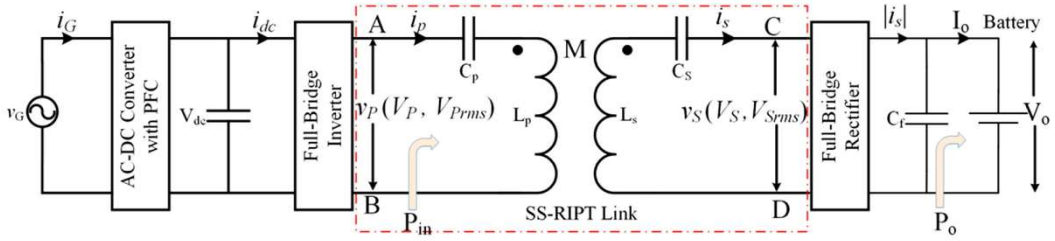

Fig. 74: The topology of IPT system for EV charging, which is considered by Aditya and Williamson in [100]. SS-RIPT link corresponds with the IPT transformer in Fig. 4. Source [100].

The full bridge inverter powers the SS compensated IPT transformer. Its output is rectified by a full bridge rectifier into DC voltage V_o and current I_o which supplies the battery which is further represented by resistance R_o. The AC equivalent load resistance is calculated as [176]:

$$R_L = \frac{8}{\pi^2}\frac{V_o^2}{P_o} \tag{125}$$

where $P_{o,DC}$ is the power consumed by the load. The relationship between R_o and R_L is then:

$$R_L = \frac{8}{\pi^2}R_o \tag{126}$$

The secondary side voltage v_s is a square wave due to the filter capacitor after the rectifier, which minimized the ripple of V_o. In the first harmonic approximation, it can be approximated by the output voltage $\hat{V}_{out}$. The secondary side current i_s is then represented by the output current $\hat{I}_{out}$ in the equivalent circuit schematics (see Fig. 16). The amplitude of its effective value (marked as RMS, root-mean square) is calculated as:

$$I_{s,RMS} = 2\sqrt{2}\frac{V_o}{\pi R_L} \tag{127}$$

The magnitude of the primary side voltage V_p is assumed to be equal to the grid voltage amplitude V_G, as the grid rectifier typically includes the PFC, which can adjust the DC link voltage V_{dc} to provide $V_p = V_G$. Again, the fundamental component of the primary side voltage v_p corresponds with the input voltage $\hat{V}_{in}$ in the equivalent circuit schematics (see Fig. 16). The primary current i_p corresponds with the input current $\hat{I}_{in}$ in Fig. 16. The effective value of the input current amplitude I_p is calculated as:

$$I_{p,RMS} = \frac{P_{in}}{V_{p,RMS}} \tag{128}$$

where P_{in} is the input active power.

The mutual inductance value can be calculated from the known values of the input and output currents I_{in} and I_{out} for the desired amount of the output power as follows. The secondary ESR R_s is neglected and the system is operated at secondary resonance frequency f_{0s}. Then the mutual inductance can be obtained from the Kirchhoff voltage law equation for the secondary side:

$$\left|j\omega_{0s}Mi_p\right| = R_L|i_s| \tag{129}$$

where the left side represent the voltage induced in the secondary side and the right side the voltage at the load.

The secondary inductance L_s is calculated from the secondary loaded quality factor Q_{Ls} (37). According to Aditya and Williamson in [100], its value is selected between 2 and 10, because the higher value can make the system difficult to tune, and lower value may result in increased harmonics in the current and voltage waveform. The inductance L_s is then calculated from Q_{Ls} as:

$$L_s = \frac{Q_{Ls}R_L}{\omega_{0s}} \tag{130}$$

The value of the coupling coefficient is then selected to be smaller than the critical coupling coefficient k_c, which is calculated from:

$$k_c = \frac{1}{Q_{Ls}}\sqrt{1 - \frac{1}{4Q_{Ls}^2}} \tag{131}$$

Equation (131) for k_c can be derived from the formula for the boundary BB3 (54). Equation (39) describing the relationship between k and Q_{Lp}, Q_{Ls} is substituted for Q_{Ls} in (54) and the resulting equation is solved for Q_{Ls}.

Equation (131) determines the minimal air gap between the coils. If the air gap would be lowered under this value, the system coupling coefficient k would exceed k_c resulting in phase bifurcation. Selecting $k < k_c$ for the nominal position, i.e., when both coils are aligned, will ensure that k is maximal possible value of the coupling – when the coils are misaligned, the coupling is always lower in comparison with the aligned coils. Thanks to this, no possible change of coil mutual position will result in phase bifurcation, if R_L is at its nominal value used to calculate Q_{Ls}.

After the value of k is selected, the primary inductance is calculated according to:

$$L_p = \frac{M^2}{L_s k^2} \tag{132}$$

According these guidelines, Aditya and Williamson in [100] designed a 3.6 kW IPT system for EV charging. The system parameters are in Table 31. The secondary loaded quality factor Q_{Ls} was selected as 4 and thus the critical coupling coefficient k_c is 0.248. The inductances in Table 31 correspond with the nominal coupling coefficient of 0.2, which authors selected to meet the critical coupling k_c of 0.248 with sufficient margin. The nominal value of the DC output voltage V_o is set to 168 V, thus the DC load resistance $R_{o,n}$ is 7.84 Ω and the equivalent load resistance $R_{L,n}$ is calculated according to (125) as 6.35 Ω ([100] lists only the value of $R_{o,n}$).

Table 31: Nominal circuit parameters of IPT system designed by Aditya and Williamson in [100].

Parameter	Symbol	Value
Primary inductance	L_p	400.65 µH
Secondary inductance	L_s	101.10 µH
Mutual inductance	M	40.23 µH
Initial resonance frequency	$f_{0,i}$	40 kHz
Nominal equivalent load resistance	$R_{L,n}$	6.35 Ω
Primary ESR	R_p	0.13 Ω
Secondary ESR	R_s	0.06 Ω

According these guidelines, Aditya and Williamson in [100] designed a 3.6 kW IPT system for EV charging. The system parameters are in Table 31. The secondary loaded quality factor Q_{Ls} was selected as 4 and thus the critical coupling coefficient k_c is 0.248. The inductances in Table 31 correspond with the nominal coupling coefficient of 0.2, which authors selected to meet the critical coupling k_c of 0.248 with sufficient margin. The nominal value of the DC output voltage V_o is set to 168 V, thus the DC load resistance $R_{o,n}$ is 7.84 Ω and the equivalent load resistance $R_{L,n}$ is calculated according to (125) as 6.35 Ω ([100] lists only the value of $R_{o,n}$).

Let us depict the designed IPT system and the possible ranges of R_L and k in the 2D Q_L state diagram as an operating area (see Chapter 7.3), to evaluate the phase bifurcation occurrence.

The system was designed for charging a 6.1 kWh battery. Two stage charging is assumed, at first it is charged by constant current (CC), then by constant voltage (CV). Fig. 75 displays the charging process. Aditya and Williamson do not explicitly specify the load range in [100]; however it can be obtained from Fig. 75. Fig. 76 shows the values of R_L corresponding with each charging stage in Fig. 75, which were calculated according to (125) from V_o and I_o extracted by WebPlotDigitizer [200] from Fig. 75. During the charging process, R_L increases from the initial value of 5.1 to 18.8 Ω, which corresponds with DC load resistance R_o of 6.32 to 23.1 Ω.

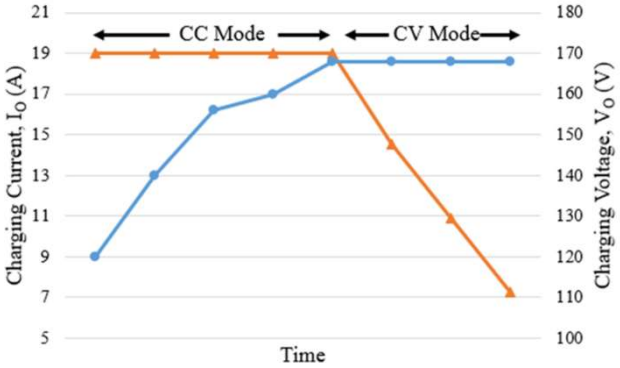

Fig. 75: Piecewise linear model of Li-ion battery charging profile. Note that time was not specified. Source [100].

To construct the operating area of the designed system in the 2D Q_L state diagram, also the trajectory of the coupling coefficient change is necessary. However, Aditya and Williamson do not specify it in [100] either. Only in the evaluation of phase bifurcation in Fig. 13 in [100], k gains values of 0.1, 0.2 (nominal value) and 0.3. Thus, for the sake of the analysis, let us assume that k changes from 0.1 to 0.3, and that only M changes, while L_P and L_s remain constant. The operating area given by k from 0.1 to 0.3 and R_L from 5.1 to 18.8 Ω describe all the possible operating points of the designed IPT system.

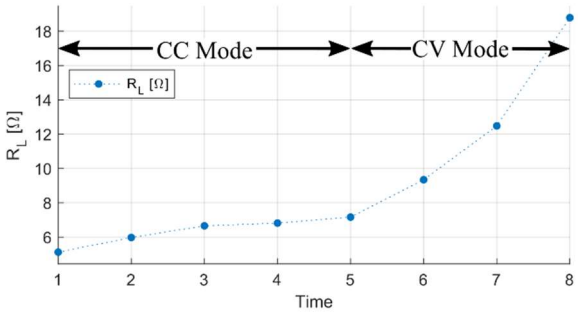

Fig. 76: Equivalent load resistance R_L values corresponding with charging cycle in Fig. 75.

Resulting operating area depicted in Fig. 77 shows a good match with the frequency responses in Fig. 13 in [100], which are in Fig. 77 represented by the operating points – the phase bifurcation occurs only for point R_L = 5.1 Ω and k = 0.3. For the k range of 0.1 to 0.2, the designed IPT system operates outside the phase bifurcation for any value of R_L, even though the point R_L = 5.1 Ω and k = 0.2 is at the phase bifurcation boundary BB3.

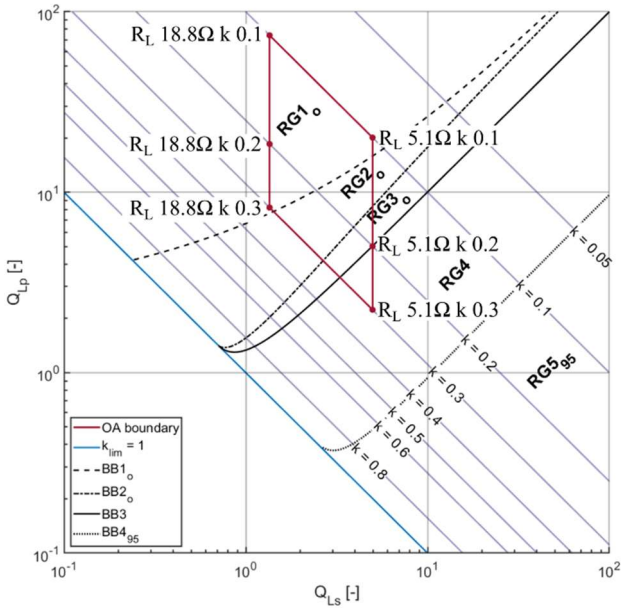

Fig. 77: Resulting operating area for k from 0.1 to 0.2 and R_L from 5.1 to 18.8 Ω, corresponding with R_o from 6.32 to 23.1 Ω.

To prevent phase bifurcation, i.e., three crossings of zero by the input phase, Aditya and Williamson detune the IPT system. The primary resonance frequency f_{0p} is set to 39.03 kHz and the secondary resonance frequency f_{0s} to 41.43 kHz. (The fixed operating frequency f of the inverter is then set f_{0s} [100].) Aditya and Williamson refer to this type of tuning as "ZVS tuning".

Aditya and Williamson do not specify any procedure for selecting for f_{0p} and f_{0s}. However, it can be derived from the operating area depicted the 2D Q_L state diagram in Fig. 77, that the critical point is R_L = 5.1 Ω and k = 0.3 – the corner of the operating area, which is furthest in region RG4. If the resonance frequencies for f_{0p} and f_{0s} are adjusted for this critical point that the input phase would be shifted that there is only a single zero crossing, then for any other point of the operating area there will be only a single zero crossing too.

To examine the impacts of detuning of the primary and secondary ($f_{0p} \neq f_{0s}$) on the IPT system, it is analyzed for the operating point of R_L = 5.1 Ω and k = 0.3, which is furthest in region RG4. Fig. 78 depicts the frequency responses of the input phase φ_{in} (Fig. 78 (a)), input impedance amplitude Z (Fig. 78 (b)), output power P_{out} (Fig. 78 (c)) and IPT transformer efficiency η_{tr} (Fig. 78 (d)) for an IPT system with varying rate of detuning. The secondary resonance frequency f_{0s} is set to constant value of 40 kHz, and the primary resonance frequency f_{0p} is varied from 35 kHz to 45 kHz with a step of 2.5 kHz. Rest of the circuit parameters correspond with Table 31, except R_L set to 5.1 Ω and M corresponding with k = 0.3.

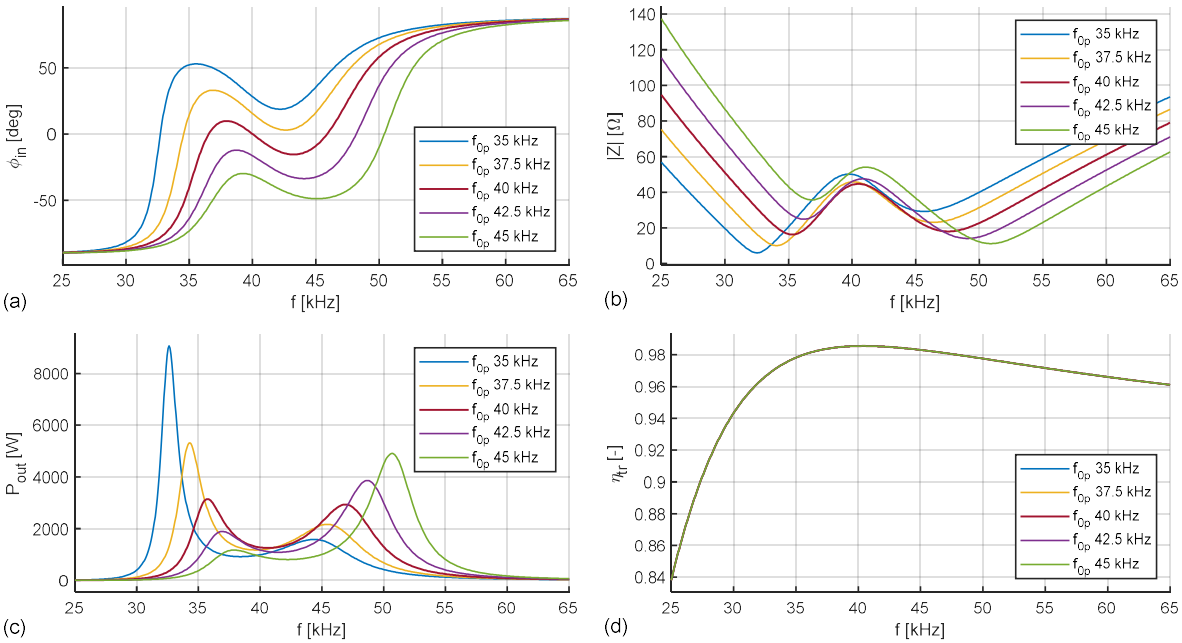

Fig. 78: Frequency responses for varying primary resonance frequency f_{0p} and constant secondary resonance frequency f_{0s} = 40 kHz. (a) Input phase φ_{in}. (b) Input impedance amplitude Z. (c) Output power P_{out}. (d) IPT transformer efficiency η_{tr}.

When $f_{0p} < f_{0s}$ (i.e., f_{0p} is 35 kHz (blue) and 37.5 kHz (yellow)), the frequency response of φ_{in} is shifted above its original course (f_{0s} = 40 kHz) – see Fig. 78 (a). When the difference between f_{0p} and f_{0s} is high enough, there is a single zero crossing, which is at lower frequency than the original ZPA frequency $f_{\varphi 1}$. Correspondingly, for $f_{0p} > f_{0s}$, the frequency response of φ_{in} is shifted below its original course, and there is a single zero crossing at higher frequency the original ZPA frequency $f_{\varphi 0}$. However, in either case the curve of the frequency response still does not become monotonous, as it is the case in the regions RG1 to RG3, which are free of phase bifurcation.

Detuning of the primary side does not remove two minima of the input impedance amplitude Z (Fig. 78 (b)), it only changes their value and frequency. This corresponds with the changes in frequency response of the output power P_{out}.

Similarly, as the frequency response of Z, the frequency response of the output power P_{out} has two peaks (see Fig. 78 (c)). However, for $f_{0p} < f_{0s}$, the peak corresponding with lower OAB frequency f_{ao1} becomes more pronounced, while the peak corresponding with f_{ao2} decreases. Also, both peaks shift to lower frequencies. On the contrary, for $f_{0p} > f_{0s}$, the peak corresponding with the higher OAB frequency f_{ao2} increases and the peak corresponding with f_{ao} diminishes. Both peaks are shifted to higher frequencies.

Change of f_{0p} has no impact on the frequency response of IPT transformer efficiency η_{tr}. It remains unchanged when f_{0s} is constant – see Fig. 78 (d). On the other hand, if f_{0p} is constant and f_{0s} changes, the frequency response of η_{tr} shifts accordingly – Fig. 79.

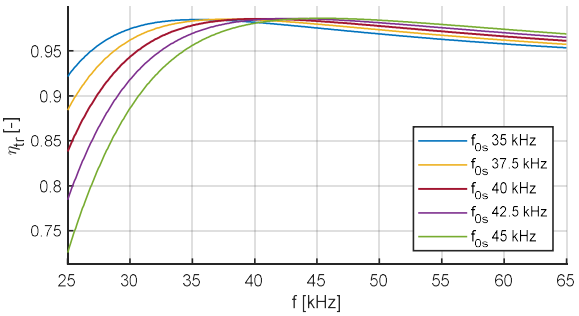

Fig. 79: Frequency response of efficiency for constant primary resonance frequency f_{0p} = 40 kHz and varying secondary resonance frequency f_{0s}.

In conclusion, Aditya and Williamson provide useful guidelines for designing an IPT system for EV charging, which prevent phase bifurcation due to displacement. Suggested "ZVS tuning" based on selecting f_{0p} lower than f_{0s} will remove the three zero crossings at the frequency response of the input phase and thus enable use of ZVS. However, it does not remove all the impacts of bifurcation phenomena, such as the splitting of the output power maxima or not-monotonous curve of the input phase frequency response.

9.1.2 Lee et. al. – Antiparallel Resonant Loops

Lee et al. presents in [104] a method aimed to prevent the occurrence of OAB (frequency splitting) due to the change of coupling. The paper is focused on high-frequency IPT (f_0 = 13.56 MHz), which utilizes the printed circuit board (PCB) based coils. Thus, the coils do not have any magnetic cores, and the change of coupling is reflected only by the change of the mutual inductance M.

As the distance between the coils decreases, the mutual inductance M grows. After M passes its critical value given by the boundary $BB2_o$ (92), OAB occurs – see Fig. 80. To prevent this, Lee et al. in [104] proposes a coil structure with antiparallel loops. Fig. 81 (a) depicts the conventional coil structure with unidirectional loops, while Fig. 81 (b) the coil structure where small reverse loops are placed in the middle of the forward loop. (Arrows in Fig. 81 mark the direction of current flowing through the loops.) The reverse loops are connected antiparallelly with the forward coil, thus the setup of the forward and reverse loops is called antiparallel loops.

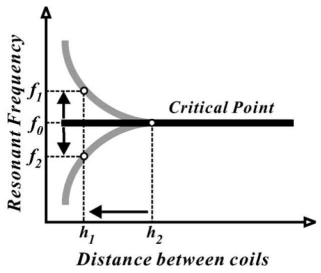

Fig. 80: OAB (frequency splitting) due increasing mutual inductance M. Source [104].

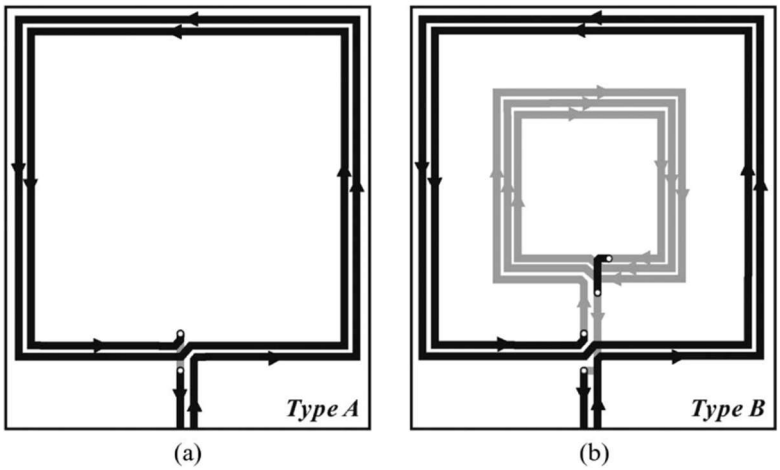

Fig. 81: PCB coil structures. (a) Coil structure (Type A) with the conventional unidirectional resonant loop. (b) Coil structure (Type B) with antiparallel loops proposed in [104]. (In two-layer PCB, the black pattern is on the top layer, while the gray patter is on the bottom layer). Source [104].

When the conventional unidirectional coils (Type A) moved closer, their mutual inductance M increases and OAB may occur (see Fig. 82 (a)). Thanks to the opposite directions of loops in the case of Type B, the total mutual inductance M_t is given as $M_t = M_f - M_r$, where M_f is the mutual between the forward loop and receiver coil, while M_r is the mutual between the reverse loop and receiver coil. As the transmitting coil moves closer to the receiving coil, the reverse loop has the effect of suppressing the increase of the mutual inductance (see Fig. 82 (b)). If the antiparallel loop is designed properly, M_t remains constant in the whole operating range.

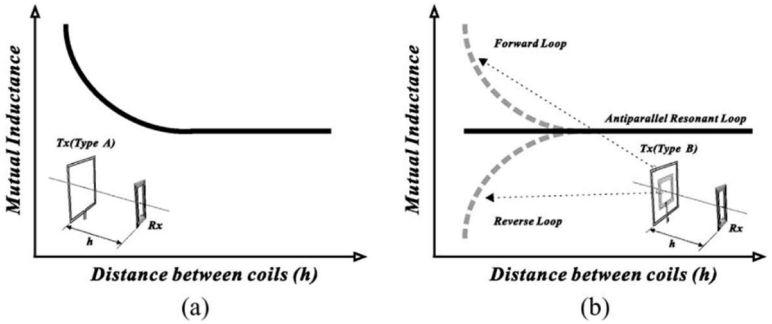

Fig. 82: Mutual inductance change with respect to distance between coils. (a) Type A coil as transmitter. (b) Type B coil as transmitter. Source [104].

Lee et al. provides in [104] guidelines for designing the both the forward and reverse loops to achieve constant mutual inductance M_t between the transmitting and receiving coil. Design parameters include dimensions and number of turns of each loop. Dependency of mutual inductance M_t on distance for optimal design is depicted in Fig. 83. The design is verified by measurement of S_{21} parameter under varying displacement for Type A coil (Fig. 84 (a)) and Type B coil (Fig. 84 (b)). As Fig. 84 (b) shows, the influence of varying distance is almost eliminated by the use of antiparallel loops as the transmitting coil.

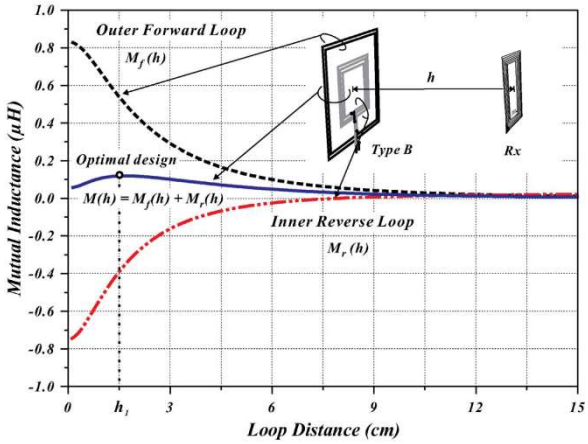

Fig. 83: Optimal design of antiparallel loops. Source [104].

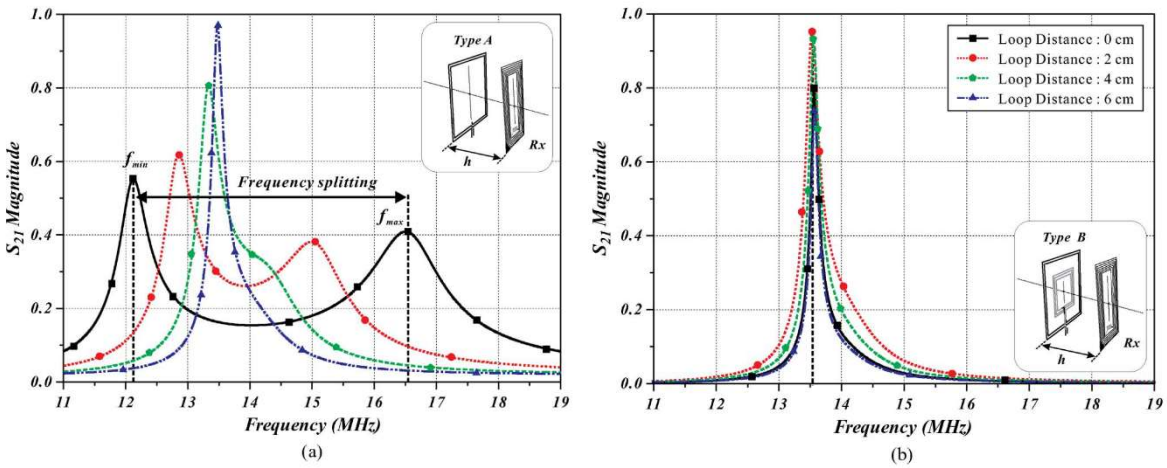

Fig. 84: Comparison of varying distance impacts on frequency response of S_{21} magnitude for (a) unidirectional coil (Type A) and (b) antiparallel coil (Type B). Source [104].

9.1.3 Shin et al. - Adding Series Inductors to Both Sides

Shin et al. presented in [199] a method to reduce impacts of bifurcation phenomena by adding series inductances both in the primary and secondary side. Shin et al. are primarily focused on reducing the electromagnetic interference (EMI). When the distance between the coils is decreased under a certain level, the coils become over-coupled and OAB occurs. The odd harmonic component of the input impedance decreases, which results in the increase of odd harmonic currents. This worsens the EMI issues [199].

Analysis of EMI is above the scope of this work. However, let us examine the impacts of adding series inductances on PB, IAB and OAB. Shin et al. designed an IPT system with parameters in Table 32. The system has the same equivalent circuit as in Fig. 16. Table 32 describes system for air gap of 30 mm and without any series inductors. The primary and secondary coils have no magnetic core. Identical toroidal inductors with parameters Table 33 are added to each side. In the following description, L_{add} and L_{add2} stand for the inductances added to the primary and secondary side, respectively. Compensation capacitances are adjusted to keep the resonance frequency of each side at 60 kHz.

Table 32: Circuit parameters for air gap of 30 mm and without series inductors.

Parameter	Symbol	Value
Primary inductance	L_p	35.40 µH
Secondary inductance	L_s	35.50 µH
Primary capacitance	C_p	200 nF
Secondary capacitance	C_s	200 nF
Mutual inductance	M	14.33 µH
Equivalent load resistance	R_L	2.4 Ω
Resonance frequency	f_0	60 kHz
Primary ESR	R_p	0.059 Ω
Secondary ESR	R_s	0.054 Ω
Input voltage amplitude	V_{in}	13.86 V

Table 33: Parameters of the additional inductors.

Inductance	Resistance
L_{add}	R_{add}
30 µH	0.066 Ω
60 µH	0.116 Ω
90 µH	0.370 Ω

Adding series inductors has no impact on the parameters of the IPT transformer itself, thus inductances L_{coil1}, L_{coil2} and M do not change. However, the side inductances L_p and L_s, which are given as $L_p = L_{coil1} + L_{add1}$ and $L_s = L_{coil2} + L_{add}$, increase. This decreases the total coupling coefficient of the system:

$$k = \frac{M}{\sqrt{(L_{coil1} + L_{add1})(L_{coil2} + L_{add2})}} \tag{133}$$

which is lower than the original coupling coefficient.

This impacts the bifurcation asymptotes u_{1a} and u_{2a} given by (52) and (53), respectively. The asymptotes come closer to each other. This is well visible from the frequency responses of the input phase φ_{in} (Fig. 85 (a)), input impedance amplitude Z (Fig. 85 (b)) and output power P_{out} (Fig. 85 (c)).

The change of inductances L_p and L_s corresponds with the movement of the operating point depicted in Fig. 86. As it is visible from the 2D Q_L state diagram, the increase of both L_p and L_s due to added inductors moves the operating point only in direction of decreasing k, thus it is kept in the region RG4. The slight movement of the operating point for L_{add} = 90 µH towards the boundary BB3 is caused by the increasing ESR R_s, which is considered in the calculation of loaded quality factors Q_{Lp} and Q_{Ls} according to (41).

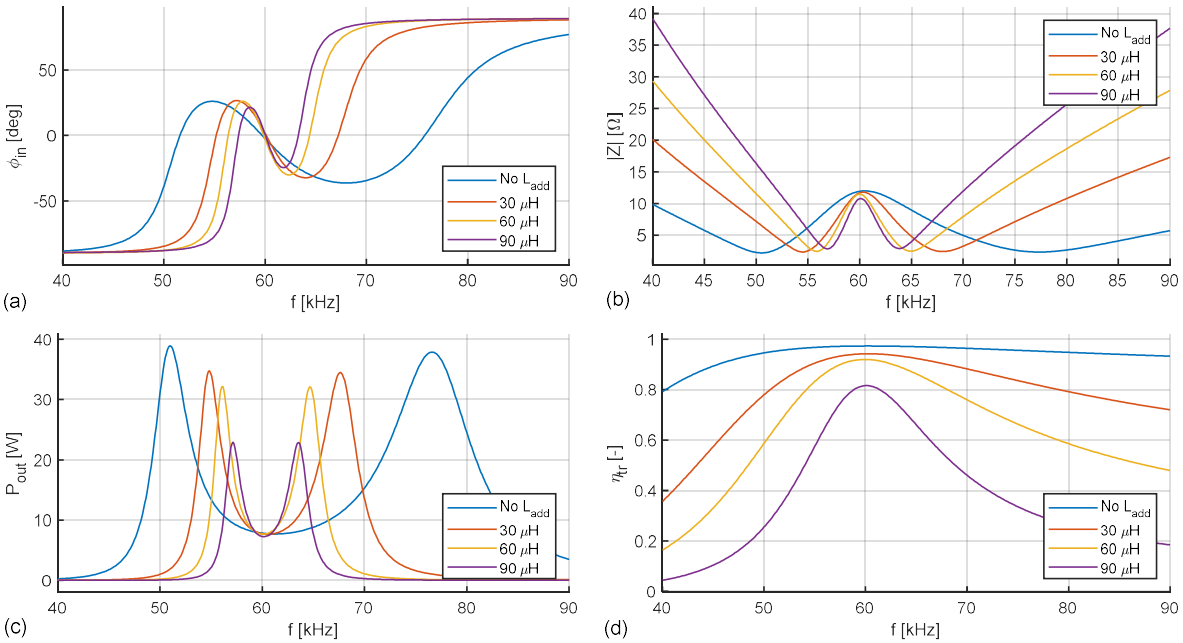

Fig. 85: Influence of added series inductors to both sided of IPT system on the frequency responses. (a) Input phase φ_{in}. (b) Input impedance amplitude Z. (c) Output power P_{out}. (d) IPT transformer efficiency η_{tr}.

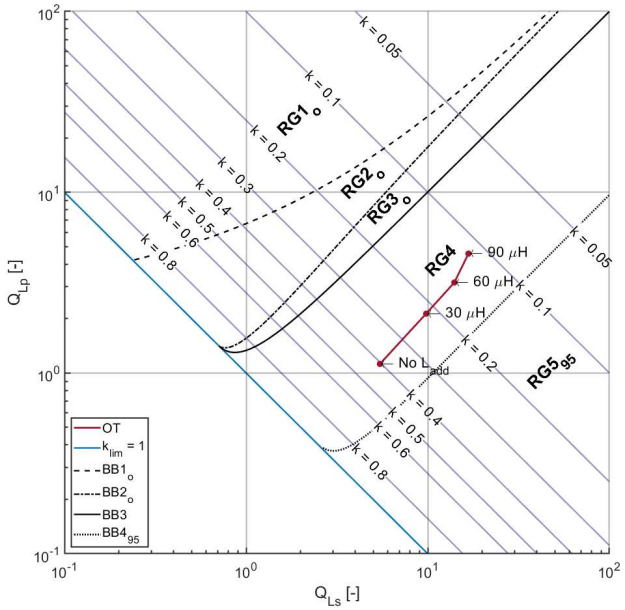

Fig. 86: Movement of operating point due to the added series inductors to both sides of the IPT system.

Shin et al. do not provide in [199] any calculation of L_{add} to obtain desirable frequency response, they only examine impacts of their increasing value on the curve of frequency response and on EMI. However, a rule for L_{add} selection can be derived from the formulas of the bifurcation asymptotes u_{1a} and u_{2a} given by (52) and (53), respectively. Let us say, that the goal is to achieve the target difference between u_{1a} and u_{2a}, which is defined as:

$$\Delta u = u_{2a} - u_{1a} = \frac{1}{\sqrt{1-k}} - \frac{1}{\sqrt{1+k}} \tag{134}$$

The desired coupling coefficient k_t is then calculated as:

$$k_t = \sqrt{1 - \frac{2}{\Delta u^4} - \frac{2}{\Delta u^2} + \frac{2\sqrt{1+2\Delta u^2}}{\Delta u^4}} \tag{135}$$

Then it is possible to calculate the additional inductance L_{add} as:

$$L_{add} = \frac{-k_t^2(L_{coil1} + L_{coil2}) + \sqrt{k_t^4 L_{coil1}^2 - 2k_t^4 L_{coil1} L_{coil2} + k_t^4 L_{coil2}^2 + 4k_t^2 M^2}}{2k_t^2} \quad (136)$$

Equation (136) is derived from (133), considering $L_{add} = L_{add1} = L_{add2}$.

The bifurcation control method proposed by Shin et al. in [199] can be evaluated from the perspective of bifurcation control as follows. Decreasing k compresses the course of bifurcation by moving the asymptotes u_{1a} and u_{2a} closer to each other and thus it mitigates bifurcation phenomena. If inductances with high enough value are added, the source of the IPT system could operate with a fixed frequency f above yet close to f_0 even in the regions RG4 and RG5. The downside is that series inductances introduce additional losses to the system, and thus decrease the efficiency of the system (see Fig. 85 (d)). Also, additional inductors are not very practical for high power systems, where they would be rather bulky and expensive. Thus, this method is applicable for low power applications which tolerate increased losses.

9.1.4 Adding Series Inductor to the Primary Side

Bifurcation control method presented by Shin et al. in [199] mitigates the impacts of bifurcation by adding series inductors to each side, which compresses the bifurcation asymptotes u_{1a} and u_{2a} closer to each other. However, if the series inductor would be added only to the primary side, the occurrence of bifurcation could be prevented.

Let us assume, that adding the series inductor should prevent PB. Thus, the coupling coefficient k of the IPT system should meet the condition $k < k_c$, where k_c is the critical coupling coefficient for boundary BB3. k_c is calculated from (131). System designed by Shin et al. in [199] with parameters listed in Table 32, has k_c of 0.18 and k of 0.4, when no series inductors are added. To keep a margin from boundary BB3, target value of coupling coefficient k_t was selected as 0.15.

Required additional inductance then can be calculated as:

$$L_{add} = \frac{M^2}{L_s k_t^2} - L_{coil1} \quad (137)$$

Equation (137) is derived from (133), assuming $L_s = L_{coi}$, $L_{add} = L_{ad}$, $L_{ad} = 0$. Obtained value of L_{ad} is then 221.68 µH. High value of L_{add} is caused by high equivalent load resistance R_L = 2.4 Ω. As the additional inductance could be used the inductor 1422435C. from MURATA, which has inductance of 220 µH and ESR of 0.096 Ω.

Fig. 87 shows the resulting movement of the operating point in the 2D Q_L state diagram. As described in Chapter 7.2.1, increase of L_p moves the operating point along the Q_{Lp}-isoline in direction of decreasing Z_{r0} (i.e., diminishing bifurcation phenomena). In this case, the operating point is moved from region RG4 to region RG3. The impacts of the operating point shift on the frequency responses are depicted in Fig. 88, where the calculated frequency responses were verified by the simulated results. Simulated frequency responses were obtained from the Simulink model described in Chapter 4.2 with the use of circuit parameters listed in Table 32, with a series inductor represented by a Simscape block inserted between blocks representing primary compensation and primary coil.

Frequency responses in Fig. 88 show that adding the series inductor into the primary enables the use of inverter with ZVS which operates at fixed frequency slightly above f_0 = 60 kHz. As PB is removed, the input phase φ_{in} becomes inductive above f_0 (Fig. 88 (a)). While both IAB and OAB remains, their impacts on input impedance amplitude Z (Fig. 88 (b)) and output power P_{out} (Fig. 88 (c)) is small, creating relatively flat and wide section of P_{out} for frequencies between 57.0 and 63.5 kHz. Also, P_{out} practically do not change for this frequency range in comparison with the original operating point (No L_{add} in Fig. 88). Because the inductor is added only in the primary side and its ESR is relatively small, the IPT transformer efficiency η_{tr} (Fig. 88 (d)) is close to the original value near f_0 (0.97 for no L_{add} vs 0.96 for L_{add} = 220 µH at f_0).

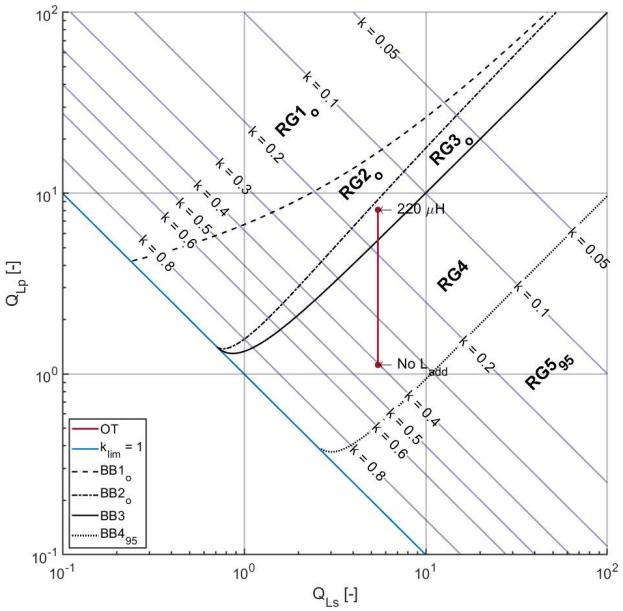

Fig. 87: Movement of operating point due to the added series inductor to the primary side of the IPT system.

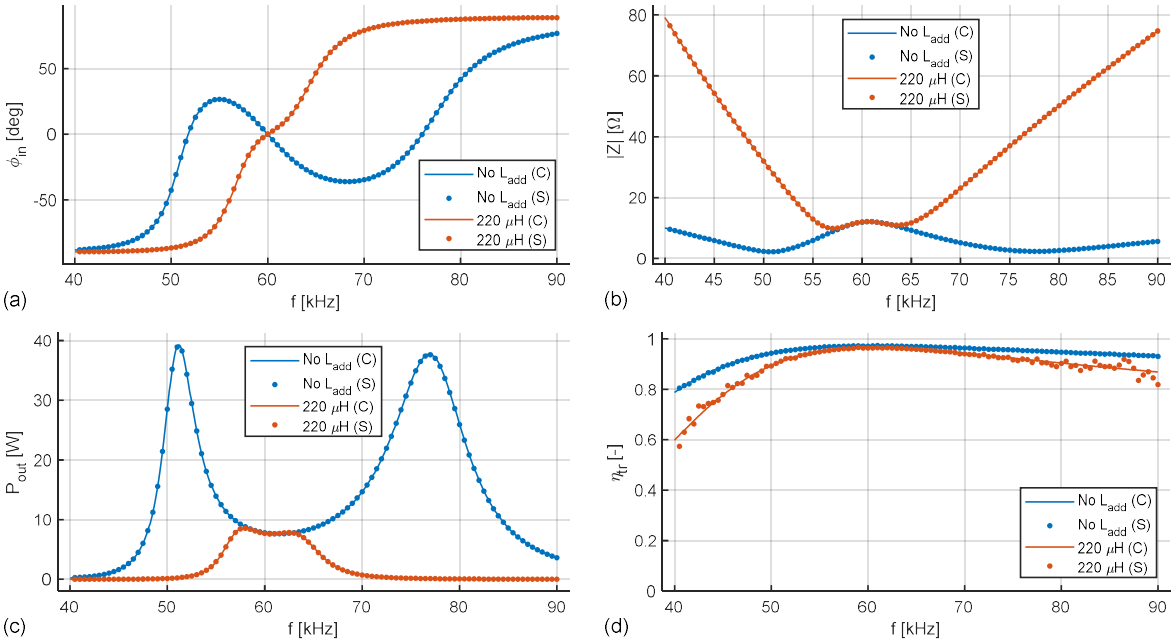

Fig. 88: Influence of added series inductor to the primary side of IPT system on the frequency responses. (a) Input phase φ_{in}. (b) Input impedance amplitude Z. (c) Output power P_{out}. (d) IPT transformer efficiency η_{tr}. Labels (C) and (S) mark the calculated and simulated frequency responses, respectively.

9.1.5 Decrease of Resonance Frequency

In IPT systems where resonance frequency f_0 is not given by a standard and it can be selected arbitrarily, the choice of f_0 or its adjustment can be used to prevent the bifurcation phenomena occurrence.

To examine its influence on IPT system, f_0 was decreased from 150 kHz to 30 kHz with step of 20 or 30 kHz. Resulting circuit parameters are listed in Table 34, which were obtained with measurement setup described in Chapter 4.1. Decreasing f_0 slightly affects the inductances L_p and L_s, which decrease with f_0. Similarly, the ESRs R_p and R_s decrease with f_0, which is caused by the influence of ferrites [178]. Corresponding frequency responses are depicted in Fig. 89, which illustrates depicts the input phase φ_{in} (Fig. 89 (a)), input impedance amplitude Z (Fig. 89 (b)), output power P_{out} (Fig. 89 (c)) and the IPT transformer efficiency η_{tr} (Fig. 89 (d)). The frequency responses of φ_{in}, Z and P_{out} show that bifurcation phenomena decrease, as f_0 lowers, which

corresponds with the operating point movement in the 2D Q_L state diagram shown in Fig. 90. As described in Chapter 7.2.1, change of f_0 moves the operating point along the k-isoline.

Table 34: IPT system parameters for decreasing resonance frequency f_0.

Parameter	Symbol	f_{0A}	f_{0B}	f_{0C}	f_{0D}	f_{0E}	f_{0F}
Input voltage amplitude	V_{in} [V]	8.65	8.65	8.65	8.65	8.65	8.65
Operating frequency range	f [kHz]	100-210	90-180	70-150	50-150	30-80	20-50
Primary inductance	L_p [µH]	30.5	30.1	29.9	29.6	29.4	29.4
Secondary inductance	L_s [µH]	18.2	17.9	17.9	17.8	17.8	17.8
Primary capacitance	C_p nF	36.36	58.30	84.47	133.43	343.60	957.33
Secondary capacitance	C_s nF	62.11	97.45	140.52	221.66	570.68	1577.60
Mutual inductance	M [µH]	7.9	7.9	7.9	7.9	7.9	7.9
Load resistance range	R_L [Ω]	3.58	3.58	3.58	3.58	3.56	3.55
Resonance frequency	f_0 [kHz]	150	120	100	80	50	30
Primary ESR	R_p [Ω]	458.8	364.947	298.02	260	248.7	173.778
Secondary ESR	R_s [Ω]	423.2	295.5	256.7	200.46	178.98	157.4

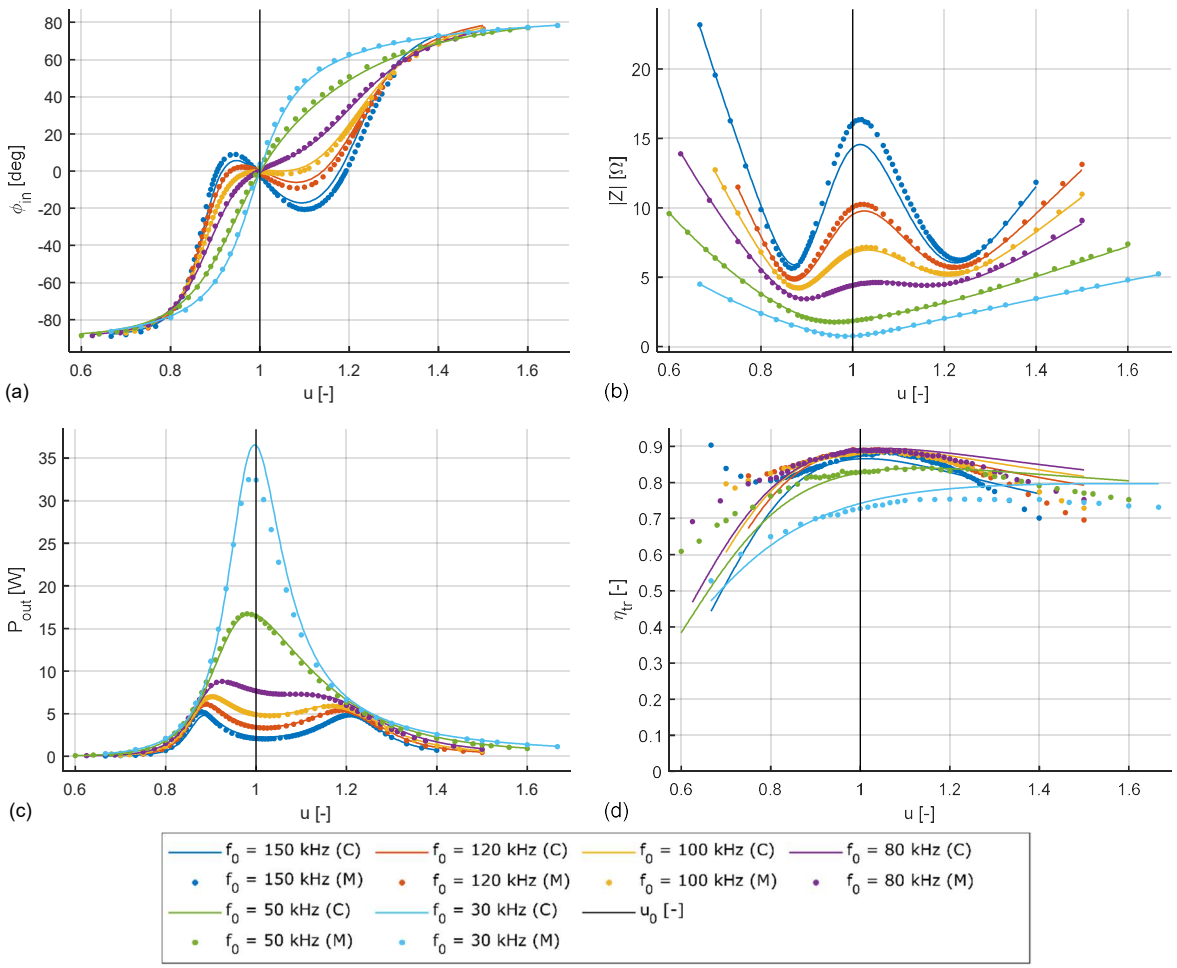

Fig. 89: Influence of the resonance frequency selection on the frequency responses. (a) Input phase φ_{in}. (b) Input impedance amplitude Z. (c) Output power P_{out}. (d) IPT transformer efficiency η_{tr}. Labels (C) and (M) mark the calculated and measured frequency responses, respectively.

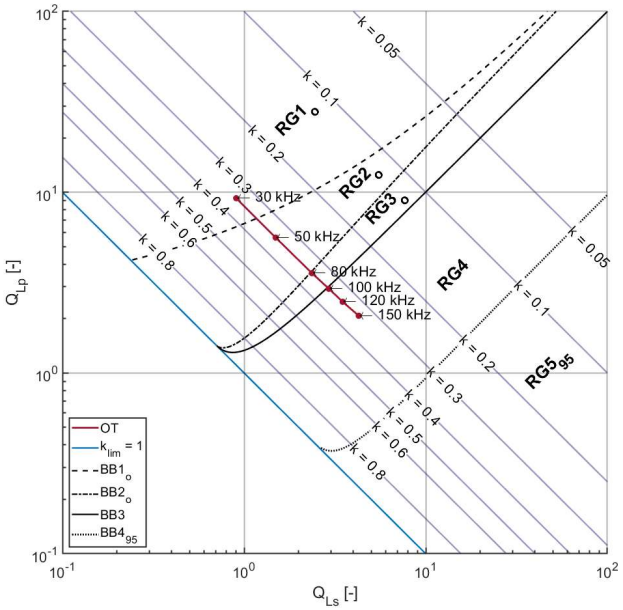

Fig. 90: Movement of operating point due to decreasing resonance frequency f_0 of the IPT system.

9.1.6 Evaluation of Bifurcation for a Range of Varying Coupling or Load

When the IPT system is supposed to work without bifurcation while disturbances in coupling or load occur, it is necessary to evaluate the impact of selected passive bifurcation control method not only on a single operating point, but on all possible operating points given by the disturbances.

The disturbances in coupling are represented by the interval of mutual inductance $\langle M_m, M_M \rangle$ or intervals of coupled inductances L_p, L_s and M, depending if the IPT system uses air-core coils or coils with magnetic cores (see Chapter 7.2). The disturbances in the load interval of equivalent load resistance $\langle R_{L,m}, R_{L,M} \rangle$. If only one of M or R_L change due to the disturbance, all possible operating points are described by an operating trajectory given by interval $\langle M_m, M_M \rangle$ or $\langle R_{L,m}, R_{L,M} \rangle$, respectively. The construction of the operating trajectories is described in Chapter 7.2.

To ensure that the selected control method will prevent the bifurcation occurrence for any possible disturbance described by interval of M or R_L, it is necessary to evaluate it for the points corresponding with the interval limits, as the trajectories given by M or R_L correspond with isolines described by Table 19. However, if the IPT system has coils with magnetic cores, resulting operating trajectory given by coupled L_p, L_s and M might be more complicated. In such a case, it is useful to plot it in the 2D Q_L state diagram to verify, if some of the operating points between the trajectory beginning and ending points does not exceed any of the bifurcation boundaries.

If both of M and R_L change due to disturbances, all possible operating points are described by an operating area, which is given by both intervals $\langle M_m, M_M \rangle$ and $\langle R_{L,m}, R_{L,M} \rangle$. The rules for operating area construction are described in Chapter 7.3 both for two independent parameters (i.e., M and R_L corresponding with the air-core coils) and for one independent and one set of coupled parameters (i.e., coupled L_p, L_s and M and R_L corresponding with the coils with magnetic cores).

Similarly, as in the case of the operating trajectories, if the operating is given by M and R_L, the bifurcation control method effectiveness should be evaluated in the corner points of the operating area, which are given by pairs M_m, $R_{L,m}$; M_m, $R_{L,M}$; M_M, $R_{L,m}$ and M_M, $R_{L,M}$. (For example, this approach was used in evaluating the obtained IPT system in Chapter 9.1.1 based on its operating area depicted in Fig. 77.) Again, in the case coils with magnetic cores, the boundary segments given by the set of coupled L_p, L_s and M could have more complicated boundary and thus in such a case it may be necessary to add additional boundary points to the evaluation. These points can be obtained by plotting the area boundary it in the 2D Q_L state diagram and comparing its position with respect to bifurcation boundaries.

The evaluation of a bifurcation control method for IPT system under disturbances in coupling and load is demonstrated on following example, where phase bifurcation occurrence is prevented by decrease of the resonance frequency f_0. Change of any circuit parameters figuring in calculation of loaded quality factors Q_{Lp}, Q_{Ls} given by (41) (i.e., L_p, L_s, M, f_0 and R_L) results in the movement of the operating area. Thus, control methods, which are

based on the change of one of these parameters (i.e., adding series inductor in the primary described in Chapter 9.1.4 and decrease of f_0 in Chapter 9.1.5), can be easily evaluated by comparing the position of the moved operating area with respect to the selected boundary.

IPT system with circuit parameters in Table 35 is used. Parameter values were obtained as averages of values in Table 34. The varying load is described by R_L change from 2 to 3 Ω and the coupling variation is described by change of M from 5 to 7.9 µH. (Even though the coils have magnetic cores, only the change of M was considered for simplicity of the analysis).

Table 35: Circuit parameter for operating area movement evaluation.

Parameter	Symbol	Value
Primary inductance	L_p	29.8 µH
Secondary inductance	L_s	17.9 µH
Mutual inductance range	M	5.0-7.9 µH
Resonance frequency values	f_0	150 kHz, 80 kHz, 50 kHz
Load resistance range	R_L	2.00-3.00 Ω
Primary ESR	R_p	0.30 Ω
Secondary ESR	R_s	0.25 Ω

The initial position of operating area corresponds with f_0 = 150 kHz is depicted in Fig. 91 as $A_1B_1C_1D_1$ (red). If f_0 is decreased to 80 kHz, most of the resulting operating area $A_2B_2C_2D_2$ (green) would be above the boundary BB3 marking the PB occurrence. However, the corners A_2 and B_2 corresponding with R_L = 3 Ω, M = 7.9 µH and R_L = 2 Ω, M = 7.9 µH, respectively are still under the boundary BB3. Thus, it is necessary to decrease f_0 further to 50 kHz to obtain the final operating area $A_3B_3C_3D_3$ (purple), which is fully above the boundary BB3 and thus PB does not occur for any combination of R_L and M.

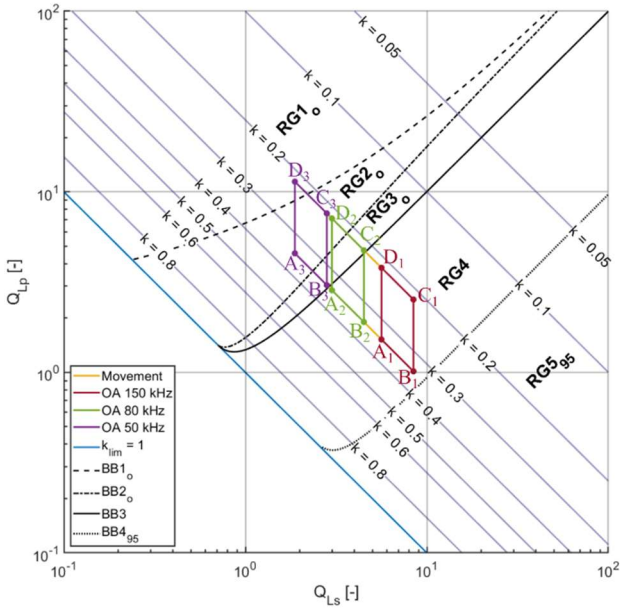

Fig. 91: Movement of operating area given by $M = \langle 5\mu H, 7.9\mu H \rangle$ and $R_L = \langle 2\Omega, 3\Omega \rangle$ due to decreasing f_0.

Fig. 92 depicts the frequency responses for input phase φ_{in} for each corner of the operating area under resonance frequency f_0 change from 150 kHz to 80 kHz and finally to 50 kHz. Simulated results were obtained from the Simulink model described in Chapter 4.2, using the circuit parameters listed in Table 35. Obtained frequencies verify that to prevent PB for given disturbances, the resonance frequency f_0 must be set to 50 kHz.

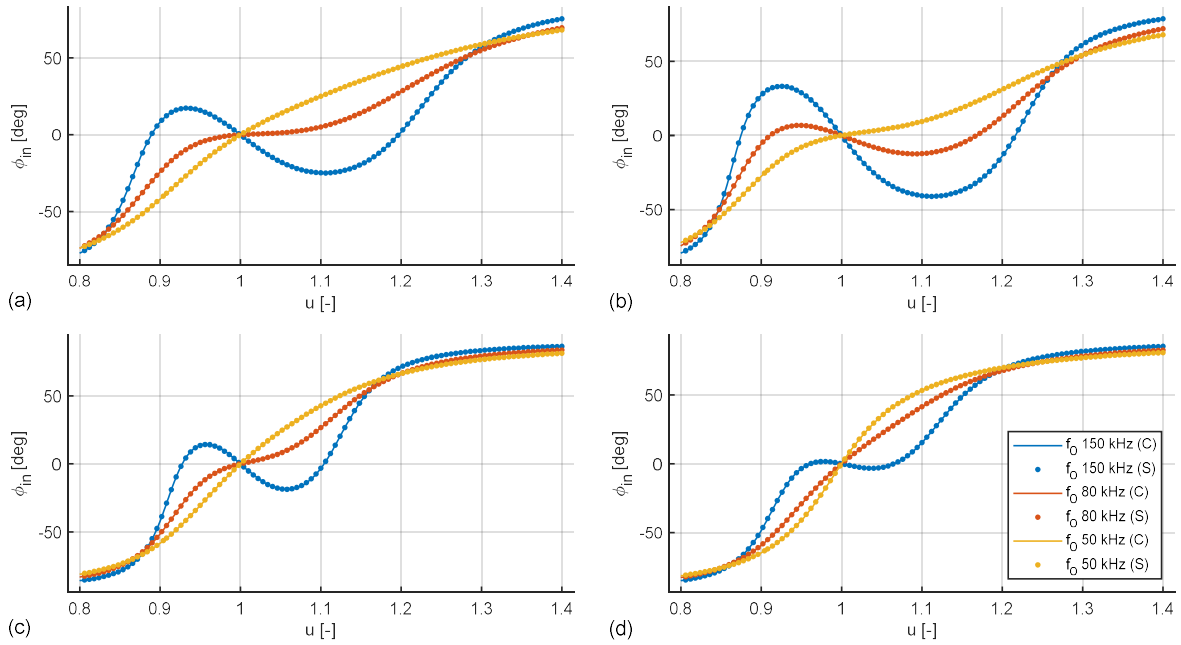

Fig. 92: Frequency responses of input phase φ_{in} for operating area corners under varying resonance frequency f_0. (a) Corner A R_L = 3 Ω, M = 7.9 µH. (b) Corner B R_L = 2 Ω, M = 7.9 µH. (c) Corner C R_L = 2 Ω, M = 5 µH. (c) Corner D R_L = 3 Ω, M = 5 µH.

9.2 Active Bifurcation Control Methods

On the contrary to the passive methods which are set in design phase, active methods adaptively adjust the system parameters during operation to prevent the bifurcation negatively impacting the IPT system. There is a large variety of active control methods in literature, because bifurcation due to varying coupling or load is a common issue occurring in IPT systems. In this section, two typical approaches for fixed frequency and variable frequency control are examined. The adaptive impedance matching (AIM) networks are used in the high frequency IPT systems, which typically operate at fixed frequency due to narrow bandwidth of ISM bands [146], [147], [201]. The AIM networks adjust the circuit parameters to keep maximum power transfer at fixed frequency. In the IPT systems with variable frequency (typically low frequency IPT), the negative impacts of bifurcation are avoided by constant voltage tracking, which is based on tracking the frequency of ZPA between the input voltage $\hat{V}_{in}$ and output current $\hat{I}_{out}$ [202]–[206]. Description of both approaches follows.

9.2.1 Adaptive Impedance Matching

According to [201], impedance matching is a measure commonly used in power transfer or communication systems to improve efficiency of the system. It is based on inserting a matching network such as an LC circuit between the source and the load to minimize the wave reflection ratio. Adaptive impedance matching (AIM) networks change their parameters to keep maximal power transfer at the selected operating frequency.

The principle of matching network can be explained on Fig. 93. The power source is represented by AC voltage source and impedance $\hat{Z}_{source}$. The primary reactance and reflected impedance are represented together by $\hat{Z}_{TR}$. The purpose the primary side matching circuit is to adjust the impedance of the load viewed by the source (i.e., $\hat{Z}_{TR}$) in order to make the power transfer maximal. This is achieved, when $\hat{Z}_{source}$ is the conjugate of $\hat{Z}_{TR}$[201]:

$$\hat{Z}_{source} = \hat{Z}_{TR}^{*} \tag{138}$$

Beh et al. presented in [201] an AIM method based on L-type matching circuit (see Fig. 94), which is intended for high frequency IPT operating at ISM band of 13.56 MHz. Beh et al. assumes a symmetrical system (i.e., $L = L_p = L_s$, $C = C_p = C_s$, $Z_0 = Z_{source} = Z_{load}$) and coil ESRs are neglected. In such a case, OAB and PB frequencies match, thus P_{out} (or S_{21} parameter) maxima and zero crossings of φ_{in} are at the same frequencies [21]. In [201], the L-type matching circuit is tested for two-coil arrangement, where it is placed between the power source and SS compensated IPT transformer.

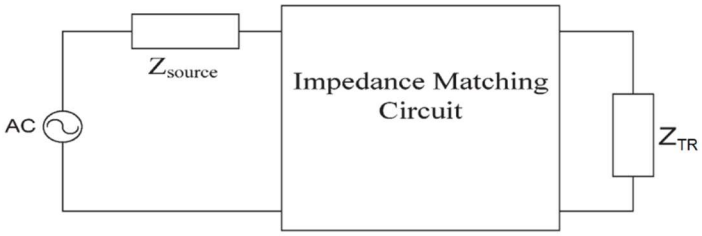

Fig. 93: Equivalent circuit for explanation of impedance matching princople. Source [201] (adjusted).

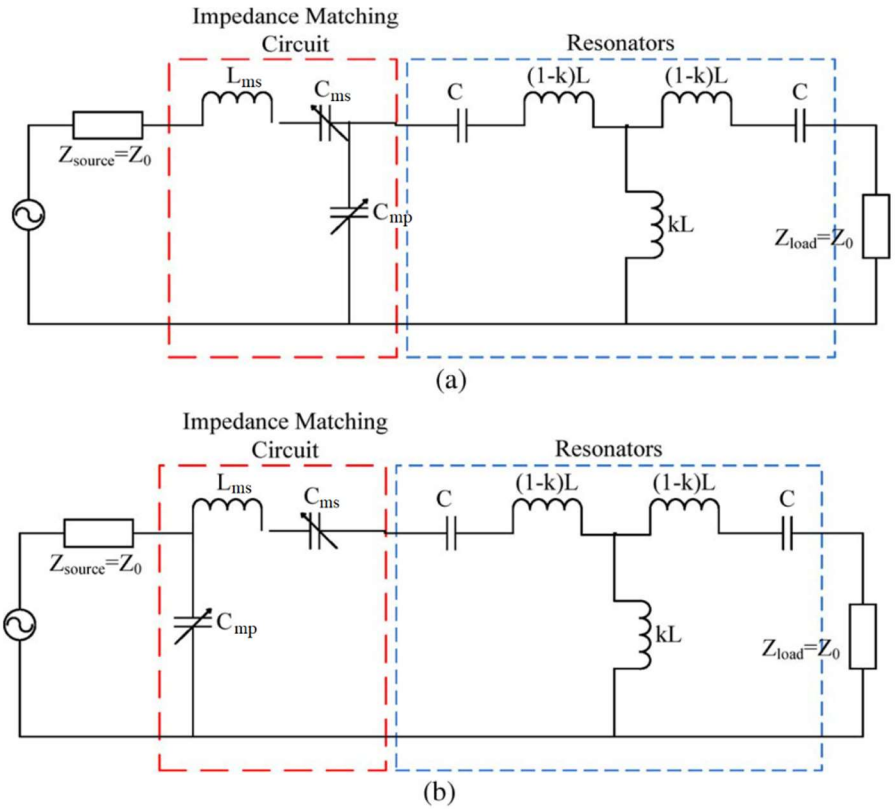

Fig. 94: (a) L-type matching circuit. (b) Inverted L-type matching circuit. Source [201] (adjusted).

Beh et al. presented L-type matching circuit in two variants, the first is regular (Fig. 94 (a)) and the second inverted (Fig. 94 (b)). The matching circuit consists of series inductor L_{ms}, series capacitor C_{ms} and parallel capacitor C_{mp}. (The symbols were adjusted to avoid confusion, in [201] they are denoted as L_s, C_s and C_p, respectively.) The high frequency IPT systems are bound to operate ISM bands, which are relatively narrow (13.56 MHz band has bandwidth of 14 kHz from 13.553 to 13.567 MHz). Thus, they use fixed frequency sources operating at the resonance frequency f_0 of 13.56 MHz. The operating frequency f cannot be adjusted to match the OAB frequencies f_{ao1} and f_{ao2}, which move away from f_0. AIM proposed by Beh et al. in [201] is designed to keep maximum of S_{21} parameter corresponding with f_{ao1} at fixed f, despite varying air gap resulting in change of mutual inductance M. This is achieved by automated system, which adjusts the values of L_{ms}, C_{ms} and C_{mp} to maintain condition (138).

The operation of AIM is demonstrated in Fig. 95, where the frequency responses of the IPT system without AIM (i) and with AIM (ii) evaluated for increasing air gap. The parameters η_{11} and η_{21} are calculated from [201]:

$$\eta_{11} = |S_{11}|^2 \times 100\ [\%] \tag{139}$$

$$\eta_{21} = |S_{21}|^2 \times 100\ [\%] \tag{140}$$

where S_{11} and S_{21} represent the wave reflection and transmission ratios, respectively [201].

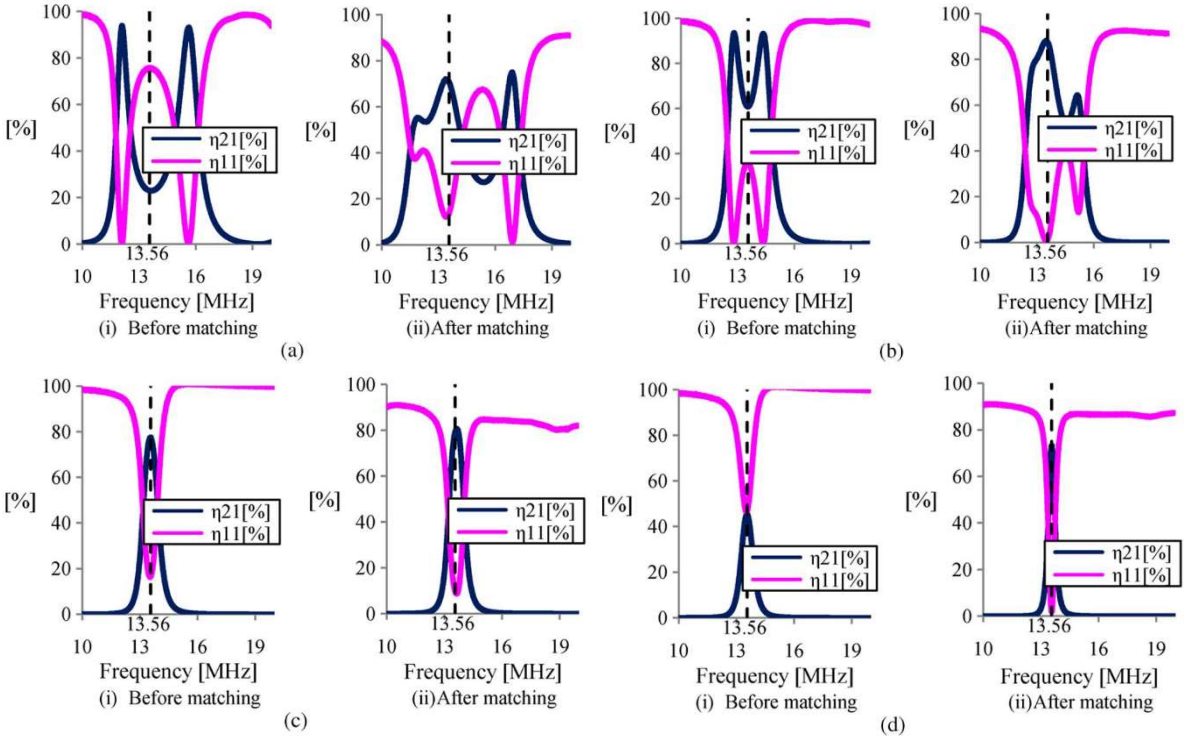

Fig. 95: Experimental results of L-type matching network with automated control system for increasing air gap. (a) 6 cm. (b) 12 cm. (c) 24 cm. (d) 30cm. Source [201].

Performance of L-type AIM proposed in [201] controlled by automated system is evaluated in Fig. 96, where it is compared with the case without AIM and manually tuned AIM. Even though the efficiency at the nominal position is slightly lower due to additional losses, AIM (both manually and automatically tuned) improves the system operation by widening the air gap range, in which the efficiency is high.

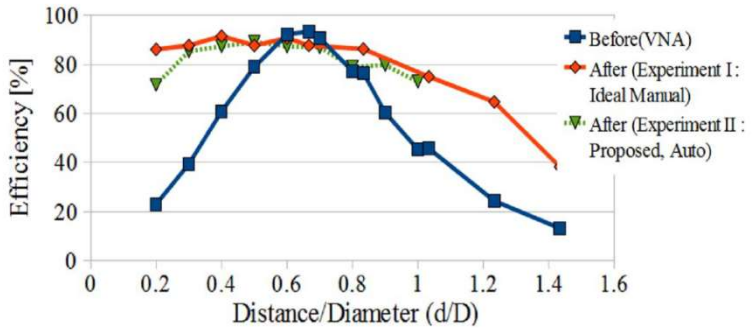

Fig. 96: Comparison of IPT system efficiency for the case without AIM (blue), manually tuned AIM (orange) and automated AIM (green). Source [201].

Lim et al. presented in [147] an improved version of L-type AIM, which uses of capacitor matrix. The IPT system operating at fixed frequency of 13.56 MHz employs two matching networks (see Fig. 97), the first is placed between the power source and IPT transformer, the second is placed between the IPT transformer and the rectifier (load). The primary matching network is regular L-type matching circuit (see Fig. 94 (a)) while the secondary matching network is inverted L-type matching circuit (see Fig. 94 (b)).

The primary matching network is adaptive and employs the capacitor matrix, the secondary is passive (L_{ms}, C_{ms} and C_{mp} are constant). Fig. 98 displays the L-type AIM with capacitor matrix. The individual capacitors can be either connected to the line for serial connection or to the line for parallel connection (Fig. 98 (a)), forming the series capacity or parallel capacity of L-type AIM (Fig. 98 (c)). Lim et al. presents in [147] a window prediction based search algorithm to effectively select the serial or parallel connection of the capacitors to achieve optimal matching. Resulting AIM improves the transfer efficiency up to 88 % for varying air gap.

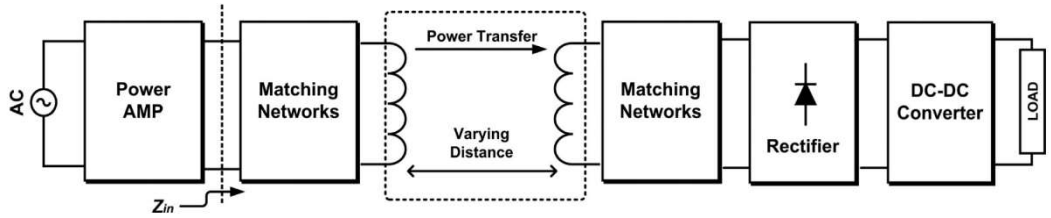

Fig. 97: IPT system presented in [147] which uses two L-type matching networks. The primary AIM is based on capacitor matrix. Source [147].

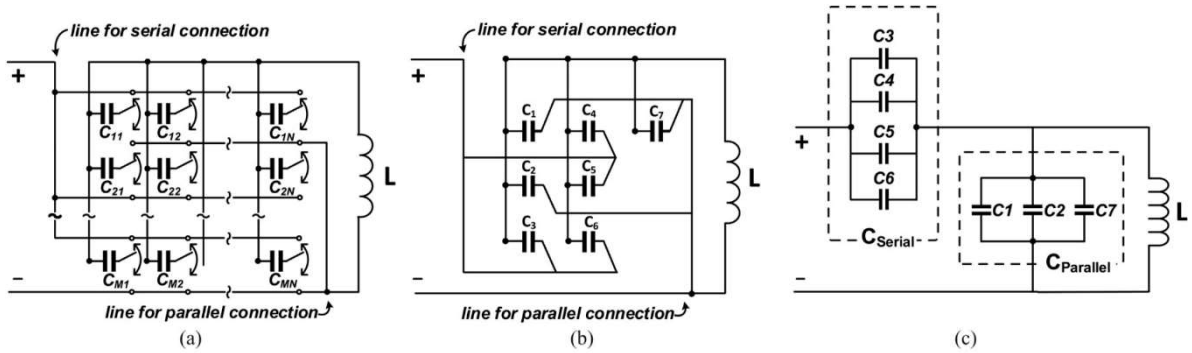

Fig. 98: (a) M x N capacitor matrix circuit. (b) Example of capacitor matrix with seven capacitors. (c) Equivalent circuit of (b). Source [147].

Even more complex AIM networks were proposed to improve the performance of high frequency IPT under varying coupling. Sample et al. presented in [146] low pass π-match networks formed by a fixed inductor and two variable capacitors, which are placed in the primary and secondary of a 4-coil IPT system – see Fig. 99. Again, the system operates with fixed frequency of 13.56 MHz.

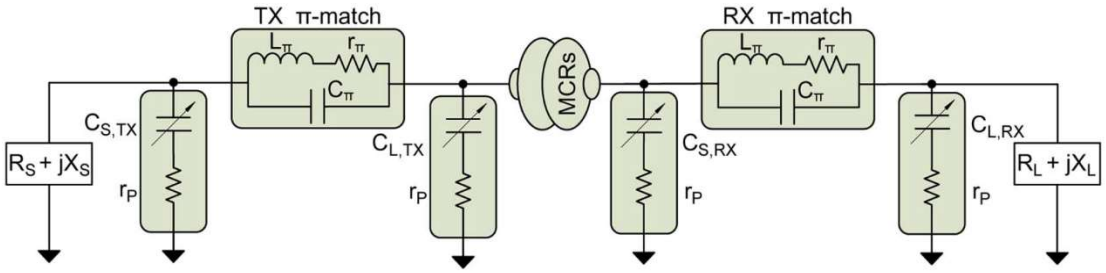

Fig. 99: An IPT system with π-match AIM placed both in the primary and secondary side, which was proposed in [146]. Source [146].

9.2.2 Constant Output Voltage Tracking

There is a frequency at which the output voltage $\hat{V}_{out}$ of the SS compensated system independent on the variation of the equivalent load resistance R_L. If the system is designed properly, $\hat{V}_{out}$ is independent also on k. This frequency can be found as a frequency of zero phase angle (ZPA) between the input voltage $\hat{V}_{in}$ and the output current $\hat{I}_{out}$. The first concepts of this control method were explored in [202]. It is was further elaborated by [203]–[205] and finally by [206].

Note that on the contrary to this method, in which $\hat{V}_{in}$ is the reference, the input current $\hat{I}_{in}$ was considered as the reference in the previous analyses (i.e., Chapters 3 through 8). The phase shift from $\hat{I}_{in}$ to $\hat{I}_{out}$ gains values between 0° and 180°, while the phase shift from $\hat{V}_{in}$ to $\hat{I}_{out}$ gains values between -90° and 270°.

Based on the same equivalent circuit schematics as in Fig. 16. The summary of the main points of the method's theoretical background based on [206] follows. The phase γ between input voltage $\hat{V}_{in}$ and output current $\hat{I}_{out}$ is calculated as:

$$\gamma = arctan\left(\frac{Re\left\{\frac{\hat{V}_{in}}{\hat{I}_{out}}\right\}}{Im\left\{\frac{\hat{V}_{in}}{\hat{I}_{out}}\right\}}\right) = arctan\left(\frac{\left(\omega L_p - \frac{1}{\omega C_p}\right)\left(\omega L_s - \frac{1}{\omega C_s}\right) - R_p(R_L + R_s) - \omega^2 M^2}{(R_L + R_s)\left(\omega L_p - \frac{1}{\omega C_p}\right) + R_p\left(\omega L_s - \frac{1}{\omega C_s}\right)}\right) \tag{141}$$

The angular frequencies at which is phase γ equal to 0° (marked as ω_{ZPA}) or 180° (marked as $\omega_{180°}$) are calculated as:

$$\underset{180°}{\omega_{ZPA}} = \sqrt{\frac{\frac{L_s}{C_p} + \frac{L_p}{C_s} + R_p(R_L + R_s) \pm \sqrt{\left(\frac{L_s}{C_p} - \frac{L_p}{C_s}\right) + \frac{4M^2}{C_p C_s} + R_p(R_L + R_s)\left(2\left(\frac{L_s}{C_p} + \frac{L_p}{C_s}\right) + R_p(R_L + R_s)\right)}}{2\left(L_p L_s - M\right)}} \tag{142}$$

If the coil ESRs R_p and R_s are neglected, frequencies ω_{ZPA} and $\omega_{180°}$ can be simplified to:

$$\underset{180°}{\omega_{ZPA}} = \sqrt{\frac{L_p C_p + L_s C_s \pm \sqrt{\left(L_s C_s - L_p C_p\right)^2 + 4k^2 L_p L_s C_p C_s}}{2L_p L_s C_p C_s (1 - k^2)}} \tag{143}$$

The voltage gain for both ω_{ZPA} and $\omega_{180°}$ is described by:

$$G_V(j\omega) = \frac{\hat{V}_{out}}{\hat{V}_{in}} = \frac{\hat{I}_{out} R_L}{\hat{V}_{in}} = \frac{\underset{180°}{\omega_{ZPA}^2} C_p k \sqrt{L_p L_s}}{\underset{180°}{\omega_{ZPA}^2} L_p C_p - 1} \tag{144}$$

As it is visible from (143) and (144), the voltage gain G_V is load independent for both frequencies ω_{ZPA} and $\omega_{180°}$ (ref 22 and 33 in [206]). However, the voltage gain G_V is still dependent on the coupling coefficient k, thus with varying mutual position of the coils, G_V will change. To design the system independent on k, the primary side must be tuned to the secondary ($f_{0p} = f_{0s}$) according to [206]. Then $L_p C_p = L_s C_s$ then (144) can be simplified as:

$$G_V(j\omega) = \pm\sqrt{\frac{L_s}{L_p}} \tag{145}$$

where $+\sqrt{\frac{L_s}{L_p}}$ corresponds with ω_{ZPA} and $-\sqrt{\frac{L_s}{L_p}}$ with $\omega_{180°}$.

When $f_{0p} = f_{0s}$ and one of the frequencies ω_{ZPA} and $\omega_{180°}$ is tracked, then the voltage gain G_V is independent on both the load and coupling. If the coil inductances are also selected as equal ($L_p = L_s = L$ and consequently $C_p = C_s = C$), then equation (143) describing ω_{ZPA} and $\omega_{180°}$ is reduced to:

$$\underset{180°}{\omega_{ZPA}} = \sqrt{\frac{1}{CL(1 \mp k)}} = \frac{1}{\sqrt{(1 \mp k)}}\omega_0 \tag{146}$$

This is an interesting result, because for the IPT system where $f_{0p} = f_{0s}$ and $L_p = L_s$ the frequencies u_{ZPA} and $u_{180°}$ normalized according to (38) correspond with the bifurcation asymptotes $u_{2a} = \frac{1}{\sqrt{1-k}}$ and $u_{1a} = \frac{1}{\sqrt{1+k}}$, respectively, which are descibed in Chapters 6.2.2 and 6.6.

The output power P_{out} of such system is given by

$$P_{out} = \frac{1}{2}\frac{V_{in}^2}{R_L} \tag{147}$$

which is similar as the load would be directly connected to the input power source [206].

The main advantage of this control scheme is the constant output voltage, which is independent on R_L and k. Thus, it is able to provide stable charging power, which is not impacted by disturbances. This is especially important for the dynamic applications.

However, this control scheme has following disadvantages. It requires reliable and fast communication between the secondary and the primary, which poses increased demands on the device architecture. The load independent voltage gain and maximum efficiency cannot be achieved at the same operating frequency, as [205] shows. The efficiency can be improved by suitable device design. Also, according to [206], the inverter must able to drive capacitive loads.

Gati et al. in [206] developed a 1-kW prototype, where they implement this frequency control scheme for dynamic charging applications. They envision their IPT system to be used for charging of unmanned aerial or underwater vehicles (UAVs and UUVs, respectively), which are in the continuous movement in relation to the charger. For illustration, a UAV is charged while hovering above the charger in windy weather or a UUV is affected by underwater currents.

The prototype of IPT system is depicted in Fig. 100. The primary side is powered by a single phase full-bridge inverter comprised of SiC MOSFETs. The coil topologies are not planar, but they are solenoids. The primary coil is wound on an I-shaped core, while the secondary has a U-shaped core. The output of the secondary side is rectified by a full-bridge diode rectifier and loaded by a programable electronic load.

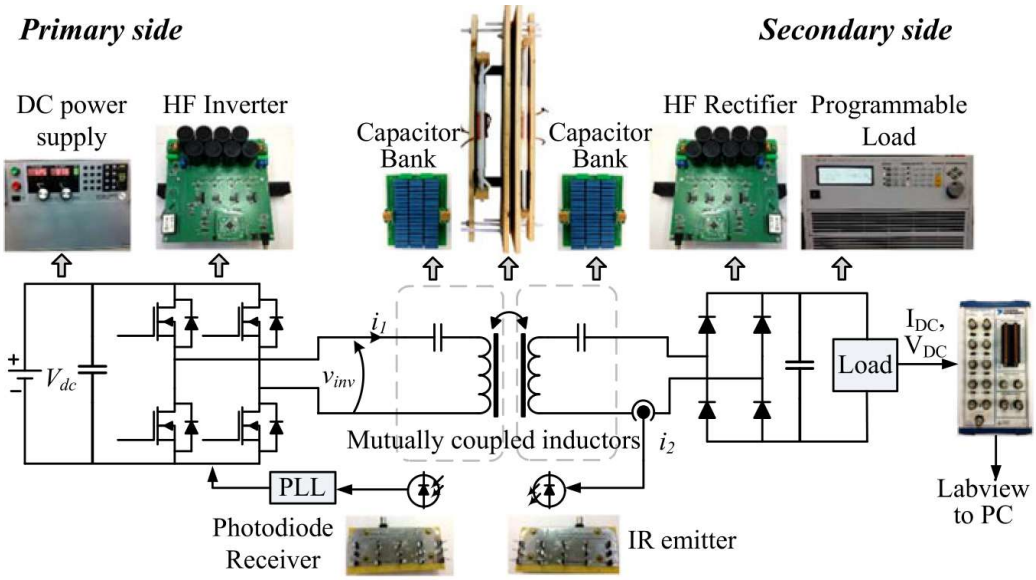

Fig. 100: Experimental setup presented in [206], which implements the constant voltage tracking control. Source [206].

The circuit pa parameters of the IPT system are listed in Table 36 for the nominal position of the coils. The equivalent load resistance R_L, n was calculated from the DC load resistance $R_{o,n}$ according to (126), as the system also uses a full-bridge rectifier. Gati et al. intended to make both of the coils with the same inductance and thus make the system independent on the coupling coefficient k, as described in the theoretical background of the method. However, due to different ferrite cores, the coil inductances slightly vary (5% difference), which results in a small ripple of the output voltage, respective output power with coupling change.

The secondary side current $\hat{I}_{out}$ is measured with a LEM sensor. The value of $\hat{I}_{out}$ is then optically transferred to the primary side. An arrangement of multiple infrared diodes amplifies the signal and increases the transmission range. Similarly, the receiver at the primary side consists of multiple photodiodes, which are linked in parallel through an OR gate. In the primary, the signal is connected to a phase-locked loop (PLL), where together with the switching signals for the transistors it is used to generate the value of phase γ between $\hat{V}_{in}$ and $\hat{I}_{out}$. The obtained value of γ is consequently used for tracking of ω_{ZPA}. The control scheme implemented in [206] has fast response time (settling time less than 400 μs).

The optical communication is an improvement in comparison with the previous implementations of the ZPA frequency control method which employed inductive coupling for communication [203], [204]. These systems require complex sensor design and shielding to eliminate electromagnetic interference. Also, they require special compensation circuits for correcting the phase delays in the sensing loops [206].

The coils are placed in a wooden construction, which separates them and allows displacement of the secondary with respect to the primary. As Fig. 101 shows, the secondary arrangement is connected to a motor, which moves the secondary, emulating the periodical motion of sea waves.

Table 36: Circuit parameters for IPT system presented in [206]. Parameters correspond with the nominal position of k = 0.18.

Parameter	Symbol	Value
Primary inductance	L_p	183 µH
Secondary inductance	L_s	193 µH
Nominal mutual inductance	M	33.8 µH
Primary capacitance	C_p	28.2 nF
Secondary capacitance	C_s	28.2 nF
Primary resonance frequency	f_{0p}	70.06 kHz
Secondary resonance frequency	f_{0s}	68.22 kHz
Nominal DC load resistance	$R_{o,n}$	15 Ω
Nominal equivalent load resistance	R_L, n	12.16 Ω

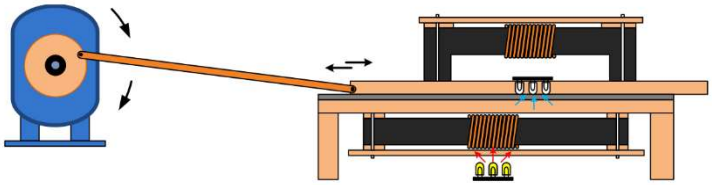

Fig. 101: Experimental setup for emulation of dynamic operation. Source [206].

Three frequency control schemes were tested under displacement:

1) Fixed frequency 75.7 kHz, where the output power is maximal (f = 75.7 kHz).

2) Fixed frequency 70 kHz, which corresponds with the primary side resonance frequency f_{0p} (f = 70 kHz).

3) Proposed ZPA frequency tracking scheme ($f = f_{PLL}$), which corresponds with $\omega_{ZPA}/2\pi$.

Due to output power oscillations in first two control schemes, was the power decreased to approximately one third of its nominal value of 1 kW. Fig. 102 depicts the output power P_{out} under periodical displacement for all three frequency control schemes. Fig. 102 shows that control at f_{PLL} provides higher average output power and significantly less ripple (40 W vs 270 W for 75.7 kHz or 280 W for 70 kHz) in comparison with the fixed frequency control schemes. The ripple of f_{PLL} follows the variation in k caused by difference in coil inductances (condition $f_{0p} = f_{0s}$ is not perfectly met).

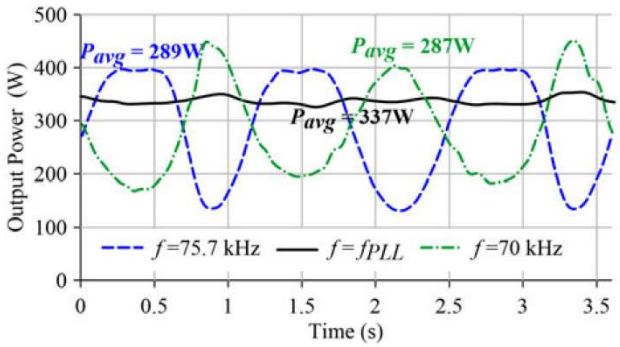

Fig. 102: Obtained output power P_{out} under displacement for all three frequency control schemes. Source [206].

According to [206], the charging may get dangerous in low coupling positions for the second control scheme (f = 70 kHz, which corresponds with f_{0p}). Due to the low coupling and operation at f_{0p}, the overcurrent may occur at the inverter and consequently overvoltage at the primary coil and the capacitive compensation. High currents are caused by small values of input impedance $\hat{Z}$ given by $\hat{Z}_p + \hat{Z}_r$: Small coupling results in minimal

reflected impedance $\hat{Z}_r$ according to (11), and due to operation at f_{0p}, the primary impedance $\hat{Z}_p$ is given only by the primary ESR R_p. In case of the first control scheme ($f = 75.7$ kHz), the input currents are limited by primary side reactance X_p which is 12.5 Ω for parameters in Table 36 and $f = 75.7$ kHz.

The DC-to-DC efficiency during one displacement cycle is depicted in Fig. 103. Even though the efficiency ZPA frequency tracking scheme ($f = f_{PLL}$) is lower than for the fixed frequency control at f_{0p} ($f = 70$ kHz) by approximately 5 %, it is still above 85 % for most of the cycle.

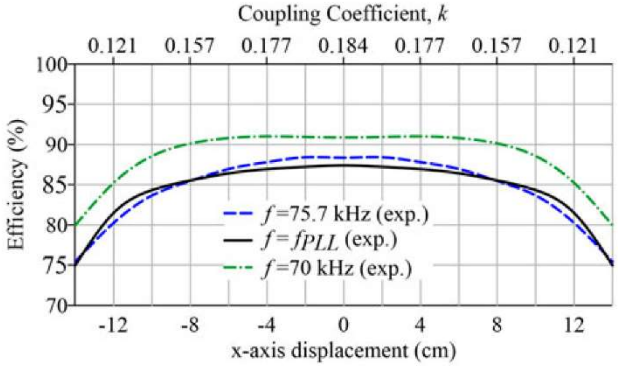

Fig. 103: DC-to-DC efficiency with respect to x axis displacement for all three frequency control schemes. Source [206].

The system is tested for variation in RL, where it performs also well (see Fig. 104).

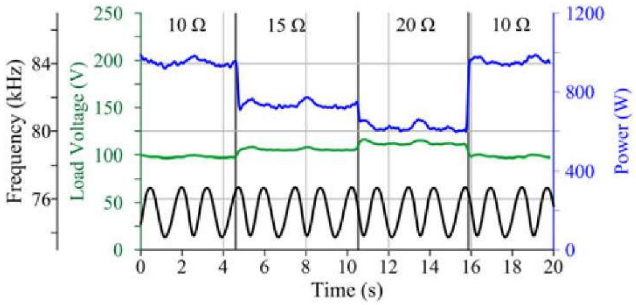

Fig. 104: Output power P_{out} and DC load voltage for varying load and periodical displacement. Source [206].

The IPT system presented in [206] performs well under displacement and load change. It demonstrates possibility of this type of frequency control to avoid impacts of bifurcation phenomena even under very dynamic conditions. However, if it was used as designed, it would be probably unusable for UUV applications, as water absorbs the infrared radiation with a significant rate. Thus, the communication based on infrared would work only for a very limited distance between primary and secondary.

9.3 Summary of Bifurcation Control Methods

This chapter examined the control methods to prevent the bifurcation phenomena occurrence or mitigate its impacts during the device operation. The first part of the chapter is focused on the passive control methods, which are applied during the design phase. The overview of the selected main control methods presented in literature is listed. These methods include:

- Design guidelines to place the operating point in the bifurcation free regions [100].
- Use of antiparallel loops, which prevent the OP movement into bifurcation [104].
- Detuning (i.e., $f_{0p} \neq f_{0s}$) [100] and adding the series inductors in both sides of IPT system [199] to mitigate impacts of bifurcation.

Two novel control methods to prevent bifurcation occurrence are presented. In the first method, the series inductor is added in the primary side, which moves the operating point above the selected boundary $BB2_o$ (to prevent OAB) or BB3 (to prevent PB). The second is based on decreasing the resonance frequency f_0, which also moves the operating point above the selected boundary. Both methods were evaluated by measurement and simulations. Also, the guidelines based on the 2D Q_L state diagram are presented for evaluating bifurcation in multiple operating points given by variation of coupling or load.

The active control methods are examined in the second part of the chapter. On the contrary to the passive methods which are set in design phase, active methods adaptively adjust the circuit parameters or operating frequency during operation to prevent the bifurcation negatively impacting the IPT system. Overviews of two widely used methods were presented. The first considered the adaptive impedance matching which is aimed for fixed frequency system. The second examined the constant output voltage tracking for variable frequency systems, which is based on tracking the frequency of ZPA between the input voltage $\hat{V}_{in}$ and output current $\hat{I}_{out}$ [202]–[206].

Each presented control method has its advantages and disadvantages; thus, their use depends on the specific application. However, in the author opinion, the design of any IPT system should begin by applying the guidelines in Chapter 9.1.1 and the IPT system should be tailored for the given application and its disturbances, instead of trying to make one design work in different applications by adding extra circuitry.

10 Conclusions

This work addresses the bifurcation phenomena from the perspective of their mathematical description, mechanism of their emergence, their impacts on the device operation and control methods to prevent their occurrence or mitigate their negative impacts. Initially, only bifurcation viewed as the splitting of the input phase φ_{in}. However, due to its close relationship, the analysis was extended to the frequency splitting of the output power P_{out}. To examine their mechanisms, the mathematical description of the input impedance amplitude Z splitting was also developed.

The examination of their mechanism showed that a shift of perspective is necessary: These are not three separate phenomena, but three manifestations of a single underlying phenomenon, which is the of growing secondary side influence (represented by the reflected impedance $\hat{Z}_r$) on the primary side.

To reflect this finding and improve the comprehensives of the thesis the nomenclature was adjusted: Namely, the underlying process of growing secondary side influence on the primary is called "bifurcation". It manifests as the splitting of the input phase φ_{in} zero crossing ("phase bifurcation" or "PB"), the splitting of the input impedance amplitude Z minimum ("input impedance amplitude" or "IAB") and splitting of the output power P_{out} maximum ("output amplitude impedance" or "OAB").

In this work, a general parameter model describing bifurcation phenomena was developed together with novel visual tools for analysis of bifurcation. Using the developed model, the influence of circuit parameter on bifurcation occurrence and the mechanism of each bifurcation phenomena was examined. The impacts of bifurcation on device design and operation were analyzed. Also, a novel method which employs bifurcation to estimate the coupling coefficient k was developed. Existing active and passive control methods to prevent the bifurcation occurrence or mitigate the impacts of bifurcation on IPT system operation were examined and two novel passive control methods for preventing the bifurcation occurrence were proposed.

10.1 Overview of Results

Chapter 2 is considered as an overview of the current state of IPT technology. Different pad (i.e., coil) types are examined together with materials comprising the winding, magnetic core and shielding. Discussion of main compensation topologies follows. The chapter is closed with an overview of electronic converters for IPT, which debates investigates used converter topologies, semiconductor components and control methods.

Chapter 3 establishes the equivalent AC circuit model of the IPT system with SS compensation. It also presents the main equations describing the circuit impedances and input and output voltages and currents. The equations for input and output power and efficiency are also derived. These equations are used in further analyses throughout the thesis.

Chapter 4 presents the instruments, which were used for verification of mathematical model and bifurcation control strategies proposed in the thesis. These instruments include a measurement setup and model in MATLAB Simulink. The measurement setup is specifically designed for the bifurcation phenomena analysis; thus, it is powered from a sinusoidal source and allows control of all circuit parameters. Also, some specific issues connected with measurement of frequencies in order of 100 kHz are discussed, such as the influence of current shunt inductance or necessity of active tuning.

Chapter 5 provides an overview of bifurcation phenomena, which occur in IPT systems. All three bifurcation phenomena (splitting of the input phase φ_{in} zero crossing, splitting of the input impedance amplitude Z minimum and splitting of the output power P_{out} maximum) are linked to the reflected impedance $\hat{Z}_r$, which is reflected by establishing the novel nomenclature (PB, OAB and IAB). The term "course of bifurcation" is defined as the process of growing secondary side influence (represented by the reflected impedance $\hat{Z}_r$) on the primary side which gradually manifests as IAB, OAB and PB.

Chapter 6 summarizes the mathematical description of bifurcation and all its manifestations in the general parameter model. To unify the mathematical descriptions of PB and OAB, a novel description of OAB is developed based on the normalization approach presented by Wang et al. in [17] for PB. The description of IAB is also based on the normalized impedance amplitude; however, due to the high order of its governing equation only the numerical solution was possible. Thanks to the normalization, PB, IAB and OAB could be unified under a single general parameter model, which describes any system only by three parameters: primary and secondary loaded quality factors Q_{Lp} and Q_{Ls}, and normalized frequency u. The mathematical description is summarized in the Q_L state diagram. This novel visual tool places the operating point, trajectory, or area of the IPT system in the context of the bifurcation phenomena. It allows comprehensive evaluation of the bifurcation influence on the input and quantities, e.g., input phase φ_{in}, output voltage V_{out}, current I_{out}, or power P_{out} and efficiency η_{tr}. Thanks to this it improves the analysis of system regulation.

Chapter 7 analyzes the bifurcation phenomena under the framework of general parameter model. At first, the behavior of bifurcation frequencies for different combinations of Q_{Lp} and Q_{Ls} is examined with the use of the 2D Q_L state diagram. Analysis of the influence of the circuit parameters L_p, L_s, M, f_0 and R_L figuring in calculation of the loaded quality factors Q_{Lp} and Q_{Ls} shows that change of any of these parameters may cause bifurcation. The distinction between the independent and coupled parameters was discussed, with ways to evaluate the influence of a set of coupled parameters on the operating point movement. Based on these findings, the rules for construction of the operating trajectories and operating areas were developed, together with examining their movement due to a parameter change.

The mechanism of IAB, OAB and PB is analyzed in the context of the course of bifurcation. At first, the input impedance amplitude Z and phase φ_{in} splitting is discussed as the product of the interactions between the reflected impedance $\hat{Z}_r$ and primary impedance. Then the transition from the input impedance amplitude Z to the output power P_{out} is examined to analyze the mechanism of OAB. These analyses confirm the connection between the reflected impedance $\hat{Z}_r$ change and IAB, OAB and PB. They also showed that the splitting of input current amplitude I_{in} is also described by IAB. Similarly, the splitting of the output voltage V_{out} and current I_{out}, together with the splitting of the input active power P_{in} is described by OAB.

The role of the primary and secondary ESR R_p and R_s in the mechanism of bifurcation is discussed and their influence on the bifurcation boundary values is examined.

Chapter 8 examines the selection of the optimal operating area from the perspective of efficiency maximization, input phase φ_{in}, and ZVS, and ways to achieve required output power P_{out} in the context of the course of bifurcation. The impacts of bifurcation on system regulation are also discussed. Specifically, it is showed that the OAB frequencies form limits of stability for frequency regulation, which is demonstrated with an example using a Qi based regulation approach.

Bifurcation does not have only negative impacts – it can be advantageously employed for estimation of the coupling coefficient k. In this chapter a novel method presented, which estimates k based on the asymptotes of ZPA frequencies in deep bifurcation. The method involves temporarily operating the system in bifurcation by short-circuiting the load and measuring the zero phase angle frequencies at the primary. The method can be used by control algorithms that require the value of k, and is especially suitable for implementation at the startup of certain applications such as EV stationary charging. The proposed method provides good estimates (average absolute error of 3.62%) for a wide range of coupling coefficients ($k \in \langle 0.08, 0.36 \rangle$).

Chapter 9 focuses on the control methods to prevent the bifurcation phenomena occurrence or mitigate its impacts during the device operation. The first part of the chapter is focused on the passive control methods, which are applied during the design phase. The second part of the chapter examines the active control methods, which adaptively adjust the circuit parameters or operating frequency during operation to prevent the bifurcation negatively impacting the IPT system.

An overview of existing methods is provided, together with presenting two novel passive control methods. In the first method the series inductor is added in the primary side, and in the second the resonance frequency of the IPT system is decreased, which in both cases results is the operating point movement outside bifurcation. Both methods were evaluated by measurement and simulations.

The author considers the most significant contributions of the thesis to be the general parameter model and the novel method for estimation of the coupling coefficient k. Thanks to the applied normalization, the general parameter model has the following main benefits:

1. Simplification, which is especially impactful in the case of OAB (frequency splitting), making the resulting formulas of P_{out} local extrema significantly shorter in comparison with their counterparts based on the equivalent circuit model.

2. Easy comparison of the bifurcation phenomena in different systems – the bifurcation occurrence depends only on Q_{Lp} and Q_{Ls} (u does not affect the bifurcation occurrence), which may gain the same values for very different systems (e.g., phone charger vs electric vehicle charger).

3. The generalized conditions for the bifurcation phenomena occurrence are given only by Q_{Lp} and Q_{Ls}. Thanks to this, they apply to any operating trajectory, regardless of whether the trajectory follows the change of one circuit parameter (e.g., change of equivalent load resistance R_L) or multiple circuit parameters (e.g., or change of the primary, secondary, and mutual inductances due to misalignment).

The novel method for estimation of the coupling coefficient k provides accurate estimates (average absolute error of 3.62%) for a wide range of coupling coefficients ($k \in \langle 0.08, 0.36 \rangle$), yet it does not require a-priori information about the system (except for an approximate frequency range for the frequency response measurement) and it also requires only the primary side measurements.

10.2 Fulfillment of the Thesis Objectives

I consider all the objectives presented in Chapter 1.3 fulfilled. Specifically, the presented work meets the objectives as follows.

1) Compose an overview of inductively coupled power transfer systems, existing descriptions of the bifurcation phenomena and the bifurcation control methods.
Overview of the inductively coupled power transfer technology is presented in Chapters 1.2 and 2. Existing descriptions of the bifurcation phenomena are listed in Chapters 6.2 and 6.3. Overview of the existing passive and active bifurcation control methods are listed in Chapters 9.1 and 9.2, respectively.

2) Choose a suitable mathematical model of a selected IPT system for the bifurcation analysis.
Initial equivalent circuit model is presented in Chapter 2. Novel general parameter model is developed in Chapter 6.

3) Specify and explain the term "bifurcation phenomena".
Term "bifurcation phenomena", which encompasses phase bifurcation, output amplitude bifurcation (frequency splitting) and input amplitude bifurcation is specified in Chapter 5.

4) Assemble or derive the suitable mathematical description of the bifurcation phenomena for the analysis.
The mathematical description of the bifurcation phenomena is presented in Chapter 6.

5) Verify the mathematical description by measurement and simulation.
Measurement setup and Simulink model for verification is presented in Chapter 4. The verification of mathematical description is listed together with each respective mathematical description in Chapter 6. The influence of the primary and secondary ESRs R_p and R_s on the bifurcation boundaries is examined in Chapter 7.5.

6) Analyze the bifurcation mechanism and its impacts on device operation.
The mechanism of bifurcation and influence of circuit parameters is analyzed in Chapter 7. Impacts of bifurcation on the device operation are examined in Chapter 8.

7) Examine the existing methods for bifurcation control or if necessary, develop new control methods.
The existing passive methods for bifurcation control are examined in Chapters 9.1.1 through 9.1.3 and the active methods for bifurcation control in Chapter 9.2. Two novel passive methods for preventing bifurcation occurrence are proposed. The first method, which is based on adding a series inductor to the primary side is presented in Chapter 9.1.4. The second method is based on decreasing the resonance frequency f_0 and it is presented in Chapter 9.1.5. Evaluation of bifurcation phenomena and control method performance for parameter ranges, which uses the 2D Q_L state diagram is presented in Chapter 9.1.6.

8) Verify the selected bifurcation control methods by measurement and simulation.
The proposed passive bifurcation control methods are tested by measurement and simulation in Chapters 9.1.4 and 9.1.5.

9) Evaluate the obtained results of simulations and measurement.
The obtained measurement and simulation results for selected bifurcation control methods are evaluated in Chapters 9.1.4 and 9.1.5.

10.3 Suggestions for Future Work

The general parameter model, 2D Q_L state diagram and diagram sections allow easy examination of bifurcation phenomena under various condition. The methodology of their use in device design and evaluation should be further elaborated.

Presented analysis of the bifurcation phenomena was limited on the two-coil IPT system with series-series compensation. It is recommended to extend the analysis to other basic compensation topologies (SP, PS, PP) followed by the more complex topologies such as LCC, double LCC, LCC-SP, and also other coil arrangements (e.g., four-coil IPT systems).

Similarly, it should be explored how the method for coupling coefficient k estimation based on the bifurcation asymptotes can be extended to other compensation topologies. Also, its performance including dynamic characteristics (e.g., minimal necessary measurement time) should be evaluated in a non-idealized setup by implementing it in an inverter.

11 References

[1] Z. Zhang, H. Pang, A. Georgiadis, and C. Cecati, “Wireless Power Transfer - An Overview,” *IEEE Trans. Ind. Electron.*, vol. 66, no. 2, pp. 1044–1058, Feb. 2019, doi: 10.1109/TIE.2018.2835378.

[2] G. A. Covic and J. T. Boys, “Inductive Power Transfer,” *Proc. IEEE*, vol. 101, no. 6, pp. 1276–1289, Jun. 2013, doi: 10.1109/JPROC.2013.2244536.

[3] G. A. Covic and J. T. Boys, “Modern Trends in Inductive Power Transfer for Transportation Applications,” *IEEE J. Emerg. Sel. Top. Power Electron.*, vol. 1, no. 1, pp. 28–41, Mar. 2013, doi: 10.1109/JESTPE.2013.2264473.

[4] N. Tesla, “System of transmission of electrical energy,” U. S. Patent 645,576, Mar. 20, 1900.

[5] A. W. Green and J. T. Boys, “10 kHz inductively coupled power transfer-concept and control,” in *1994 Fifth International Conference on Power Electronics and Variable-Speed Drives*, Oct. 1994, pp. 694–699, doi: 10.1049/cp:19941049.

[6] S. Li and C. Mi, “Wireless Power Transfer for Electric Vehicle Applications,” *IEEE J. Emerg. Sel. Top. Power Electron.*, vol. 3, no. 1, pp. 4–17, Mar. 2015, doi: 10.1109/JESTPE.2014.2319453.

[7] M. P. Kazmierkowski and A. J. Moradewicz, “Unplugged But Connected: Review of Contactless Energy Transfer Systems,” *IEEE Ind. Electron. Mag.*, vol. 6, no. 4, pp. 47–55, Dec. 2012, doi: 10.1109/MIE.2012.2220869.

[8] S. Y. Hui, “Planar wireless charging technology for portable electronic products and Qi,” *Proc. IEEE*, vol. 101, no. 6, pp. 1290–1301, Jun. 2013, doi: 10.1109/JPROC.2013.2246531.

[9] J. S. Ho, S. Kim, and A. S. Y. Poon, “Midfield wireless powering for implantable systems,” *Proc. IEEE*, vol. 101, no. 6, pp. 1369–1378, Jun. 2013, doi: 10.1109/JPROC.2013.2251851.

[10] A. Ma and A. S. Y. Poon, “Midfield wireless power transfer for bioelectronics,” *IEEE Circuits Syst. Mag.*, vol. 15, no. 2, pp. 54–60, 2015, doi: 10.1109/MCAS.2015.2418999.

[11] D. van Wageningen and T. Staring, “The Qi Wireless Power Standard,” in *Proceedings of 14th International Power Electronics and Motion Control Conference EPE-PEMC 2010*, Sep. 2010, pp. S15-25-S15-32, doi: 10.1109/EPEPEMC.2010.5606673.

[12] The Wireless Power Consortium, “The Qi Wireless Power Transfer System Power Class 0 Specification Parts 1 and 2: Interface Definitions,” Feb. 2018. https://www.wirelesspowerconsortium.com (accessed Jun. 11, 2021).

[13] The Wireless Power Consortium, “The Qi Wireless Power Transfer System Power Class 0 Specification Part 4: Reference Designs,” Feb. 2018. https://www.wirelesspowerconsortium.com (accessed Jun. 11, 2021).

[14] “AirFueI Alliance Resonant Wireless Power Transfer (WPT) System Baseline System Specification (BSS),” AFA TS-0010-A v2.00, Jul. 2018.

[15] “Wireless power transfer for light-duty plug-in/electric vehicles and alignment methodology,” SAE J2954, 2020.

[16] “Electric vehicle wireless power transfer (WPT) systems - Part 1: General requirements,” IEC 61980-1:2020, 2020.

[17] C.-S. Wang, G. A. Covic, and O. H. Stielau, “Power transfer capability and bifurcation phenomena of loosely coupled inductive power transfer systems,” *IEEE Trans. Ind. Electron.*, vol. 51, no. 1, pp. 148–157, Feb. 2004, doi: 10.1109/TIE.2003.822038.

[18] A. P. Sample, D. T. Meyer, and J. R. Smith, “Analysis, Experimental Results, and Range Adaptation of Magnetically Coupled Resonators for Wireless Power Transfer,” *IEEE Trans. Ind. Electron.*, vol. 58, no. 2, pp. 544–554, Feb. 2011, doi: 10.1109/TIE.2010.2046002.

[19] R. Huang, B. Zhang, D. Qiu, and Y. Zhang, “Frequency Splitting Phenomena of Magnetic Resonant Coupling Wireless Power Transfer,” *IEEE Trans. Magn.*, vol. 50, no. 11, pp. 1–4, Nov. 2014, doi: 10.1109/TMAG.2014.2331143.

[20] M. Kosik, A. D. Scher, and J. Lettl, “Description, Mechanism and Impacts of Bifurcation and Frequency Splitting on Inductive Power Transfer,” *IEEE Access*, 2021 (in review).

[21] W. Q. Niu, J. X. Chu, W. Gu, and A. D. Shen, “Exact Analysis of Frequency Splitting Phenomena of Contactless Power Transfer Systems,” *IEEE Trans. Circuits Syst. I Regul. Pap.*, vol. 60, no. 6, pp. 1670–1677, Jun. 2013, doi: 10.1109/TCSI.2012.2221172.

[22] H. Feng, R. Tavakoli, O. C. Onar, and Z. Pantic, “Advances in High-Power Wireless Charging Systems: Overview and Design Considerations,” *IEEE Trans. Transp. Electrif.*, vol. 6, no. 3, pp. 886–919, Sep. 2020, doi: 10.1109/TTE.2020.3012543.

[23] A. A. S. Mohamed, A. A. Shaier, H. Metwally, and S. I. Selem, “A comprehensive overview of inductive pad in electric vehicles stationary charging,” *Appl. Energy*, vol. 262, p. 114584, 2020, doi: 10.1016/j.apenergy.2020.114584.

[24] M. G. L. Roes, J. L. Duarte, M. A. M. Hendrix, and E. Lomonova, “Acoustic energy transfer: a review,” *Ind. Electron. IEEE Trans.*, vol. 60, no. 1, pp. 242–248, Jan. 2013, doi: 10.1109/TIE.2012.2202362.

[25] J. Charthad, M. J. Weber, T. C. Chang, and A. Arbabian, “A mm-Sized Implantable Medical Device (IMD)

With Ultrasonic Power Transfer and a Hybrid Bi-Directional Data Link," *IEEE J. Solid-State Circuits*, vol. 50, no. 8, pp. 1741–1753, Aug. 2015, doi: 10.1109/JSSC.2015.2427336.

[26] H. Basaeri, D. B. Christensen, and S. Roundy, "A review of acoustic power transfer for bio-medical implants," *Smart Mater. Struct.*, vol. 25, no. 12, pp. 1–23, Nov. 2016, doi: 10.1088/0964-1726/25/12/123001.

[27] C. A. Balanis, *Advanced Engineering Electromagnetics*, 2nd Editio. New Jersey: John Wiley & Sons, 2012.

[28] J. Kraček, "Wireless Power Transmission," CTU in Prague, Prague, 2015.

[29] C. R. Valenta and G. D. Durgin, "Harvesting wireless power: Survey of energy-harvester conversion efficiency in far-field, wireless power transfer systems," *IEEE Microw. Mag.*, vol. 15, no. 4, pp. 108–120, Jun. 2014, doi: 10.1109/MMM.2014.2309499.

[30] X. Lu, P. Wang, D. Niyato, D. I. Kim, and Z. Han, "Wireless Charging Technologies: Fundamentals, Standards, and Network Applications," *IEEE Commun. Surv. Tutorials*, vol. 18, no. 2, pp. 1413–1452, 2016, doi: 10.1109/COMST.2015.2499783.

[31] W. C. Brown, "The History of Power Transmission by Radio Waves," *IEEE Trans. Microw. Theory Tech.*, vol. 32, no. 9, pp. 1230–1242, Sep. 1984, doi: 10.1109/TMTT.1984.1132833.

[32] K. Takayama, S. Hiramatsu, and M. Shiho, "CW 100 MW microwave power transfer in space," in *Particle Accelerator Conference, 1991. Accelerator Science and Technology., Conference Record of the 1991 IEEE*, 1991, pp. 2625–2627.

[33] M. Kline, I. Izyumin, B. Boser, and S. Sanders, "Capacitive power transfer for contactless charging," in *2011 Twenty-Sixth Annual IEEE Applied Power Electronics Conference and Exposition (APEC)*, Mar. 2011, pp. 1398–1404, doi: 10.1109/APEC.2011.5744775.

[34] J. Dai and D. C. Ludois, "A Survey of Wireless Power Transfer and a Critical Comparison of Inductive and Capacitive Coupling for Small Gap Applications," *IEEE Trans. Power Electron.*, vol. 30, no. 11, pp. 6017–6029, Nov. 2015, doi: 10.1109/TPEL.2015.2415253.

[35] S. Y. R. Hui, W. Zhong, and C. K. Lee, "A Critical Review of Recent Progress in Mid-Range Wireless Power Transfer," *IEEE Trans. Power Electron.*, vol. 29, no. 9, pp. 4500–4511, Sep. 2014, doi: 10.1109/TPEL.2013.2249670.

[36] A. Foote and O. C. Onar, "A review of high-power wireless power transfer," in *2017 IEEE Transportation Electrification Conference and Expo (ITEC)*, Jun. 2017, pp. 234–240, doi: 10.1109/ITEC.2017.7993277.

[37] B. K. Kusserow, "The use of a magnetic field to remotely power an implantable blood pump. Preliminary report," *Trans. Am. Soc. Artif. Intern. Organs*, vol. 6, no. 1, pp. 292–294, 1960.

[38] J. C. Schuder, "Powering an Artificial Heart: Birth of the Inductively Coupled-Radio Frequency System in 1960," *Artif. Organs*, vol. 26, no. 11, pp. 909–915, 1960.

[39] J. G. Bolger, F. A. Kirsten, and L. S. Ng, "Inductive power coupling for an electric highway system," in *28th IEEE Vehicular Technology Conference*, Mar. 1978, vol. 28, pp. 137–144, doi: 10.1109/VTC.1978.1622522.

[40] M. Eghtesadi, "Inductive power transfer to an electric vehicle-analytical model," in *40th IEEE Conference on Vehicular Technology*, May 1990, pp. 100–104, doi: 10.1109/VETEC.1990.110303.

[41] "Roadway powered electric vehicle project track construction and testing program phase 3D," Systems Control Technology, Inc., Palo Alto, CA, USA, California PATH research paper UCB-ITS-PRR-94-07, 10551425, 1994.

[42] S. Y. R. Hui and W. W. C. Ho, "A New Generation of Universal Contactless Battery Charging Platform for Portable Consumer Electronic Equipment," *IEEE Trans. Power Electron.*, vol. 20, no. 3, pp. 620–627, May 2005, doi: 10.1109/TPEL.2005.846550.

[43] G. Wang, W. Liu, M. Sivaprakasam, and G. A. Kendir, "Design and Analysis of an Adaptive Transcutaneous Power Telemetry for Biomedical Implants," *IEEE Trans. Circuits Syst. I Regul. Pap.*, vol. 52, no. 10, pp. 2109–2117, Oct. 2005, doi: 10.1109/TCSI.2005.852923.

[44] P. Si *et al.*, "Wireless Power Supply for Implantable Biomedical Device Based on Primary Input Voltage Regulation," in *2007 2nd IEEE Conference on Industrial Electronics and Applications*, May 2007, pp. 235–239, doi: 10.1109/ICIEA.2007.4318406.

[45] A. Kurs, A. Karalis, R. Moffatt, J. D. Joannopoulos, P. Fisher, and M. Soljačić, "Wireless power transfer via strongly coupled magnetic resonances," *Science (80-.).*, vol. 317, no. 5834, pp. 83–86, 2007.

[46] "Wireless Power Consortium, Inc." https://www.wirelesspowerconsortium.com/ (accessed May 27, 2021).

[47] "AirFuel Alliance." https://airfuel.org/ (accessed May 27, 2021).

[48] "Plugless Power, Inc." https://www.pluglesspower.com/ (accessed May 27, 2021).

[49] "WiTricity Corporation." https://witricity.com/ (accessed May 27, 2021).

[50] G. A. J. Elliott, S. Raabe, G. A. Covic, and J. T. Boys, "Multiphase Pickups for Large Lateral Tolerance Contactless Power-Transfer Systems," *IEEE Trans. Ind. Electron.*, vol. 57, no. 5, pp. 1590–1598, May 2010, doi: 10.1109/TIE.2009.2031184.

[51] S. Lukic and Z. Pantic, "Cutting the Cord: Static and Dynamic Inductive Wireless Charging of Electric Vehicles," *IEEE Electrif. Mag.*, vol. 1, no. 1, pp. 57–64, Sep. 2013, doi: 10.1109/MELE.2013.2273228.

[52] J. T. Boys and G. A. Covic, “The Inductive Power Transfer Story at the University of Auckland,” *IEEE Circuits Syst. Mag.*, vol. 15, no. 2, pp. 6–27, 2015, doi: 10.1109/MCAS.2015.2418972.

[53] C. C. Mi, G. Buja, S. Y. Choi, and C. T. Rim, “Modern Advances in Wireless Power Transfer Systems for Roadway Powered Electric Vehicles,” *IEEE Trans. Ind. Electron.*, vol. 63, no. 10, pp. 6533–6545, Oct. 2016, doi: 10.1109/TIE.2016.2574993.

[54] K. W. Klontz, D. M. Divan, D. W. Novotny, and R. D. Lorenz, “Contactless Power Delivery System for Mining Applications,” *IEEE Trans. Ind. Appl.*, vol. 31, no. 1, pp. 27–35, Jan. 1995, doi: 10.1109/28.363053.

[55] “Power electronics - The University of Auckland.” https://www.auckland.ac.nz/en/engineering/our-research/discover/research-areas-and-facilities/power-electronics.html (accessed May 26, 2021).

[56] O. H. Stielau and G. A. Covic, “Design of loosely coupled inductive power transfer systems,” in *Power System Technology, 2000. Proceedings. PowerCon 2000. International Conference on*, 2000, vol. 1, pp. 85–90 vol.1, doi: 10.1109/ICPST.2000.900036.

[57] C.-S. Wang, O. H. Stielau, and G. A. Covic, “Design considerations for a contactless electric vehicle battery charger,” *IEEE Trans. Ind. Electron.*, vol. 52, no. 5, pp. 1308–1314, Oct. 2005, doi: 10.1109/TIE.2005.855672.

[58] N. A. Keeling, G. A. Covic, and J. T. Boys, “A Unity-Power-Factor IPT Pickup for High-Power Applications,” *IEEE Trans. Ind. Electron.*, vol. 57, no. 2, pp. 744–751, Feb. 2010, doi: 10.1109/TIE.2009.2027255.

[59] Z. Luo, X. Wei, M. G. S. Pearce, and G. A. Covic, “Multiobjective Optimization of Inductive Power Transfer Double-D Pads for Electric Vehicles,” *IEEE Trans. Power Electron.*, vol. 36, no. 5, pp. 5135–5146, May 2021, doi: 10.1109/TPEL.2020.3029789.

[60] M. Budhia, J. T. Boys, G. A. Covic, and C. Y. Huang, “Development of a single-sided flux magnetic coupler for electric vehicle IPT charging systems,” *IEEE Trans. Ind. Electron.*, vol. 60, no. 1, pp. 318–328, Jan. 2013, doi: 10.1109/TIE.2011.2179274.

[61] M. Budhia, G. A. Covic, and J. T. Boys, “Design and Optimization of Circular Magnetic Structures for Lumped Inductive Power Transfer Systems,” *IEEE Trans. Power Electron.*, vol. 26, no. 11, pp. 3096–3108, Nov. 2011, doi: 10.1109/TPEL.2011.2143730.

[62] G. A. Covic, J. T. Boys, M. L. G. Kissin, and H. G. Lu, “A Three-Phase Inductive Power Transfer System for Roadway-Powered Vehicles,” in *IEEE Transactions on Industrial Electronics*, Dec. 2007, vol. 54, no. 6, pp. 3370–3378, doi: 10.1109/TIE.2007.904025.

[63] V. Zahiri Barsari, D. J. Thrimawithana, and G. A. Covic, “An Inductive Coupler Array for In-Motion Wireless Charging of Electric Vehicles,” *IEEE Trans. Power Electron.*, pp. 1–1, 2021, doi: 10.1109/TPEL.2021.3058666.

[64] A. P. Hu, C. Liu, and H. L. Li, “A Novel Contactless Battery Charging System for Soccer Playing Robot,” in *2008 15th International Conference on Mechatronics and Machine Vision in Practice*, Dec. 2008, pp. 646–650, doi: 10.1109/MMVIP.2008.4749606.

[65] L. Huang, A. P. Hu, A. K. Swain, and Y. Su, “Z-Impedance Compensation for Wireless Power Transfer Based on Electric Field,” *IEEE Trans. Power Electron.*, vol. 31, no. 11, pp. 7556–7563, Nov. 2016, doi: 10.1109/TPEL.2016.2557461.

[66] “Oak Ridge National Laboratory - Electric Drives Research Group.” https://www.ornl.gov/group/electric-drives-research (accessed May 26, 2021).

[67] O. C. Onar, J. M. Miller, S. L. Campbell, C. Coomer, C. P. White, and L. E. Seiber, “A Novel Wireless Power Transfer for In-Motion EV/PHEV Charging,” in *2013 Twenty-Eighth Annual IEEE Applied Power Electronics Conference and Exposition (APEC)*, Mar. 2013, pp. 3073–3080, doi: 10.1109/APEC.2013.6520738.

[68] O. C. Onar, J. M. Miller, S. L. Campbell, C. Coomer, C. P. White, and L. E. Seiber, “Oak Ridge National Laboratory Wireless Power Transfer Development for Sustainable Campus Initiative,” in *2013 IEEE Transportation Electrification Conference and Expo (ITEC)*, Jun. 2013, pp. 1–8, doi: 10.1109/ITEC.2013.6574506.

[69] J. M. Miller, O. C. Onar, and M. Chinthavali, “Primary-Side Power Flow Control of Wireless Power Transfer for Electric Vehicle Charging,” *IEEE J. Emerg. Sel. Top. Power Electron.*, vol. 3, no. 1, pp. 147–162, Mar. 2015, doi: 10.1109/JESTPE.2014.2382569.

[70] J. Pries, V. P. N. Galigekere, O. C. Onar, and G. J. Su, “A 50-kW Three-Phase Wireless Power Transfer System Using Bipolar Windings and Series Resonant Networks for Rotating Magnetic Fields,” *IEEE Trans. Power Electron.*, vol. 35, no. 5, pp. 4500–4517, May 2020, doi: 10.1109/TPEL.2019.2942065.

[71] J. M. Miller *et al.*, “Demonstrating Dynamic Wireless Charging of an Electric Vehicle: The Benefit of Electrochemical Capacitor Smoothing,” *IEEE Power Electron. Mag.*, vol. 1, no. 1, pp. 12–24, Mar. 2014, doi: 10.1109/MPEL.2014.2300978.

[72] J. M. Miller, P. T. Jones, J. M. Li, and O. C. Onar, “ORNL Experience and Challenges Facing Dynamic Wireless Power Charging of EV’s,” *IEEE Circuits Syst. Mag.*, vol. 15, no. 2, pp. 40–53, 2015, doi: 10.1109/MCAS.2015.2419012.

[73] V. P. Galigekere *et al.*, “Design and Implementation of an Optimized 100 kW Stationary Wireless

Charging System for EV Battery Recharging," in *2018 IEEE Energy Conversion Congress and Exposition (ECCE)*, Sep. 2018, pp. 3587–3592, doi: 10.1109/ECCE.2018.8557590.

[74] S. Lee, J. Huh, C. Park, N. S. Choi, G. H. Cho, and C. T. Rim, "On-Line Electric Vehicle Using Inductive Power Transfer System," in *2010 IEEE Energy Conversion Congress and Exposition*, Sep. 2010, pp. 1598–1601, doi: 10.1109/ECCE.2010.5618092.

[75] J. Huh, S. W. Lee, W. Y. Lee, G. H. Cho, and C. T. Rim, "Narrow-Width Inductive Power Transfer System for Online Electrical Vehicles," *IEEE Trans. Power Electron.*, vol. 26, no. 12, pp. 3666–3679, Dec. 2011, doi: 10.1109/TPEL.2011.2160972.

[76] J. Shin *et al.*, "Design and Implementation of Shaped Magnetic-Resonance-Based Wireless Power Transfer System for Roadway-Powered Moving Electric Vehicles," *IEEE Trans. Ind. Electron.*, vol. 61, no. 3, pp. 1179–1192, Mar. 2014, doi: 10.1109/TIE.2013.2258294.

[77] S. Y. Jeong, J. H. Park, G. P. Hong, and C. T. Rim, "Autotuning Control System by Variation of Self-Inductance for Dynamic Wireless EV Charging with Small Air Gap," *IEEE Trans. Power Electron.*, vol. 34, no. 6, pp. 5165–5174, Jun. 2019, doi: 10.1109/TPEL.2018.2866412.

[78] E. S. Lee, Y. H. Sohn, B. G. Choi, S. H. Han, and C. T. Rim, "A Modularized IPT with Magnetic Shielding for a Wide-Range Ubiquitous Wi-Power Zone," *IEEE Trans. Power Electron.*, vol. 33, no. 11, pp. 9669–9690, Nov. 2018, doi: 10.1109/TPEL.2017.2789201.

[79] J. H. Kim *et al.*, "Plane-Type Receiving Coil with Minimum Number of Coils for Omnidirectional Wireless Power Transfer," *IEEE Trans. Power Electron.*, vol. 35, no. 6, pp. 6165–6174, Jun. 2020, doi: 10.1109/TPEL.2019.2952907.

[80] S. Y. Jeong, V. X. Thai, J. H. Park, and C. T. Rim, "Self-Inductance-Based Metal Object Detection With Mistuned Resonant Circuits and Nullifying Induced Voltage for Wireless EV Chargers," *IEEE Trans. Power Electron.*, vol. 34, no. 1, pp. 748–758, Jan. 2019, doi: 10.1109/TPEL.2018.2813437.

[81] "Wireless Power Lab at Imperial College London." https://www.imperial.ac.uk/wireless-power (accessed May 26, 2021).

[82] S. Aldhaher, D. C. Yates, and P. D. Mitcheson, "Design and Development of a Class EF2 Inverter and Rectifier for Multimegahertz Wireless Power Transfer Systems," *IEEE Trans. Power Electron.*, vol. 31, no. 12, pp. 8138–8150, Dec. 2016, doi: 10.1109/TPEL.2016.2521060.

[83] J. M. Arteaga, S. Aldhaher, G. Kkelis, D. C. Yates, and P. D. Mitcheson, "Multi-MHz IPT Systems for Variable Coupling," *IEEE Trans. Power Electron.*, vol. 33, no. 9, pp. 7744–7758, Sep. 2018, doi: 10.1109/TPEL.2017.2768244.

[84] J. M. Arteaga, S. Aldhaher, G. Kkelis, C. Kwan, D. C. Yates, and P. D. Mitcheson, "Dynamic Capabilities of Multi-MHz Inductive Power Transfer Systems Demonstrated with Batteryless Drones," *IEEE Trans. Power Electron.*, vol. 34, no. 6, pp. 5093–5104, Jun. 2019, doi: 10.1109/TPEL.2018.2871188.

[85] C. H. Kwan, J. M. Arteaga, S. Aldhaher, D. C. Yates, and P. D. Mitcheson, "A 600W 6.78MHz Wireless Charger for an Electric Scooter," in *2020 IEEE PELS Workshop on Emerging Technologies: Wireless Power Transfer (WoW)*, Nov. 2020, pp. 278–282, doi: 10.1109/WoW47795.2020.9291303.

[86] S. Aldhaher, P. D. Mitcheson, J. M. Arteaga, G. Kkelis, and D. C. Yates, "Light-Weight Wireless Power Transfer for Mid-Air Charging of Drones," in *2017 11th European Conference on Antennas and Propagation (EUCAP)*, Mar. 2017, pp. 336–340, doi: 10.23919/EuCAP.2017.7928799.

[87] S. Aldhaher and P. D. Mitcheson, "500W 13.56MHz Class EF Push-pull Inverter for Advanced Dynamic Wireless Power Applications," in *2019 IEEE PELS Workshop on Emerging Technologies: Wireless Power Transfer (WoW)*, Jun. 2019, pp. 263–267, doi: 10.1109/WoW45936.2019.9030603.

[88] J. Lawson, D. C. Yates, and P. D. Mitcheson, "High Q Coil Measurement for Inductive Power Transfer," *IEEE Trans. Microw. Theory Tech.*, vol. 67, no. 5, pp. 1962–1973, May 2019, doi: 10.1109/TMTT.2019.2901442.

[89] J. M. Arteaga, N. Pucci, L. Lan, and P. D. Mitcheson, "Load Characterisation in High Frequency IPT Systems using Class EF Switching Waveforms," *IEEE Trans. Power Electron.*, vol. 36, no. 10, pp. 11036–11044, Apr. 2021, doi: 10.1109/TPEL.2021.3074751.

[90] V. Kindl, T. Kavalir, R. Pechanek, B. Skala, and J. Sobra, "Key construction aspects of resonant wireless low power transfer system," in *2014 ELEKTRO*, May 2014, pp. 303–306, doi: 10.1109/ELEKTRO.2014.6848907.

[91] V. Kindl, T. Kavalir, and R. Pechanek, "Key construction aspects of low frequency wireless power transfer system using parallel resonance," in *2015 17th European Conference on Power Electronics and Applications (EPE'15 ECCE-Europe)*, Sep. 2015, pp. 1–5, doi: 10.1109/EPE.2015.7311758.

[92] "WPT Home Page - IEEE WPT." https://wpt.ieee.org/ (accessed May 27, 2021).

[93] Daifuku, "Non-Contact Power Supply Transport System Technology." https://www.daifuku.com/gb/solution/technology/wirelesspower/ (accessed May 27, 2021).

[94] "Conductix Wampfler - Inductive Power Transfer IPT." https://www.conductix.cz/cz/produkty/inductive-power-transfer-iptr (accessed May 27, 2021).

[95] Y. Fang and B. M. H. Pong, "Multiple Harmonics Analysis for Variable Frequency Asymmetrical Pulsewidth-Modulated Wireless Power Transfer Systems," *IEEE Trans. Ind. Electron.*, vol. 66, no. 5, pp. 4023–4030, May 2019, doi: 10.1109/TIE.2018.2850015.

[96] M. Kasper, R. M. Burkart, G. Deboy, and J. W. Kolar, "ZVS of Power MOSFETs Revisited," *IEEE Trans. Power Electron.*, vol. 31, no. 12, pp. 8063–8067, Dec. 2016, doi: 10.1109/TPEL.2016.2574998.

[97] Y. Jiang, L. Wang, J. Fang, R. Li, R. Han, and Y. Wang, "A High-Efficiency ZVS Wireless Power Transfer System for Electric Vehicle Charging With Variable Angle Phase Shift Control," *IEEE J. Emerg. Sel. Top. Power Electron.*, vol. 9, no. 2, pp. 2356–2372, Apr. 2021, doi: 10.1109/JESTPE.2020.2984575.

[98] C. Chen *et al.*, "Modeling and Decoupled Control of Inductive Power Transfer to Implement Constant Current/Voltage Charging and ZVS Operating for Electric Vehicles," *IEEE Access*, vol. 6, pp. 59917–59928, Oct. 2018, doi: 10.1109/ACCESS.2018.2875413.

[99] U. Iruretagoyena, A. Garcia-Bediaga, L. Mir, H. Camblong, and I. Villar, "Bifurcation limits and non-idealities effects in a three-phase dynamic IPT system," *IEEE Trans. Power Electron.*, vol. 35, no. 1, pp. 208–219, Jan. 2020, doi: 10.1109/TPEL.2019.2915834.

[100] K. Aditya and S. S. Williamson, "Design guidelines to avoid bifurcation in a series-series compensated inductive power transfer system," *IEEE Trans. Ind. Electron.*, vol. 66, no. 5, pp. 3973–3982, May 2019, doi: 10.1109/TIE.2018.2851953.

[101] A. Karalis, J. D. Joannopoulos, and M. Soljačić, "Efficient wireless non-radiative mid-range energy transfer," *Ann. Phys. (N. Y).*, vol. 323, no. 1, pp. 34–48, Jan. 2008.

[102] Y. Zhang, Z. Zhao, and K. Chen, "Frequency-splitting analysis of four-coil resonant wireless power transfer," *IEEE Trans. Ind. Appl.*, vol. 50, no. 4, pp. 2436–2445, Jul. 2014, doi: 10.1109/TIA.2013.2295007.

[103] Y. Zhang and Z. Zhao, "Frequency-splitting analysis of two-coil resonant wireless power transfer," *IEEE Antennas Wirel. Propag. Lett.*, vol. 13, pp. 400–402, 2014, doi: 10.1109/LAWP.2014.2307924.

[104] W. S. Lee, W. I. Son, K. S. Oh, and J. W. Yu, "Contactless Energy Transfer Systems Using Antiparallel Resonant Loops," *IEEE Trans. Ind. Electron.*, vol. 60, no. 1, pp. 350–359, Jan. 2013, doi: 10.1109/TIE.2011.2177611.

[105] Y. L. Lyu *et al.*, "A Method of Using Nonidentical Resonant Coils for Frequency Splitting Elimination in Wireless Power Transfer," *IEEE Trans. Power Electron.*, vol. 30, no. 11, pp. 6097–6107, Nov. 2015, doi: 10.1109/TPEL.2014.2387835.

[106] M. Petersen and F. W. Fuchs, "Investigation on power electronics topologies for inductive power transfer (IPT) systems in high power low voltage applications," in *2015 17th European Conference on Power Electronics and Applications (EPE'15 ECCE-Europe)*, Sep. 2015, pp. 1–10, doi: 10.1109/EPE.2015.7309132.

[107] J. Choi, D. Tsukiyama, Y. Tsuruda, and J. Rivas, "13.56 MHz 1.3 kW Resonant Converter with GaN FET for Wireless Power Transfer," in *2015 IEEE Wireless Power Transfer Conference (WPTC)*, May 2015, pp. 1–4, doi: 10.1109/WPT.2015.7140167.

[108] S. Wang, M. A. de Rooij, W. G. Odendaal, J. D. van Wyk, and D. Boroyevich, "Reduction of high-frequency conduction losses using a planar litz structure," *IEEE Trans. Power Electron.*, vol. 20, no. 2, pp. 261–267, Mar. 2005, doi: 10.1109/TPEL.2004.843022.

[109] A. Roßkopf, E. Bär, and C. Joffe, "Influence of inner skin- and proximity effects on conduction in litz wires," *IEEE Trans. Power Electron.*, vol. 29, no. 10, pp. 5454–5461, Oct. 2014, doi: 10.1109/TPEL.2013.2293847.

[110] Q. Deng *et al.*, "Frequency-Dependent Resistance of Litz-Wire Square Solenoid Coils and Quality Factor Optimization for Wireless Power Transfer," *IEEE Trans. Ind. Electron.*, vol. 63, no. 5, pp. 2825–2837, May 2016, doi: 10.1109/TIE.2016.2518126.

[111] T. Mizuno, S. Enoki, T. Asahina, T. Suzuki, M. Noda, and H. Shinagawa, "Reduction of proximity effect in coil using magnetoplated wire," *IEEE Trans. Magn.*, vol. 43, no. 6, pp. 2654–2656, Jun. 2007, doi: 10.1109/TMAG.2007.893716.

[112] T. Mizuno, S. Yachi, A. Kamiya, and D. Yamamoto, "Improvement in efficiency of wireless power transfer of magnetic resonant coupling using magnetoplated wire," *IEEE Trans. Magn.*, vol. 47, no. 10, pp. 4445–4448, Oct. 2011, doi: 10.1109/TMAG.2011.2158525.

[113] Z. Pantic and S. Lukic, "Computationally-Efficient, Generalized Expressions for the Proximity-Effect in Multi-Layer, Multi-Turn Tubular Coils for Wireless Power Transfer Systems," *IEEE Trans. Magn.*, vol. 49, no. 11, pp. 5404–5416, Nov. 2013, doi: 10.1109/TMAG.2013.2264486.

[114] N. Sekiya and Y. Monjugawa, "A Novel REBCO Wire Structure That Improves Coil Quality Factor in MHz Range and its Effect on Wireless Power Transfer Systems," *IEEE Trans. Appl. Supercond.*, vol. 27, no. 4, pp. 1–5, Jun. 2017, doi: 10.1109/TASC.2017.2660058.

[115] "Wireless Power Transfer for Light-Duty Plug-In/Electric Vehicles and Alignment Methodology," SAE TIR J2954 NOV2017, 2017.

[116] J. Kulikowski, "Soft magnetic ferrites — Development or stagnation?," *J. Magn. Magn. Mater.*, vol. 41, no. 1–3, pp. 56–62, 1984, doi: 10.1016/0304-8853(84)90136-7.

[117] A. Ahmad, M. S. Alam, and R. Chabaan, "A Comprehensive Review of Wireless Charging Technologies for Electric Vehicles," *IEEE Trans. Transp. Electrif.*, vol. 4, no. 1, pp. 38–63, Mar. 2017, doi: 10.1109/TTE.2017.2771619.

[118] A. Tejeda, C. Carretero, J. T. Boys, and G. A. Covic, "Ferrite-Less Circular Pad With Controlled Flux

Cancelation for EV Wireless Charging," *IEEE Trans. Power Electron.*, vol. 32, no. 11, pp. 8349–8359, Nov. 2017, doi: 10.1109/TPEL.2016.2642192.

[119] R. Bosshard, J. W. Kolar, J. Mühlethaler, I. Stevanović, B. Wunsch, and F. Canales, "Modeling and η-α-Pareto optimization of inductive power transfer coils for electric vehicle," *IEEE J. Emerg. Sel. Top. Power Electron.*, vol. 3, no. 1, pp. 50–64, Mar. 2015, doi: 10.1109/JESTPE.2014.2311302.

[120] G. M. S. Pearce, G. A. Covic, and J. T. Boys, "Robust Ferrite-Less Double D Topology for Roadway IPT Applications," *IEEE Trans. Power Electron.*, vol. 34, no. 7, pp. 6062–6075, 2019, doi: 10.1109/TPEL.2018.2883129.

[121] ICNIRP, "ICNIRP guidelines for limiting exposure to time-varying electric and magnetic fields (1 Hz to 100 kHz)," *Health Phys.*, vol. 99, no. 6, pp. 818–836, Dec. 2010, doi: 10.1097/HP.0b013e3181f06c86.

[122] J. Kim *et al.*, "Coil Design and Shielding Methods for a Magnetic Resonant Wireless Power Transfer System," *Proc. IEEE*, vol. 101, no. 6, pp. 1332–1342, Jun. 2013, doi: 10.1109/JPROC.2013.2247551.

[123] A. A. S. Mohamed, A. Meintz, P. Schrafel, and A. Calabro, "Testing and Assessment of EMFs and Touch Currents From 25-kW IPT System for Medium-Duty EVs," *IEEE Trans. Veh. Technol.*, vol. 68, no. 8, pp. 7477–7487, Aug. 2019, doi: 10.1109/TVT.2019.2920827.

[124] M. Mohammad, E. T. Wodajo, S. Choi, and M. E. Elbuluk, "Modeling and Design of Passive Shield to Limit EMF Emission and to Minimize Shield Loss in Unipolar Wireless Charging System for EV," *IEEE Trans. Power Electron.*, vol. 34, no. 12, pp. 12235–12245, Dec. 2019, doi: 10.1109/TPEL.2019.2903788.

[125] S. Kim, H. Park, and J. Kim, "Design and Analysis of a Resonant Reactive Shield for a Wireless Power Electric Vehicle," *IEEE Trans. Microw. Theory Tech.*, vol. 62, no. 4, pp. 1057–1066, Apr. 2014, doi: 10.1109/TMTT.2014.2305404.

[126] S. Y. Choi, B. W. Gu, S. W. Lee, W. Y. Lee, J. Huh, and C. T. Rim, "Generalized Active EMF Cancel Methods for Wireless Electric Vehicles," *IEEE Trans. Power Electron.*, vol. 29, no. 11, pp. 5770–5783, Nov. 2014, doi: 10.1109/TPEL.2013.2295094.

[127] A. Zaheer, H. Hao, G. A. Covic, and D. Kacprzak, "Investigation of multiple decoupled coil primary pad topologies in lumped IPT systems for interoperable electric vehicle charging," *IEEE Trans. Power Electron.*, vol. 30, no. 4, pp. 1937–1955, Apr. 2015, doi: 10.1109/TPEL.2014.2329693.

[128] D. Patil, M. K. McDonough, J. M. Miller, B. Fahimi, and P. T. Balsara, "Wireless Power Transfer for Vehicular Applications: Overview and Challenges," *IEEE Trans. Transp. Electrif.*, vol. 4, no. 1, pp. 3–37, Mar. 2018, doi: 10.1109/TTE.2017.2780627.

[129] M. Budhia, G. Covic, and J. Boys, "A new IPT magnetic coupler for electric vehicle charging systems," *IECON 2010 - 36th Annu. Conf. IEEE Ind. Electron. Soc.*, pp. 2487–2492, Nov. 2010, doi: 10.1109/IECON.2010.5675350.

[130] M. Budhia, G. A. Covic, J. T. Boys, and C. Y. Huang, "Development and evaluation of single sided flux couplers for contactless electric vehicle charging," in *2011 IEEE Energy Conversion Congress and Exposition:*, Sep. 2011, pp. 614–621, doi: 10.1109/ECCE.2011.6063826.

[131] G. A. Covic, M. L. G. Kissin, D. Kacprzak, N. Clausen, and H. Hao, "A Bipolar Primary Pad Topology for EV Stationary Charging and Highway Power by Inductive Coupling," in *2011 IEEE Energy Conversion Congress and Exposition*, Sep. 2011, pp. 1832–1838, doi: 10.1109/ECCE.2011.6064008.

[132] S. Kim, A. Zaheer, G. A. Covic, and J. T. Boys, "Tripolar pad for inductive power transfer systems," in *IECON 2014 - 40th Annual Conference of the IEEE Industrial Electronics Society*, Oct. 2014, pp. 3066–3072, doi: 10.1109/IECON.2014.7048947.

[133] S. Kim, G. Covic, and J. Boys, "Tripolar Pad for Inductive Power Transfer Systems for EV Charging," *IEEE Trans. Power Electron.*, vol. 32, no. 7, pp. 5045–5056, Jul. 2017, doi: 10.1109/TPEL.2016.2606893.

[134] W. Zhang, J. C. White, A. M. Abraham, and C. C. Mi, "Loosely Coupled Transformer Structure and Interoperability Study for EV Wireless Charging Systems," *IEEE Trans. Power Electron.*, vol. 30, no. 11, pp. 6356–6367, Nov. 2015, doi: 10.1109/TPEL.2015.2433678.

[135] D. Kurschner, G. Ombach, and S. Mathar, "DD vehicle coil as interoperable solution for stationary wireless EV charging," in *Electric Vehicle Symposium & Exhibition - EVS 29 Symposium*, Jun. 2016, pp. 1–12.

[136] N. H. Kutkut and K. W. Klontz, "Design considerations for power converters supplying the SAE J-1773 electric vehicle inductive coupler," in *Proceedings of APEC 97 - Applied Power Electronics Conference*, Feb. 1997, vol. 2, pp. 841–847, doi: 10.1109/APEC.1997.575743.

[137] K. N. Mude and K. Aditya, "Comprehensive review and analysis of two-element resonant compensation topologies for wireless inductive power transfer systems," *Chinese J. Electr. Eng.*, vol. 5, no. 2, pp. 14–31, Jun. 2019, doi: 10.23919/CJEE.2019.000008.

[138] J. L. Villa, J. Sallán, J. Francisco, S. Osorio, and A. Llombart, "High-Misalignment Tolerant Compensation Topology For ICPT Systems," *IEEE Trans. Ind. Electron.*, vol. 59, no. 2, pp. 945–951, Feb. 2012, doi: 10.1109/TIE.2011.2161055.

[139] C. Wang, G. A. Covic, and O. H. Stielau, "Investigating an LCL Load Resonant Inverter for Inductive Power Transfer Applications," *IEEE Trans. Power Electron.*, vol. 19, no. 4, pp. 995–1002, Jul. 2004, doi: 10.1109/TPEL.2004.830098.

[140] S. Dieckerhoff, M. J. Ryan, and R. W. De Doncker, "IGBT-based LCL-Resonant Inverter for High-

Frequency Induction Heating," in *Conference Record of the 1999 IEEE Industry Applications Conference. Thirty-Forth IAS Annual Meeting (Cat. No.99CH36370)*, Oct. 1999, vol. 3, pp. 2039–2045, doi: 10.1109/IAS.1999.806017.

[141] J. Yang, X. Zhang, K. Zhang, X. Cui, C. Jiao, and X. Yang, "An LCC-SP Compensated Inductive Power Transfer System and Design Considerations for Enhancing Misalignment Tolerance," *IEEE Access*, vol. 8, pp. 193285–193296, 2020, doi: 10.1109/ACCESS.2020.3032793.

[142] N. Keeling, G. A. Covic, F. Hao, L. George, and J. T. Boys, "Variable Tuning in LCL Compensated Contactless Power Transfer Pickups," in *2009 IEEE Energy Conversion Congress and Exposition*, Sep. 2009, pp. 1826–1832, doi: 10.1109/ECCE.2009.5316169.

[143] Z. Pantic, S. Bai, and S. M. Lukic, "ZCS LCC-Compensated Resonant Inverter for Inductive-Power-Transfer Application," *IEEE Trans. Ind. Electron.*, vol. 58, no. 8, pp. 3500–3510, Aug. 2011, doi: 10.1109/TIE.2010.2081954.

[144] Y. Wang, Y. Yao, X. Liu, D. Xu, and L. Cai, "An LC/S Compensation Topology and Coil Design Technique for Wireless Power Transfer," *IEEE Trans. Power Electron.*, vol. 33, no. 3, pp. 2007–2025, Mar. 2018, doi: 10.1109/TPEL.2017.2698002.

[145] Y. Yao, S. Member, Y. Wang, S. Member, and X. Liu, "Particle Swarm Optimization-Based Parameter Design Method for S / CLC -Compensated IPT Systems Featuring High Tolerance to Misalignment and Load Variation," *IEEE Trans. Power Electron.*, vol. 34, no. 6, pp. 5268–5282, Jun. 2019, doi: 10.1109/TPEL.2018.2870530.

[146] A. P. Sample, B. H. Waters, S. T. Wisdom, and J. R. Smith, "Enabling Seamless Wireless Power Delivery in Dynamic Environments," *Proc. IEEE*, vol. 101, no. 6, pp. 1343–1358, Jun. 2013, doi: 10.1109/JPROC.2013.2252453.

[147] Y. Lim, H. Tang, S. Lim, and J. Park, "An Adaptive Impedance-Matching Network Based on a Novel Capacitor Matrix for Wireless Power Transfer," *IEEE Trans. Power Electron.*, vol. 29, no. 8, pp. 4403–4413, Aug. 2014, doi: 10.1109/TPEL.2013.2292596.

[148] A. P. Hu, J. T. Boys, and G. A. Covic, "ZVS frequency analysis of a current-fed resonant converter," in *7th IEEE International Power Electronics Congress. Technical Proceedings. CIEP 2000 (Cat. No.00TH8529)*, Oct. 2000, pp. 217–221, doi: 10.1109/CIEP.2000.891417.

[149] S. Samanta and A. K. Rathore, "A New Current-Fed CLC Transmitter and LC Receiver Topology for Inductive Wireless Power Transfer Application: Analysis, Design, and Experimental Results," *IEEE Trans. Transp. Electrif.*, vol. 1, no. 4, pp. 357–368, Dec. 2015, doi: 10.1109/TTE.2015.2480536.

[150] Witricity, "DRIVE 11 Evaluation System," 2019. Accessed: May 27, 2021. [Online]. Available: https://witricity.com/wp-content/uploads/2019/11/DRIVE_11_20191104-1.pdf.

[151] J. Tritschler, B. Goeldi, S. Reichert, and G. Griepentrog, "Comparison of different control strategies for series-series compensated inductive power transmission systems," in *2015 17th European Conference on Power Electronics and Applications (EPE'15 ECCE-Europe)*, Sep. 2015, pp. 1–8, doi: 10.1109/EPE.2015.7309309.

[152] P. Schumann, T. Diekhans, O. Blum, U. Brenner, and A. Henkel, "Compact 7 kW inductive charging system with circular coil design," in *2015 5th International Electric Drives Production Conference (EDPC)*, Sep. 2015, pp. 1–5, doi: 10.1109/EDPC.2015.7323222.

[153] T. Kan, R. Mai, P. P. Mercier, and C. C. Mi, "Design and Analysis of a Three-Phase Wireless Charging System for Lightweight Autonomous Underwater Vehicles," *IEEE Trans. Power Electron.*, vol. 33, no. 8, pp. 6622–6632, Aug. 2018, doi: 10.1109/TPEL.2017.2757015.

[154] M. Bojarski, E. Asa, K. Colak, and D. Czarkowski, "Analysis and Control of Multiphase Inductively Coupled Resonant Converter for Wireless Electric Vehicle Charger Applications," *IEEE Trans. Transp. Electrif.*, vol. 3, no. 2, pp. 312–320, Jun. 2017, doi: 10.1109/TTE.2016.2566921.

[155] H. Hao, G. A. Covic, and J. T. Boys, "A Parallel Topology for Inductive Power Transfer Power Supplies," *IEEE Trans. Power Electron.*, vol. 29, no. 3, pp. 1140–1151, Mar. 2014, doi: 10.1109/TPEL.2013.2262714.

[156] Y. Li, T. Lin, R. Mai, L. Huang, and Z. He, "Compact Double-Sided Decoupled Coils-Based WPT Systems for High-Power Applications: Analysis, Design, and Experimental Verification," *IEEE Trans. Transp. Electrif.*, vol. 4, no. 1, pp. 64–75, Mar. 2018, doi: 10.1109/TTE.2017.2745681.

[157] N. Xuan Bac, D. M. Vilathgamuwa, and U. K. Madawala, "A SiC-Based Matrix Converter Topology for Inductive Power Transfer System," *IEEE Trans. Power Electron.*, vol. 29, no. 8, pp. 4029–4038, Aug. 2014, doi: 10.1109/TPEL.2013.2291434.

[158] M. Moghaddami and A. I. Sarwat, "Single-Phase Soft-Switched AC-AC Matrix Converter with Power Controller for Bidirectional Inductive Power Transfer Systems," *IEEE Trans. Ind. Appl.*, vol. 54, no. 4, pp. 3760–3770, Jul. 2018, doi: 10.1109/TIA.2018.2820640.

[159] K. Colak, E. Asa, M. Bojarski, D. Czarkowski, and O. C. Onar, "A Novel Phase-Shift Control of Semibridgeless Active Rectifier for Wireless Power Transfer," *IEEE Trans. Power Electron.*, vol. 30, no. 11, pp. 6288–6297, Nov. 2015, doi: 10.1109/TPEL.2015.2430832.

[160] W. Chen, R. A. Chinga, S. Yoshida, J. Lin, C. Chen, and W. Lo, "A 25.6 W 13.56 MHz wireless power transfer system with a 94% efficiency GaN Class-E power amplifier," in *2012 IEEE/MTT-S International*

Microwave Symposium Digest, Jun. 2012, pp. 1–3, doi: 10.1109/MWSYM.2012.6258349.

[161] R. Rupp, T. Laska, O. Häberlen, and M. Treu, "Application specific trade-offs for WBG SiC, GaN and high end Si power switch technologies," in *2014 IEEE International Electron Devices Meeting*, Dec. 2014, pp. 2.3.1-2.3.4, doi: 10.1109/IEDM.2014.7046965.

[162] A. Kadavelugu *et al.*, "High-frequency design considerations of dual active bridge 1200 V SiC MOSFET DC-DC converter," in *2011 Twenty-Sixth Annual IEEE Applied Power Electronics Conference and Exposition (APEC)*, Mar. 2011, pp. 314–320, doi: 10.1109/APEC.2011.5744614.

[163] R. Bosshard and J. W. Kolar, "Multi-Objective Optimization of 50 kW/85 kHz IPT System for Public Transport," *IEEE J. Emerg. Sel. Top. Power Electron.*, vol. 4, no. 4, pp. 1370–1382, Dec. 2016, doi: 10.1109/JESTPE.2016.2598755.

[164] H. L. Li, A. P. Hu, G. A. Covic, and C. Sen Tang, "A new primary power regulation method for contactless power transfer," in *2009 IEEE International Conference on Industrial Technology*, Feb. 2009, pp. 1–5, doi: 10.1109/ICIT.2009.4939680.

[165] J. M. Miller, C. P. White, O. C. Onar, and P. M. Ryan, "Grid side regulation of wireless power charging of plug-in electric vehicles," in *2012 IEEE Energy Conversion Congress and Exposition (ECCE)*, Sep. 2012, pp. 261–268, doi: 10.1109/ECCE.2012.6342814.

[166] S. Krishnan, S. Bhuyan, V. P. Kumar, W. Wang, J. Al Afif, and K. S. Lim, "Frequency agile resonance-based wireless charging system for Electric Vehicles," in *2012 IEEE International Electric Vehicle Conference, IEVC 2012*, Mar. 2012, pp. 1–4, doi: 10.1109/IEVC.2012.6183212.

[167] H. H. Wu, G. A. Covic, J. T. Boys, and D. J. Robertson, "A Series-Tuned Inductive-Power-Transfer Pickup With a Controllable AC-Voltage Output," *IEEE Trans. Power Electron.*, vol. 26, no. 1, pp. 98–109, Jan. 2011, doi: 10.1109/TPEL.2010.2052069.

[168] C. Y. Huang, J. T. Boys, and G. A. Covic, "LCL Pickup Circulating Current Controller for Inductive Power Transfer Systems," *IEEE Trans. Power Electron.*, vol. 28, no. 4, pp. 2081–2093, Apr. 2013, doi: 10.1109/TPEL.2012.2199132.

[169] T. Diekhans and R. W. De Doncker, "A Dual-Side Controlled Inductive Power Transfer System Optimized for Large Coupling Factor Variations and Partial Load," *IEEE Trans. Power Electron.*, vol. 30, no. 11, pp. 6320–6328, Nov. 2015, doi: 10.1109/TPEL.2015.2393912.

[170] H. H. Wu, A. Gilchrist, K. D. Sealy, and D. Bronson, "A High Efficiency 5 kW Inductive Charger for EVs Using Dual Side Control," *IEEE Trans. Ind. Informatics*, vol. 8, no. 3, pp. 585–595, Aug. 2012, doi: 10.1109/TII.2012.2192283.

[171] M. Borage, S. Tiwari, and S. Kotaiah, "Analysis and design of an LCL-T resonant converter as a constant-current power supply," *IEEE Trans. Ind. Electron.*, vol. 52, no. 6, pp. 1547–1554, Dec. 2005, doi: 10.1109/TIE.2005.858729.

[172] W. P. Choi, W. C. Ho, X. Liu, and S. Y. R. Hui, "Comparative study on power conversion methods for wireless battery charging platform," in *Proceedings of 14th International Power Electronics and Motion Control Conference EPE-PEMC 2010*, Sep. 2010, pp. S15-9-S15-16, doi: 10.1109/EPEPEMC.2010.5606675.

[173] B. Sharp and H. Wu, "Asymmetrical voltage-cancellation control for LCL resonant converters in inductive power transfer systems," in *2012 Twenty-Seventh Annual IEEE Applied Power Electronics Conference and Exposition (APEC)*, Feb. 2012, pp. 661–666, doi: 10.1109/APEC.2012.6165889.

[174] R. W. Erickson and D. Maksimovic, *Fundamentals of Power Electronics*, 2nd ed. Boston, MA, USA: Springer, 2001.

[175] S. Aldhaher, "Design and Optimization of Switched-Mode Circuits for Inductive Links," Cranfield University, Cranfield, U.K., 2014.

[176] M. K. Kazimierczuk and D. Czarkowski, *Resonant Power Converters*. Hoboken, New Jersey: John Wiley & Sons, Inc., 2011.

[177] T. Huria, M. Ceraolo, J. Gazzarri, and R. Jackey, "High fidelity electrical model with thermal dependence for characterization and simulation of high power lithium battery cells," in *2012 IEEE International Electric Vehicle Conference*, Mar. 2012, pp. 1–8, doi: 10.1109/IEVC.2012.6183271.

[178] M. Bartoli, A. Reatti, and M. K. Kazimierczuk, "High-frequency models of ferrite core inductors," *Proc. IECON'94 - 20th Annu. Conf. IEEE Ind. Electron.*, vol. 3, no. 39, pp. 1670–1675, Sep. 1994, doi: 10.1109/IECON.1994.398065.

[179] G. Ombach, D. Kurschner, S. Mathar, and W. Chlebosz, "Optimum magnetic solution for interoperable system for stationary wireless EV charging," in *2015 Tenth International Conference on Ecological Vehicles and Renewable Energies (EVER)*, Mar. 2015, pp. 1–8, doi: 10.1109/EVER.2015.7112996.

[180] P. Seibold, "Sine Fitting," *MATLAB Central File Exchange*, 2021. https://www.mathworks.com/matlabcentral/fileexchange/66793-sine-fitting (accessed Mar. 17, 2021).

[181] R. Huang and B. Zhang, "Frequency, Impedance Characteristics and HF Converters of Two-Coil and Four-Coil Wireless Power Transfer," *IEEE J. Emerg. Sel. Top. Power Electron.*, vol. 3, no. 1, pp. 177–183, Mar. 2015, doi: 10.1109/JESTPE.2014.2315997.

[182] F. E. Terman, *Radio Engineers' Handbook*. New York: McGraw-Hill, 1943.

[183] M. Košík and J. Lettl, "Analysis of Bifurcation in Series-Series and Series-Parallel Compensated Inductive

Power Transfer," in *2019 IEEE PELS Workshop on Emerging Technologies: Wireless Power Transfer (WoW)*, Jun. 2019, pp. 75–80, doi: 10.1109/WoW45936.2019.9030605.

[184] S. Li, W. Li, J. Deng, T. D. Nguyen, and C. C. Mi, "A Double-Sided LCC Compensation Network and Its Tuning Method for Wireless Power Transfer," *IEEE Trans. Veh. Technol.*, vol. 64, no. 6, pp. 2261–2273, Jun. 2015, doi: 10.1109/TVT.2014.2347006.

[185] E. W. Weisstein, "Quartic Equation. From MathWorld - A Wolfram Web Resource [Online]," Nov. 2011. https://mathworld.wolfram.com/QuarticEquation.html (accessed Apr. 05, 2021).

[186] M. Košík and J. Lettl, "A Study of a Bifurcation Evaluation Method for IPT," in *2018 IEEE PELS Workshop on Emerging Technologies: Wireless Power Transfer (Wow)*, Jun. 2018, pp. 1–6, doi: 10.1109/WoW.2018.8450911.

[187] M. Košík, A. D. Scher, and J. Lettl, "Novel Method of Coupling Coefficient Estimation Based on the Bifurcation Phenomena in Inductive Power Transfer," *Electronics*, vol. 10, no. 2548, pp. 1–18, Oct. 2021, doi: 10.3390/ electronics10202548.

[188] K. Aditya and S. S. Williamson, "A Review of Optimal Conditions for Achieving Maximum Power Output and Maximum Efficiency for a Series-Series Resonant Inductive Link," *IEEE Trans. Transp. Electrif.*, vol. 3, no. 2, pp. 303–311, Jun. 2017, doi: 10.1109/TTE.2016.2582559.

[189] S. De Simone, "LLC resonant half-bridge converter design guideline, Rev 6," Mar. 2014. [Online]. Available: https://www.st.com/resource/en/application_note/cd00143244-llc-resonant-half-bridge-converter-design-guideline-stmicroelectronics.pdf.

[190] Y. Jiang, L. Wang, Y. Wang, J. Liu, X. Li, and G. Ning, "Analysis, Design, and Implementation of Accurate ZVS Angle Control for EV Battery Charging in Wireless High-Power Transfer," *IEEE Trans. Ind. Electron.*, vol. 66, no. 5, pp. 4075–4085, May 2019, doi: 10.1109/TIE.2018.2795523.

[191] I.-W. Iam *et al.*, "Constant-Frequency and Non-Communication-Based Inductive Power Transfer Converter for Battery Charging," *IEEE J. Emerg. Sel. Top. Power Electron.*, pp. 1–1, 2020, doi: 10.1109/JESTPE.2020.3004259.

[192] Y. Narusue, Y. Kawahara, and T. Asami, "Maximizing the efficiency of wireless power transfer with a receiver-side switching voltage regulator," *Wirel. Power Transf.*, vol. 4, no. 1, pp. 42–54, 2017, doi: 10.1017/wpt.2016.14.

[193] A. D. Scher, M. Kosik, P. Pham, D. Costinett, and E. Hossain, "Stability Analysis and Efficiency Optimization of an Inductive Power Transfer System with a Constant Power Load," *IEEE Access*, vol. 8, pp. 209762–209775, 2020, doi: 10.1109/ACCESS.2020.3039181.

[194] Y. Zhang, T. Kan, Z. Yan, and C. C. Mi, "Frequency and Voltage Tuning of Series–Series Compensated Wireless Power Transfer System to Sustain Rated Power Under Various Conditions," *IEEE J. Emerg. Sel. Top. Power Electron.*, vol. 7, no. 2, pp. 1311–1317, Jun. 2019, doi: 10.1109/JESTPE.2018.2871636.

[195] J.-S. Hong and M. J. Lancaster, *Microstrip Filters for RF/Microwave Applications*. New York: John Wiley & Sons, Inc., 2001.

[196] V. Jiwariyavej, T. Imura, and Y. Hori, "Coupling Coefficients Estimation of Wireless Power Transfer System via Magnetic Resonance Coupling Using Information From Either Side of the System," *IEEE J. Emerg. Sel. Top. Power Electron.*, vol. 3, no. 1, pp. 191–200, Mar. 2015, doi: 10.1109/JESTPE.2014.2332056.

[197] S. Bai, Z. Pantic, and S. Lukic, "A Comparison Study of Control Strategies for ZVS Resonant Converters," *IECON Proc. (Industrial Electron. Conf.*, vol. 1, pp. 256–262, Nov. 2010, doi: 10.1109/IECON.2010.5675019.

[198] R. Bosshard, J. W. Kolar, and B. Wunsch, "Control method for Inductive Power Transfer with high partial-load efficiency and resonance tracking," in *2014 International Power Electronics Conference (IPEC-Hiroshima 2014 - ECCE ASIA)*, May 2014, pp. 2167–2174, doi: 10.1109/IPEC.2014.6869889.

[199] Y. Shin *et al.*, "Design Considerations for Adding Series Inductors to Reduce Electromagnetic Field Interference in an Over-Coupled WPT System," *Energies*, vol. 14, no. 10, pp. 1–28, May 2021, doi: 10.3390/en14102791.

[200] A. Rohatgi, "Webplotdigitizer: Version 4.4," 2020. https://automeris.io/WebPlotDigitizer (accessed May 19, 2021).

[201] T. C. Beh, M. Kato, T. Imura, S. Oh, and Y. Hori, "Automated impedance matching system for robust wireless power transfer via magnetic resonance coupling," *IEEE Trans. Ind. Electron.*, vol. 60, no. 9, pp. 3689–3698, 2013, doi: 10.1109/TIE.2012.2206337.

[202] D. A. G. Pedder, A. D. Brown, and J. Andrew Skinner, "A contactless electrical energy transmission system," *IEEE Trans. Ind. Electron.*, vol. 46, no. 1, pp. 23–30, Feb. 1999, doi: 10.1109/41.744372.

[203] K. Yan, Q. Chen, J. Hou, X. Ren, L. Cao, and X. Ruan, "Self-Oscillating Contactless Resonant Converter With Phase Detection Contactless Current Transformer," *IEEE Trans. Power Electron.*, vol. 29, no. 8, pp. 4438–4449, Aug. 2014, doi: 10.1109/TPEL.2014.2300938.

[204] L. Xu, Q. Chen, X. Ren, S. C. Wong, and C. K. Tse, "Self-Oscillating Resonant Converter with Contactless Power Transfer and Integrated Current Sensing Transformer," *IEEE Trans. Power Electron.*, vol. 32, no. 6, pp. 4839–4851, Jun. 2017, doi: 10.1109/TPEL.2016.2598556.

[205] W. Zhang, S. C. Wong, C. K. Tse, and Q. Chen, "Analysis and Comparison of Secondary Series- and

Parallel-Compensated Inductive Power Transfer Systems Operating for Optimal Efficiency and Load-Independent Voltage-Transfer Ratio," *IEEE Trans. Power Electron.*, vol. 29, no. 6, pp. 2979–2990, Jun. 2014, doi: 10.1109/TPEL.2013.2273364.

[206] E. Gati, G. Kampitsis, and S. Manias, "Variable Frequency Controller for Inductive Power Transfer in Dynamic Conditions," *IEEE Trans. Power Electron.*, vol. 32, no. 2, pp. 1684–1696, Feb. 2017, doi: 10.1109/TPEL.2016.2555963.

12 List of Author's Publications

12.1 Publications Related to the Thesis

12.1.1 Publications in Journals with Impact Factor

M. Kosik, A. D. Scher, and J. Lettl, "Novel Method of Coupling Coefficient Estimation Based on the Bifurcation Phenomena in Inductive Power Transfer," *Electronics*, vol. 10, no. 2548, pp. 1–18, Oct. 2021
Impact factor 2020: 2.397 (Q3)
Contribution: 65 %
Number of citations in WoS: 0

M. Kosik, A. D. Scher, and J. Lettl, "Description, Mechanism and Impacts of Bifurcation and Frequency Splitting on Inductive Power Transfer," *IEEE Access*, (**in review**)
Impact factor 2020: 3.367 (Q2)
Contribution: 65 %
Number of citations in WoS: 0

A. D. Scher, M. Kosik, P. Pham, D. Costinentt, and E. Hossain, "Stability Analysis and Efficiency Optimization of an Inductive Power Transfer System with a Constant Power Load," in *IEEE Access*, vol. 8, pp. 209762–209775, 2020
Impact factor 2020: 3.367 (Q2)
Contribution: 20 %
Number of citations in WoS: 0

12.1.2 Publications Cited in Web of Science

M. Kosik, and J. Lettl, "Study of Bifurcation Evaluation Method for IPT ," *2018 IEEE PELS Workshop on Emerging Technologies: Wireless Power Transfer (WOW)*, Montreal, 2018, pp. 1-6
Contribution: 50 %
Number of citations in WoS: 0

M. Kosik, R. Fajtl, and J. Lettl, "Analysis of Bifurcation in Two-Coil Inductive Power Transfer," *2017 IEEE 18th Workshop on Control and Modeling for Power Electronics (COMPEL)*, Stanford, 2017, pp. 1-8
Contribution: 33.3 %
Number of citations in WoS: 3

M. Košík, R. Fajtl and J. Lettl, "Theoretical evaluation of bifurcation in dependence on resonance frequency in two-coil inductive power transfer," *2017 International Conference on Applied Electronics (AE)*, Pilsen, 2017, pp. 1-6
Contribution: 33.3 %
Number of citations in WoS: 0

12.1.3 Other Publications

M. Kosik and J. Lettl, "Analysis of Bifurcation in Series-Series and Series-Parallel Compensated Inductive Power Transfer," *2019 IEEE PELS Workshop on Emerging Technologies: Wireless Power Transfer (WoW)*, London, 2019, pp. 75-80
Contribution: 50 %

M. Kosik, Fajtl, R., Buhr, K., and Lettl, "Model of Power Electronics Used for Electric Vehicles Contactless Charging", PIERS 2015 Proceedings, Electromagnetics Academy, Cambridge, 2015, pp. 1-6
Contribution: 25 %

M. Kosik, "Electric Vehicle Charger Utilizing Contactless Power Transfer", *POSTER 2015 - 19th International Student Conference on Electrical Engineering*, 2015, Czech Technical University, Prague, 2015, pp. 1-7, 2015, ISBN 978-80-01-05728-5
Contribution: 100 %

12.2 Publications Unrelated to the Thesis

M. Kosik, "Control System for Electric Vehicle", *POSTER 2014 - 18th International Student Conference on Electrical Engineering*, 2014, Czech Technical University, Prague, pp. 1-5, 2014, ISBN 978-80-01-05499-4
Contribution: 100 %

Appendices

A1. Additional Information for Measurement Setup Components

Linear Amplifier

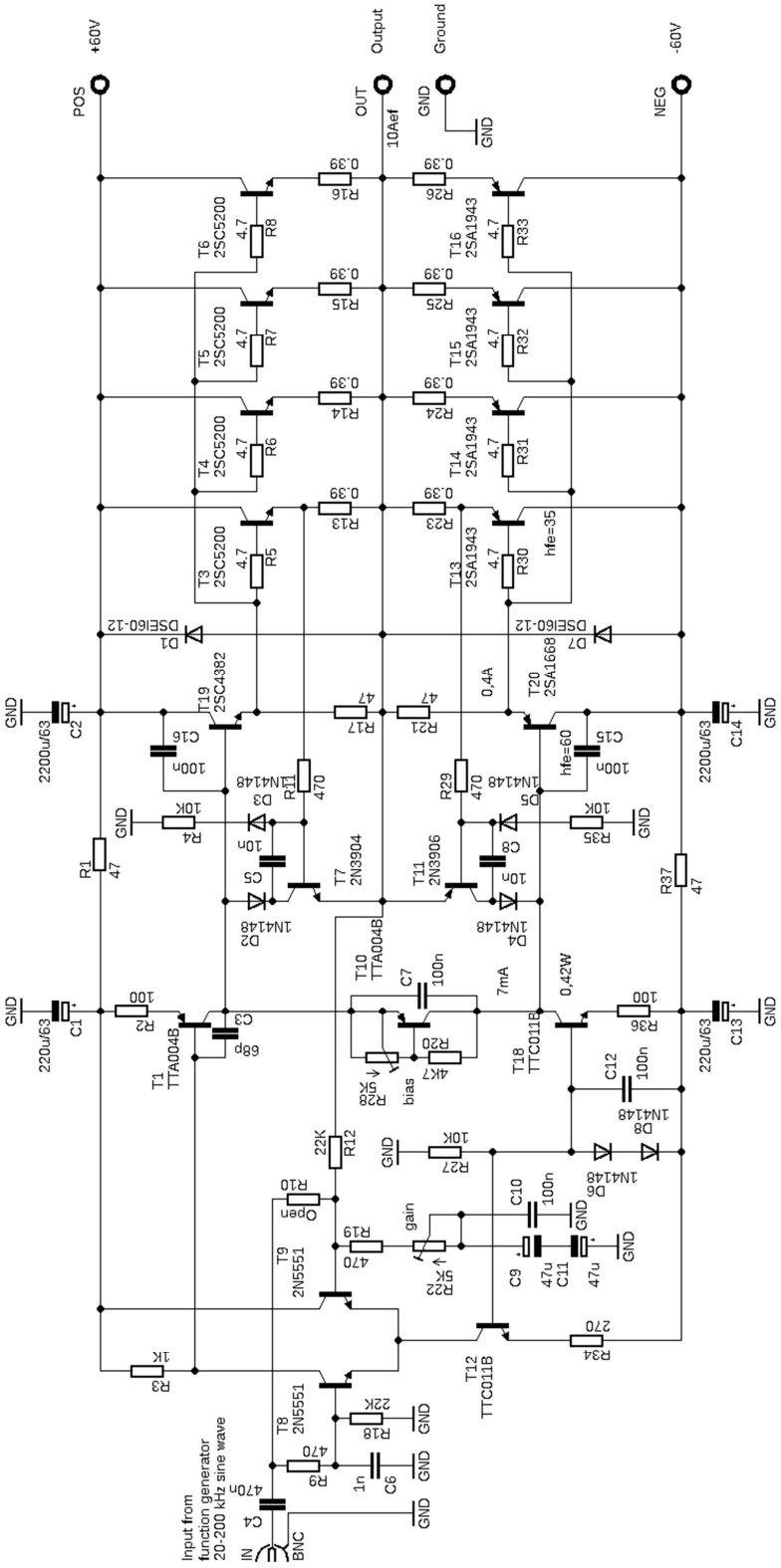

Fig. 105: Linear amplifier schematics. Resistors R9 and R10 are used to select, whether the amplifier output will be in phase (R9 mounted) or inverted (R10 mounted) with respect to the amplifier input form the generator. Both would have the same value of 470 Ω.

Pads

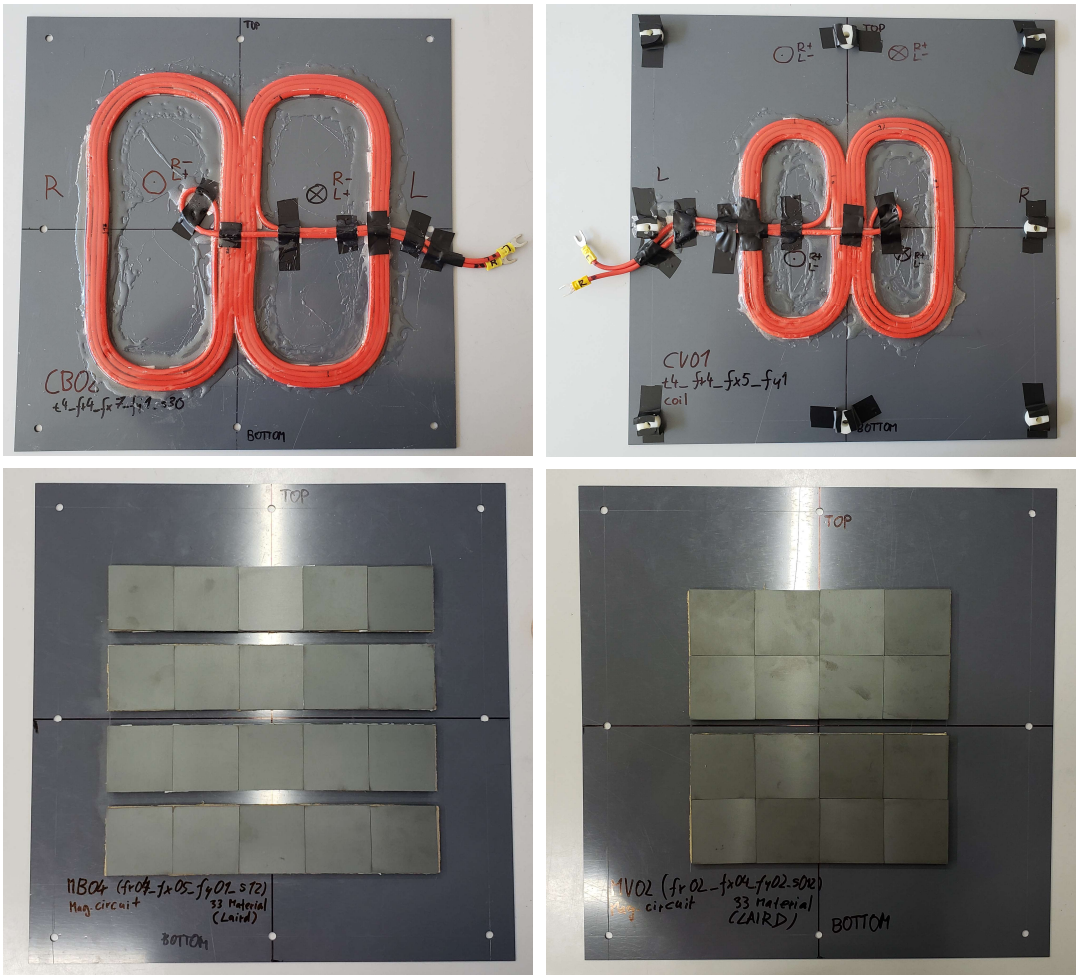

Fig. 106: Pad assembly. Transmitter pad (a) winding, (c) magnetic core. Receiver pad (b) winding, (d) magnetic core. All parts are placed on the plastic sheets of the same size. For each respective pad, its winding outer dimensions match the outer dimensions of the magnetic core.

Capacitive Decade

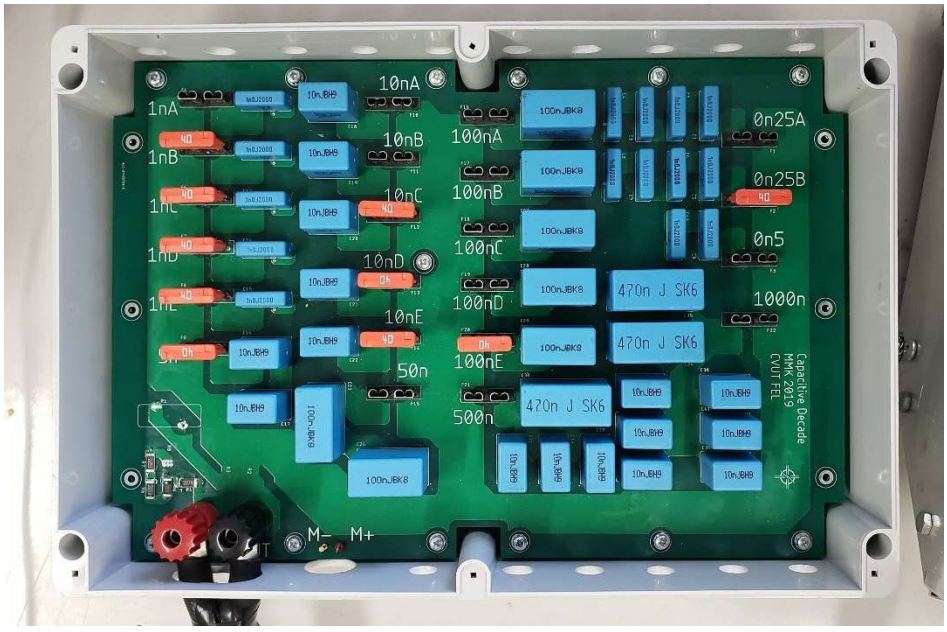

Fig. 107: Photo of capacitive decade for the secondary compensation. Decade for the primary compensation is identical.

Resistive Decade

Table 37: Resistor values of the resistive decade.

	Cell	1	2	3	4	5	6	7
Block 1	Resistor	R1A	R1B	R2	R3A	R3B	R4A	R4B
	Value	1 Ω	1 Ω	1 Ω	4.7 Ω	4.7 Ω	4.7 Ω	4.7 Ω
	Connection	Series	Parallel	Series	Series	Parallel	Series	Parallel
Block 2	Section 2	R5	R6A	R6B	R7	R8	R9A	R9B
	Value	4.7 Ω	10 Ω	10 Ω	15 Ω	22 Ω	100 Ω	100 Ω
	Connection	Input	Series	Parallel	Series	Series	Series	Parallel

Resistor values were selected to cover the range of 0.5-150 Ω with step approximately of 0.5 Ω from resistors available at the market. Resistors marked by B are connected in parallel by the blade fuses with their counterparts marked by A. Blade fuses at series cells short circuit the resistors (both marked with A and those marked by B connected in series.

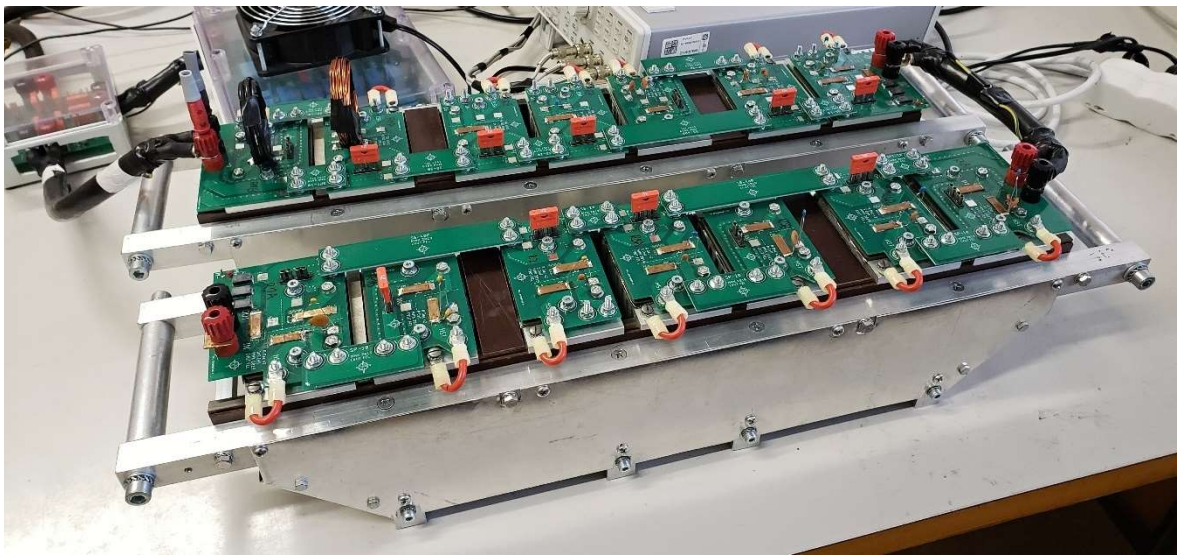

Fig. 108: Photo of resistive decade used as the load.

Switchboards

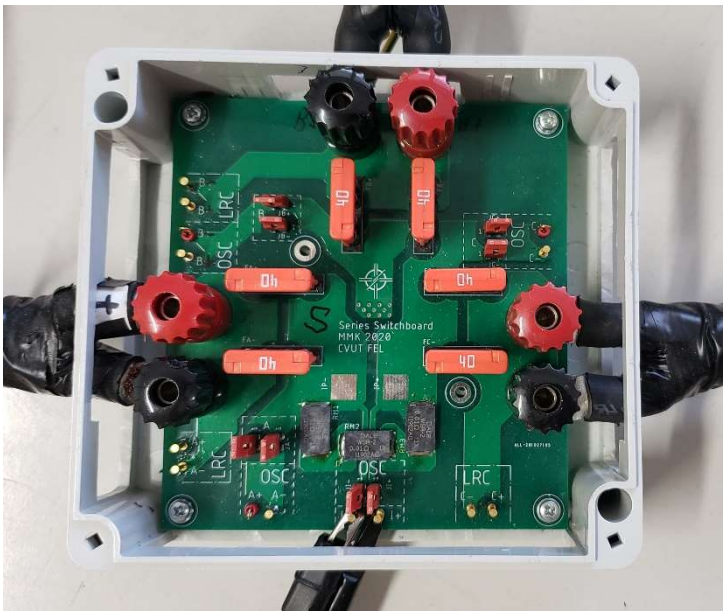

Fig. 109: Secondary side switchboard for series compensation. Primary side switchboard is identical.

A2. Measurement of Current Shunt Parameters

The current shunt resistance and especially its inductance are too small to be measured with a LRC meter, thus a more complicated approach has to be taken. The current shunt parameters were calculated from voltages and currents obtained in following procedure. The same setup was used as for the regular IPT operation (see Fig. 17). The system was loaded by resistor decade combination yielding 32 Ω (R8 in series with R6A) at which the phase shift was too small to be measurable even at 200 kHz. Thanks to its large value, the measurement of its parameters by LRC meter is not impacted by parasitic influences such as transition resistance, uncompensated inductance of probe cables, etc. as is the measurement of 30 mΩ current shunt. Thus, 32 Ω load can be used as a reference for the calculation of the current shunt parameters. The load resistance parameters were measured with the LRC meter in the frequency range 1-200 kHz – see Table 38. The load resistance values were fitted with the second order polynomial to obtain its model used in the further calculations. The phase was considered zero in the whole frequency range.

Table 38: Frequency dependence of 32 Ω load used for shunt calibration.

f [kHz]	1.00	10.00	20.00	40.00	50.00	72.00	100.00	120.00	150.00	180.00	200.00
Z [Ω]	31.652	31.670	31.684	31.706	31.714	31.728	31.752	31.766	31.781	31.799	31.812
φ [deg]	0.013	0.037	0.052	0.056	0.051	0.190	0.016	-0.084	0.024	0.030	-0.063
R [Ω]	31.652	31.670	31.684	31.706	31.714	31.728	31.752	31.766	31.781	31.799	31.812

The switchboard with measured shunt was placed in the secondary side so the same current flow through the shunt as through the load. The frequency responses of voltages $\hat{V}_L$ and $\hat{V}_{CS}$ were measured at the load and the current shunt, respectively for resonance frequencies 30 kHz, 50kHz, 80kHz, 100 kHz and 150kHz. Each frequency response had between 25 – 50 points. All samples generate frequency range of 25-165 kHz. These values are used the most in bifurcation analysis.

For each point the current amplitude I_L was calculated from V_L (the same current flows through the shunt and the load as they are in the series) at the and load resistance model. Current phase φ_L was considered equal at zero as the load is considered the pure resistance. From the calculated I_L and current shunt voltage amplitude V_{CS} and phase φ_{CS} (with respect to $\hat{V}_L$) obtained by the measurement, the shunt resistance R_{cs} and inductance L_{cs} was calculated as:

$$Z_{CS} = \frac{V_{CS}}{I_L} \tag{148}$$

$$R_{CS} = Z_{CS} cos\varphi_{CS} \tag{149}$$

$$L_{CS} = \frac{Z_{CS} cos\varphi_{CS}}{2\pi f} \tag{150}$$

Plotting of R_{cs} and L_{cs} showed, that there is a correlation between their values and frequency (see Fig. 110 (b) and (d)). For this reason, R_{cs} and L_{cs} values were fitted with the first order polynomial to obtain frequency dependent models (red in Fig. 110 (b) and (d)):

$$R_{CS} = 6.6066 \cdot 10^{-9} f + 3.0063 \cdot 10^{-2}\ [\Omega] \tag{151}$$

$$L_{CS} = -4.1765 \cdot 10^{-15} f + 1.2213 \cdot 10^{-8}\ [H] \tag{152}$$

Listed models of R_{cs} and L_{cs} belong to the secondary switchboard current shunt.

These models are further used in processing of the current shunt voltage $\hat{V}_L$ – in the correction of the phase shift and calculation of the current. Fig. 110 (a) depicts φ_{CS} across the measured frequency range and Fig. 110 (c) – red represents φ_{CS} calculated from the models of R_{cs} and L_{cs}. The difference between the calculated and measured φ_{CS} is showed in Fig. 110 (d). For most of the data, it fits in range of ±0.3 degree.

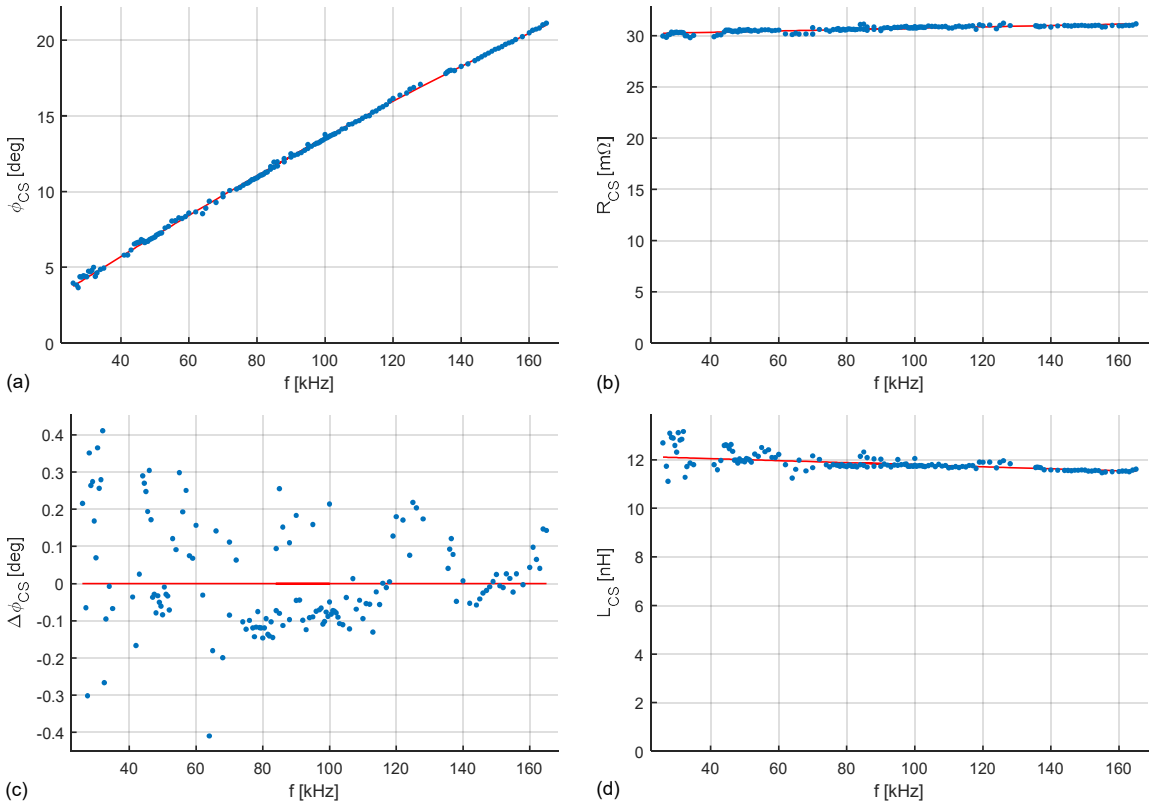

Fig. 110: Obtaining the parameter models of secondary switchboard current shunt. Red – value calculated from the model. Blue – measured data. (a) Phase shift of the current shunt, which needs to be corrected. (c) Difference of φ_{CS} calculated from the model and measured φ_{CS}. (b) Current shunt resistance R_{CS}. (d) Current shunt inductance L_{CS}.

A3. Numerical Approach to Obtain IAB Frequencies

The numerical approach to solve the input amplitude bifurcation (IAB) governing equation (96) is based on the bisection method adjusted to employ MATLAB matrix operations capabilities. The numerical approximation of the roots consists of two cycles – the superordinate goes through the R_L interval and in each step the subordinate searches for the numerical solution of (96) for all of its positive roots.

In general, the numerical solution can be divided in two main parts: setting the root search interval and root approximation method, which is applied to the root search interval. The superordinate cycle always starts for the lowest value of R_L, which correlates with deep region RG4. Thanks to this, a following set of observations based on Fig. 35 (a) can be applied:

(A) If R_L is small enough, the roots u_{ai0}, u_{ai1}, u_{ai} near closely to their corresponding PB roots $u_{\varphi 0}$, $u_{\varphi 1}$, $u_{\varphi 2}$.

(B) With increasing R_L, roots u_{ai} , u_{ai2} only move closer to 1.

Thanks to the observation (A), the initial root search interval can be calculated from the $u_{\varphi 1}$, $u_{\varphi 2}$ values as (A3.1), where c_{R1} is the initial range extension coefficient – u_{ai} is always slightly lower than $u_{\varphi 1}$ and u_{ai2} slightly higher than $u_{\varphi 2}$ for small R_L.

$$u_{aI,1} = \langle u_{\varphi 1}(1 - c_{R1}), u_{\varphi 2}(1 + c_{R1}) \rangle \tag{A3.1}$$

Due to observation (B), the initial root search interval for the following steps of the superordinate cycle is calculated from the values of u_{ai} , u_{ai} , u_{ai} approximated in the previous step as $\langle u_{aI,iB}, u_{aI,iT} \rangle$:

$$u_{aI,iB} = min(u_{a0}, u_{a1}, u_{a2})(1 - c_R) \tag{A3.2}$$

$$u_{aI,iT} = \mathrm{max}(u_{a0}, u_{a1}, u_{a2})(1 + c_R) \tag{A3.3}$$

where c_R is the range extension coefficient. The 1st derivative of Z_n is always continuous on the root search interval.

Because the goal is to find three roots and it is not simple to determine their individual root search areas, the method has two phases. In the first phase, the initial root search interval described previously is searched for the raw individual root search intervals of u_{a0}, u_{a1}, u_{a2}. In the second phase these individual root search intervals are searched iteratively to obtain the root approximations with the maximal allowed error $u_{e,Max}$. In the presented method, until the result calculation, the roots are not represented by a single point, but by a root interval, inside which the real root value is with probability of 1.

In both phases, the same algorithm is applied. The algorithm evaluates input root interval for presence of roots based on the zero crossing and to each root assigns a new root interval with the increased precision. Over the searched interval u_{aI}, a vector of evenly spaced n points is generated (selected number of points is 100). For the vector, the value of the normalized impedance amplitude 1st derivative Z_{1d} is calculated (left side of (96). The set of values is stored as Z_{1d}. The Z_{1d} values are circularly shifted one position to left and stored as $Z_{1d,CS}$. The product of Z_{1d} and $Z_{1d,CS}$ is calculated. It is always positive except the first point of the point pair, between which the zero crossing occurs. Based on this, all roots can be detected by the product value lower than 0. Their interval is given by the point with the negative product value and the next point.

However, this approach results in an apparent zero crossing, if the number of roots is odd – due to the circular shift is multiplied the first and the last point of the root interval u_{aI}, which results in the negative value at the end of the interval. This does not impact the method, because if the crossing is between the points 1,2, it will be flagged at 1, and if it is between the points n-1, n, it will be flagged at n-1. Thus, this apparent crossing can be removed without any consequences.

The algorithm returns the set of the root intervals. In the first phase of the subordinate cycle, there will be three root intervals for IAB and one root interval outside the bifurcation phase. In the second phase, the algorithm is employed for each root iteratively (resulting root interval of the last step is the input for the following step), until the interval error $u_{ax,e}$ calculated as

$$u_{ax,e} = \frac{u_{axI,H} - u_{axI,L}}{2} \tag{A3.4}$$

is smaller than the maximal allowed error $u_{e,Max}$. The root is then calculated as:

$$u_{ax} = \frac{u_{axI,L} + u_{axI,H}}{2} \tag{A3.5}$$

In both cases, $u_{axI,L}$ and $u_{axI,H}$ are the limit points of the root interval $u_{axI} = \langle u_{axI,L}, u_{axI,H} \rangle$.